A new atmospheric dataset for High Asia

Development, validation and applications
in climatology and in glaciology

vorgelegt von
Fabien Maussion
aus Berlin

Von der Fakultät VI – Planen Bauen Umwelt
der Technische Universität Berlin
zur Erlangung des akademischen Grades

Doktor der Naturwissenschaften
- Dr. rer. nat. -

genehmigte Dissertation

Promotionsausschuss:

Vorsitzende: Prof. Dr. Birgit Kleinschmit
Gutachter: Prof. Dr. Dieter Scherer
Gutachter: Prof. Dr. Christoph Schneider
Gutachter: Prof. Dr. Georg Kaser

Tag der wissenschaftlichen Aussprache: 21.02.2014

Berlin 2014
D 83

List of Papers

This thesis is based on the following papers:

I. **Maussion, F.**, Scherer, D., Finkelnburg, R., Richters, J., Yang, W., and Yao, T. (2011): WRF simulation of a precipitation event over the Tibetan Plateau, China – an assessment using remote sensing and ground observations, *Hydrology and Earth System Sciences*, 15, 1795-1817, doi:10.5194/hess-15-1795-2011

II. **Maussion, F.**, Scherer, D., Mölg, T., Collier, E., Curio, J. and Finkelnburg, R. (2014): Precipitation seasonality and variability over the Tibetan Plateau as resolved by the High Asia Reanalysis, *Journal of Climate*, 27, 1910-1927, doi:10.1175/JCLI-D-13-00282.1

III. Mölg, T., **Maussion, F.**, Yang, W., and Scherer, D. (2012): The footprint of Asian monsoon dynamics in the mass and energy balance of a Tibetan glacier, *The Cryosphere*, 6, 1445-1461, doi:10.5194/tc-6-1445-2012

IV. Kropacek, J., **Maussion, F.**, Chen, F., Hoerz, S., and Hochschild, V. (2013): Analysis of ice phenology of lakes on the Tibetan Plateau from MODIS data, *The Cryosphere*, 7, 287-301, doi:10.5194/tc-7-287-2013

V. Bolch, T., Yao, T., Kang, S., Buchroithner, M. F., Scherer, D., **Maussion, F.**, Huintjes, E., and Schneider, C. (2010): A glacier inventory for the western Nyainqentanglha Range and Nam Co Basin, Tibet, and glacier changes 1976–2009, *The Cryosphere*, 4, 419-433, doi:10.5194/tc-4-419-2010

The author made following contributions to the thesis' papers:

I, II: responsible for the study design, numerical simulations, data preparation, data analysis, figures and writing

III: responsible for the field work, measurement data acquisition/preparation, atmospheric simulations; contribution to the study design and data analysis; minor contribution to the writing

IV: responsible for climate data preparation; contribution to the figures, analysis and writing

V: contribution to the literature review, minor contribution to the analysis and writing

The author also contributed to following publications/manuscripts which are of relevance for the thesis:

i. Collier, E., Mölg, T., **Maussion, F.**, Scherer, D., Mayer, C., and Bush, A. B. G. (2013): High-resolution interactive modelling of the mountain glacier-atmosphere interface: an application over the Karakoram, *The Cryosphere*, 7, 779-795, doi:10.5194/tc-7-779-2013

ii. Dietze, E., **Maussion, F.**, Ahlborn, M., Diekmann, B., Hartmann, K., Henkel, K., Kasper, T., Lockot, G., Opitz, S., Haberzettl, T. (2014): Sediment transport processes across the Tibetan Plateau inferred from robust grain size end-members in lake sediments, *Clim. Past*, 10, 91-106, doi:10.5194/cp-10-91-2014

iii. Mölg, T., **Maussion, F.**, Scherer, D. (2014): Mid-latitude westerlies as a driver of glacier variability in monsoonal High Asia, *Nature Climate Change*, 4, 68-73, doi:10.1038/nclimate2055

Contents

Nomenclature

AWS	Automatic Weather Station
BMBF	Bundesministerium für Bildung und Forschung
CAME	Central Asia – Monsoon dynamics and Geo-ecosystems (BMBF Programme)
CAS	Chine Academy of Sciences
CRU	Climate Research Unit
DFG	Deutsche Forschung Gemeinschaft
DynRG-TiP	Dynamic Response of Glaciers on the Tibetan Plateau to Climate Change (DFG Project)
ECMWF	European Centre for Medium-Range Weather Forecasts
ERA	ECMWF re-analysis
GCM	General Circulation Model
GPCC	Global Precipitation Climatology Centre
GPCP	Global Precipitation Climatology Project
HAR	High Asia Reanalysis
IPCC	Intergovernmental Panel on Climate Change
ISM	Indian Summer Monsoon
ITP	Institute of Tibetan Plateau Research, CAS
LAM	Limited Area Model
MAD	Mean Absolute Deviation
MB	Mass Balance
MD	Mean Deviation (bias)
MODIS	Moderate Resolution Imaging Spectroradiometer
NCAR	National Center for Atmospheric Research
NCEP	National Centers for Environmental Prediction
NWP	Numerical Weather Prediction (model)
PBL	Planetary Boundary Layer
RCM	Regional Climate Model
RMSD	Root Mean Squared Deviation
SEB	Surface Energy Balance
ST	Surface Temperature
TP	Tibetan Plateau and surrounding mountain ranges
TRMM	Tropical Rainfall Measuring Mission
WET	Variability and Trends in Water Balance Components of Benchmark Drainage Basins on the Tibetan Plateau (BMBF Project)
WRF	Weather Research and Forecasting (model)

Tibetan Nomads and Nyainqentanglha Range near Nam Co lake. Photo by F.M., May 2009.

"Le Ningling-Tanla attire plus longtemps nos regards. Cette chaîne développe devant nous son arête poudrée de neige et nous barre parfaitement l'horizon. On est surpris de sa régularité, de l'altitude presque égale à l'œil de cette suite de cimes surmontant des contreforts qui s'abaissent vers le lac, bien alignés comme le pourraient être les tentes d'une armée. Et juste au milieu, précisément au point où s'avance en grand'garde ce que nous supposons être un promontoire, si ce n'est une île, on voit, dominant majestueusement tout le paysage, quatre grands pics de glace que les Tibétains révèrent, car derrière eux est Lhaça, la ville des Esprits. [...] On constate la véracité du mot tibétain: 'L'eau du Namtso est faite de la neige du Ningling Tanla'."

Gabriel Bonvalot (1892)[1]: "*De Paris au Tonkin à travers le Tibet inconnu*", field trip realised 1989-1890.

[1] Bonvalot, according to another famous explorer of Tibet Sven Hedin, was probably the first European to see the Nam Co lake. He described with very accurate and poetic words the Nyainqentanglha Range ("Ningling-Tanla") as he saw it when coming from the North.

Abstract

The Tibetan Plateau and adjacent mountain ranges (TP) is one of the most prominent geological features on Earth. It plays a significant role in influencing global atmospheric circulation, is the source of several major Asian rivers, and stores large amounts of ice, snow and permafrost. The climate on the TP is described as being under the influence of both the mid-latitude westerlies and the Asian Monsoon, but their contributions to regional climate variability and change, as well as their interactions, are not yet understood in detail. Observed glacier retreat and lake level fluctuations are indicators of climate change, but the strong spatial variability of these indicators make interpretations difficult in terms of climatic drivers.

Despite its crucial importance, knowledge about the TP's climate and hydrology is still limited. For historical, political and logistical reasons, *in situ* observations are scarce and biased towards lower elevations. To address this issue, I present a new high-resolution atmospheric dataset: the High Asia Reanalysis (HAR), generated by dynamical downscaling of global analysis data using the Weather Research and Forecasting (WRF) model for the period of 2001–2011. The new dataset provides three-dimensional meteorological variables at high spatial (up to 10 km) and temporal (hourly) resolution.

In order to find a suitable design for HAR, several model designs and configurations were tested and compared to observations during a strong precipitation event on the TP. New methods of evaluation were developed to address issues related to the unknown accuracy and the low spatial representativeness of available observations. Additionally, an automatic weather station was installed at 5600 m a.s.l. on Zhadang Glacier, south-central TP, which provides exceptional observations of a high-altitude environment.

Results show that HAR reproduces previously reported spatial patterns and seasonality of precipitation. The high resolution of HAR adds value to existing datasets regarding snowfall retrieval, precipitation frequency and orographic precipitation. Precipitation seasonality patterns on the TP are complex and characterised by a winter regime in the west, a spring regime in northern and southern TP, and a summer regime elsewhere. Implications for the interpretation of glacier changes are illustrated with a new classification of glacier accumulation regimes. Additionally, regions with higher inter-annual variability and/or that are prone to severe precipitation events are identified. Since an additional goal of HAR is to provide forcing data for impact models (e.g. hydrological or glaciological models), the potential of HAR as a "replacement" for observations is demonstrated, focusing on the Zhadang Glacier.

The strong spatial variability of precipitation features is of particular interest, in light of (i) large-scale drivers of the climate system like the westerlies and the Asian Monsoon, as well as (ii) local influences, such as lakes and topography. In this respect, multidisciplinary projects are presented, which develop new approaches combining HAR with field measurements, remote sensing techniques and glaciological modelling. Area changes acquired from satellite imagery show that the Zhadang Glacier is retreating since at least 1976. A physically based modelling chain permits the mass balance at Zhadang to be linked to Asian Monsoon dynamics, and reveals that the timing of monsoon onset leaves a clear footprint on the glacier through the albedo effect. The later the monsoon is established in a particular year, the higher the resulting mass loss on the glacier. Using HAR and idealised model experiments, the nearby Nam Co lake is identified as another important factor affecting local precipitation, by weakening convection in summer and enhancing snowfall in autumn. Most lakes on the TP freeze in winter. The timing of freezing and other ice phenology metrics hold useful information about climate variability, as shown in a further study linking HAR temperature data with ice phenology metrics obtained from satellite observations.

This thesis provides a robust scientific framework for related regional reanalysis projects at TU Berlin or elsewhere. The HAR dataset, which is freely available to the scientific community, provides a valuable basis for improving our understanding of atmospheric, cryospheric and hydrospheric processes on the TP.

Zusammenfassung

Das Tibet-Plateau mit seinen angrenzenden Gebirgszügen (TP) ist eines der markantesten geologischen Merkmale auf der Erde. Es spielt eine wesentliche Rolle als beeinflussender Faktor der globalen atmosphärischen Zirkulation, auf ihm entspringen mehrere der größten asiatischen Flüsse und große Mengen Eis, Schnee und Permafrost sind auf ihm gespeichert. Das Klima auf dem TP unterliegt sowohl dem Einfluss der Westwinde der mittleren Breiten, als auch des asiatischen Monsuns. Allerdings ist die Interaktion dieser beiden Faktoren und ihr jeweiliger Beitrag zu regionaler Klimavariabilität und Klimawandel noch ungenügend verstanden. Der beobachtete Rückgang von Gletschern und Seespiegelschwankungen deutet auf einen möglichen Klimawandel hin, aber die starke räumliche Variabilität dieser Phänomene erschwert die Interpretation bezüglich klimatischer Antriebe.

Trotz dieser Relevanz ist das Wissen über Klima und Wasserkreislauf des Tibet-Plateaus stark begrenzt. Aus geschichtlichen und politischen Gründen sind direkte Messdaten aus der Region spärlich und für die hohen Lagen des Tibet-Plateaus kaum vorhanden. In dieser Arbeit stelle ich einen Lösungsansatz für dieses Problem vor: einen neuen hochaufgelösten atmosphärischen Datensatz, die High Asia Reanalysis (HAR). Die HAR wurde mittels dynamischem Downscaling globaler Analysedaten unter Verwendung des Weather Research and Forecasting (WRF) Modells für die Periode 2001-2011 generiert. Dieser neue Datensatz liefert bodennahe und atmosphärische Variablen in hoher räumlicher (bis zu 10 km) und zeitlicher (stündlich) Auflösung.

Um eine geeignete Modellkonfiguration zur Erstellung der HAR zu ermitteln, wurden verschiedene Konfigurationen getestet und mit Beobachtungen während eines Starkniederschlagsereignisses auf dem TP verglichen. Dies ging mit der Entwicklung neuer Evaluierungsmethoden einher, um die unbekannte Genauigkeit und die mangelhafte räumliche Repräsentation der Verhältnisse auf dem TP durch Beobachtungen zu berücksichtigen. Zusätzlich wurde eine automatische Wetterstation (AWS) auf dem Zhadang-Gletscher (südzentrales TP) in 5600 m ü.NN installiert. Diese AWS liefert einmalige Daten aus großer Höhe für diese Region.

Die Ergebnisse zeigen, dass HAR bekannte räumliche Niederschlagsmuster und deren Saisonalität reproduziert. Zudem liefert sie im Vergleich zu bereits existierenden Datensätzen auf Grund ihrer hohen Auflösung wichtige Zusatzinformationen im Bereich der Schneefalleigenschaften, Niederschlagsfrequenzen oder orographischen Niederschläge. Die Muster der Niederschlagssaisonalität auf dem TP sind komplex und durch ein Winterregime im Westen, ein

Frühlingsregime im nördlichen und südlichen TP und ein Sommerregime in den übrigen Regionen bestimmt. Zusammenhänge zur Interpretation der Gletscherveränderungen werden durch eine neue Klassifikation von Gletscherakkumulationsregimen veranschaulicht. Zusätzlich treten Regionen mit höherer interannueller Variabilität und Anfälligkeit für Starkniederschlagsereignisse hervor. Ein weiteres Ziel der HAR ist die Bereitstellung von Antriebsdaten für Wirkmodelle (z.B. hydrologische und glaziologische Modelle). Daher wird das Potenzial der HAR als "Ersatz" für Beobachtungen am Beispiel der komplexen räumlichen Begebenheiten am Zhadang-Gletscher gezeigt.

Es ist von besonderem Interesse die starke räumliche Variabilität des Niederschlags und seiner Charakteristika im Hinblick auf sowohl (i) großskalige Antriebsfaktoren des Klimasystems wie die Westwinde und den Asiatischen Monsun, als auch (ii) lokale Einflüsse wie Seen und Topographie zu analysieren. In diesem Zusammenhang präsentiert die Arbeit interdisziplinäre Projekte, die neue Herangehensweisen entwickeln und die HAR mit Feldmessungen, Fernerkundungsmethoden und glaziologischer Modellierung kombinieren. Aus Satellitenbildern gewonnene Flächenänderungen zeigen, dass der Zhadang Gletscher mindestens seit 1976 zurückgeht. Eine physikalisch basierte Modellkette ermöglicht es, die Massenbilanz am Zhadang mit der Dynamik des Asiatischen Monsuns in Verbindung zu bringen. Sie zeigt, dass der Zeitpunkt des Monsunbeginns einen deutlichen Fußabdruck auf dem Gletscher durch den Albedoeffekt hinterlässt. Je später im Jahr sich die Monsunzirkulation einstellt, desto höher ist der resultierende Massenverlust auf dem Gletscher. Unter Verwendung der HAR und idealisierter Modellexperimente wurde der nahegelegene Nam Co See als ein weiterer wichtiger Faktor identifiziert, der den lokalen Niederschlag durch Abschwächung der Konvektion im Sommer und Verstärkung des Schneefalls im Herbst beeinflusst. Die meisten Seen auf dem TP frieren im Winter zu. Der Zeitpunkt des Zufrierens und weitere Eisphänologiemaße enthalten nützliche Informationen zur Klimavariabilität. In diesem Sinn bringt eine weitere Studie die HAR Temperaturdaten mit satellitengestützten Eisphänologiemaßen in Zusammenhang.

Die vorliegende Arbeit bietet ein solides wissenschaftliches Gerüst für ähnliche Projekte, die sich mit regionaler Reanalyse befassen. Der HAR Datensatz ist für die wissenschaftliche Community frei verfügbar und schafft eine neue Grundlage zum besseren Verständnis von atmosphärischen, kryosphärischen und hydrologischen Prozessen auf dem TP.

Chapter 1

Introduction

1.1 Motivation

With an area of about 2.5×10^6 km^2 and an average elevation of more than 4500 m a.s.l., the Tibetan Plateau and surrounding mountain ranges (TP) is one of the most prominent geological features on Earth. Its exploration by western geographers occurred late in History. They were facing harsh conditions and had to travel in secret, since entering the "Roof of the World" was forbidden to foreigners (see e.g. Edel, 2007, who gathered field reports from six scientific expeditions on the TP between 1889 and 1908). Their expedition diaries probably account for many myths and stories still anchored in our collective imagination. For historical and political reasons, knowledge about the TP geography, ecology and climate is still limited today.

Despite (or because) of these difficulties, the scientific interest for the TP is considerable. Several of the largest Asian rivers find their source on the "Asian Water Tower" (e.g. Immerzeel et al., 2010). Due to the large amounts of ice, snow and permafrost stored on the TP, several authors also named this region the "Third Pole" (Qiu, 2008; Kang et al., 2010). Like in most parts of the world (IPCC, 2013), glaciers receded almost throughout the entire TP during recent decades (Yao et al., 2012; Bolch et al., 2012), but they show contrasting patterns of shrinkage (Kaab et al., 2012) or even balanced mass budget in some regions in central TP (Gardner et al., 2013; Neckel et al., 2013). Local factors (e.g. exposition, topography, debris coverage...) partly account for these differences, but spatial and temporal heterogeneity of climate and climate change (e.g. Palazzi et al., 2013; Kang et al., 2010) play a role that has yet to be quantified, especially in the regions where in-situ measurements are non-existent. Glaciers play a significant role in the hydrological budget, but their relative importance varies between regions and watersheds (Kaser et al., 2010), also between lake basins on the TP (Phan et al., 2013). Therefore, direct observations of glacier mass balance and their linkage to meteorological conditions are highly necessary on the TP.

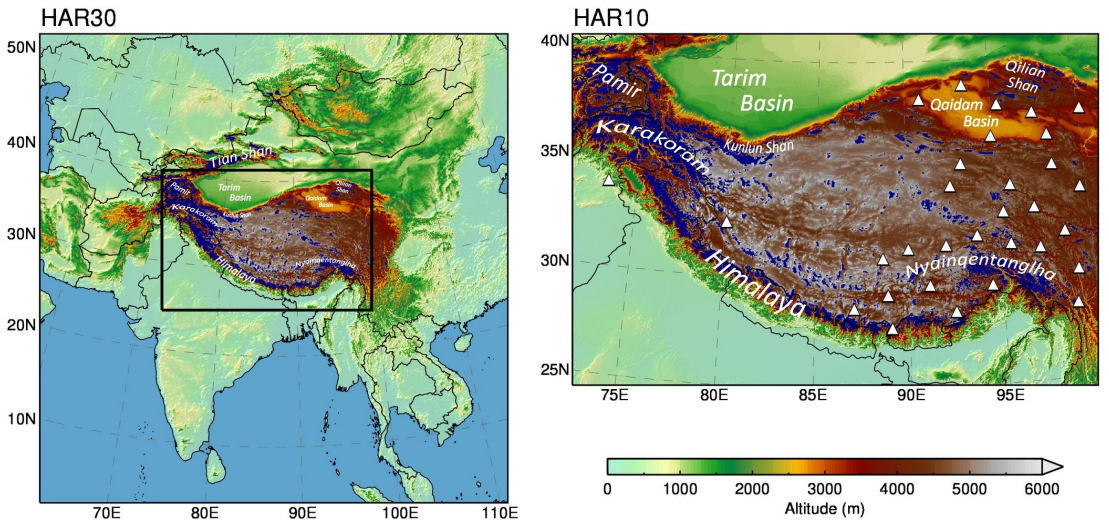

Figure 1.1: Maps of the model domains HAR30 (South-Central Asia domain, 30 km resolution, 200×200 grid points) and HAR10 (High Asia domain, 10 km resolution, 270×180 grid points). Glacier outlines from the Randolph Glacier Inventory are drawn in blue, and the positions of the NCDC stations used for the validation are indicated by white triangles. Geographical locations mentioned in the text are indicated.

The TP is one of the largest and highest lake systems in the world. Jiang et al. (2008) counted 6882 lakes larger than 0.1 km^2, and 1260 larger 1 km^2 for a total area of more than 43000 km^2. Past lake level and shore extent are proxies of climate and hydrological changes, and lake basins are a great source of information for paleoclimate, past glaciation and sediment deposition studies (e.g Dietze et al., 2014; Daut et al., 2010; Stauch et al., 2012; Opitz et al., 2012). In general, lake levels are currently increasing throughout the TP, threatening grazing and habitable areas (76% out of 200 studied lakes rose between 2003 and 2010 according to Zhang et al., 2013b).

It was acknowledged early that the TP, which reaches the mid-troposphere, would have an important influence on atmospheric circulation at hemispheric scale (Flohn, 1957; Ye, 1981; Tao and Ding, 1981). Located at approx. 30°N, the TP acts as a giant natural barrier to zonal and meridional air motion. It blocks cold outbreaks from the north in winter, affects the position and strength of the northern hemisphere westerly jet (e.g. Wang, 2006; Held et al., 2002; Takahashi and Battisti, 2007) and plays a significant role in the Asian summer monsoon (ASM) system (e.g. Hahn and Manabe, 1975). However, the question whether the TP controls on the ASM are more thermal or mechanical (or both) is still under active debate (e.g. Boos and Kuang, 2010, 2013; Rajagopalan and Molnar, 2013; Wu et al., 2012). Understanding the influences of the TP on the large-scale circulation is particularly relevant to link past climatic changes to the uplift of the TP at geological time-scales (e.g. Molnar et al., 2010).

There is an abundant literature about the role of the TP on atmospheric circulation. By contrast, the regional climate of the TP and its large-scale atmospheric drivers remain less studied so far. The lack of suitable observations is one probable reason. *In situ* observations are scarce and biased towards populated areas and lower elevations (Qin et al., 2009), and therefore are not representative of the high mountain conditions. Available global meteorological datasets are of coarse resolution that limits their representation of the mountainous topography. Of all

climatological elements affected by topography, precipitation is probably the most complex and the most poorly represented by coarse resolution grids (e.g. You et al., 2012).

The climate on the TP is described as being under the influence of the westerlies and of the monsoons, but these influences vary regionally as well as seasonally (e.g. Benn and Owen, 1998, and examples in Fig. 1.2). How exactly and with which strength do these influences operate is yet unclear, and is an active field of research (e.g. Bothe et al., 2010, 2012; Yao et al., 2013; Feng and Zhou, 2012; Chen et al., 2012).

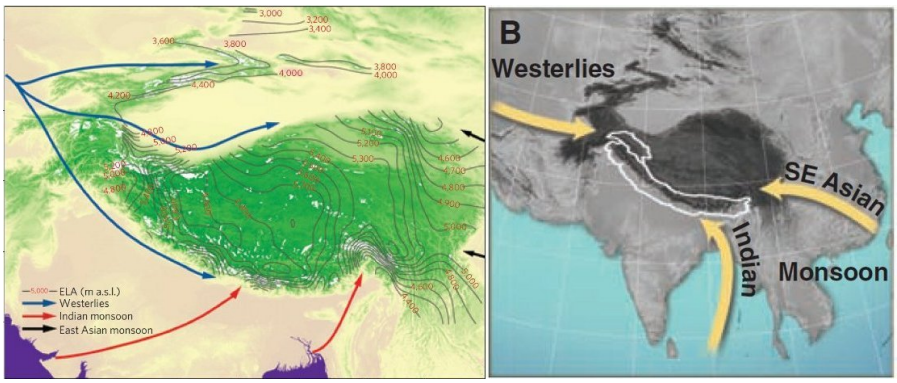

Figure 1.2: Examples of the schematic representation of the wind systems influencing the climate of the TP (Yao et al., 2012; Bolch et al., 2012).

Focusing on the monsoon history over the past, present and future, a Sino-German Priority Programme (*Tibetan Plateau: Formation – Climate – Ecosystems*) was initiated by the German Research Foundation (DFG) to develop a multidisciplinary approach dealing with the interactions taking place between the major driving forces on the TP. The DynRG-TiP project (*Dynamic Response of Glaciers on the Tibetan Plateau to Climate Change*[1]) is part of this priority programme. This project was complemented by a Federal Ministry of Education and Research (BMBF) programme (*Central Asia – Monsoon dynamics and Geo-ecosystems*), in which the WET project was initiated (*Variability and Trends in Water Balance Components of Benchmark Drainage Basins on the Tibetan Plateau*[2]). The work presented in this thesis took place within this frame.

Research programs of this scale not only bring many scientists from various backgrounds together, they also allowed us to start a fruitful cooperation with the Chinese Academy of Sciences (CAS) and with our principal partner, the Institute of Tibetan Plateau Research (ITP[3]). Located in Beijing and in Lhasa, the ITP is a multidisciplinary institute which operates several research facilities on the TP. With its support, seven sino-german field campaigns on the TP were successfully completed.

[1] `www.klima.tu-berlin.de/DynRG-TiP`. The DynRG-TiP project, lead by D. Scherer (TU Berlin), C. Schneider (RWTH Aachen) and M. Buchroithner (TU Dresden), was initially funded for two years and has been prolonged for a total duration of six years (2008-2014).

[2] `www.klima.tu-berlin.de/WET`. Lead by D. Scherer and coordinated by the author of this thesis, this project bundles six universities (TU Berlin, U Marburg, RWTH Aachen, TU Dresden, U Tübingen and U Jena) and is funded for an initial period of three years (2011-2014).

[3] `http://english.itpcas.cas.cn/`. Partners: Yao Tandong, Kang Shichang, Yang Wei.

1.2 Objectives

This thesis is built around the following key questions:

1. How can we overcome the problem of scarce meteorological data availability in this region of complex terrain? What accuracy can we reach, at which spatio-temporal resolution?

2. What are the features of climate variables on the TP? How do they vary regionally, seasonally?

3. What are the respective roles of the components of the TP hydrological budget (precipitation, evaporation, snow, ice, permafrost, lakes)? Are they stable, or did they undergo significant changes in the recent past?

4. What are the large scale and local drivers of climate variability on the TP? How do these drivers affect the hydrological components mentioned above?

The first objective of the thesis is to present one possible answer to Question 1. Here, I describe the development and implementation of a new atmospheric dataset for the TP: the High Asia Reanalysis (HAR), generated by dynamical downscaling of large-scale meteorological data using a numerical weather prediction model for the period of 2001–2011. This dataset provides meteorological variables at the surface and in the atmosphere at high spatial (up to 10 km, Fig. 1.1) and temporal (hourly) resolution. The HAR intends to provide a "best estimate" of the state of the atmosphere at any time in the last decade. The dataset's accuracy is evaluated by comparison with in-situ measurements and remote sensing data. The added value of HAR is discussed, as well as its shortcomings and uncertainties.

Based on HAR, we can address Question 2. This thesis contributes to our understanding of atmospheric processes that lead to precipitation on the TP, by describing the characteristics of precipitation at monthly to annual time scales. Dynamical downscaling approaches like HAR provide a way to resolve the full process chain of synoptic- to regional-scale dynamics. In a case study I show that HAR can also be used in a meteorological context, e.g. by analysing a strong precipitation event on a daily basis.

One major goal of HAR is to be used as forcing data for impact models such as hydrological or glaciological models, in order to address Questions 3 and 4. For this purpose, multidisciplinary projects were initiated to develop new approaches combining HAR with field measurements, remote sensing techniques and glaciological modelling. Selected case studies at Zhadang Glacier and at Nam Co lake demonstrate that with these methods we were able to provide unprecedented insights about the current and past state of a glaciated catchment on the TP.

1.3 Structure of the thesis

This thesis is based on the content of five peer-reviewed papers, outcome of the collaborative work of several authors. The main part of my thesis is the present synthesis, which summarizes and enlightens the major results of the individual studies to put them in the broader context of the research questions listed above. The synthesis is intended to be a stand-alone document, however a certain familiarity with the content of the five thesis papers would be advantageous.

Chapter 1, Introduction provides a short overview of the current scientific challenges and defines the objectives of the thesis.

Chapter 2, The High Asia Reanalysis presents the reasons to develop HAR, the configuration choices, and validation results.

Chapter 3, The climate of the TP is a short introduction to the atmospheric circulation in Asia, and develops the possibilities offered by HAR to study the climate of the TP.

Chapter 4, A Tibetan Glacier case study presents scientific advances at Zhadang, a glacier which has been the subject of an intensive field program in recent years. It is therefore a perfect test bed for the multidisciplinary approaches described above.

Chapter 5, Lakes on the Tibetan Plateau addresses two functions of the lakes in the climate system: (i) as "sensors" of climate variability by studying the variability of lake ice phenology and (ii) as "actors" of their local climate by analysing their influence on precipitation.

Chapter 6, Conclusions and outlook concludes the thesis and identifies directions for future research.

The synthesis is followed by the thesis papers, which are reproduced in their original Journal format, and by two appendices:

Appendix A, Glaciological field studies at Zhadang Glacier is a report published in the "Extended abstracts and recommendations" booklet from the "Workshop on the use of automatic measuring systems on glaciers in Pontresina", 2011.

Appendix B, Influence of the Nam Co lake on local precipitation patterns is a manuscript in preparation based on HAR and two other model experiments, designed to address the question of the influence of lakes on the local climate and to assess the capability of the WRF model to reproduce these effects.

Chapter 2

The High Asia Reanalysis (HAR)

This Chapter deals with the core of this thesis, the High Asia Reanalysis (HAR). Section 2.1 provides a short review of the currently available meteorological datasets, and gives reasons to why HAR was developed. Section 2.2 describes the design and configuration choices. Section 2.3 presents the results of the validation studies.

2.1 Context

2.1.1 Global meteorological datasets

Since the end of the 19^{th} century (modern instrumental period) the amount and quality of meteorological data increased almost continuously. Nowadays, they stem from various sources such as weather stations, atmospheric radio-soundings, radars, planes, buoys, ships, or satellites. Because of the strategical importance of reliable weather forecasts, these huge amounts of data are gathered, treated and redistributed continuously by several institutions worldwide.

Due to the varying standards and the irregular spatio-temporal distribution of data sources, it became apparent that the data could not be objectively used in climatological analyses. Consequently, two strategies were developed and both relied on producing *gridded data* (Oliver, 2005). The first strategy is the *homogenization* of datasets applied to either station or satellite data, or to a combination of both (e.g. CRU, GPCC, GPCP, Mitchell and Jones, 2005; Becker et al., 2013; Adler et al., 2003). The second strategy is the production of assimilated datasets of atmospheric fields that were used by weather forecast institutions (*Operational Analysis*, starting in the 1980s).

Operational Analyses can be seen as smart, physically based interpolations of all available meteorological observations. They rely on a short-range forecast model and a variational assimilation system capable of ingesting observational data from various sensors. For example, the National Centers for Environmental Prediction (NCEP) provide the Final (FNL) Operational Model Global Tropospheric Analyses, generated with the Global Forecast System (GFS). The latest product (ds083.2, NCEP, 2000) is continuing from 2000 onwards and provides an estimate of the state of the whole atmosphere at regular time intervals (6 hours) with a spatial resolution of 1.0°.

Global analysis projects do not intend to be retroactive: when it became apparent that operational changes were responsible for "climate" changes in the records, the *Atmospheric Reanalysis* projects were developed. They address (more or less successfully) the issue of changing observational systems by using a frozen analysis system over longer time spans (e.g. Uppala et al., 2005). Global reanalysis data are widely used by scientists of all disciplines. However, their popularity can lead to blind trust in their accuracy or homogeneity (see e.g. Bengtsson et al., 2004, for a discussion about trend calculation from reanalysis data).

An overview of some of the most widely used global meteorological datasets is given in Fig. 2.1. For more information about these datasets, refer to the new collaborative information platform, the "Climate Data Guide" (Schneider et al., 2013).

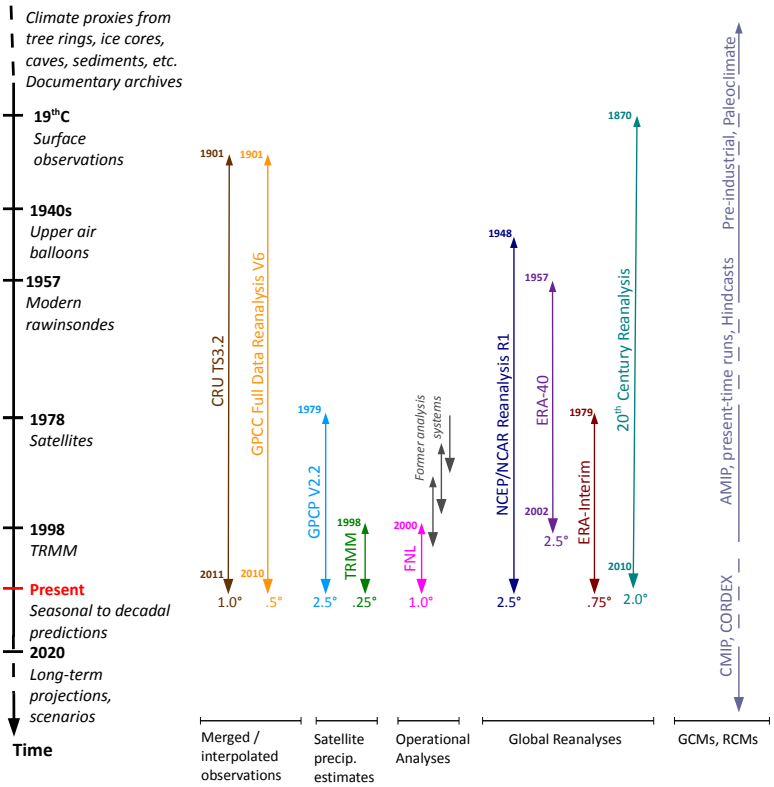

Figure 2.1: Non-exhaustive overview of available global gridded datasets, with their temporal extent and spatial resolution (realised after: Oliver, 2005; NCAR, 2013; Shea et al., 1994).

2.1.2 The "scale issue"

For most applications (e.g. climatology, hydrology, glaciology), spatially and temporally complete gridded datasets are needed. The scale dependency of the processes involved depends on the application, but for many cases resolutions of a few hundred meters up to 10 km are a pre-requisite. In Fig. 1.1, we indicated all available meteorological stations providing precipitation data during the last decade on the TP. Located in populated areas (valleys) with several hundreds of kilometres between them, these stations alone do not allow to build a climate reconstruction based on interpolation only. To obtain meteorological information we therefore have to rely on global atmospheric datasets. The variational assimilation system's ability to exploit physical information (implicit in the model equations) is mostly beneficial where observations are sparse (Dee et al., 2011). Thus we have confidence in the global analyses' accuracy, at least for the upper atmospheric dynamics above the Planetary Boundary Layer (PBL).

Unfortunately, the major drawback of these datasets is their low spatio-temporal resolution. The problem is best described with a sketch as in Mölg and Kaser (2011) (their Fig. 01). The authors schematize the process chain (including feedbacks) linking large-scale dynamics to the mountain PBL and finally to the surface (in this case a glacier). The operation of "bridging the gap" between scales is often referred to as *downscaling* (e.g. Wilby and Wigley, 1997; Wang et al., 2004; Maraun et al., 2010; Laprise et al., 2008). Two fundamentally different approaches exist: the *dynamical* approach (chosen to produce HAR) and the *statistical* approach which establishes empirical relationships between climate variables at the global dataset's resolution and local climate. A review of the strengths and weaknesses of these two methods can be found in Fowler et al. (2007). The major disadvantage of statistical downscaling methods is the need for long and reliable observed historical data series for calibration, rendering them particularly difficult to apply on the TP.

2.1.3 Currently available gridded datasets for the TP

Only a few datasets are used for climate or climate change studies on the TP. Gridded datasets relying on weather stations only (e.g. CRU, GPCC) are rarely used on the TP, appart for global studies (e.g. Marzeion et al., 2012) or the validation of climate simulations (e.g. Mannig et al., 2013). Weather stations alone provide the major data source for e.g. climate change and trend calculations (see the review by Kang et al., 2010), since some station data (e.g. Lhasa) are available since the 60's. Station measurements can be extrapolated to distant places like a glacier (e.g. Caidong and Sorteberg, 2010), combined to remote sensing products (e.g. Qin et al., 2009) or combined to global reanalysis data (e.g. You et al., 2010). Some studies point out several inconsistencies between the reanalysis datasets and observations (You et al., 2012; Biskop et al., 2012) and several studies use "ensemble" (or combined) approaches to reduce uncertainty (Tong et al., 2013; Feng and Zhou, 2012). For precipitation, TRMM is widely used to study for example convection activity (Yaodong et al., 2008), precipitation diurnal cycle (Zhou et al.,

2008), himalayan hydrology (Bookhagen and Burbank, 2010), etc. Also worth noting is the APHRODITE dataset (Yatagai et al., 2012) which is a daily rain-gauge based dataset for Asia spanning 57-years at 0.25°.

2.1.4 Motivations to develop HAR

In this context, the approach that was chosen at the Chair of Climatology, TU Berlin, is the dynamical downscaling of global analysis data using a limited area (mesoscale) atmospheric model. One of our basic requirements is that the downscaled data should represent as closely as possible the information that suitable observations would have delivered, at whatever time scale. This is an important property which distinguishes our approach from climate modelling. It implies that the conditions at the Earth's surface influencing atmospheric processes, particularly in the PBL, need to be described in sufficient spatial detail.

This idea was promoted by two funding agencies in Germany. Following arguments can be advanced:

i. Physically based approaches allow a full representation of the process-chain up to the resolution chosen for a specific purpose (2 km is our current objective for selected benchmark regions).

ii. Dynamical downscaling does not rely on statistical relationships which may not remain valid under varying boundary conditions or time scales. Instead, the model relies on understood physical relationships (or partially understood at least).

iii. The dataset will be made available for all project partners and interested scientists. In this regard, the developers of the dataset have the responsibility to test and document the provided data as accurately as possible.

Once the decision to fund the project has been reached, many important tasks remained to do before the finalisation of the products. The learning process that accompany the production of this dataset provide the content of this chapter and of large parts of my thesis.

2.2 Modelling concept

A comprehensive description of the modelling strategy followed to produce HAR is found in the introduction and methodology sections of Papers I and II. The atmospheric model used is the Weather Research and Forecasting model (WRF, Skamarock and Klemp, 2008). To date, the WRF model is one of the most widely used model of its art. Its strengths and weaknesses have been independently analysed and discussed for barely any region of the world, but it is interesting to notice that our efforts are among the pioneering studies using the WRF model on the TP. It is a community model, meaning that it is open source, freely available, regularly maintained and improved by the community.

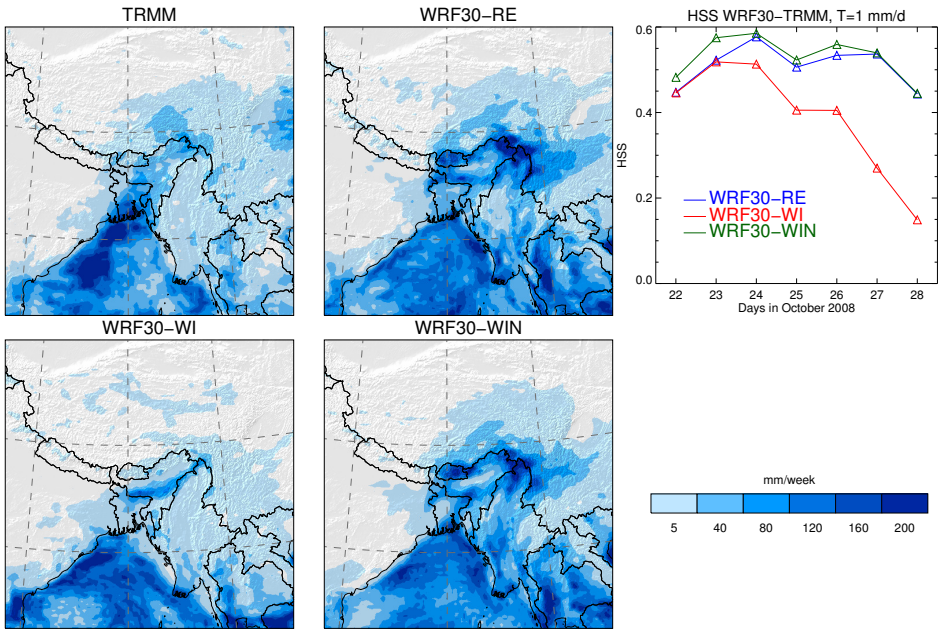

Figure 2.2: Sensitivity to the forcing strategy during a one-week period (22-28 October 2008). Left: one-week precipitation (mm/week) for TRMM, WRF30–RE (daily reinitialisation), WRF30–WI (weekly reinitialisation) and WRF30–WIN (weekly reinitialisation with nudging) over a subset of the large domain. Right: daily HSS curves from WRF30 with respect to TRMM for the 1 mm/day precipitation threshold over the same subset. Reproduced from Paper I.

Forcing strategy

The basic principle of all Limited Area Models (LAMs) is to concentrate on a specific region, where the model is run at a higher resolution. Therefore the LAM has to be initialised and then driven (or forced) at it's boundaries during the simulation time. Typically, a global atmospheric dataset is used to drive the LAM, for example (re-)analysis products or GCM output. The choice was made to use the Final Analysis dataset from the GFS (ds083.2, NCEP, 2000). The supplementary material from Paper II provides reasons for this choice, by comparing FNL with ERA-Interim forcing.

Three distinct model initialisation and forcing strategies are commonly used: (i)short-term, when the model is run over a few days to obtain the best forecast accuracy, (ii) mid-term, with week-long simulations up to a few months, (iii) long-term, with simulation durations of months to decades, which is the traditional RCM approach. Theoretically, all three methods could be used to simulate the time-span 2001-2011 and it was one of the objective of Paper I to discuss this aspect. The HAR is produced with the *short-term* approach: the dataset is comprised from consecutive model runs of 36 h time integration. The first twelve hours from each run are discarded for spin-up, the remaining 24 h of model output provide one day of the 11-year long time series. Figure 2.2 illustrates best the reasons for this choice. It is clear that after two days of integration the model, without being reinitialised, is not able to reproduce accurately the observed patterns of precipitation.

Nesting strategy

The capability to *nest* smaller domains to reach a higher resolution for the modelled region is a common characteristic of LAMs. For the production of HAR, a nesting strategy with spatial resolutions of 30 - 10 - 2 km was chosen. The larger domain covers large parts of Asia at low computational costs. The resolution of 10 km is the typical mesoscale resolution, below which the processes and scales represented by traditional convective parametrisations become inconsistent with the features that are not well resolved by the model grid (e.g. Arakawa, 2004; Kain, 2004). The 2 km resolution allows an explicit resolution of most cloud processes, making the convective parametrisation obsolete. The HAR 2 km resolution products are not available yet, but the concept was tested in Paper I and during a four years period for use in Paper III.

Additionally, the WRF model allows for one-way or two-way nesting options. The nesting strategy of HAR is based on a novel method presented in Paper I, solving a scientific conflict currently discussed concerning the advantages and disadvantages of one-way versus two-way nesting. We are therefore using a cascade of simulations (first the 10 km resolution domain is run with two-way nesting option, then the 30 km resolution is run alone). This approach allows benefiting from the two-way nesting approach in the respective child domain (Fig. 7 in Paper I illustrates the positive effect of two-way nesting) while concurrently avoiding artefacts in the respective parent domain.

Physical parameterisation and options

The WRF model offers a broad spectrum of parameterisation schemes for subgrid-scale processes such as convection, cloud microphysics, surface-air interactions, soil processes, etc. Unfortunately, there is no general recommendation for the "best practice" of downscaling. The constant evaluation of these schemes for various regions and fields of applications is an active field of research (e.g. Pohl et al., 2011; Yang and Tung, 2003; Rakesh et al., 2007). Such evaluations were never performed for the WRF model applied to the TP region: Paper I aimed to provide an estimation of the model sensitivity to changes in parameterisation schemes (Paper I, Section 3.2).

Unlike the evaluation of the forcing strategy, it appeared that the interpretation of the results of the sensitivity experiments was not straightforward. The eight experiments revealed that there is no optimal model strategy applicable for the high-altitude TP, its fringing high-mountain areas and the low-altitude land and sea regions from which much of the precipitation on the TP is originating. The simulated precipitation proved to be more sensitive to PBL and convection parametrisations than land-surface and microphysics (Paper I, Fig. 9). No physical parametrization scheme outperformed the others for all the tests, but much effort went into choosing the model setup that performs best to produce HAR (Paper I Table 1).

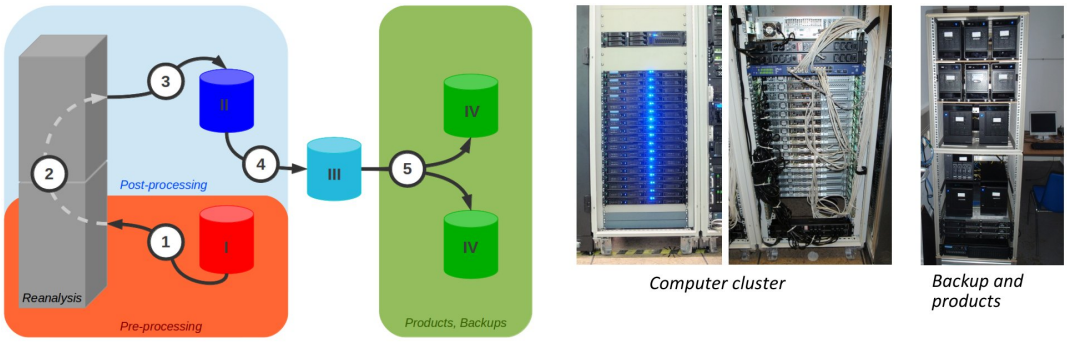

Figure 2.3: Left: Reanalysis production workflow. Roman numerals indicate states of data processing: Input data (I), raw model output (II), post-processed model output (III), products and analyses from post-processed model output (IV). Arabic numerals indicate processing steps: WRF pre-processing (1), job distribution, control and logging (2), file output (3), post-processing (4), product generation and backup (5).
Right: pictures of the computer cluster (front and back) where the steps 1 to 4 are realized and of the backup and product generation cluster where the step 5 is realized.
Modified after (Finkelnburg, 2013).

Implementation

The operational production of a such a dataset requires a considerable infrastructure which was set up and maintained by our team at the Chair of Climatology since 2008. Large amounts of data[1] have to be processed, stored, and analysed in a (semi) automatic manner (Fig. 2.3).

Specific tools were developed for the production of HAR and related datasets[2]: a *job controlling* system adapted to the daily reinitialisation strategy, and a *post-processing* system to generate separate yearly product files per variable (including additional diagnostic variables) and per time aggregate (daily, monthly, yearly). These product files are organized in a hierarchical directory structure which makes them easy to find, copy, share and handle programmatically. A webpage has been created for HAR users where the data can be downloaded[3].

2.3 Validation

I find it appropriate to start with this famous quote by George E. P. Box: '*Remember that all models are wrong; the practical question is how wrong do they have to be to not be useful*' (Box and Draper, 1986). The question of "how wrong HAR can be while still being useful" is dependant on the research question and the intended use of the data. As data provider we are in charge to provide enough information to potential users so that they can make an informed, hopefully appropriate choice wether to use HAR or not. The *verification* of every HAR production step is obviously impossible, for practical as well as philosophical reasons (Oreskes et al., 1994). For the accurate representation of the "real atmosphere" by the large scale input dataset or for the "correctness" of the physical relationships in the WRF model we have to rely on the

[1] at the time of writing, all HAR data products and the additional sensitivity experiments represent about 45 TB of data
[2] European Arctic Reanalysis (EAR), Northwest Africa Reanalysis (NwAR), Central European Reanalysis (CER)
[3] `http://www.klima.tu-berlin.de/HAR`

developers/testers of both tools. Here I provide a partial *assessment* or *benchmarking* of the HAR products.

2.3.1 Objectives and methods

In Paper I one question of the study was formulated as: '*Which validation methods and data sets are suitable for assessing the accuracy of simulated precipitation fields of high spatio-temporal resolution over the TP?*'. This question is less frequently addressed in similar studies since observations are usually taken as an absolute reference. However, the particularities of the TP do not ensure the applicability of validation approaches that have been proven to be suitable in other regions. In Paper I, the objectives were to (i) demonstrate the feasibility of the regional reanalysis of precipitation and (ii) use the developed assessment methods to take a decision about a specific model set-up. In Paper II, the validation had the objective to give us confidence[1] in the HAR precipitation data, used to address the scientific questions raised in the paper (description of e.g. precipitation patterns, type, seasonality, frequency, intensity, inter-annual variability).

For a comprehensive description of the validation datasets and methods see Papers I and II. At the time of writing most assessment efforts were oriented towards surface precipitation (Papers I and II), air temperature (Klein, 2013, Master thesis) or the whole set of meteorological data used in an impact model, for example a glacier surface melt model (Mölg et al., 2014) or a hydrological model (Biskop et al., 2013, manuscript in preparation).

2.3.2 Results

Near surface temperature

Figure 2.4 shows the seasonal Mean Deviation (*MD*, or bias) of HAR30 2 m air temperature at each station location. The biases exhibit regional patterns like a DJF warm bias in the north of the domain and a DJF cold bias over the TP. Several stations appear to be statistical and geographical outliers. The geopolitical dependency of station spatial density is striking (e.g. differences Thailand/Burma) but biases may also reflect country borders (e.g. Pakistan border in JJA versus India). The HAR results are closer to observations in summer than in winter as shown in Fig. 2.5 for the TP. A majority of stations have a cold bias in winter. Because of the linear dependency of temperature with altitude, we could expect a limited impact of high-resolution modelling, but HAR10 still shows an improvement to HAR30 for both skills. In general, the performances of HAR for daily temperatures are good, as illustrated exemplary at two stations in Fig. 2.6. Relevant quantities like the annual range, seasonality and single stochastic events are well reproduced.

[1] the term "confidence" refers to a simple probabilistic confidence: The more we test HAR accuracy, the smaller is the probability that the HAR products are not suitable for a specific usage

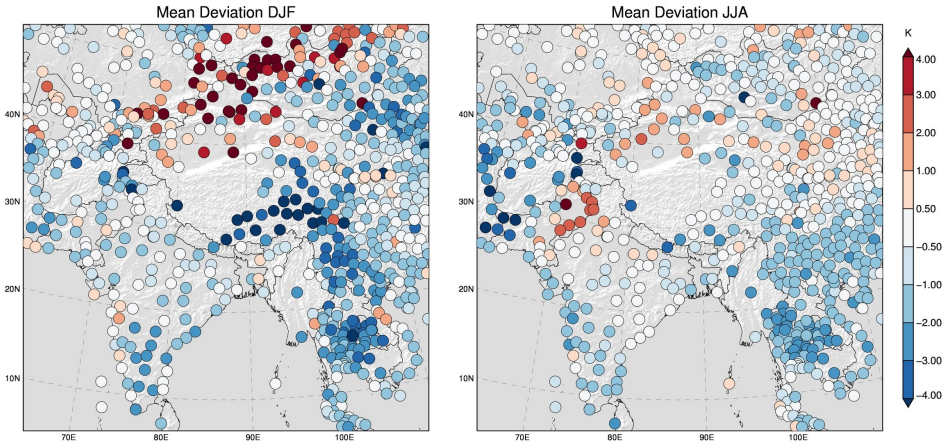

Figure 2.4: Mean deviation of near surface (2 m) air temperature (747 stations) in DJF (left) and JJA (right). A constant temperature lapse rate of 6.5 K km^{-1} is used to transfer the HAR temperature at the station altitude.

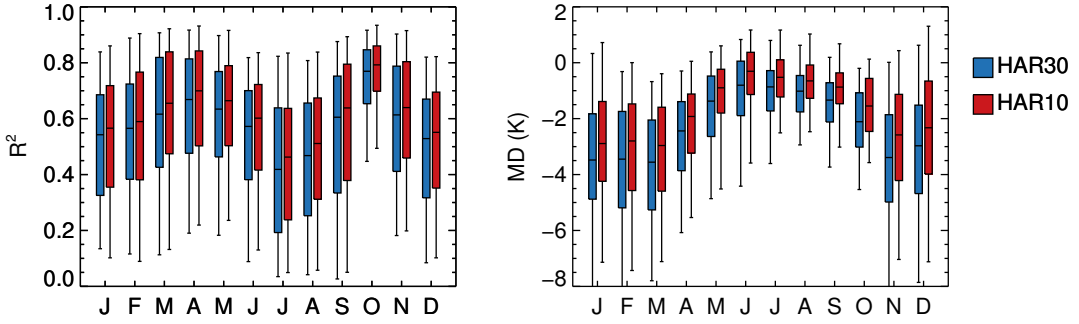

Figure 2.5: Boxplots of monthly coefficients of determination (R^2, left) and monthly Mean Deviations (MD, right) for HAR daily 2 m air temperature at each station located above 2000 m a.s.l. within the High Asia domain (32 stations) and each year. The R^2 show a bimodal annual cycle related to the standard deviation of temperature which is higher in spring and autumn.

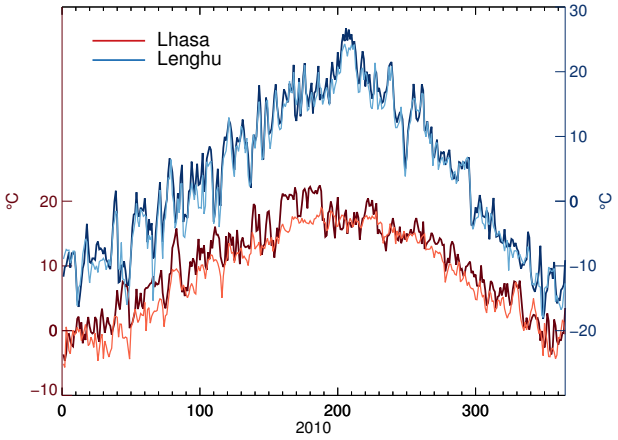

Figure 2.6: Daily 2 m temperature in 2010 at Lenghu (upper curve, blue) and Lhasa (lower curve, red). Dark thick lines are observations, light thin lines are HAR10. Note the different axis for both stations. Lenghu, located in the Qaidam Basin is the best performing station for this year and Lhasa is one of the worse.

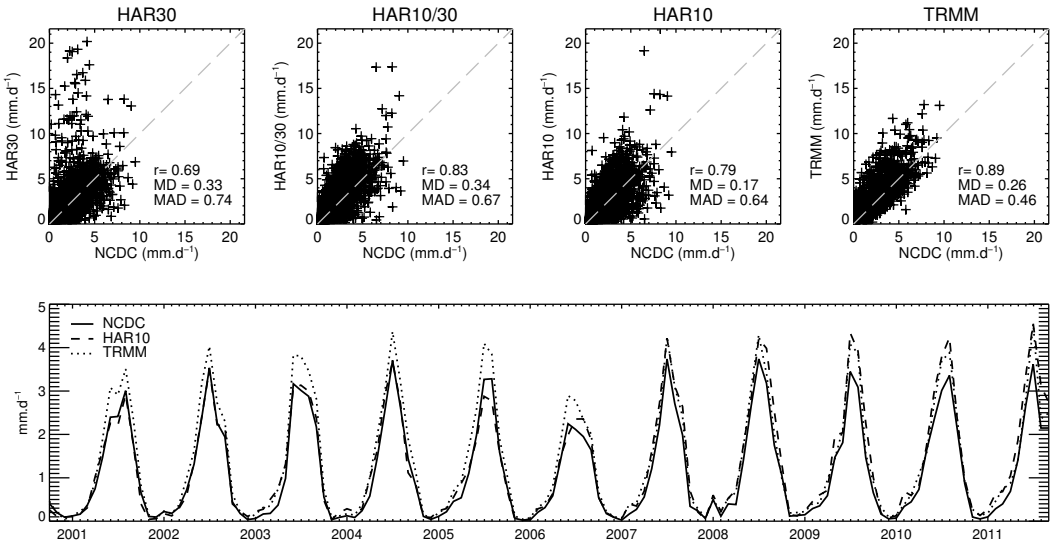

Figure 2.7: Comparison of monthly precipitation rates (mm d^{-1}, 2001-2011) with NCDC stations observations (31 stations, 4007 valid months). *Upper panel*: scatterplots of HAR30, HAR10/30, HAR10 and TRMM3B43 and statistical scores *r* (Pearson correlation coefficient), *MD* (Mean Deviation, mm d^{-1}), *MAD* (Mean Absolute Deviation, mm d^{-1}). HAR10/30 is constructed by spatially averaging HAR10 on the HAR30 grid. *Lower panel*: monthly precipitation timeseries (mm d^{-1}) averaged for all stations. (Paper II)

Precipitation

The various factors that affect air temperature are generally well represented by NWPs. Precipitation, in contrast, is possibly one of the less well reproduced phenomena, principally because of the highly complex nature of cloud-atmosphere interactions (e.g. Arakawa, 2004). Additionally, it is considerably more difficult to assess the precipitation forecasts accuracy. As discussed in both papers, the problems are multiple: spatial scale mismatch between gridded data and observations, gauge under catch, observational bias towards populated areas and valleys, etc.

In Paper I, we showed that TRMM was less accurate than the WRF model for the considered event when compared to station observations (Paper I Table. 3) and therefore not suitable for benchmarking alone. Thus we developed a new assessment method based on MODIS snow cover which allowed a precise (down to 500 m) evaluation of the simulated snowcover (Paper I Fig. 3). The method is based on MODIS scenes after and before the snowfall event, where the extent of snowfall can be estimated (but not the snowfall amounts). With this method we demonstrated the positive effect of higher resolution (Paper I Fig. 6) and of two-way versus one-way nesting (Paper I Fig. 7).

The day by day analysis realised in Paper I is an example of the meteorological aspect of HAR. In Paper II, the validation was done for the eleven years period. The monthly precipitation rates are compared with station observations (Fig. 2.7). The results indicate an improvement from HAR30 to HAR10. Interestingly, this improvement remains when HAR10 is aggregated to the HAR30 resolution. TRMM3B43 has a larger positive bias (MD) but explains better the variance at the stations (higher correlation and lower MAD), in contradiction with our results from

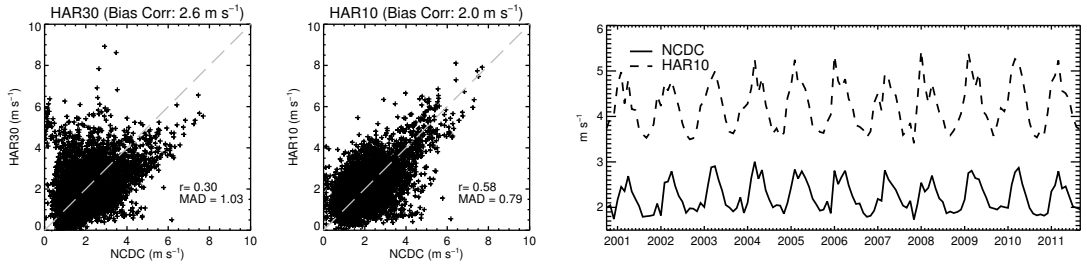

Figure 2.8: Comparison of monthly wind speed (m s^{-1}, 2001-2011) with NCDC stations observations on the TP (32 stations, 4104 valid months). There is a constant bias between observations and HAR, which I assume to be related to different measurements heights. *Left*: scatterplots of HAR30 and HAR10 and statistical scores r (Pearson correlation coefficient), $BCMAD$ (Bias Corrected Mean Absolute Deviation, m s^{-1}). *Right*: monthly wind speed timeseries (m s^{-1}) averaged for all stations.

Paper I. However, we clearly show added value from HAR with respect to daily precipitation (Paper II Fig. 4), topography (Paper II Fig. 5), or snowfall (Paper II Fig. 6).

Other variables

Figure 2.8 shows validation analyses for near surface wind speed on the TP. Despite of a constant bias of approx. 2 m s^{-1} which is probably related to different measurements heights, the agreement with observations is quite high ($r = 0.58$ for monthly values). The added value of increased resolution is more evident for wind speed than for temperature or precipitation. The annual cycle of wind speed on the TP corresponds to observations (maximum in winter/spring, minimum in summer). In Appendix B, we conduct an evaluation of the HAR cloud cover frequencies over the Nam Co lake and show that the diurnal and annual cycle of cloud frequencies over the lake are in accordance with observations.

Zhadang Glacier

The Automatic Weather Station installed on the Zhadang Glacier (see Section 4.3) provides a unique opportunity to test the HAR in high altitude glaciated environments (Fig. 2.9). These results are of particular importance, since they show that (i) the HAR accuracy for the most relevant variables of the surface energy budget is very high, (ii) substantially better than for neighbouring NCDC stations (e.g. Lhasa presented above), (iii) despite of the coarse resolution, HAR10 can represent the local climate satisfyingly and (iv) the increase of resolution mostly improves wind flow simulation, by a better representation of topography.

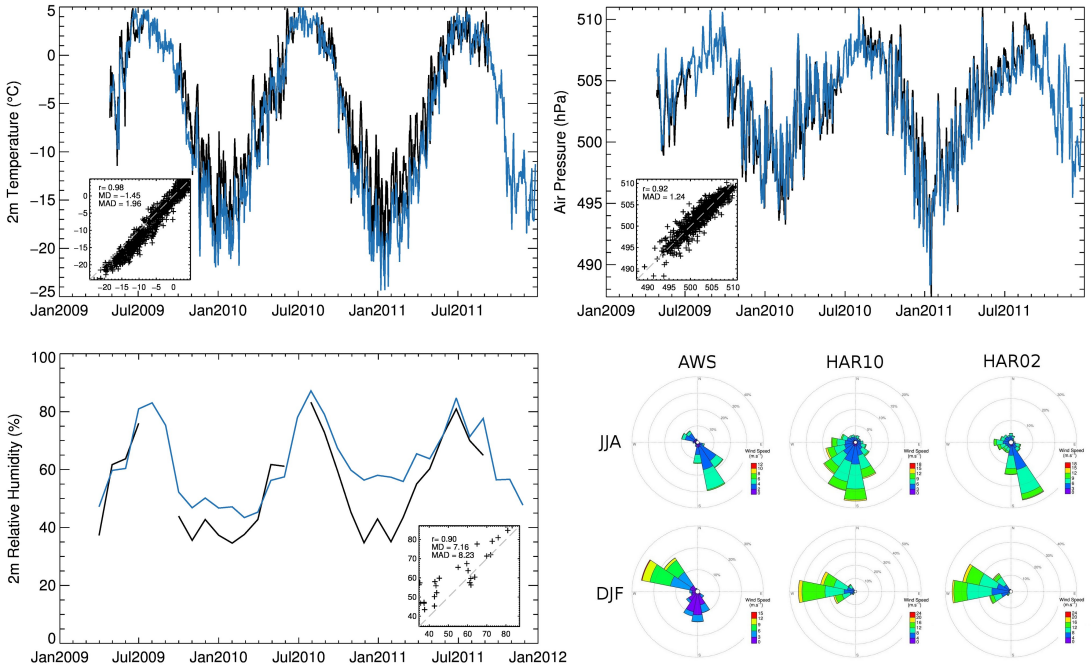

Figure 2.9: Examples of HAR validation at the Zhadang AWS (black: AWS, blue: HAR10). *Upper left*: daily air temperature. *Upper Right*: daily air pressure, bias corrected. *Down left*: monthly relative humidity. *Down right*: windroses based on hourly values from AWS, HAR10 and HAR02 for summer and winter. HAR02 is showed here to illustrate the positive impact of high resolution for wind flow simulations, while other variables have very similar accuracies (not shown). Incoming short-wave radiation is not shown here since the glacier model relies on HAR cloud fraction (evaluated in App. B).

2.3.3 Summary

i. The HAR temperature fits well to observations in general. The major issue is the significant winter cold bias. For most impact studies its effect is secondary since restricted to winter (less "relevant" season for the hydrological cycle). The time dependency of this bias however is more problematic (Klein, 2013), and seems to be related to changes in the FNL system. According to these results, winter temperature inter-annual variability should be analysed only with care and trend analyses based on HAR are not robust.

ii. The HAR precipitation fits well to observations, especially the high resolution products. Shortcomings are unavoidable but several indicators indicate an improvement from HAR to TRMM and other coarser datasets. It is not possible to provide uncertainty estimates of precipitation everywhere on the TP but the local and spatial features (variability, frequency, seasonality, type) are expected to be well reproduced.

iii. Mölg et al. (2014) and Biskop et al. (2013) could reproduce, respectively, observed surface mass balance at Zhadang and Lake Level at Nam Co, with HAR only as input data for glaciological and hydrological models. These results indirectly validate the whole model chain, however not without appropriate care with respect to the assumptions and calibration factors used in both impact models.

Chapter 3

The climate of the Tibetan Plateau

The objective of this chapter is to give an overview of the climate of the TP and to demonstrate the possibilities offered by HAR as they have been used in Papers I to IV, Dietze et al. (2014) and Mölg et al. (2014). In Section 3.1 I present several important synoptic features of atmospheric circulation in south-central Asia as resolved by HAR. In Section 3.2 I show some examples of the high resolution HAR10 products and how they were used.

3.1 Synoptic and mesoscale climatology

Some features of atmospheric circulation in the HAR30 domain are presented in Fig. 3.1, and represent quite well the two major drivers of climate variability on the TP: the westerlies and the monsoons. In winter a geopotential height gradient generates strong westerly winds in the mid- to upper-troposphere, and an anticyclonic system is formed over India, producing a land to see breeze characteristic of the winter monsoonal flow. In summer, the Somali Jet and a depression system over India cause the reversal of this flow. Two mid-troposphere low pressure systems characterize the mean atmospheric circulation patterns at 500 hPa: the monsoonal depression over India (which extends from the surface up to 400 hPa) and the thermal low over the TP (confined to the TP boundary layer). The upper-tropospheric high pressure system centred south of the plateau[1] dominates the global upper tropospheric circulation.

[1] Tibetan High, attributed to the diabatic heating processes associated with deep convective rainfall in south-east Asia and possibly also to the sensible and convective heating over the elevated Tibetan Plateau (Wang, 2006).

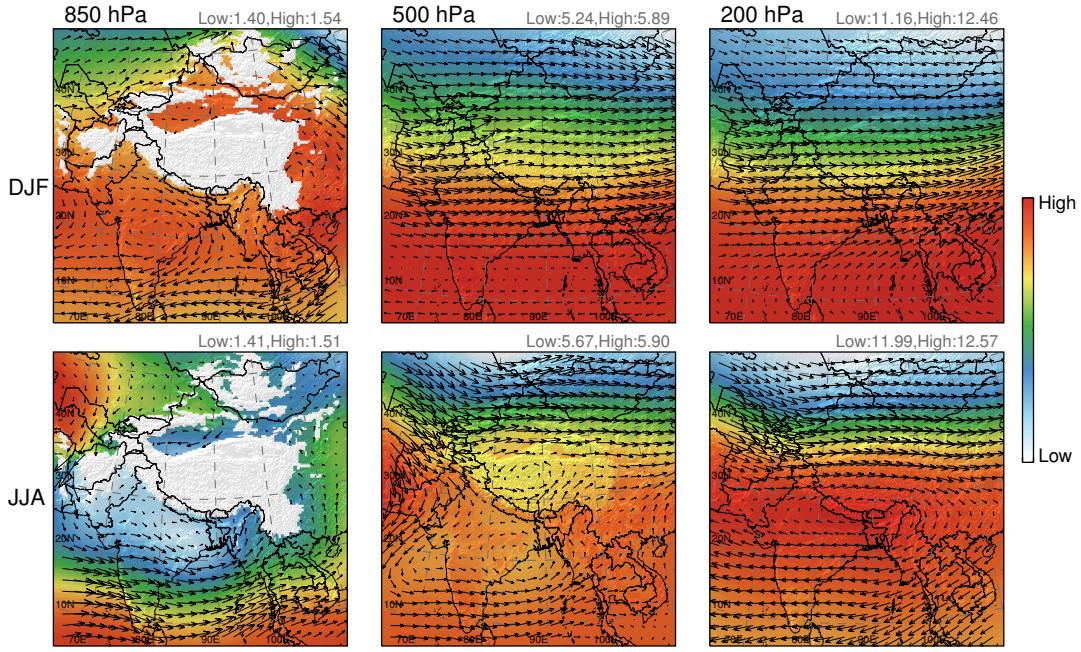

Figure 3.1: Decadal averages of geopotential height (km) and wind vectors in DJF and JJA at 850-, 500- and 200-hPa over the HAR30 domain. Extended from Paper II, Fig. 2.

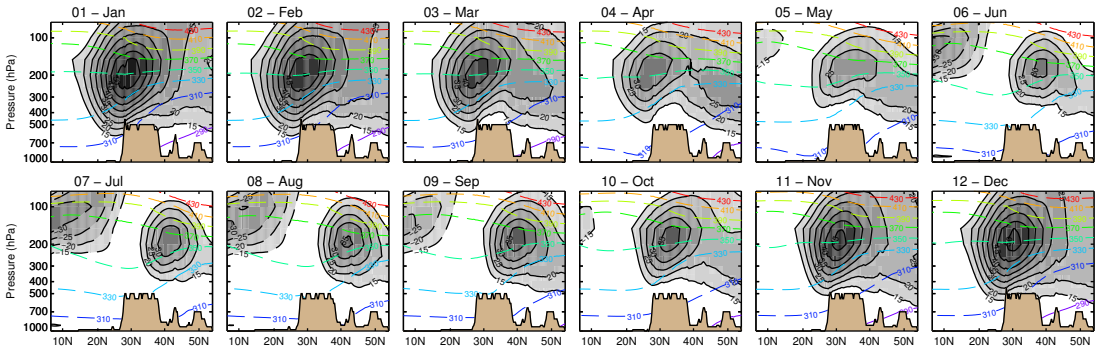

Figure 3.2: Decadal monthly averages in a latitudinal-vertical cross section at 90°E. Gray shading correspond to the horizontal wind speed (m s^{-2}, solid contour lines indicate positive zonal wind, dashed lines negative zonal wind), dashed coloured lines correspond to potential temperature (K). Extended from Paper II, Fig. 2.

A latitudinal cross section at 90°E illustrates best the strong seasonality of the westerly flow over the TP (Fig. 3.2). In winter the maximum averaged zonal wind speed is located south of the TP, but the flow is strong down to the Plateau surface. April to June marks the transition to summer conditions, and the elongated profiles indicate a high variability of the jet stream location during these months (Schiemann et al., 2009). The elevated heat source of the TP is visible in the temperature profiles in summer, as well as the potential temperature maxima at 200 hPa south of the TP. In summer the westerly flow is weaker and concentrated north of the TP while the tropical easterly jet forms close to the Equator.

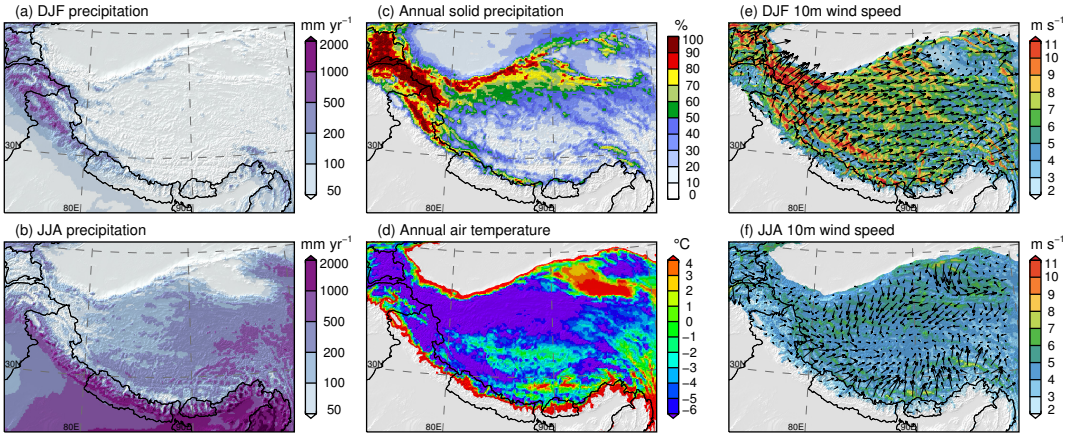

Figure 3.3: Average climate variables from HAR10. For (d), (e), (f) the altitudes below 2000 m a.s.l. are masked for clarity.

3.2 Spatio-temporal patterns of climate variables on the TP – added value of HAR

The dynamical features presented above are consistent with those presented in other studies based on global reanalysis datasets[1]. This was to expect since HAR is strongly constrained by the observed large-scale atmospheric flow. The added-value of HAR lies in the consistent process-chain which links these large-scale features to local conditions, since at 10 km resolution, surface conditions such as topography, land cover, lakes, are represented with more detail. Therefore, surface variables like temperature (Paper IV, Mölg et al., 2014), precipitation (Papers I, II, III) or surface wind (Paper IV, Dietze et al., 2014) were extracted from the HAR10 dataset for analysis (Fig. 3.3).

In Paper II, we provide a detailed analysis of the dynamical and mechanical factors that lead to precipitation on the TP. We discuss the importance of relief an topography on precipitation patterns: For example, the uplift caused by the Himalayan range generates an orographically induced "precipitation barrier", leaving the regions north of the range with drier air masses and less precipitation. Selected profiles along the Himalaya range show that precipitation mimics the topographic profiles (Paper II, Fig. 7) which is not the case with HAR30 which has a too coarse resolution.

A special attention was given to precipitation seasonality. In general, the annual cycle of precipitation on the TP is characterized by a winter precipitation regime in the west, a spring precipitation regime in northern and southern TP and a summer precipitation regime elsewhere (Paper II, Fig. 8). With a closer look at the seasonal cycle of precipitation on a monthly basis (Paper II, Fig. 9), we obtain more complex patterns than commonly assumed, especially on the central and northern TP where spring precipitation represents a substantial part of the annual amounts. Furthermore, we identified regions with higher precipitation variability, either

[1] e.g. Bohner (2006); Schiemann et al. (2009); Wang (2006); Molnar et al. (2010); Boos and Kuang (2010)

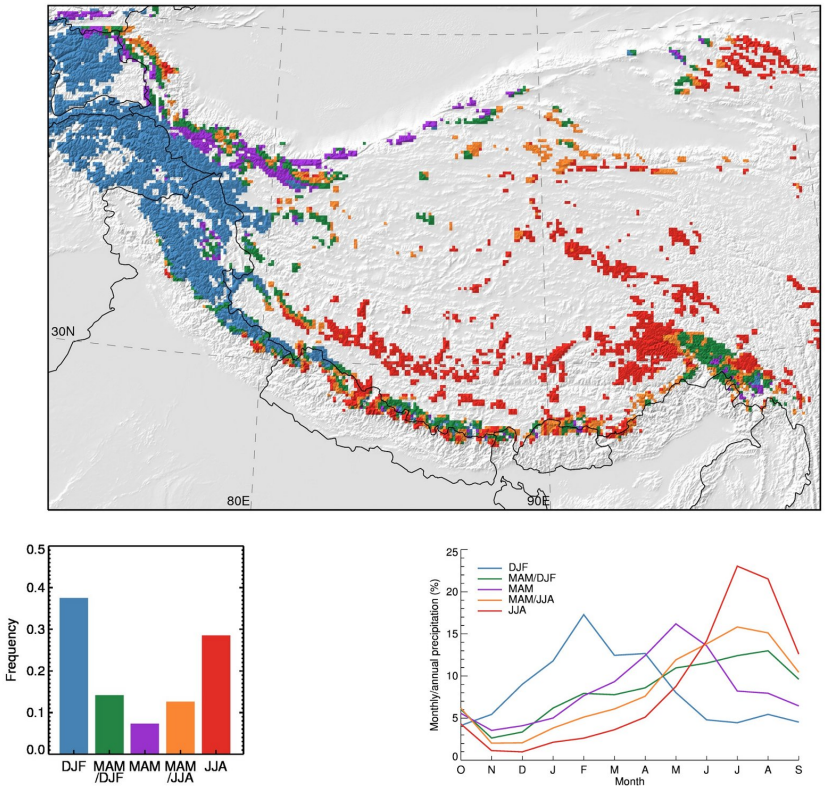

Figure 3.4: Classification of glacier accumulation regimes according to precipitation seasonality. A k-means clustering algorithm is run on three input variables (percentage of precipitation falling in DJF, MAM and JJA) and with five output clusters. The clusters are named after their cluster centre characteristics, as seen in the seasonal course (lower left plots). Modified after Paper II Figs. 14 and 15

by analysing the occurrence of strong precipitation events (Paper II, Fig. 10) or by showing regional anomalies of the annual coefficient of variation (Paper II, Figs. 10 and 11). We see that both indicators of extremal precipitation are high for some regions, for example in Pakistan and north-western India. On the TP, precipitation days are of rather constant intensity during summer, due to frequent convective activity. The inter-annual variability in central and western TP is higher than for the neighbouring TP regions, which can be explained by inter-annual variability of the outreach of the summer precipitation events.

In Paper II we emphasized the high sensitivity of glaciers on the TP to precipitation seasonality. Shi and Liu (2000) proposed a classification of the glaciers on the TP according to their continentality (maritime, sub-continental, continental). Rupper and Roe (2008) proposed another grouping into three classes (Western, Eastern and Northern) according to the characteristics of glaciers during the last glacial cycle. In Fig. 3.4, we further propose a new classification based on precipitation seasonality only, computed using an objective clustering approach. This analysis emphasizes that glaciers on the TP are diverse regarding their accumulation patterns. An adapted version of the cluster analysis was also used in Mölg et al. (2014) to identify regions where the special mechanisms described in the study might also operate (glaciers of the summer accumulation type).

Chapter 4

A Tibetan Glacier case study: Zhadang

The Zhadang Glacier has been chosen as benchmark region for the combined HAR – glaciological – hydrological modelling system defined in the DynRG-TiP and WET projects, and has been the subject of an intensive field program in recent years. This chapter presents the study region and the reasons for choosing Zhadang (Section 4.1), observed regional glacier changes in recent decades (Section 4.2, Paper V), the field observations and their outcome (Section 4.3, Appendix A), and the results of the first Surface Energy and Mass Balance (SEB/SMB) modelling study at Zhadang (Section 4.4, Paper III).

4.1 Study region

Zhadang Glacier is a small valley glacier (2009: 2.36 km^2, altitude 5500–6000 m a.s.l.) located in the Nyainqentanglha Range, about 200 km North from Lhasa (Fig. 4.1). The glacier is exposed to the northwest and drains into Lake Nam Co (4725 m a.s.l.). The western Nyainqentanglha Range strikes approx. 230 km in length, and reaches heights between 5000 and 7162 m (Mount Nyainqentanglha). Glaciers in this region correspond to the "summer accumulation type" as shown in Fig. 3.4.

The Nam Co lake is Tibet's largest salt water lake with noticeable variations in size since the Last Glacial Maximum (Schütt et al., 2008), and also since 1970. From 1970 until 2006 the lake expanded its area by more than 50 km^2 (Liu et al., 2010). Due to its relatively easy access, it is probably one of the best studied regions of the TP. The Nam Co Monitoring and Research station, located close to the lake, is used as base for scientists all year round.

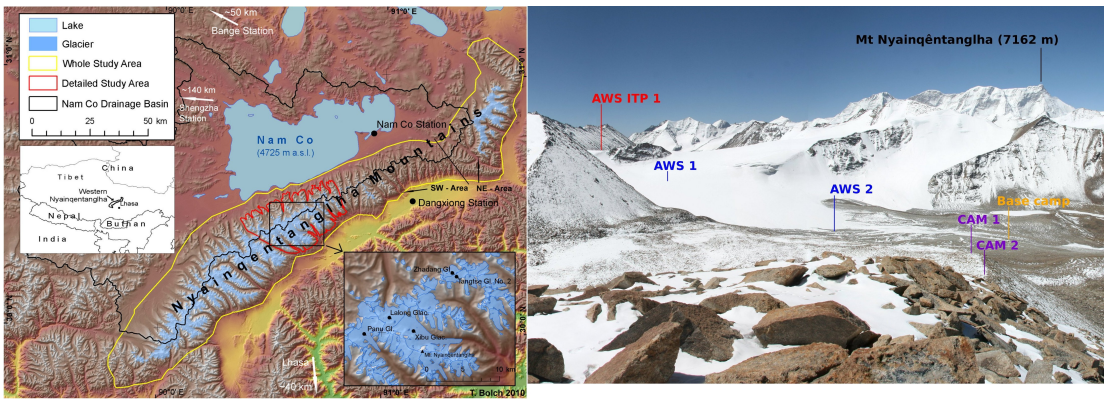

Figure 4.1: Left: Overview of the Nyainqentanglha Range, including a zoom into the Zhadang Glacier area (after Paper V). Right: Panorama of Zhadang Glacier, with locations of the AWS and camera installations.

4.2 Glaciers changes 1976–2009 in the western Nyainqentanglha Range

With the funding of the DynRG-TiP project and the beginning of our collaboration with the ITP, Tobias Bolch (at this time at the TU Dresden) lead the first collaborative study of the project (Paper V). Using remote sensing and GIS techniques, the study provides a glacier inventory and glaciers changes 1976–2009. In the years around 2001 the whole mountain range contained about 960 glaciers covering an area of 795.6 ± 22.3 km^2 and the glacier area decreased by $-6.1 \pm 3\%$ between 1976 and 2001. The Zhadang Glacier lost about 14.2% of its surface and retreated of 295 m in the same period (Fig. 4.2). My role in this study was to discuss the possible climatic drivers of these glacier changes (Paper V, Section 5.2). At the time of writing, HAR did not yet exist and the weather station was recently installed on the glacier. Thus, we had to rely on nearby stations and previous analyses from the literature. Several studies reported a warming trend in the region and a possible increase of precipitation (e.g. You et al., 2010; Caidong and Sorteberg, 2010). We assumed that the observed warming in the wet season is the major driver for glacier changes, since changes in the summer temperature affect both the glacier melt and the snow line altitude. Our recent results put these assumptions in a new perspective (Paper III, Mölg et al., 2014).

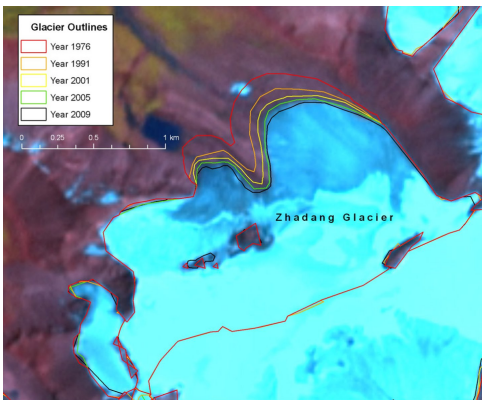

Figure 4.2: Area changes of Zhadang Glacier (Paper V, T.B.).

Linking the presented glacier area and length changes to climate variations is not straightforward, mainly because (i) the glacier changes are only indirect signals and depend especially on glacier response times, (ii) the availability of the climate data in the study area is very scarce. The present knowledge about the response of polythermal, summer-accumulation type glaciers

Figure 4.3: Field work in Tibet.

to climate changes at different time scales is still limited. In the study we also stated that: "Ongoing investigations (e.g. direct mass balance measurements, meteorological energy balance measurements on Zhadang Glacier, acquisition of gridded climate data) [...] will help to adjust existing glacier models to the specific situation in the study area". This is a great example of how things can actually happen according to long term objectives.

4.3 Field observations

The Zhadang Glacier has been chosen by our colleagues from the ITP as an intensive measurement site several years ago. They operate two Automatic Weather Stations (AWS) since 2005[1], supplemented by mass balance measurements applying the glaciological method. The installations have been complemented in May 2009 by our teams in cooperation with the ITP and especially with Yang Wei (associate professor at the ITP). Seven campaigns took place since then, five under my responsibility. At the TU Berlin and RWTH Aachen we were in charge for the AWS design and maintenance, which is now realised by our Chinese partners.

Since the conditions for field expeditions on the TP are very peculiar, we wrote a report which was published in the "Extended abstracts and recommendations" booklet from the workshop on the use of automatic measuring systems on glaciers in Pontresina (Maussion et al., 2011b, reproduced in Appendix A). We give details on the instruments and methods we used and we relate the success or failures of these campaigns, to hopefully prevent others from reproducing some of our mistakes in the future. Despite some data-gaps, the outcome of these field campaigns is exceptional. It lead to major scientific achievements: at least three peer-reviewed publications (Zhang et al., 2013a; Mölg et al., 2014, Paper III, and this will certainly increase in the future). But the successes were also humane, starting with a fruitful collaboration with our German and Chinese colleagues through life-changing encounters and experiences (Fig. 4.3).

[1] According to our colleagues, it appears however that the stations did not work properly and the data have not been published yet.

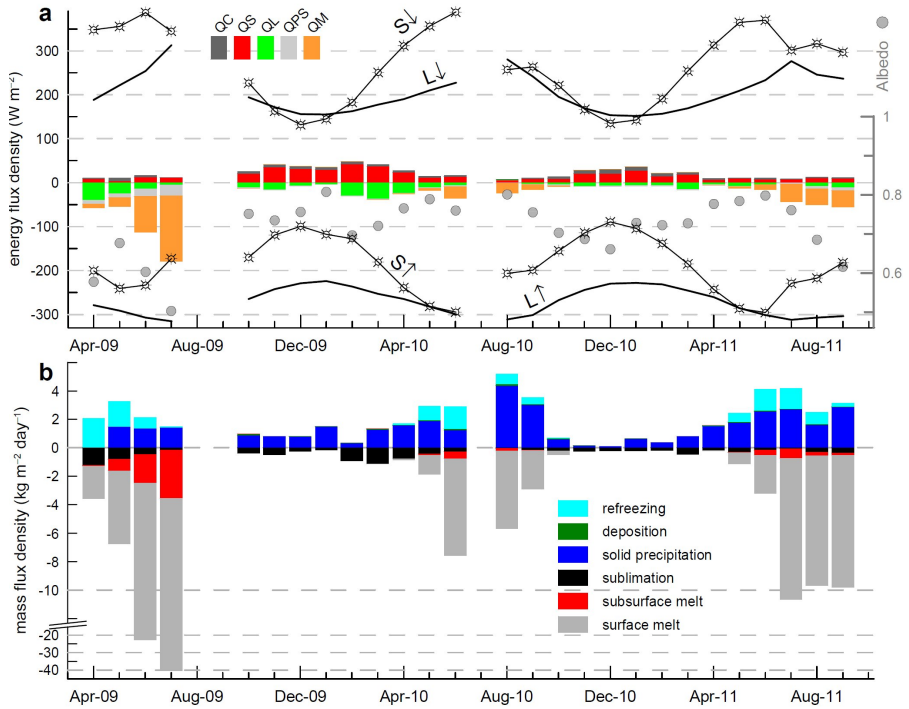

Figure 4.4: Glacier-wide mean monthly (a) SEB components with surface radiation terms shown as lines, albedo as dots, and the remaining fluxes as bars (see Paper II for abbreviations) and (b) MB components from April 2009 to September 2011 in the reference run. Note the y-axis break and variable scaling in (b) due to large melt amounts in 2009. (Figure from Paper III, T.M.)

4.4 Asian Monsoon footprint on the Energy and Mass Balance of Zhadang Glacier

From the data basis acquired at Zhadang, a study of glacier-wide mass and energy balance fluxes was made possible. Paper III was written by a team of authors from the TU Berlin and the ITP lead by Thomas Mölg. The study had several objectives: (i) provide the first study of detailed distributed surface energy balance (SEB) and mass balance (MB) at Zhadang, to complement the very few other studies on the TP, (ii) introduce a new method to estimate MB uncertainty using Monte Carlo and ensemble strategies, and (iii) linking the SEB/MB at Zhadang to multi-temporal monsoon dynamics on the inter-annual and intra-seasonal scales (this is the main objective of the study).

These objectives could be reached with the combination of the multi-year observational data set at Zhadang and with the utilisation of a comprehensive SEB/SMB model (Mölg et al., 2008, 2009) updated for this study. Additionally, two variables that are not available from measurements where taken from a special HAR experiment at 2 km resolution for Nam Co: cloud cover fraction and local precipitation (Paper III Section 2.2 and Fig. 2). However, we had to constrain the HAR precipitation with a factor of 0.56 to take into account possible overestimation from the model as well as other effects such as gauge undercatch and loss of snow by wind drift and wind

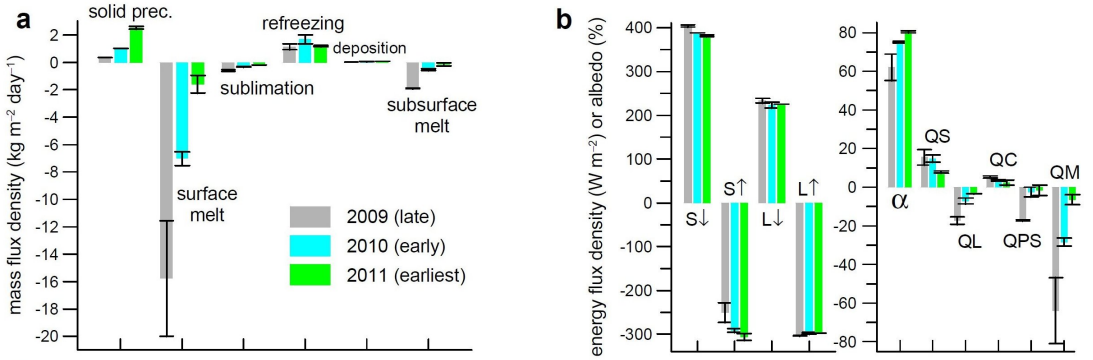

Figure 4.5: Glacier-wide (a) MB and (b) SEB components during monsoon onset for 2009–2011. (Figure from Paper III, T.M.)

sublimation (processes which are not included in both models). The Indian Summer Monsoon (ISM) dynamics were characterized using an index identifying active and break periods of the ISM on the basis of a horizontal wind shear index (Prasad and Hayashi, 2007). With this index the onset, core and cessation periods of the ISM could be defined as well as the intra-seasonal ISM variability (active and break) periods (Paper III Fig. 4).

The MB model performance could be assessed (Paper III Figs. 5 and 6) thanks to the direct measurements of mass balance at several ablation stakes as well as surface temperature and surface height changes at the AWS location on a hourly basis[1]. Observed surface height changes were also used to select the plausible realisations out of 1000 Monte Carlo simulations to provide an uncertainty range (Paper III Appendix A). The MB model performance is good (surface temperature RMSD of 1.69 K, surface height changes RMSD of 7.3 cm), and captures the differential ablation between 2009 (strong) and 2011 (weak) very well.

On this robust basis the processes that drive the variability of the glacier-wide MB could be analysed independently (Fig. 4.4). In general, global (S↓) and incoming long-wave radiation (L↓) dominate energy input, while reflected shortwave (S↑) and outgoing longwave radiation (L↑) are the major energy sinks at the surface. Sensible and latent heat fluxes (QS and QL) are more important in winter and spring, respectively. A salient feature of the variability is the period of April–June both in 2010 and 2011, when S↑ developed into an equally strong energy sink as L↑ . The pattern was different in 2009, when anomalously low albedo weakened this process of energy removal. This, in combination with the highest L↓ in the record, resulted in exceptionally high availability of melt energy in June–July 2009.

It appears that the role of the Asian monsoon in the SEB and MB processes is most important during the monsoon onset phase. A series of systematic differences in the MB components is evident in (Fig. 4.5): the later the onset of the ISM, the (i) less accumulation by solid precipitation, (ii) more sublimation, (iii) more melt at the surface, and (iv) more subsurface melt as well. The higher latent energy flux of melting is controlled by low albedo and reduced reflection of solar radiation. Thus, the timing of monsoon onset leaves a clear footprint on the glacier through the

[1] for the surface height changes, a special instrument was used (Sonic Ranger SR50, see Appendix A).

albedo effect, which leads to higher mass loss on the glacier the later the ISM is established in a particular year. The ISM footprint at the end of the monsoon season is of little importance (Paper III Fig. 9). Surprisingly, atmospheric variability over the ISM area does not seem to directly influence the Zhadang region during the core season either (Paper III Fig. 10).

These analyses provided a first evidence that the atmospheric processes occurring during the onset phase of the ISM (i.e. approx. June) were determinant in controlling annual mass balance. Further, the individual contributions of the energy fluxes at the surface could be analysed precisely, which is rare in this region. The results from Paper III were extended and confirmed by a further study (Zhang et al., 2013a) and call for further research on longer time scales and including other large scale dynamic processes (Mölg et al., 2014).

Chapter 5

Lakes and endorheic basins on the Tibetan Plateau – sensors and actors of the climate system

In this Chapter, I will discuss two functions of the lakes in the climate system. First, we use lakes as sensors of climate variability by linking observations of lake ice phenology to climate variables extracted from HAR (Section 5.1, Paper IV). Second, we study the role of lakes in the climate system by analysing the influence of the presence of a lake on local precipitation spatio-temporal variability (Section 5.2, Appendix B).

5.1 Lake ice phenology and its relation to climate

Using a snow cover product derived from satellite data, Jan Kropacek (TU Dresden and University of Tübingen) and co-authors derived the ice phenology of 59 lakes during the period 2001 to 2010 (Paper IV). The lake ice phenology for each winter is described with the timing of following events: Freeze Onset (FO, when ice is detected), Freeze-up (FU, when the lake is fully ice-covered), Break-up (BU, appearance of a detectable ice-free water surface and no more total freeze-up occurs), and Water Clean of Ice (WCI, when no more ice could be detected). Two more variables describe the duration of ice cover: Duration of Ice cover (DI, which is the time span between FO and WCI), and Duration of Complete Ice cover (DCI, which is the time span between FU and BU). The average ice phenology durations for each lake are shown in Fig. 5.1 (Left).

Ice cover duration varies greatly between lakes. Some geographical features can be recognized, for example in the North where temperatures are lower and the ice durations longer. In order to find which lake characteristics influence lake ice duration, the ice phenology variables for each

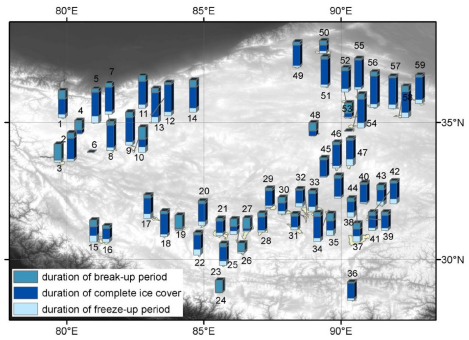

	DCI	DI	FO	FU	BU	WCI
longitude	0.28	0.29	−0.33	0.18	0.11	**−0.63**
latitude	0.46	0.45	**−0.63**	0.52	0.16	**−0.63**
altitude	**0.75**	**0.73**	−0.54	0.36	0.31	0.50
mean temp.	**−0.80**	**−0.81**	**0.85**	**−0.73**	−0.47	**0.64**
thawing index	**−0.74**	**−0.75**	**0.81**	**−0.72**	−0.46	**0.66**
freezing index	**−0.82**	**−0.83**	**0.85**	**−0.73**	−0.47	**0.61**
perimeter/area	**0.79**	0.49	−0.49	0.43	0.26	−0.05
area	−0.32	−0.27	0.31	−0.07	0.14	−0.08

Figure 5.1: Left: Ice cover duration for the studied lakes on the TP showing duration of freeze-up period, duration of complete ice cover (DCI) and duration of break-up period as heights of the respectively coloured sections of bar symbols, whereas the total size of the bar represents the duration of ice cover (DI). Right: Correlation of ice phenology dates with climate and local parameters calculated for lakes larger than 300 km^2 (18 largest lakes). Statistically significant values at the level of significance 0.02 are bold. Figure and Table from Paper IV, acronyms are explained in the text.

lake were correlated with local parameters such as latitude, altitude, perimeter/area index, area, and three temperature indicators (annual average temperature, thawing and freezing index) extracted from HAR (Paper IV Table 4). To reduce noise, the same analysis is reproduced for the 18 largest lakes only (Fig. 5.1 Right). The air temperature and related indexes appear to be the most important predictors for the ice phenology metrics. The high correlation of phenology metrics with latitude indicate the decrease of temperature and solar radiation towards north. However, as discussed in the paper, many other parameters other than climate can influence ice phenology. Lake bathymetry and salinity, for example, probably play an important role which is not possible to quantify due to the lack of data.

Paper IV contains further discussion about trends and grouping of the lake according to their characteristics. This study was the first of this scale for the TP and showed that lake ice phenology is an important indicator of climate change and climate variability. Inter-annual variability was only superficially addressed in the paper, because methodological aspects and presentation of the climatologies did not leave enough room for more analyses. This aspect should be addressed in a future study.

5.2 Influence of lakes on local climate – a case study with HAR

While temperature affects lake ice phenology, the lake ice regime can in turn influence local climate. Freeze-up and break-up processes lead to an abrupt change of lake surface properties (e.g. albedo, roughness), affecting mass and energy exchange between the water surface and the atmosphere. The lakes basically act as heat sinks in summer and heat sources in autumn and winter (Wilson, 1977) before freezing. In Appendix B (manuscript in preparation) we run an idealized experiment where the Nam Co lake has been replaced by grasslands to quantify the influence of the presence of the lake on precipitation spatio-temporal variability. Furthermore, we investigate the influence of assimilating satellite-derived lake surface temperatures (ST) instead of using the standard WRF initialization approach used currently in HAR.

We find that assimilating lake ST has a positive impact on the simulated cloud frequencies and precipitation patterns, especially during the months of August to December when the standard HAR approach leads to too cold ST (Fig. 5.2). The lake, colder in summer than its surroundings, inhibits convection as shown by observations and by HAR in Fig. 5.3 (left), where cloud frequencies are reduced of more than 15% by the presence of the lake in summer. This effect is enhanced in HAR without improved ST. We conclude that future versions of HAR, especially the 2 km products, should assimilate lake ST using the method presented here.

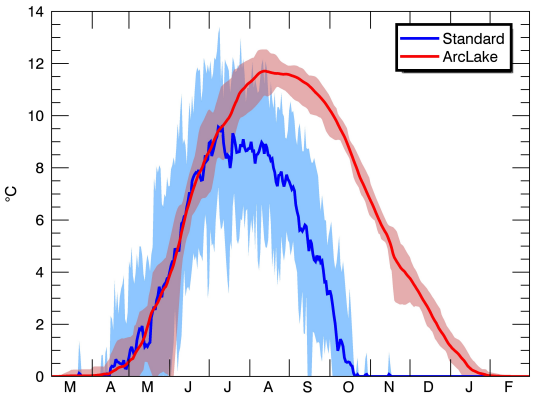

Figure 5.2: Decadal mean of the Nam Co lake daily SST, according to the WRF Standard parametrization (blue) and to the ArcLake dataset (red). Shaded areas indicate the decadal minimum and maximum range.

According to our simulations, the presence of the lake reduces precipitation averaged over the Nam Co drainage catchment of about 8% (Fig. 5.3 right). This percentage becomes larger when considering the neighbouring regions on the eastern (lee) side of the lake. This result is interesting in the context of glacier extent on the Nyainqentanglha range (Paper V). There is a much larger area of ice on the southern than on the northern range. In Paper V we argued that this difference could be due to rain-shadow effects on the monsoonal south-easterly moisture flow. Our results suggest an alternative explanation: the presence of the lake can be responsible for less precipitation on the northern side and therefore less accumulation and lower albedo. This should be quantified using a glacier model forced with the idealised simulation.

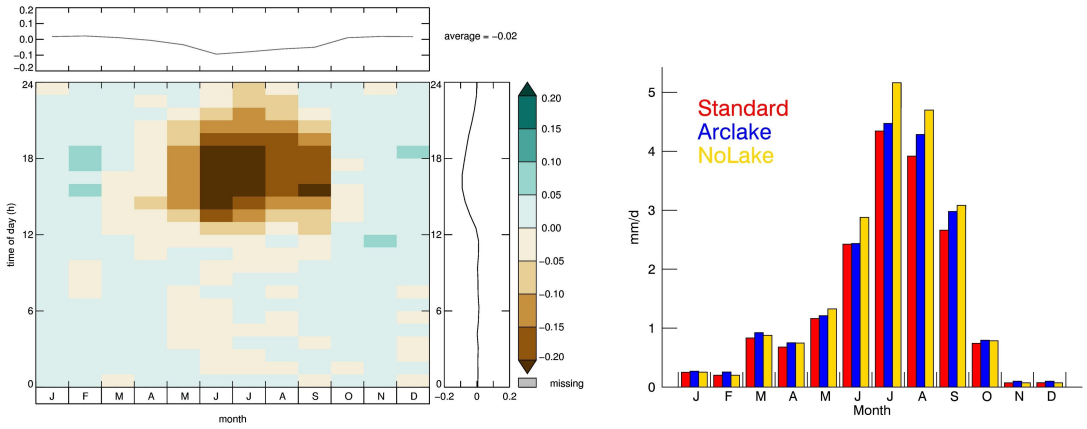

Figure 5.3: *Left*: Differences in cloud frequency for each month and time of day (CST) between the WRF ArcLake and NoLake experiments over the lake surface. Brown colours indicate that there are less clouds over the lake than over land. *Right*: Monthly precipitation (mm d^{-1}) averaged over the Nam Co basin for the three WRF experiments Standard (HAR), Arclake (with assimilated ST), NoLake (lake removed).

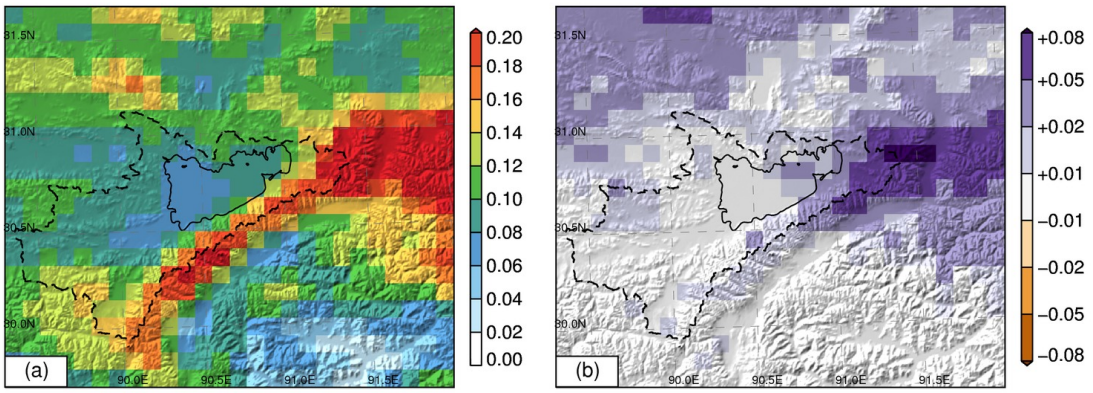

Figure 5.4: (a) frequency of snowfall events (> 0.1 mm d^{-1}) during the October to December period for the ArcLake experiment. **(b)** Difference between the ArcLake and the Standard experiment during the same period (positive values indicate that there are more snowfall events in the ArcLake experiment).

We also observe lake-effect snowfall events in autumn and early winter (Fig. 5.4). These occur when cold and dry air passes above the warmer lake and lead to more frequent precipitation on the lee side of the lake. The influence of these events on yearly precipitation amounts is less significant than the dampening of precipitation in summer. However, it plays an important role for local nomadic populations, who have to move their tents, family and animals to the north-side of the lake each winter.

Chapter 6

Conclusions and outlook

In this thesis, several issues related to a better description and understanding of components of the atmosphere, cryosphere and hydrosphere on the TP have been addressed. A central tool developed for this purpose, the High Asia Reanalysis, has been presented.

Crucial steps were the optimisation of the WRF model set-up used to produce HAR and the evaluation of the meteorological products. This task was made difficult by the scarcity of meteorological observations and issues related to their unknown accuracy and their low spatial representativeness. Furthermore, several tools had to be developed and tested for the operational production of the HAR data products. In this regard, the present thesis provides a robust scientific and technical framework for related projects, at the TU Berlin or elsewhere. On this basis the update of HAR to later periods (i.e. 2012, 2013, up to a almost instantaneous retrieval) is an easy task and will offer new possibilities, for example for monitoring applications.

So far, the HAR alone helped to improve our understanding of the TP precipitation climate (Papers I and II). The analyses showed the strong spatial variability of precipitation seasonality, and revealed possible implications for the interpretation of glacier changes. Regions with higher inter-annual variability and/or prone to extremal precipitation events were identified. Further studies will follow and will address detailed aspects of the drivers of precipitation variability. Current work focuses on atmospheric water fluxes to trace the origin of atmospheric moisture over the TP (Curio et al., 2013), as well as on linking large scale influences to the precipitation anomalies. These studies will rely on the work realised in this thesis.

In combination with other datasets (e.g. satellite or *in situ* observations) and impact models, HAR contributed to advances in various disciplines. For example, in Paper IV we determined the climatic factors of ice phenology acquired from remote sensing products. In Paper III, HAR precipitation and cloud products replaced observations that were missing or incomplete at the Zhadang Glacier. The physically based model chain applied at Zhadang helped to rethink the

possible drivers of glacier changes advanced in Paper V. Dietze et al. (2014) could use wind shear stress data from HAR for comparison with the particle size distributions extracted from sediment cores at several lakes on the TP, in order to describe sediment transport processes. This kind of integrated approaches are rare, and were made possible thanks to interdisciplinary and international projects such as the DFG-TiP and the BMBF-CAME Programmes. Within the WET project, several studies related to the TP hydrology will follow: Huintjes et al. (2013) tested HAR in the remote region of the Purogangri where no observations at all are available except for a decadal glacier surface elevation change acquired from satellite based digital elevation measurements (Neckel et al., 2013), and Biskop et al. (2013) drove a hydrological model with HAR at lake Nam Co and developed new methods adapted to the specificity of glaciated basins on the TP.

While the two latter studies were able to apply HAR successfully they also pointed out certain issues regarding its accuracy, especially a possible over-estimation of precipitation by the model (also discussed in Paper III). No overestimation could be detected in comparison to observations in Paper I and II. This enlightens the necessity to evaluate HAR accuracy by other means but also suggests possible omissions of processes (e.g. snowdrift) of a model chain. The HAR is a downscaling effort based on a numerical model, which has unavoidable shortcomings. Some of them are known and discussed in this thesis, and others will be detected in further stages. The new GPM system (Global Precipitation Measurement, Hou et al., 2013) or innovative cloud detection algorithms (Rüthrich et al., 2013) may help to improve the evaluation in the future.

Using Monte Carlo and ensemble strategies, Paper III and Mölg et al. (2014) proposed a method to deal with uncertainty while using HAR as "replacement" for *in situ* observations at Zhadang during an eleven years period, providing one of the longest surface energy and mass balance time series in the region. The Mölg et al. (2014) study illustrates well how to use HAR in a meaningful and robust aspect: the study of variability and its large scale drivers. Using indices extracted from large-scale datasets unrelated to the HAR production, the study shows how and to which extent the intensity of Indian Summer Monsoon onset and mid-latitude dynamics affect mass balance variability at Zhadang. The analysis is complemented by inter-annual anomaly analyses extracted from HAR30 and HAR10, proving a physical interpretation to the statistical correlation between circulation indices and annual mass balance. This study provides a prototype for further analyses and opened new research directions.

The advances reported in this thesis were made possible thanks to international collaborations, and to the support and involvement of people on the field, at the TU Berlin and at partner universities. The vast majority of the tools and datasets used in this thesis are made freely available by their developers. The HAR follows this philosophy and will be available to any interested users.

Thesis papers

Paper I

WRF simulation of a precipitation event over the Tibetan Plateau, China – an assessment using remote sensing and ground observations

Maussion, F., Scherer, D., Finkelnburg, R., Richters, J., Yang, W., and Yao, T. (2011): WRF simulation of a precipitation event over the Tibetan Plateau, China – an assessment using remote sensing and ground observations, *Hydrololgy and Earth System Sciences*, 15, 1795-1817, doi:10.5194/hess-15-1795-2011

Status: Published.

Own contribution:

- design of the study
- numerical simulations
- data preparation
- data analysis
- graphics and tables
- writing

Hydrol. Earth Syst. Sci., 15, 1795–1817, 2011
www.hydrol-earth-syst-sci.net/15/1795/2011/
doi:10.5194/hess-15-1795-2011

Hydrology and Earth System Sciences

WRF simulation of a precipitation event over the Tibetan Plateau, China – an assessment using remote sensing and ground observations

F. Maussion[1], D. Scherer[1], R. Finkelnburg[1], J. Richters[1], W. Yang[2], and T. Yao[2]

[1]Institut für Ökologie, Technische Universität Berlin, 12165 Berlin, Germany
[2]Institute of Tibetan Plateau Research, Chinese Academy of Sciences (CAS), Beijing 100085, China

Received: 30 May 2010 – Published in Hydrol. Earth Syst. Sci. Discuss.: 16 June 2010
Revised: 21 March 2011 – Accepted: 22 May 2011 – Published: 10 June 2011

Abstract. Meteorological observations over the Tibetan Plateau (TiP) are scarce, and precipitation estimations over this remote region are difficult. The constantly improving capabilities of numerical weather prediction (NWP) models offer the opportunity to reduce this problem by providing precipitation fields and other meteorological variables of high spatial and temporal resolution. Longer time periods of years to decades can be simulated by NWP models by successive model runs of shorter periods, which can be described by the term "regional atmospheric reanalysis". In this paper, we assess the Weather Research and Forecasting (WRF) models capacity in retrieving rain- and snowfall on the TiP in such a configuration using a nested approach: the simulations are conducted with three nested domains at spatial resolutions of 30, 10, and 2 km. A validation study is carried out for a one-month period with a special focus on one-week (22–28 October 2008), during which strong rain- and snowfall was observed on the TiP. The output of the model in each resolution is compared to the Tropical Rainfall Measuring Mission (TRMM) data set for precipitation and to the Moderate Resolution Imaging Spectroradiometer (MODIS) data set for snow extent. TRMM and WRF data are then compared to weather-station measurements. Our results suggest an overall improvement from WRF over TRMM with respect to weather-station measurements. Various configurations of the model with different nesting and forcing strategies, as well as physical parameterisation schemes are compared to propose a suitable design for a regional atmospheric reanalysis over the TiP. The WRF model showed good accuracy in simulating snow- and rainfall on the TiP for a one-month simulation period. Our study reveals that there is nothing like an optimal model strategy applicable for the high-altitude TiP, its fringing high-mountain areas of extremely complex topography and the low-altitude land and sea regions from which much of the precipitation on the TiP is originating. The choice of the physical parameterisation scheme will thus be always a compromise depending on the specific purpose of a model simulation. Our study demonstrates the high importance of orographic precipitation, but the problem of the orographic bias remains unsolved since reliable observational data are still missing. The results are relevant for anyone interested in carrying out a regional atmospheric reanalysis. Many hydrological analyses and applications like rainfall-runoff modelling or the analysis of flood events require precipitation rates at daily or even hourly intervals. Thus, our study offers a process-oriented alternative for retrieving precipitation fields of high spatio-temporal resolution in regions like the TiP, where other data sources are limited.

Correspondence to: F. Maussion
(fabien.maussion@tu-berlin.de)

1 Introduction

The Tibetan Plateau (TiP) is the source of many major rivers in Central Asia, thus affecting hundreds of millions of people in the surrounding regions. Its glaciers are characteristic elements of the natural environment, forming water resources of great importance for both ecosystems and local population. Yao et al. (2007) underlined the importance of the Tibetan and Himalayan glaciers on the hydrological conditions in Asia. Several studies have shown the strong control of orography and boundary-layer structure of the TiP on the Asian monsoon system (e.g., Gao et al., 1981; Hahn and Manabe, 1975).

Focusing on the monsoon history over the past, present and future, the Sino-German Priority Programme 1372 (Appel and Mosbrugger, 2006) was initiated by the Deutsche

Published by Copernicus Publications on behalf of the European Geosciences Union.

Forschungsgemeinschaft (DFG) to develop a multidisciplinary approach dealing with the complex processes and interactions taking place between the major driving forces on the TiP. This study took place within this frame.

Located in a transition zone between the continental climate of Central Asia and the Indian Monsoon system, the Nam Co drainage basin including the western Nyainqentanglha Mountains has been pointed out as a key research area in Tibet, and is also investigated in this study. The recent rise of the lake level of Nam Co, one of the largest and highest lakes on the TiP (year 2000: 1980 km^2 area, 4724 m a.s.l. lake level altitude), has been attributed to glacier retreat as well as to an increase of precipitation in recent decades (e.g., Wu and Zhu, 2008; Krause et al., 2010). Precipitation increase in central TiP during this period has also been reported by Liu et al. (2009). However, the TiP remains a sparsely observed region, and there is limited availability of meteorological data. This is especially true for long-term weather records necessary for reliable climatological studies (Frauenfeld et al., 2005; Kang et al., 2010). In particular, no long-term data from weather stations are existing at elevations above 4800 m a.s.l. Generally, the geographical distribution of weather stations is biased towards lower altitudes, flat areas and specific land-cover types excluding high-mountain regions covered by glaciers. The question of the respective contributions of glacier retreat and precipitation increase to rising lake levels on the TiP remains unanswered, so far, for these reasons.

Besides air temperature, precipitation is considered to be a key variable for understanding recent environmental variability and trends on the TiP. Unfortunately, precipitation is strongly influenced by terrain, and can hardly be retrieved from existing gridded precipitation data sets, especially in mountainous regions. This has been discussed e.g. by Yin et al. (2008) for problems in using remotely sensed precipitation data sets derived from the Tropical Rainfall Measuring Mission (TRMM), and also for global atmospheric reanalysis data (e.g., Ma et al., 2009).

The constantly improving capabilities of numerical weather prediction (NWP) models offer the opportunity to reduce this problem by providing precipitation fields and other meteorological variables at high spatial and temporal resolution. Generally, NWP models are suitable not only for weather forecasting but also for dynamical downscaling of large-scale atmospheric processes. NWP models can be initialised and laterally forced by assimilated observational data describing the large-scale atmospheric conditions throughout the simulation period, thus keeping the model results close to observations also at finer spatial scales. This approach enables validation of the model output for single events but does not allow forecasts, since the assimilated observational data have to be available not only for the time of model initialisation but for the whole simulation period.

Longer time periods of years to decades can be simulated by NWP models by successive model runs of shorter periods of time integration of days to weeks. We will subsequently use the term "regional atmospheric reanalysis" for this kind of NWP-model application. A good example of a regional atmospheric reanalysis is given by Box et al. (2004) who used the Atmospheric Research Mesoscale Model MM5 for generating a contiguous multi-year weather data set for Greenland by dynamical downscaling of 2.5°operational analyses from the European Centre for Medium-Range Weather Forecasts (ECMWF) by a sequence of daily model runs. Box et al. (2006) used the MM5 output for driving a surface mass balance model of the Greenland Ice Sheet.

Caldwell et al. (2009) simulated the climate of California for a 40 yr period by the Weather Research and Forecasting (WRF) model, which has been re-initialised every month. The latter simulation is, however, not driven by assimilated observational data but by the output of a General Circulation Model (GCM), which makes it impossible to validate the model results also on an event-basis. Dynamical downscaling of GCM simulations required for climate reconstructions or projections could also be done by Regional Climate Models (RCM). Lo et al. (2008), for example, discussed different strategies for time integration. Fowler et al. (2007) and Laprise et al. (2008) presented in-depth discussions of approaches and challenges including e.g. hydrological applications.

The approach of Box et al. (2004) is of special interest also for the TiP. However, the capacity of the models in retrieving snow- and rainfall in complex terrain is still discussed. Using higher horizontal spatial resolution of less than 10 km has been advanced as a substantial improvement, as it allows more accurate representation of mountain regions. Mountain-valley structures in the Nyainqentanglha Mountains are often showing elevation differences of 1 to 2 km within short distances of less than 10 km, which is common for high-mountain regions all over the world. Zaengl (2007) shows that increased spatial resolutions in areas of complex terrain can be highly beneficial for simulating precipitation fields. However, higher spatial resolution does not automatically improve a NWP models skill in predicting precipitation in mountainous regions. Studies like the one from Zaengl (2007) have shown that increasing the spatial resolution does not improve the model quality for precipitation caused by embedded convection.

The effect often cited as orographic bias is described as strong over-prediction of precipitation rates along windward slopes while predicted snowfall lie under measured values (e.g., Leung and Qian, 2003). This bias stems from a variety of sources, but Caldwell et al. (2009) argue that models themselves may be the dominant cause, for instance due to inappropriate physical parameterisation schemes. However, since observations of precipitation in high-mountain areas are generally sparse and accuracy of observations is limited (especially for snowfall), quantitative analyses of orographic bias are rarely carried out and missing for the TiP. There is, so far, no general answer how to quantify precipitation

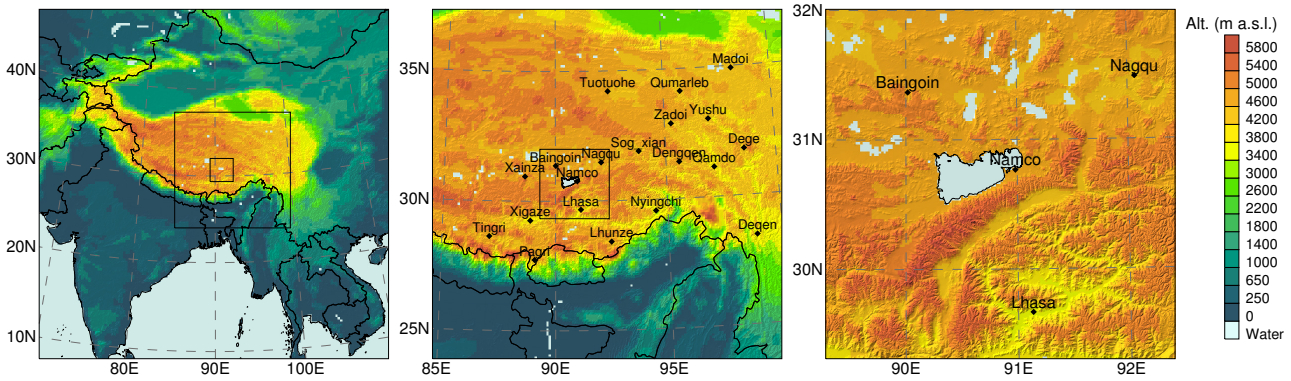

Fig. 1. WRF domains and model topography. Left: large domain (LD); the medium (MD) and small (SD) are indicated by black frames. Center: medium domain. Right: small domain. Black dots represent the locations of the available weather stations.

in high-mountain drainage basins, prerequisite to subsequent hydrological studies.

Only few studies employed the Weather Research and Forecasting (WRF) model on the TiP, by that time. Li et al. (2009) investigated the sensitivity of the WRF model to surface skin temperature of Nam Co for simulating a precipitation event. Sato et al. (2008) analysed the sensitivity of the WRF model to horizontal grid spacing with respect to simulate the diurnal cycle of precipitation. Their results show that the finest spatial resolution (7 km) is more efficient in representing diurnal cloud formation than coarser grids. So far, no study used the WRF model for a regional atmospheric reanalysis.

1.1 Objectives

The main objective of our study is optimising the design of a modelling strategy including a suitable model configuration for producing a weather data set of high spatio-temporal resolution for the study region by a regional atmospheric reanalysis. This is particularly relevant for subsequent hydrological and glaciological studies, e.g. requiring detailed precipitation fields as input data in hydrological and glaciological models. In this paper, we therefore concentrate on the capacity of the WRF model in retrieving data on solid and liquid precipitation. For this purpose, we focus on a specific precipitation event over the TiP (see Sect. 1.3) including its contribution to monthly precipitation amounts.

While dynamical downscaling studies employing RCM use integration periods from months to years or even many decades, the objective of our study is to analyse the capability of the WRF model as a NWP model to be employed for a regional atmospheric reanalysis, enabling direct comparison of model results with observations. By using a continuous sequence of short time integration periods, we prevent the model deviating too much from large-scale observations. After two days of simulation we expect the model to be less accurate than during the first two days. Therefore, our study also aims at a quantitative analysis of the effects of using different strategies for time integration.

In this study, we address two main research questions:

1. Which validation methods and data sets are suitable for assessing the accuracy of simulated precipitation fields of high spatio-temporal resolution over the TiP?

2. Is a specific set-up of the WRF model able to reanalyse precipitation fields in the mountainous and sparsely observed region of the TiP?

The first question is less frequently addressed in similar model studies since observations are usually taken as an absolute reference to assess the performance of a model. However, the particularities of the TiP do not ensure the applicability of validation approaches that have been proven to be suitable in other regions. Especially without knowing the limitations of the validation data sets the second question may not be answered appropriately.

The WRF model, like other NWP models, offers a broad spectrum of options for setting up and forcing simulations, including various parameterisation schemes for sub-scale processes. We present a sensitivity study following the general ideas as discussed e.g. by Rakesh et al. (2007) or Yang and Tung (2003) to quantify the uncertainty in the model output caused by the model itself.

The study region and the simulation period are described in Sects. 1.2 and 1.3, respectively. The design of the reference experiment, as well as the validation data sets and methods are described in Sect. 2. The results of the study, i.e., the validation of the reference experiment by three observational data sets, and those from the sensitivity study, are presented in Sect. 3. The results are further discussed in Sect. 4 to give answers to the main two research questions. Finally, we draw conclusions from our study.

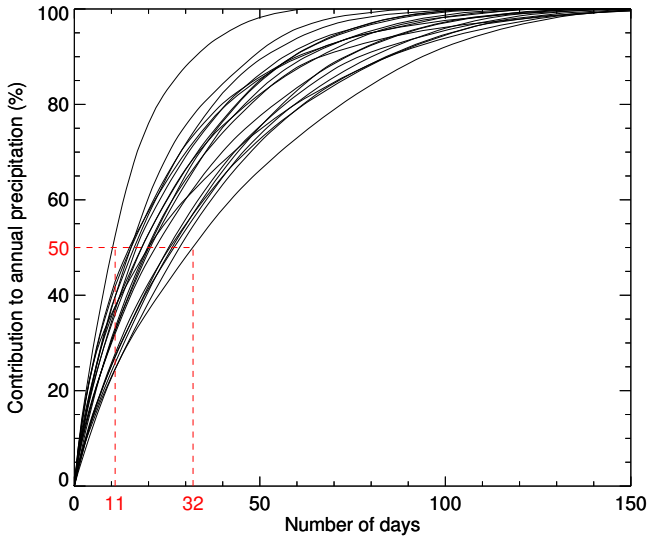

Fig. 2. Contribution (%) of accumulated daily precipitation to the annual precipitation in the year 2008 for the 19 available weather stations. The daily precipitation values are sorted in decreasing order. The number of days in which 50 % of the annual precipitation is reached are indicated for the two extremal stations.

1.2 Study region

The study region and the set-up of the three nested domains used by the WRF model are presented in Fig. 1.

The large domain (LD) covering an area of $4500 \times 4500\,km^2$ is used to capture large-scale processes and to avoid model artefacts near the lateral boundaries. The studied precipitation event originated from the Bay of Bengal, which is fully covered by the LD.

The medium domain (MD) covers an area of $1500 \times 1500\,km^2$ comprising large parts of the TiP including the western and eastern Nyainqentanglha Mountains. The southern-eastern part of the TiP is strongly influenced by the summer monsoon, and has generally lower altitudes, thus maritime (temperate) glaciers are present, while glaciers in the central, northern and western parts of the TiP are mostly continental (cold or polythermal) (see Shi and Liu, 2000, for a detailed description).

Detailed analyses are carried out for the small domain (SD) covering an area of $300 \times 300\,km^2$. The SD is centred on Nam Co and its drainage basin. The highly glaciated western Nyainqentanglha Mountains (see Bolch et al., 2010), reaching elevations of more than 7100 m a.s.l., are fully contained in the SD. Nam Co and the other lakes significantly influence local climates and atmospheric moisture content (Haginoya et al., 2009). The presence of the well-equipped Nam Co Monitoring and Research Station (30°46′ N, 90°59′ E, 4730 m a.s.l., located in the south-eastern shore of the lake; see Fig. 1), operated by the Institute of Tibetan Plateau Research (ITP) of the Chinese Academy of Sciences (CAS), makes it one of the most intensively studied regions on the TiP, and thus an ideal test bed for our study.

1.3 Simulation period

Focusing model-validation studies on short simulation periods enlightens some particularities and issues that are not visible in long-term validation studies. Short-term validation studies enable evaluation of precipitation rates and cumulated amounts on a process-oriented basis. Individual strong precipitation events are well suited for this kind of analysis, also due to the fact that relative errors in simulated precipitation are generally larger in these cases, and thus easier to detect and quantify.

The complex terrain of the high-mountain fringe of the TiP and its blocking effect on moisture transfer coming from the Indian and Pacific Oceans has a characteristic impact on the formation of orographically induced storms (Chen et al., 2007) causing strong precipitation events. The tropical cyclone Rashmi formed in the Bay of Bengal on 24 October 2008, reaching the coast on late evening of 26 October. Strong winds and heavy rainfall occurred over Bangladesh and India causing substantial damages and fatalities (the India Meteorological Department made a comprehensive description of the event in IMD, 2008). The system weakened rapidly after landfall, carrying along further precipitation, mainly as snowfall, on the Himalayas and the TiP. This precipitation event happened after the monsoon period, and is challenging the model by its complexity: cyclonal formation overseas and snowfall over the TiP.

On 27 October 2008 daily precipitation amount averaged over the 19 operational weather stations used in our study (see Sect. 2.4) is the absolute maximum of the last decade. The event was also one of the strongest snowfall events in the autumn season affecting large areas on the TiP that have been snow-free prior to the event, which allows a quantitative analysis of the simulated snowfall. Thus, October 2008 was chosen for the study as simulation period. A one-week period between 22 and 28 October 2008 was used for detailed analysis of the precipitation event.

Using a simulation period of one month offers the opportunity to include weather situations without or with only light precipitation in the validation study. In addition, monthly precipitation is frequently used in climatological studies, and many gridded climatological data sets are available on a monthly basis. Strong precipitation events are often main contributors to monthly or even annual precipitation, as demonstrated in Fig. 2. Thus, it is of high relevance for climatological purposes to understand a NWP models capability to simulate an individual weather system, especially when the model shall be employed for a regional atmospheric reanalysis. Figure 2 shows that all the stations on the TiP used in this study received half of the annual precipitation in 2008 within 12 and 32 days. The studied precipitation event contributed up to 20.75 % of the annual precipitation in 2008

(Deqen), but some of the stations far away from the cyclone track (see Sect. 3) showed almost no precipitation at the same time.

2 Methodology

2.1 Design of the reference experiment

The NWP model used in this study is the community WRF-ARW model, version 3.1.1, developed primarily at the National Center for Atmospheric Research (NCAR) in collaboration with different agencies like the National Oceanic and Atmospheric Administration (NOAA), the National Center for Environmental Prediction (NCEP), and many others. The WRF is a limited-area, non-hydrostatic, primitive-equation model with multiple options for various physical parameterisation schemes (Skamarock et al., 2008).

The three nested domains described in Sect. 1.2 and displayed in Fig. 1 are used in all the experiments of this study. Spatial resolutions of the different model grids covering the three WRF domains are 30 km for the LD grid, 30 and 10 km for the two MD grids, as well as 30, 10 and 2 km for the three SD grids. WRF model output in the three different spatial resolutions (30, 10 and 2 km) will be named WRF30, WRF10 and WRF2 to avoid confusions between model domains and spatial resolutions (e.g. WRF30-SD indicates the WRF results for the 30 km grid of the SD).

We have designed a reference experiment against which a series of further experiments are performed and analysed to understand how and why simulated precipitation fields change with modified nesting and forcing strategies, as well as with modified physical parameterisation schemes. The design of the reference experiment is resumed in Table 1. The choices for the design of the reference experiments have been following three principles:

1. The reference experiment should incorporate experience gained from comparable numerical modelling studies as far as possible, such that its design is expected to be one of the most suitable candidates for a decadal regional atmospheric reanalysis.

2. The nesting and forcing strategy of the reference experiment shall not only enable reanalysing precipitation fields but also be suitable for further model experiments, e.g. for simulations using modified boundary conditions.

3. The reference experiment shall preserve the predictive skill of the model providing the large-scale forcing fields while concurrently allowing the WRF model to utilise its predictive skills at the resolved scales.

The nesting strategy of the reference experiment is based on a novel method, solving a scientific conflict currently discussed concerning the advantages and disadvantages of one-way versus two-way nesting. Some authors (Harris and Durran, 2010) argue that two-way nesting increases the predictive skill of a NWP model within the child domain, while others (e.g., Bukovsky and Karoly, 2009) could show that two-way nesting generates artefacts in the parent domain near the borders of the child domain. We are therefore using a cascade of three simulations:

1. Results for the LD are obtained from a simulation without nesting.

Table 1. Design of the reference experiment (RE).

Map and grids	
Map projection	Lambert conformal
Centre point of domain	28.85° N , 89.57° E
Number of vertical layers	28
Horizontal grid spacing	30 km, 10 km, 2 km
Unstaggered grid points	150×150, 150×150, 150×150
Static geographical fields	USGS standard dataset at 10′, 5′, 30” resolution
Timing	
Simulation period	October 2008
Time step	120 s, 40 s, 8 s
Nesting strategy	
Nesting	Two-way nesting in cascade simulations
Forcing strategy	
Boundary conditions	NCEP/FNL from GFS Operational Model Global Tropospheric Analyses (1°, 6 hourly)
Sea surface temperature	NCEP/MMAB real-time, global, sea surface temperature (RTG_SST) analysis (0.5°, daily)
Lake surface temperature	derived from MODA11 8-DAY 1KM L3 LST
Initialisation	Daily
Runs starting time	Daily, 12:00 UTC
Runs duration	36 h
Spin up	12 h
Physical parameterisation schemes	
Short-wave radiation	Dudhia scheme (Dudhia, 1989)
Long-wave radiation	Rapid Radiative Transfer Model (RRTM) (Mlawer et al., 1997)
Cumulus parameterisation	New Grell-Devenyi 3 sheme (Grell and Devenyi, 2002) (exept for 2 km domain: no cumulus)
Microphysics	Modified Thompson scheme (Thompson et al., 2008)
Land-surface model	Noah Land-surface Model (LSM) (Chen and Dudhia, 2001)
PBL	Mellor-Yamada-Janjic TKE scheme (Janjic, 2002)

2. Results for the MD are obtained from a simulation of the LD as parent domain and the MD as a child domain using the two-way nesting capability of the WRF model.

3. Results for the SD are obtained from a nested simulation of the three domains using the two-way nesting capability of the WRF model.

This approach allows benefiting from the two-way nesting approach in the respective child domain while concurrently avoiding the artefacts in the respective parent domain. The reference experiment is based on a forcing strategy using daily re-initialisation. The simulation comprises 31 consecutive model runs of 36 h time integration. Each run starts at 12:00 UTC (all times are further specified in UTC). The WRF model (as any NWP model) requires some spin-up time to reach a balanced state with the boundary conditions. We have therefore discarded the first twelve hours from each model run, thus the remaining 24 h of model output provide one day of the one-month simulation. This forcing strategy has been analogously used by Box et al. (2004).

Meteorological input data sets are the standard final analysis (FNL) data from the Global Forecasting System (GFS) with additional sea surface temperature (SST) input (see Table 1). The employed version of the WRF pre-processing system (WPS) does not properly handle initialisation of lake temperatures. The WPS sets the water temperature either to an arbitrary value or, when SST fields are available, to the SST value. In our case, this leads to drastic errors in simulated precipitation. Water temperatures of the high-altitude lakes on the TiP are simply extrapolated from the SST of the Bay of Bengal without considering the huge elevation difference, resulting in water temperatures of about 30 °C for Nam Co in October 2008. As proposed by Li et al. (2009) we used remotely sensed skin temperatures of the Nam Co for retrieving the initial lake temperature. We used the Moderate Resolution Imaging Spectroradiometer (MODIS) eight-day land-surface temperature product (MODA11 8-DAY 1KM L3 LST, version 5, 23–30 October 2008). Mean temperature of the water-covered grid cells was computed for the day- and night-time MODIS scenes to obtain a mean skin temperature of 4.9 °C for the simulation period. This value is consistent with the lake-temperature climatology of Haginoya et al. (2009), and was used to initialise the water temperature of Nam Co and surrounding water bodies for each model run. The positive effect of this correction is clearly seen in daily precipitation amounts at the Nam Co research station on 27 October 2008: the observed precipitation amount is 8 mm, while the model computed 117 mm before the correction of the lake temperature, and 30 mm after the correction.

The parameterisation of convective processes and related formation of cumulus clouds (CU) was only applied to the 30 and 10 km model grids. Precipitation computed by the CU parameterisation scheme is stored separately from the precipitation resolved by the grid, enabling the quantification of the percentage of convective precipitation to total precipitation. The parameterisation of micro-physical processes (MP), the land-surface model (LS) and the parameterisation of processes in the planetary boundary layer (PBL) are forced by WRF to be identical in all nested domains. The parameterisation schemes for short- and long-wave radiative fluxes were kept constant in all model experiments (Table 1).

2.2 TRMM precipitation

The WRF model output is compared to the precipitation data set of the TRMM, providing precipitation estimates derived from a combination of remote sensing observations calibrated against a large number of rain gauges on a monthly basis. In this study the 3B42 version 6 product is used (Huffman et al., 2007). The data sets is covering the regions between 50° N to 50° S with a spatial resolution of 0.25°, with outputs at 3 h intervals. The three–hourly data are aggregated to daily, one-week and one-month values for the validation.

The TRMM data sets were projected to the map projection used by WRF (see Table 1) and resampled by nearest-neighbourhood interpolation to grids for each WRF domain of 30 km spatial resolution.

2.3 MODIS snow extent

MODIS refers to two instruments currently collecting data as part of NASA's Earth Observing System (EOS) program. The MODIS/Terra Snow Cover Daily L3 Global 500 m Grid (MOD10A1) contains data on snow extent, snow albedo, fractional snow cover, and Quality Assessment (QA). The MOD10A1 data set consists of $600 \times 600\,\mathrm{km}^2$ granules of 500 m spatial resolution gridded using a sinusoidal map projection. MODIS snow cover data are based on a snow-mapping algorithm that employs a Normalised Difference Snow Index (NDSI) and other criteria tests (Hall et al., 2006).

The MODIS data sets used in this study (Fig. 3) are mosaics of four adjacent granules acquired around 05:00 UTC on 22 and 29 October 2008, corresponding to mid-morning local solar times. We selected MODIS data for a day prior to and a second one after the precipitation event to compare the observed changes in snow extent with WRF snowfall predictions. Because cloud coverage does not allow retrieval of snow data from optical sensors, only MODIS data of sparse cloud coverage are suitable for validation, preventing more detailed analyses for regions that have never been cloud-free during the one-week simulation.

The MODIS data sets were reprojected to the map projection used by WRF (see Table 1) and resampled by nearest-neighbourhood interpolation to grids of 500 m spatial resolution covering the MD and the SD, respectively.

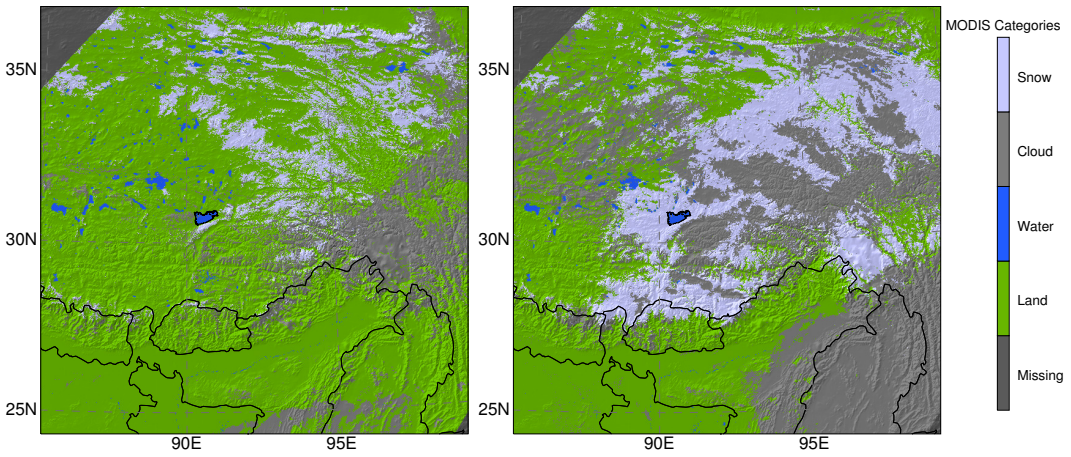

Fig. 3. MODIS snow extent before (22 October 2008) and after (29 October 2008) the Rashmi precipitation event in the MD.

2.4 Weather stations

Data from weather stations used in this study are from the "Global Summary of the Day" (http://www.ncdc.noaa.gov/oa/ncdc.html) provided by the National Climatic Data Center (NCDC) for download free of charge. The stations included in this data set follow the recommendations of the World Meteorological Organization (WMO), and data are undergoing quality control before being published.

The weather stations selected for this study follow two criteria: they must be located within the MD, and must be situated above 3000 m a.s.l. Data from just 19 operational weather stations fulfilling these criteria are available for the simulation period, showing how much the TiP still lacks of observations. The weather stations are not homogeneously distributed over the study region, since they are concentrated in more densely populated regions in the southern and eastern parts of the TiP. In addition, precipitation data measured at the Nam Co Monitoring and Research Station were used to validate the WRF model (see Fig. 1).

2.5 Scores for statistical evaluation

Scores are commonly used for validation purposes to statistically assess the performance of a model simulation relative to observations (validation) or to results of other model simulation (inter-comparison). Some of them are derived from a 2×2 matrix called "contingency table" (e.g., Wilks, 1995), where each of the elements (A, B, C, D) holds the number of combinations of model prediction and observation in a given statistical population (see Table 2). In this study, five different scores are used.

The bias score (BIAS) is defined as:

$$\mathrm{BIAS} = \frac{F}{O} = \frac{A+B}{A+C} \tag{1}$$

where F is the number of cases where the event was predicted, and O is the number of cases where the event was observed. This score is an indicator of how well the model recovers the number of occurrences of an event, regardless of the spatio-temporal distribution.

Table 2. Contingency table used in the validation and sensitivity studies.

		Observation	
	Event	Yes	No
WRF	Yes	A	B
	No	C	D

The False Alarm Rate (FAR) computes the fraction of predicted events that where not observed:

$$\mathrm{FAR} = \frac{B}{F} = \frac{B}{A+B} \tag{2}$$

The Probability Of False Detection (POFD) is the fraction of predicted events that have not been observed relative to the total number of unobserved events:

$$\mathrm{POFD} = \frac{B}{\mathrm{NO}} = \frac{B}{B+D} \tag{3}$$

Like the FAR the POFD is not a perfect indicator for validation since it depends on the number of unobserved events, but is convenient for inter-comparison since it does not depend on the number of unpredicted events.

Similarly to the POFD the Probability Of Detection (POD) is the fraction of predicted events relative to the number of observed events:

$$\mathrm{POD} = \frac{A}{\mathrm{YES}} = \frac{A}{A+C} \tag{4}$$

Finally, the frequently used Heidke Skill Score (HSS) is defined:

$$\mathrm{HSS} = \frac{S - S_{\mathrm{Ref}}}{S_{\mathrm{Perf}} - S_{\mathrm{Ref}}} \tag{5}$$

where S is the simulation score, S_{Ref} the probability of detection by chance and S_{Perf} the score obtained by a perfect simulation:

$$S = \frac{H}{N} = \frac{A+D}{N} \tag{6}$$

$$S_{\mathrm{Ref}} = \frac{(A+B)(A+C)+(B+D)(C+D)}{N^2} \tag{7}$$

$$S_{\mathrm{Perf}} = 1 \tag{8}$$

H is the number of hits, i.e., the number of cases where prediction and observation are in accordance, while N is the size of the statistical population. The HSS indicates the capability of a simulation to be better or worse than a random simulation, and ranges from -1 to 1 (1 for a perfect and 0 for a random case).

In addition to the scores based on the contingency table, the standard Mean Bias (MB) and the Root Mean Square Deviation (RMSD) are defined as:

$$\mathrm{MB} = \frac{1}{N}\sum_{i-1}^{N}(P_{\mathrm{p}} - P_{\mathrm{o}})_i \tag{9}$$

$$\mathrm{RMSD} = \sqrt{\frac{1}{N}\sum_{i-1}^{N}(P_{\mathrm{p}} - P_{\mathrm{o}})_i^2} \tag{10}$$

where P_{p} and P_{o} are the predicted and observed precipitation values.

3 Results

3.1 Validation of the control experiment

3.1.1 Validation of predicted precipitation by TRMM observations

WRF30 and TRMM daily precipitation fields during the cyclone life are presented for a subset of the LD in Fig. 4. The cyclonal precipitation patterns can be recognised in both data sets. The cyclone is traceable by the high daily precipitation following its movement. In the WRF30 output the centre of the cyclone shows a local precipitation minimum on 24 October indicating that an eye has formed, which is, however, not present in the TRMM observations. On 25 October, the maximum of daily precipitation amount observed by TRMM is following the centre of the cyclone. The eye is no longer visible in the WRF30 output of this day. Both data sets accordingly show that strong precipitation caused by the cyclone occurs in the eastern and southern parts of Bangladesh. On 26 October the cyclone reaches the coast in the late evening hours. The precipitation maximum of this day is still overseas for TRMM, whereas the WRF30 already predicts maximum precipitation over Bangladesh. This discrepancy is explainable by the difficulties in allocating the strong precipitation to the correct day. TRMM observes less precipitation over Bangladesh on 27 October than the WRF30 predicts for that day. Over the Himalayas and the TiP, precipitation patterns are generally comparable. Two precipitation maxima are seen in both data sets, which were induced by the blocking effect of the Himalayas over the slopes of Bhutan and by the eastern Nyainqentanglha Mountains. Also, both data sets show the precipitation front propagating over the TiP in a similar way.

Generally, WRF30 daily precipitation is larger than observed by TRMM, as indicated by the BIAS and FAR scores in Fig. 4. The two different threshold values used for computation of the scores in Fig. 4 show that a higher threshold lowers both the POD and the POFD. The HSS indicates that predictions based on small threshold values are generally better in accordance with TRMM than those based on high threshold values.

The spatial patterns presented in Fig. 5 reveal that WRF30–MD generally predicts more events, especially on the northern part of the TiP. Nevertheless, weather-stations measurements suggest that this northern limit is properly predicted. The two data sets are still in good agreement at 20 mm week^{-1}, but the HSS constantly decreases as the FAR increases.

Both TRMM and WRF30–MD show precipitation maxima of more than 60 mm week^{-1} in the eastern Nyainqentanglha Mountains and in north-eastern India, but more than 70 % of the 60 mm week^{-1} events predicted by WRF30–MD were not observed by TRMM. However, the maximum in weather-station measurements on the eastern Nyainqentanglha Mountains (138 mm week^{-1}) suggests that the actual precipitation pattern may extend further in the western TiP than observed by TRMM. The reason behind this finding is probably the insufficient capability of the TRMM to detect snowfall and light rain.

WRF30-MD RMSD (54.3 mm week^{-1}) and MB (24.3 mm week^{-1}) with respect to TRMM indicate generally higher values predicted by WRF30 than observed by TRMM. The one-week HSS are higher than the daily scores presented in Fig. 4, most probably due to two major reasons: (1) possible discrepancies due to timing shifts are withdrawn when looking at the one-week precipitation amounts, (2) the considered spatial subset is different with respect to precipitation patterns.

3.1.2 Validation of predicted snow depth by MODIS observations

The goal of this test is to analyse where snowfall has been simulated by the WRF model in comparison to observational data.

The two MODIS data sets do not contain data on snowfall directly. Thus, we selected areas from the MODIS data set that were snow-free prior to and snow-covered after the event. Other areas that have been snow-covered prior to the event or snow-free after the event (e.g. lakes) are excluded

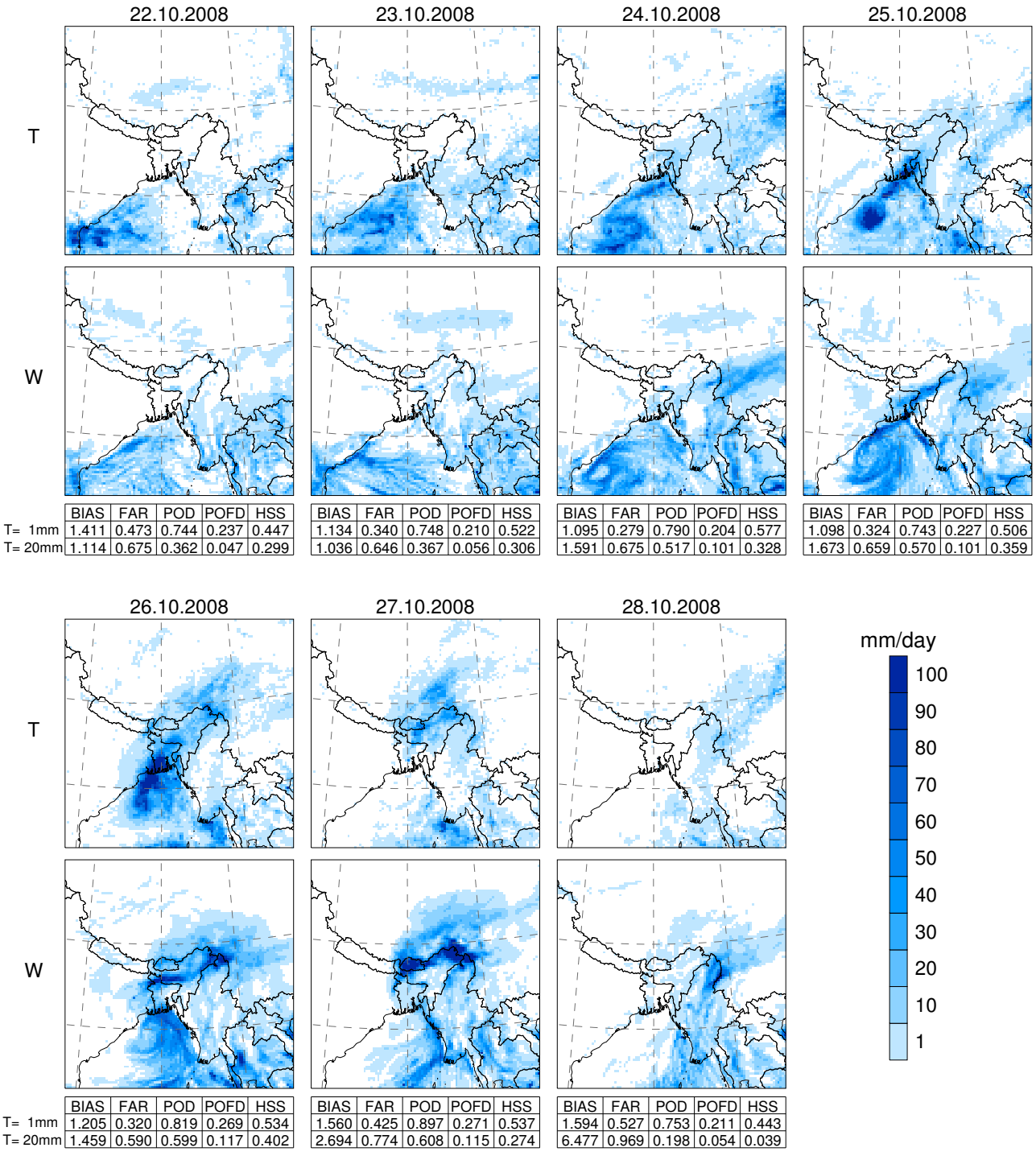

	BIAS	FAR	POD	POFD	HSS
T= 1mm	1.411	0.473	0.744	0.237	0.447
T= 20mm	1.114	0.675	0.362	0.047	0.299

	BIAS	FAR	POD	POFD	HSS
T= 1mm	1.134	0.340	0.748	0.210	0.522
T= 20mm	1.036	0.646	0.367	0.056	0.306

	BIAS	FAR	POD	POFD	HSS
T= 1mm	1.095	0.279	0.790	0.204	0.577
T= 20mm	1.591	0.675	0.517	0.101	0.328

	BIAS	FAR	POD	POFD	HSS
T= 1mm	1.098	0.324	0.743	0.227	0.506
T= 20mm	1.673	0.659	0.570	0.101	0.359

	BIAS	FAR	POD	POFD	HSS
T= 1mm	1.205	0.320	0.819	0.269	0.534
T= 20mm	1.459	0.590	0.599	0.117	0.402

	BIAS	FAR	POD	POFD	HSS
T= 1mm	1.560	0.425	0.897	0.271	0.537
T= 20mm	2.694	0.774	0.608	0.115	0.274

	BIAS	FAR	POD	POFD	HSS
T= 1mm	1.594	0.527	0.753	0.211	0.443
T= 20mm	6.477	0.969	0.198	0.054	0.039

Fig. 4. Daily precipitation fields (mm/day) from **(T)** TRMM and **(W)** WRF30 over a subset of the LD for the period 22 to 28 October 2008.

from the test, although snowfall might also have been occurring there. Unfortunately, large areas have been covered by clouds either in one or both of the two MODIS data sets, and thus have also to be marked as areas of no data.

We concentrated the validation on snow depth derived by the model from predicted snowfall. A grid point is considered to be covered by snow when the computed snow depth after one-week exceeds a certain threshold. Spatial distributions of predicted snow extent were computed for threshold values between 0.2 and 20 cm week^{-1}. Five grid points at the border of the domains are removed to avoid artefacts, and predicted snow extent was resampled to the respective 500 m

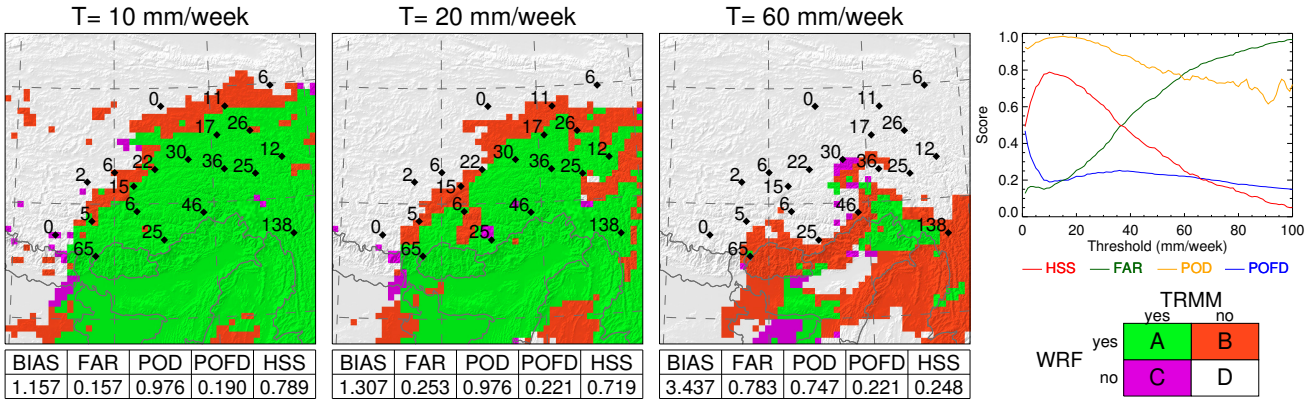

BIAS	FAR	POD	POFD	HSS
1.157	0.157	0.976	0.190	0.789

BIAS	FAR	POD	POFD	HSS
1.307	0.253	0.976	0.221	0.719

BIAS	FAR	POD	POFD	HSS
3.437	0.783	0.747	0.221	0.248

Fig. 5. Left: Spatial patterns of the contingency tables for three different thresholds (10, 20 and 60 mm week^{-1}) applied to the one-week precipitation of WRF30–MD and TRMM, together with values from ground observations at the weather stations. Right: WRF30–MD scores with respect to TRMM for the threshold range from 1 to 100 mm week^{-1}.

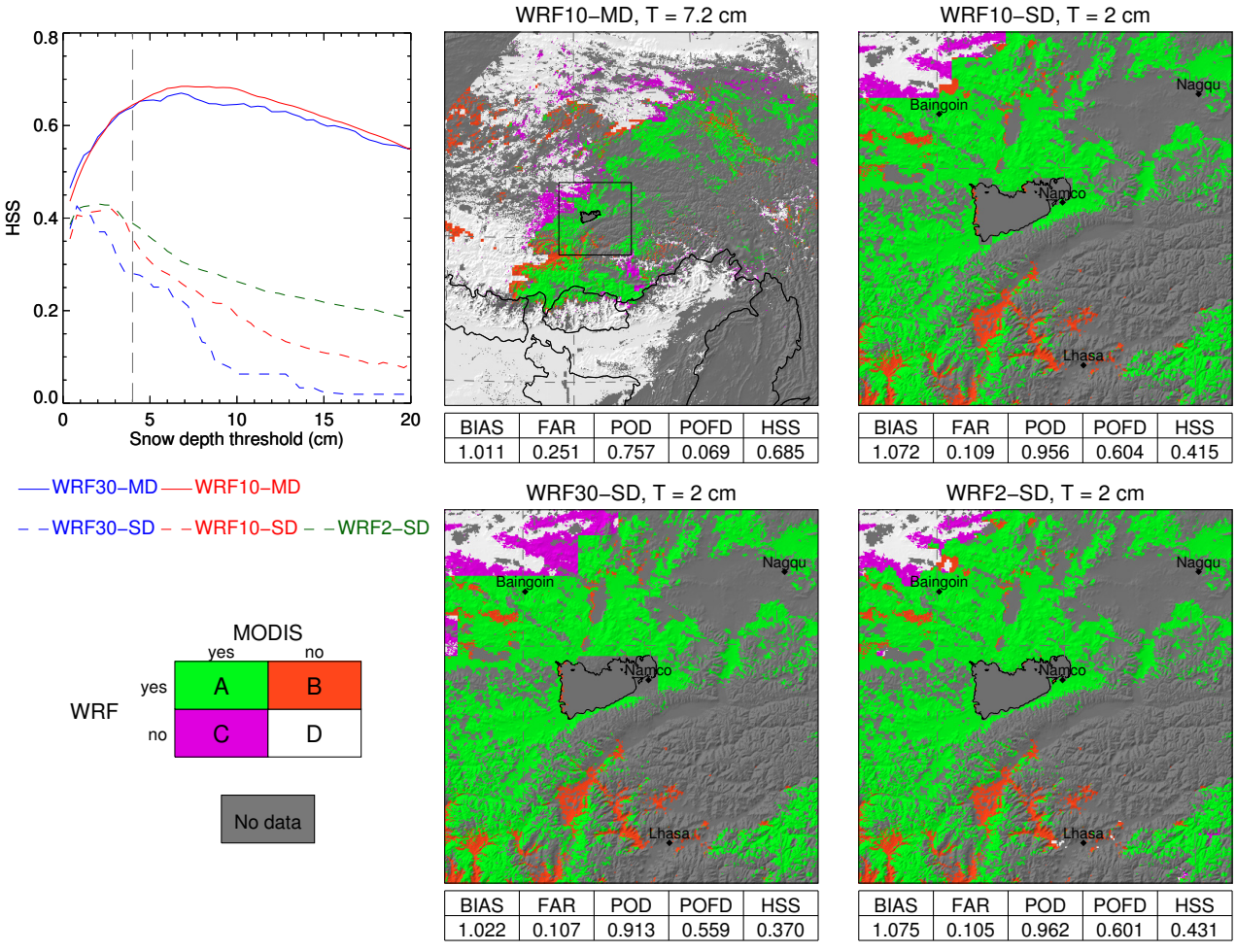

BIAS	FAR	POD	POFD	HSS
1.011	0.251	0.757	0.069	0.685

BIAS	FAR	POD	POFD	HSS
1.072	0.109	0.956	0.604	0.415

BIAS	FAR	POD	POFD	HSS
1.022	0.107	0.913	0.559	0.370

BIAS	FAR	POD	POFD	HSS
1.075	0.105	0.962	0.601	0.431

Fig. 6. Left: HSS curves for snow depth predicted by WRF simulations for thresholds between 0.2 and 20 cm with respect to snow extent observed by MODIS. Right: spatial patterns of the contingency tables for the snow depth threshold of 7.2 cm for WRF10–MD and 2 cm WRF10–SD, WRF30–SD and WRF2–SD.

Table 3. Observed precipitation (mm week^{-1}) at each weather station (19 NCDC stations and the Nam Co weather station) in comparison to the TRMM, WRF30, WRF10 and WRF2 results. The observed type of precipitation is indicated by R (rain) or S (snow). Root Mean Square Deviation (RMSD) and Mean Bias (MB) are indicated for each grid with respect to the NCDC data.

Id	Station	Lon	Lat	Alt. (m)	Type	NCDC	TRMM	WRF30	WRF10	WRF2
01	BAINGOIN	90.02	31.37	4701	S	6.1	5.7	11.2	18.0	11.1
02	DEGE	98.57	31.80	3185	R	12.2	38.8	44.3	38.2	
03	DENGQEN	95.60	31.42	3874	S	36.6	40.4	57.5	45.7	
04	DEQEN	98.88	28.45	3320	R	138.4	44.1	166.4	122.0	
05	LHASA	91.13	29.67	3650	R	6.9	26.4	44.3	29.8	28.9
06	LHUNZE	92.47	28.42	3861	S	25.1	33.2	25.0	15.7	
07	MADOI	98.22	34.92	4273	S	6.1	5.2	5.4	5.8	
08	NAGQU	92.07	31.48	4508	S	22.1	22.7	19.3	18.8	27.0
09	NYINGCHI	94.47	29.57	3001	S/R	46.2	34.3	75.2	46.3	
10	PAGRI	89.08	27.73	4300	S	65.0	55.9	114.9	107.9	
11	QAMDO	97.17	31.15	3307	S/R	25.9	24.4	20.3	32.5	
12	QUMARLEB	95.78	34.13	4176	S	11.9	7.2	28.2	15.5	
13	SOG XIAN	93.78	31.88	4024	S/R	30.2	60.0	31.3	31.8	
14	TINGRI	87.08	28.63	4300		0.0	16.4	0.0	0.0	
15	TUOTUOHE	92.43	34.22	4535	S	0.8	0.7	3.3	3.5	
16	XAINZA	88.63	30.95	4670	S	2.0	9.3	1.6	0.8	
17	XIGAZE	88.88	29.25	3837	S	5.8	10.1	34.0	16.6	
18	YUSHU	97.02	33.02	3682	S/R	26.9	6.2	27.6	31.3	
19	ZADOI	95.30	32.90	4068	S	17.3	34.8	41.6	32.8	
20	NAMCO	90.98	30.77	4730	S	15.9	11.3	25.8	30.0	37.1
				Total		501.5	487.3	777.2	643.0	
				RMSD			24.80	20.98	14.63	13.3
				MB			−0.71	13.79	7.08	10.6

grids for the test (see Sect. 2.3). The area available for the test is finally reduced to 47.8 % in the MD and to 45.3 % in the SD. Snowfall was detected by MODIS on 21.6 % of the test area for the MD and on 83.9 % of the test area for the SD.

Wang et al. (2008) evaluated MODIS snow extent in northern Xinjiang, China, and they found that MODIS has high accuracies (93 %) when mapping snow at snow depth $\geq$4 cm but does not have a proper accuracy for thinner layers. This threshold can be considered as physically reasonable: at the station Baingoin (north-west of Nam Co), 6 mm precipitation was recorded (6 cm of snow assuming a standard snow-to-liquid-equivalent ratio of 10), and the pixel was classified as snow by MODIS.

The evolution of the HSS with the threshold applied to the WRF simulated snow depth with respect to MODIS is shown in Fig. 6 (left) along with the spatial patterns of the contingency tables for two optimal thresholds for WRF10-MD and WRF-SD in the three resolutions. The HSS curves for the MD simulations are very similar, especially for lower thresholds, while there are more differences between the HSS curves for the SD. This is interpreted as an effect stemming from the higher spatial variability of snowfall in the MD due to large altitudinal variations compared to the less heterogeneous situation in the SD. In the Himalayas, the snow to rain limit is caught accurately by both WRF10 and WRF30 (not shown). Higher HSS for the simulations for model grids of higher spatial resolution, especially for higher thresholds, indicate the advantage of improved spatial resolution for predicting snowfall, particularly in the SD. The maximum HSS for the SD is reached at a smaller threshold than for the MD. This difference is attributed to the fact that altitudes in the SD are generally higher than in the MD, thus the percentage of areas affected by snowfall is higher as observed by MODIS due to generally lower air temperatures. Snow melt is less frequently occurring in the SD than in the MD, and therefore even small amounts of snowfall will increase the snow extent. This argument is also supported by the contingency maps displayed in Fig. 6, which reveal that most of the WRF2-SD snow extent not observed by MODIS is located in the lower-altitude valleys south of the western Nyainqentanglha Mountains.

The higher HSS obtained by the simulations for the MD compared to the SD are resulting from the higher percentage of unobserved snowfall in the MD, increasing the number of hits of the WRF simulations in the MD due to the high number of correctly predicted no-events. Figure 6 shows that the transitional zone between areas affected by snowfall and

Table 4. Design of the sensitivity experiments.

Name	Experiment	New parameterisation
	Nesting strategy	
TW	Nesting	Two-way nesting (all domains)
OW	Nesting	One-way nesting (all domains)
	Forcing strategy	
WI	Initialisation	Single initialisation and one-week continuous autonomous run
WIN	Forcing	Single initialisation and one-week continuous run with analysis nudging
	Physical parameterisation schemes	
CU1	Cumulus	Betts-Miller-Janjic (BMJ) (Betts and Miller, 1986; Janjic, 1994)
CU2	Cumulus	Kain-Fritsch (Kain and Fritsch, 1990)
MP1	Microphysics	WRF Single-Moment 6-class (WSM6)
MP2	Microphysics	Goddard Cumulus Ensemble (GCE) (Tao et al., 2003)
LS1	Land surface	Rapid Update Cycle (RUC) (Smirnova et al., 2000)
LS2	Land surface	Pleim-Xiu (Pleim and Xiu, 1995)
PBL1	PBL	Yonsei University (YSU) (Hong et al., 2006)
PBL2	PBL	Asymmetrical Convective Model 2 (ACM2) (Pleim, 2007)

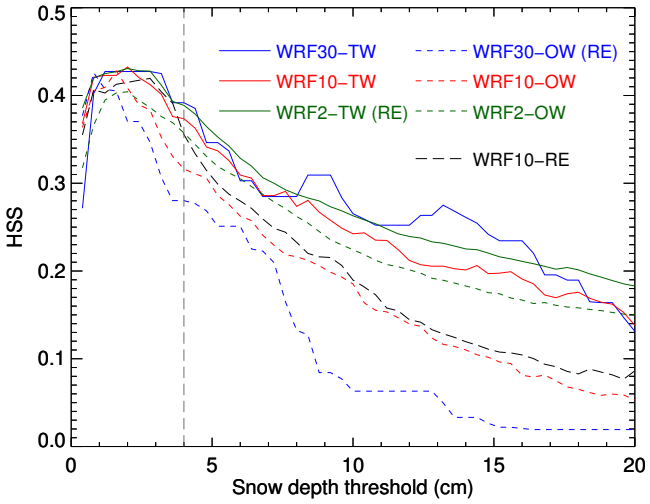

Fig. 7. Sensitivity to the nesting strategy: HSS curves for snow depth predicted by WRF simulations (TW, OW and RE) at all resolutions for thresholds between 0.2 and 20 cm, with respect to snow extent observed by MODIS on the SD.

snow-free areas is situated in the north-western part of the SD, and is well detected by the WRF2-SD for the threshold of 2 cm. Increasing the threshold shifts the transitional zone to the South-west in all WRF simulations for the MD and SD, such that the contingency maps show a switch from false alarms to unpredicted events for all areas where prediction and observation are not concordant.

3.1.3 Validation of predicted precipitation by observations at weather stations

Table 3 shows observed precipitation at each weather station in comparison to precipitation observed by TRMM and predicted by WRF30, WRF10 and WRF2. Results from the grid points nearest to the weather stations are used in the comparison.

Differences between the WRF simulations are generally small except for two stations: Nyingchi and Deqen, the later showing a large improvement from WRF30 to WRF10, illustrating the strong terrain dependency of precipitation in mountainous terrain. The RMSD and MB scores show a significant improvement from WRF30 to WRF10. Some discrepancies between station observations and TRMM could be explained by errors in one or the other data-set (at Lhasa, TRMM and WRF are in good agreement and at Deqen, station observations and WRF are concordant) and for some stations the three data-sets differ substantially. Generally, WRF10 has a lower RMSD than TRMM, but a higher MB.

Unfortunately, no in-depth evaluation for WRF2 could be made, because only four stations are situated in the SD. The results for these stations suggest a small but overall improvement to WRF10, again indicating the advantage of using model grids of higher spatial resolution.

3.2 Sensitivity study

In this section, we investigate the sensitivity of the WRF model to the nesting strategy, the forcing strategy, and various physical parameterisations schemes (PPS). Table 4 provides an overview on the sensitivity experiments carried out in this study, while Tables 5 and 6 present the results.

3.2.1 Sensitivity to the nesting strategy

Two experiments have been carried out for analysing the effect of the nesting strategy on simulated precipitation. In contrast to the nesting strategy in the reference experiment, the results of the simple two–way nesting (TW) experiment are not only used for the SD (as in the RE, i.e., the WRF2 SD results of the RE and TW experiments are identical) but also for the MD and LD, such that these results also contain some artefacts at the borders of the respective child domains. A second nesting experiment was performed using one-way nesting (OW) for a nested simulation of the three domains. Thus, the results of the RE and OW experiments for the LD are identical, but differ for the MD and SD.

Table 5. Scores used for statistical evaluation of the reference, nesting and forcing experiments. The scores that differ of more than 10 % from the RE are marked in bold, and put between parentheses if they have a lower skill than the RE.

Reference	WRF	Score	Period	RE	TW	OW	7D	7DN
TRMM	WRF30	BIAS, $T = 10\,\mathrm{mm\,week^{-1}}$	week	1.16	1.18	1.16	(**0.58**)	1.10
TRMM	WRF30	BIAS, $T = 60\,\mathrm{mm\,week^{-1}}$	week	3.44	3.37	3.44	**0.63**	3.20
TRMM	WRF30	HSS, $T = 10\,\mathrm{mm\,week^{-1}}$	week	0.79	0.79	0.79	(**0.48**)	0.86
TRMM	WRF30	HSS, $T = 60\,\mathrm{mm\,week^{-1}}$	week	0.25	0.24	0.25	**0.28**	**0.30**
TRMM	WRF30	RMSD	week	54.3	55.3	54.3	**22.5**	**44.1**
TRMM	WRF30	MB	week	24.3	25.5	24.3	**−7.4**	**19.1**
TRMM	WRF30	BIAS, $T = 10\,\mathrm{mm\,month^{-1}}$	month	1.15	1.19	1.15		
TRMM	WRF30	BIAS, $T = 60\,\mathrm{mm\,month^{-1}}$	month	1.93	1.93	1.93		
TRMM	WRF30	HSS, $T = 10\,\mathrm{mm\,month^{-1}}$	month	0.41	(**0.31**)	0.41		
TRMM	WRF30	HSS, $T = 60\,\mathrm{mm\,month^{-1}}$	month	0.44	0.48	0.44		
TRMM	WRF30	RMSD	month	105.21	111.92	105.21		
TRMM	WRF30	MB	month	58.20	(**65.55**)	58.20		
MODIS	WRF10	HSS max	week	0.69	0.69	0.68	(**0.20**)	0.70
MODIS	WRF10	HSS, $T = 4$ cm	week	0.65	0.66	0.65	(**0.09**)	0.69
MODIS	WRF2	HSS max	week	0.43	0.43	0.40	(**0.01**)	0.43
MODIS	WRF2	HSS, $T = 4$ cm	week	0.39	0.39	0.36	(**0.00**)	0.41
NCDC	WRF10	RMSD	week	14.6	14.0	13.6	(**31.2**)	**10.8**
NCDC	WRF10	MB	week	7.1	7.1	6.6	(**−20.0**)	6.7
NCDC	WRF2	RMSD	week	13.3	13.3	**11.4**	13.3	(**17.4**)
NCDC	WRF2	MB	week	10.7	10.7	**8.2**	(**−11.3**)	(**14.3**)
NCDC	WRF10	RMSD	month	27.8	26.1	29.0		
NCDC	WRF10	MB	month	18.1	**15.8**	19.1		
NCDC	WRF2	RMSD	month	13.1	13.1	**10.8**		
NCDC	WRF2	MB	month	1.95	1.95	**0.70**		

The results of all validation analyses applied to the TW and OW sensitivity experiments are presented in Table 5 together with those of the reference experiment. Generally, the differences in the overall scores between the sensitivity experiments are small, indicating that this element of the experimental design is not highly sensitive for reanalysed precipitation fields.

The most suitable analysis for assessing the performance of the nesting experiments is presented in Fig. 7, where detection of snowfall in the SD is validated by the MODIS data on snow extent. Only in the SD the three different spatial resolutions can be compared to each other. A threshold value of 4 cm is used for comparing predicted snow depth with MODIS observations since this value is considered to be physically reasonable regarding the capability of MODIS for detecting snow (see Sect. 3.1.2). HSS curves of the TW experiments for detecting snowfall in the SD are generally higher than those of the respective OW experiments. Figure 7 shows two major features of the two-way nested approach: the skill of the coarser resolutions is improved, and the higher-resolution results are also slightly meliorated by the step-wise feedback mechanism. Thus, the use of the two-way nesting option is recommended, although not being decisive for the overall performance.

3.2.2 Sensitivity to the forcing strategy

Two experiments were carried out to analyse this element of the experimental design. In contrast to the other experiments, only the one-week period of the precipitation experiment was covered by the simulations. In contrast to the reference experiment, the model runs were only initialised once (incl. the 12 h spin-up). The weekly initialisation (WI) experiment is only forced at the lateral boundaries during integration time, while in the second experiment (WIN) weekly initialisation is combined with the analysis nudging option of the WRF, i.e., the WRF30-LD simulation is nudged towards GFS input data both horizontally and vertically using a point-by-point relaxation term for temperature, pressure and specific humidity.

The results of all validation analyses applied to the WI and WIN sensitivity experiments are presented in Table 5 together with those of the reference experiment. The scores indicate the lower performance of the WI forcing strategy. This is also seen in Fig. 8 (right) where the daily scores strongly decrease over time of the simulation, and the region on the TiP affected by rain- and snowfall is not captured accurately when compared to the TRMM observations. The WRF as a limited area model is not capable of making

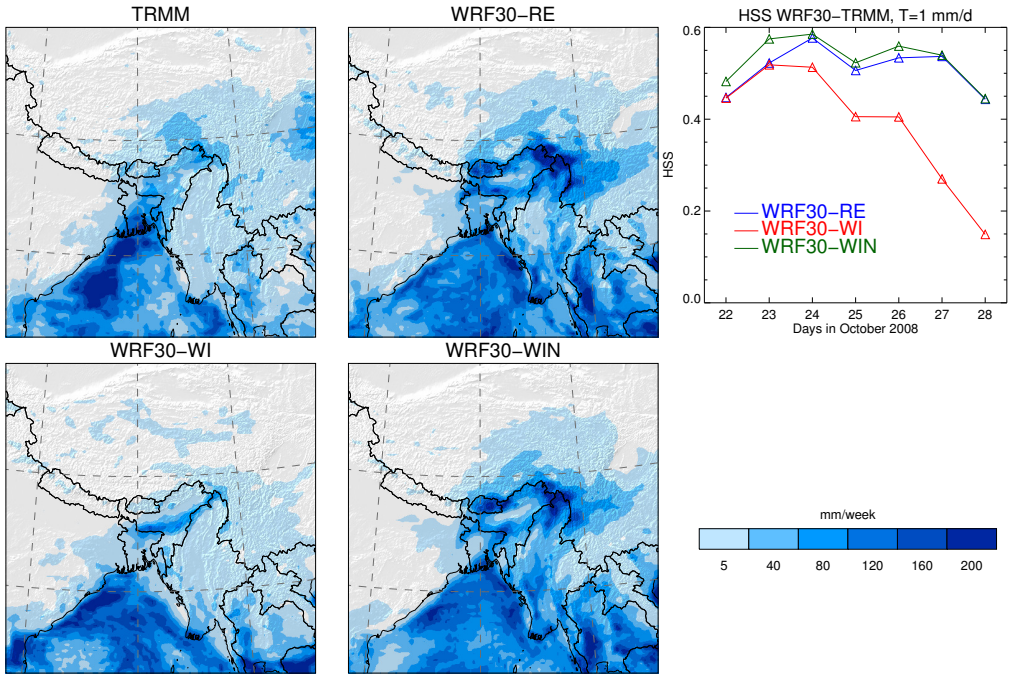

Fig. 8. Sensitivity to the forcing strategy. Left: one-week precipitation (mm week^{-1}) for TRMM, WRF30–RE, WRF30–WI and WRF30–WIN over a subset of the LD. Right: daily HSS curves from WRF30 with respect to TRMM for the 1 mm day^{-1} precipitation threshold over the same subset.

Table 6. Scores used for statistical evaluation of the reference and the eight PPS experiments. The scores that differ of more than 10 % from the RE are marked in bold, and put between parentheses if they have a lower skill than the RE.

Reference	WRF	Score	Period	RE	CU1	CU2	MP1	MP2	LS1	LS2	PBL1	PBL2
TRMM	WRF30	BIAS, T = 10 mm	week	1.16	1.12	1.12	1.14	1.14	1.19	1.18	1.13	1.10
TRMM	WRF30	BIAS, T = 60 mm	week	3.44	(**3.88**)	3.76	3.38	3.77	3.55	3.45	3.51	3.78
TRMM	WRF30	HSS, T = 10 mm	week	0.79	0.82	0.80	0.80	0.81	0.76	0.77	0.81	0.82
TRMM	WRF30	HSS, T = 60 mm	week	0.25	**0.29**	**0.30**	0.26	0.24	0.25	0.24	0.26	0.26
TRMM	WRF30	RMSD	week	54.3	(**76.5**)	(**68.7**)	55.4	56.1	54.3	55.4	53.5	(**67.9**)
TRMM	WRF30	MB	week	24.3	(**35.8**)	(**32.0**)	24.4	26.7	25.6	25.4	23.8	(**31.3**)
TRMM	WRF30	BIAS, T = 10 mm	month	1.15	1.19	1.18	1.17	1.19	1.26	1.14	1.10	1.09
TRMM	WRF30	BIAS, T = 60 mm	month	1.93	1.81	1.92	1.90	1.98	(**2.19**)	1.93	1.78	1.77
TRMM	WRF30	HSS, T = 10 mm	month	0.41	(**0.30**)	(**0.35**)	(**0.35**)	(**0.33**)	(**0.12**)	0.44	**0.52**	**0.54**
TRMM	WRF30	HSS, T = 60 mm	month	0.44	**0.49**	0.45	0.45	0.44	(**0.36**)	0.45	**0.49**	**0.49**
TRMM	WRF30	RMSD	month	105.21	112.31	105.53	106.82	106.89	107.49	112.80	95.70	102.34
TRMM	WRF30	MB	month	58.20	61.73	60.03	58.86	58.47	(**67.48**)	62.76	**50.30**	52.97
MODIS	WRF10	HSS max	week	0.69	0.69	0.68	0.68	0.68	0.70		0.69	0.69
MODIS	WRF10	HSS, T = 4 cm	week	0.65	0.65	0.66	0.63	0.64	0.70		0.67	0.66
MODIS	WRF2	HSS max	week	0.43	0.41	0.40	0.40	0.40	0.45		0.42	(**0.33**)
MODIS	WRF2	HSS, T = 4 cm	week	0.39	(**0.33**)	(**0.29**)	(**0.34**)	0.36	0.40		(**0.35**)	(**0.22**)
NCDC	WRF10	RMSD	week	14.6	13.7	**11.9**	15.8	(**19.1**)	14.2	14.2	**11.7**	**11.1**
NCDC	WRF10	MB	week	7.1	**5.2**	6.7	**1.9**	(**13.7**)	(**8.7**)	7.5	7.1	6.7
NCDC	WRF2	RMSD	week	13.3	**9.7**	(**16.8**)	**12.0**	(**17.7**)	12.7	14.0	**11.5**	(**17.0**)
NCDC	WRF2	MB	week	10.7	**7.0**	10.3	**8.0**	(**13.9**)	10.7	10.1	**8.9**	11.6
NCDC	WRF10	RMSD	month	27.8	**24.5**	**24.2**	25.9	29.1	(**34.1**)	27.4	**22.4**	**24.7**
NCDC	WRF10	MB	month	18.1	**13.3**	18.5	**12.4**	(**22.1**)	(**27.4**)	17.8	**14.7**	17.1
NCDC	WRF2	RMSD	month	13.1	15.7	(**17.8**)	12.5	(**15.3**)	12.3	13.6	**10.4**	(**17.2**)
NCDC	WRF2	MB	month	1.95	−**0.44**	(**2.55**)	(**4.35**)	(**7.07**)	(**6.22**)	−**1.12**	1.77	1.88

accurate predictions when the large-scale forcing is missing, thus WI without analysis nudging is not a suitable forcing strategy.

In contrast, the WIN experiment performs as good as the reference experiment as the scores in Table 5 and the results displayed in Fig. 8 indicate. Although there are some minor deficiencies at 2 km spatial resolution, these are compensated by some minor advantages at the lower resolution of 30 km (and partly also of 10 km).

The applicability of the WIN forcing strategy is thus depending on the specific purpose followed by a model experiment. If precipitation fields of high spatial resolution are a major objective then daily re-initialisation remains the better choice. Also, the flexibility of the daily re-initialisation with respect to parallelisation of model runs is better than in the WIN strategy. In the RE design, daily model runs are completely independent from each other, and there are only minor jumps between the results of two consecutive days, which may be more problematic in the WIN strategy (although this aspect was not analysed in this study). A further argument for the forcing strategy followed in the RE design is the fact that the WRF model is able to better utilise its predictive skills within the resolved scales, while analysis nudging strongly dampens the mesoscale processes resolved by the WRF model.

3.2.3 Sensitivity to the PPS

In this part of the sensitivity study eight experiments were carried out, applying two different schemes for any of the CU, MP, LS and PBL parameterisation schemes (Table 4).

The results of all validation analyses applied to the PPS sensitivity experiments are presented in Table 6 together with those of the reference experiment. While a comparison of the scores mainly serves to show the effects of the different PPS and to assess the overall performance, the spatial distributions of the differences between the PPS experiments and the reference experiment displayed in Fig. 9 provide insight into the mechanisms responsible for the differences.

Comparing the CU1 and CU2 experiments, the latter one has a lower performance, not only with respect to the CU1 experiment but also to the RE. The CU1 experiment improves the predictions with respect to the observations at weather stations while concurrently decreasing the predictions with respect to the TRMM observations. Figure 9 shows that the sensitivity to the CU1 and CU2 experiments is very strong in the Bay of Bengal and the high-mountain fringes of the TiP, but is low on the TiP. Generally, the CU1 and CU2 experiments are wetter than the RE, especially in these regions. The reason for this finding is the convective nature of precipitation in the sensitive regions (as will be discussed in Sect. 4), while advection dominates large parts of the TiP. The three schemes work within different closure frameworks: for example, the PPS of the RE is a cloud ensemble scheme that uses 16 ensemble members to obtain an ensemble-mean realisation at a given time and location, while the other two schemes are triggered on various conditions on the vertical uplift within an atmospheric column. Our results are in accordance with Mukhopadhyay et al. (2009) who compared convective parameterisations for RCM simulations during the monsoon season, and found that the PPS used in the CU1 and CU2 experiments underestimate the observations for lighter rain rates, and overestimate for higher rain rates, while the PPS used in the RE shows an overestimation for lighter rain rates. The predictive skill of the CU1 and CU2 PPS in the LD with respect to TRMM observations is lower than that of the RE (not shown in Table 6), thus the New Grell-Devenyi 3 scheme used in the RE could be recommended.

The scores of the MP1 and MP2 experiments presented in Table 6 reveal that the PPS of the MP2 experiment is not suitable for the TiP. The MP1 results show similar effects in Fig. 9 as discussed for the CU1 experiment: high sensitivity of this PPS in the regions of convective precipitation and low sensitivity on most parts of the TiP where advection dominates. We argue that the choices of the CU and MP PPS should also consider combinatory effects, but are less influential for simulations in regions where advection is prevailing. These findings are interesting since the MP schemes are rather new and thus not extensively discussed in the scientific literature, so far.

The two experiments regarding the LS model underlying the WRF simulations show less pronounced effects when compared with the CU and MP PPS. The scores of the LS1 experiment reveal that larger differences to the RE are negative, thus this PPS would have to be rejected from these findings. However, there are also minor improvements in the simulation of snow processes, which may give reason for using this PPS when snow-hydrological investigations are in the focus of a model study. The LS2 experiment, in contrast, shows that no stronger negative effects are arising from this PPS, but unfortunately, it does not include an explicit parameterisation of snow processes, and thus makes it inappropriate for snow-hydrological investigations. Figure 9 shows that the effects of the two LS models are weak not only on the TiP but also in the regions where the CU and MP PPS show strong sensitivities. This can be attributed to the fact that convective processes and related MP processes are only weakly influenced by the underlying land surface, but mainly depend on the atmospheric dynamics and physics themselves. Over longer time periods, the choice of the LS model is expected to become more influential, but this aspect was not investigated in our study.

Finally, two different PPS for processes in the PBL have been analysed. The scores of the PBL1 and PBL2 experiments presented in Table 6 reveal that the PPS of the PBL2 experiment is not suitable for the TiP. The PBL1 experiment shows some improvement over the RE, but the skill for predicting snowfall seems to be less than the skill of the RE. As enlightened by Braun and Tao (2000), the sensitivity of

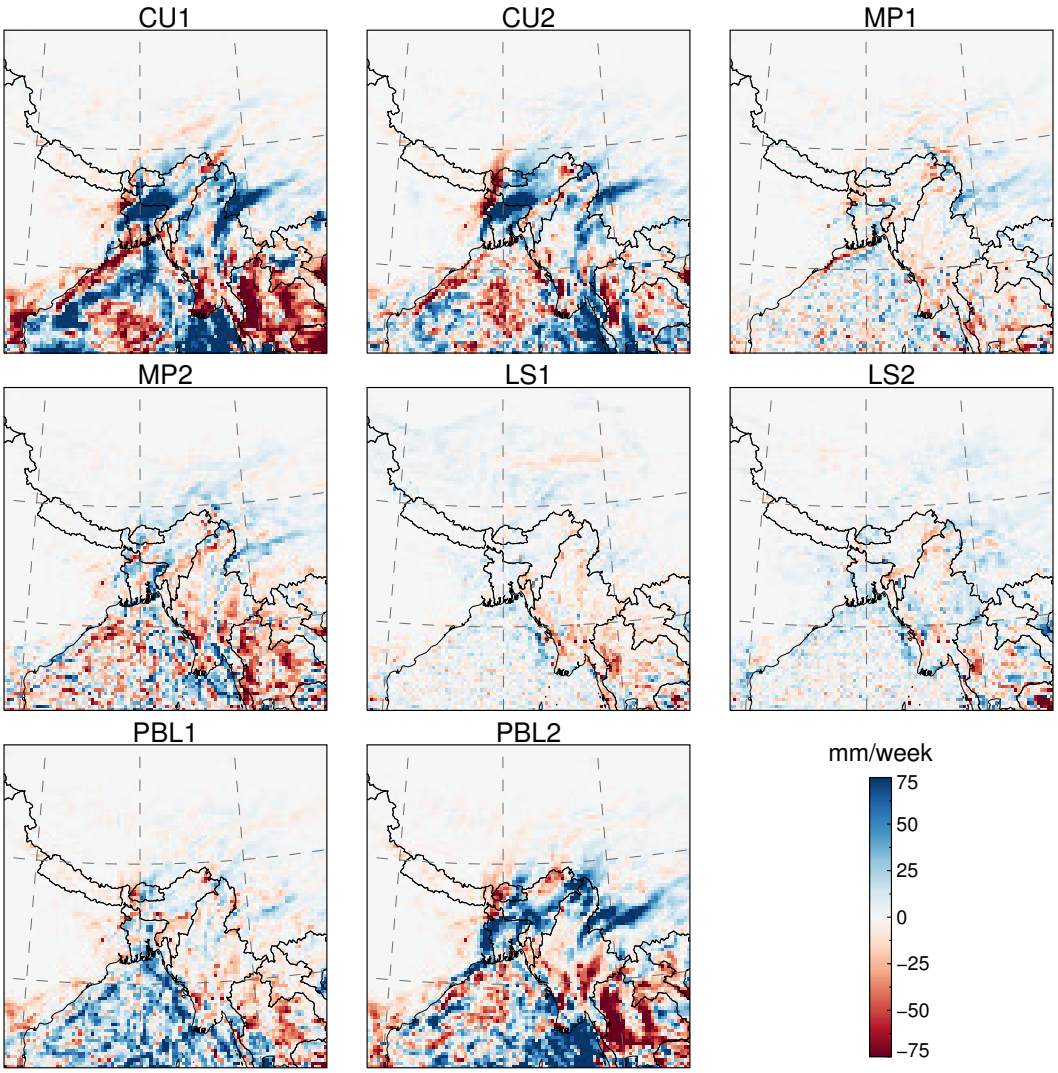

Fig. 9. Sensitivity to the physical parameterisation schemes. Difference between the one-week precipitation (mm week^{-1}) of the sensitivity experiments and the RE for WRF30 over a subset of the LD.

NWP models to the PBL parameterisation is also in this case stronger than to microphysics, at least for the regions south from the TiP. Figure 9 shows an interesting effect: the spatial pattern of the differences between the PBL2 experiment and the RE are strongly coupled to both CU PPS, since it also considers convective processes in the PBL.

In conclusion of the sensitivity studies for the PPS, we could show that there is nothing like a perfect combination of PPS, since any model-based investigation of precipitation on the TiP has to consider the oceanic regions where much of the water vapour and the convective systems influencing the southern, central and eastern parts of the TiP are formed. Yang and Tung (2003) also concluded that it was not possible to define a best performing cumulus parameterisation since each of the investigated cumulus schemes performed very differently for precipitation prediction under different synoptic forcing. Depending on the focus of an investigation, slightly modified PPS combinations may be used, but generally, the PPS combination used in the RE seems suitable for reanalysing precipitation on the TiP.

4 Discussion

In this section we will give answers to the two main research questions formulated in Sect. 1.1. The first question is discussed using the results presented in Sect. 3.1, while the discussion of the second question is based on the results shown in Sect. 3.2 and additional analyses of the simulations of precipitation fields in October 2008.

4.1 Validation methods and data sets

In this study, we proposed three data sets (TRMM, MODIS, NCDC weather stations) and several statistical methods to assess the WRF model simulations. Several climatological studies used the TRMM products, and it has been proven that TRMM 3B42 surface-rainfall rate is comparable to other surface observations (Koo et al., 2009), although the spatial scale of the rainfall data makes direct comparison to gauge data difficult. Our results also enlighten this issue: the WRF model and precipitation data sets depicted some considerable discrepancies when compared to point-by-point measurements at weather stations. TRMM showed to be less efficient than WRF10. Estimation errors due to spatial resolution may be reduced by statistical correction methods as described by Yin et al. (2008), but the authors also remind that TRMM performs poorly during the winter months, because of the presence of snow and ice over the TiP, since snow and ice on the ground scatter microwave energy in a similar fashion as ice crystals and raindrops in the atmosphere.

At the same time, TRMM offers a way to assess the mesoscale WRF30 output on a gridded spatial basis, and the two data sets are in good accordance for the spatial delineation of the 10 mm week^{-1} precipitation event. The comparison also showed differences in the occurrence of extreme events, for which WRF30 predicts higher amounts than TRMM observes. India's weather stations in the north-eastern provinces recorded precipitation amounts up to 150 mm day^{-1} during the event (IMD, 2008), which is lower than the highest values predicted by WRF (up to 500 mm week^{-1} for a few points at the high-mountain fringe of the TiP) but higher than TRMM estimations (maximum values of 130 mm week^{-1}).

One of the strengths of the WRF model is its ability to separate snow from rain. Since we are targeting on using the regional atmospheric reanalysis for hydrological and glaciological applications, snow data are of great importance, and the MODIS test that we developed proved to give valuable information on the models capacity to retrieve snowfall at high spatial resolution, as e.g. indicated by the positive effect of increasing spatial resolution and the use of two-way nesting. However, snow extent could be detected only where no snow prior to the event or clouds was present, preventing us drawing conclusions on high-mountain snowfall. Furthermore, it is rather difficult to find a suitable event or to run this test on a regular and automatic basis.

So far, no robust assessment of the WRF2 output is possible with weather stations either, as they are too scarce. Moreover, rain gauges do have a high sensitivity to wind and to the size of snow/rain particles: the snow under-catch of the four most widely used gauges can vary up to 80 % (Goodison et al., 1998). On response to this problem, we installed a Laser precipitation monitor (Distrometer) at the Nam Co station for future validation studies.

We applied a combination of different validation methods since none of the observational data sets could be unambiguously identified to serve as an absolute reference for model validation. Despite the discussed differences between the model experiments and the observational data sets (including differences between the observational data sets themselves) the model predictions and the observational data are generally concordant. Thus, we consider the validation methods and data sets principally suitable for this kind of studies.

4.2 Reanalysis of precipitation fields over the TiP

The WRF model offers a countless number of configurations, and in this study there was no intent to realise a complete review of the various possibilities. We assessed the sensitivity of the WRF model to different PPS. In general, the influence on predicted precipitation was rather small on the TiP in comparison to the forcing strategies. This can be due to frequent re-initialisation constraining the model to stay close to the large scale observations given as input data.

The comparison with observational data sets showed that the WRF model had a good accuracy in predicting snow- and rainfall of a single precipitation event. Tables 5 and 6 also present the scores for the one-month simulations carried out for October 2008, which are showing that the WRF model is generally able not only reanalysing precipitation over longer time periods including also times of no precipitation.

Figure 10 presents two results illustrating both the reason for the applicability of our approach and the hydrological relevance of individual precipitation events. The upper two maps display the contribution of convective precipitation to the total precipitation for the one-week simulation period of the Rashmi event. Except for the central and north-western part of the TiP, advection prevails and enables to retrieve accurate precipitation values within the error limits of the observations. In regions of high contribution of convective precipitation the sensitivity of the two CU and MP PPS, as well as the PBL2 PPS are much higher than in the other regions, which explains why the PPS schemes are not as important on the TiP. The dominance of advection on the TiP also allows reanalysing precipitation fields at high spatial resolution of 2 km without using a CU parameterisation scheme that is required at the lower resolutions of 10 and 30 km.

Figure 10 also shows the hydrological relevance of the Rashmi event, and reveals the complex spatial pattern of the precipitation fields on the TiP. High contributions of precipitation caused by the Rashmi cyclone to monthly precipitation in October 2008 reaches almost 100 % in some areas in the south and south-east of the TiP, while the areas of highest precipitation amounts during the event show contributions to monthly precipitation far beyond on third. This is in line with the findings shown in Fig. 2 where the importance of individual precipitation events was shown for annual precipitation in 2008 as observed at the 19 weather stations used in this study.

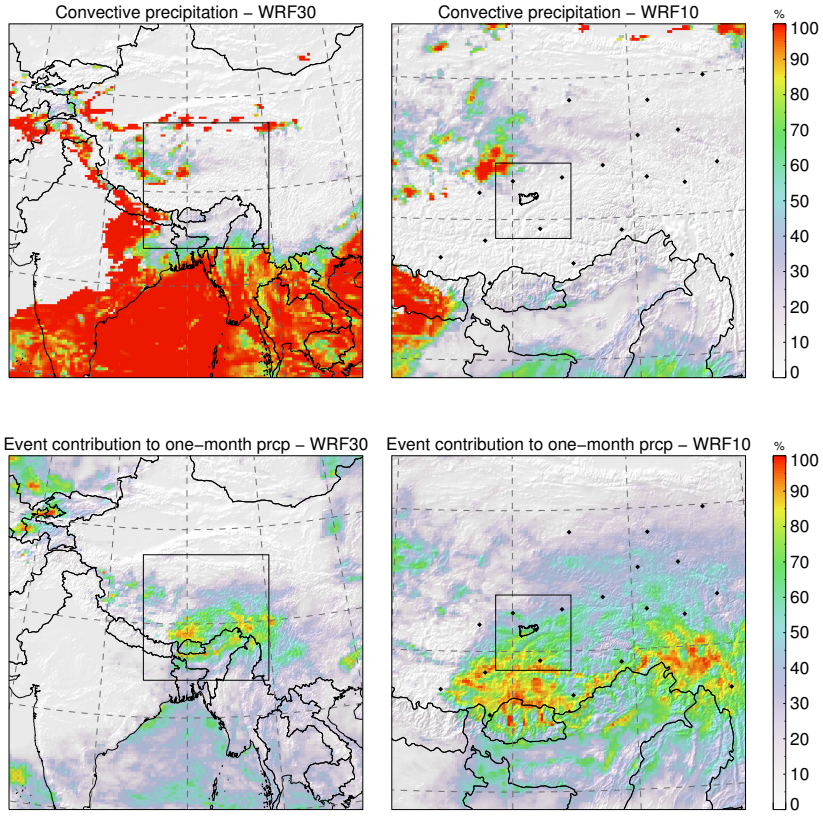

Fig. 10. Top: contribution of convective precipitation to the total precipitation for the one-week simulation period of the Rashmi event. Bottom: contribution of precipitation caused by the Rashmi event to monthly precipitation in October 2008.

Not only precipitation amounts but also the capture and timing of precipitation events is of high hydrological relevance. Figure 11 presents time-series of accumulated precipitation amounts for October 2008 from NCDC, TRMM and WRF10 at the 19 weather stations to analyse the capability of the WRF model capturing precipitation events close to the time they are also observed. In addition, we indicate the explained variance (r^2) of the daily accumulated time-series for each pair of data sets.

At five weather stations monthly precipitation amounts predicted by WRF10 are close to ground observations, while TRMM observations are close to ground measurements at four weather stations. Similar values for monthly precipitation amounts are retrieved by WRF10 and TRMM at four weather stations, where ground observations strongly differ from these values. Ground observations are much higher than TRMM or WRF10 only at two weather stations, while much lower values are reported at six weather stations. These results are in general accordance with the findings that were previously discussed for the single event.

Generally, WRF10 is better in explaining the variance in the ground observations than TRMM. With the exception of three stations WRF10 is better correlated with ground observations than TRMM. The generally very high r^2 values of WRF10 with the two observational data sets indicate that the WRF model is well-suited to retrieve precipitation dynamics, including times of no precipitation. This holds true even for many of the cases where the precipitation amounts for October 2008 simulated by WRF10 differs from one or both of the observations.

Positive mean bias values also found in other model validation studies are often interpreted as an error produced by the model. However, since the problems in observing precipitation are well-documented, resulting in systematically lower values especially for snowfall, we argue that this bias also documents the observational errors. Our study could not prove systematic, statistically significant over-prediction of precipitation by WRF10, although there are certainly individual cases, where WRF10 values are actually too high.

In Fig. 12, the monthly precipitation fields from TRMM, WRF30, WRF10 and WRF2 on the SD are presented. The general features of the precipitation pattern of October 2008, e.g. the generally high values in the south-eastern and eastern parts and the decrease in precipitation amounts towards the north-western areas, are observable in each of the data sets. However, the well-known orographic control exerted by the high-mountain areas on precipitation is only recognisable in the WRF10 and WRF2 results. The TRMM 3B42 estimations do not represent the small scale changes that are to expect over this complex topography, due to its low spatial

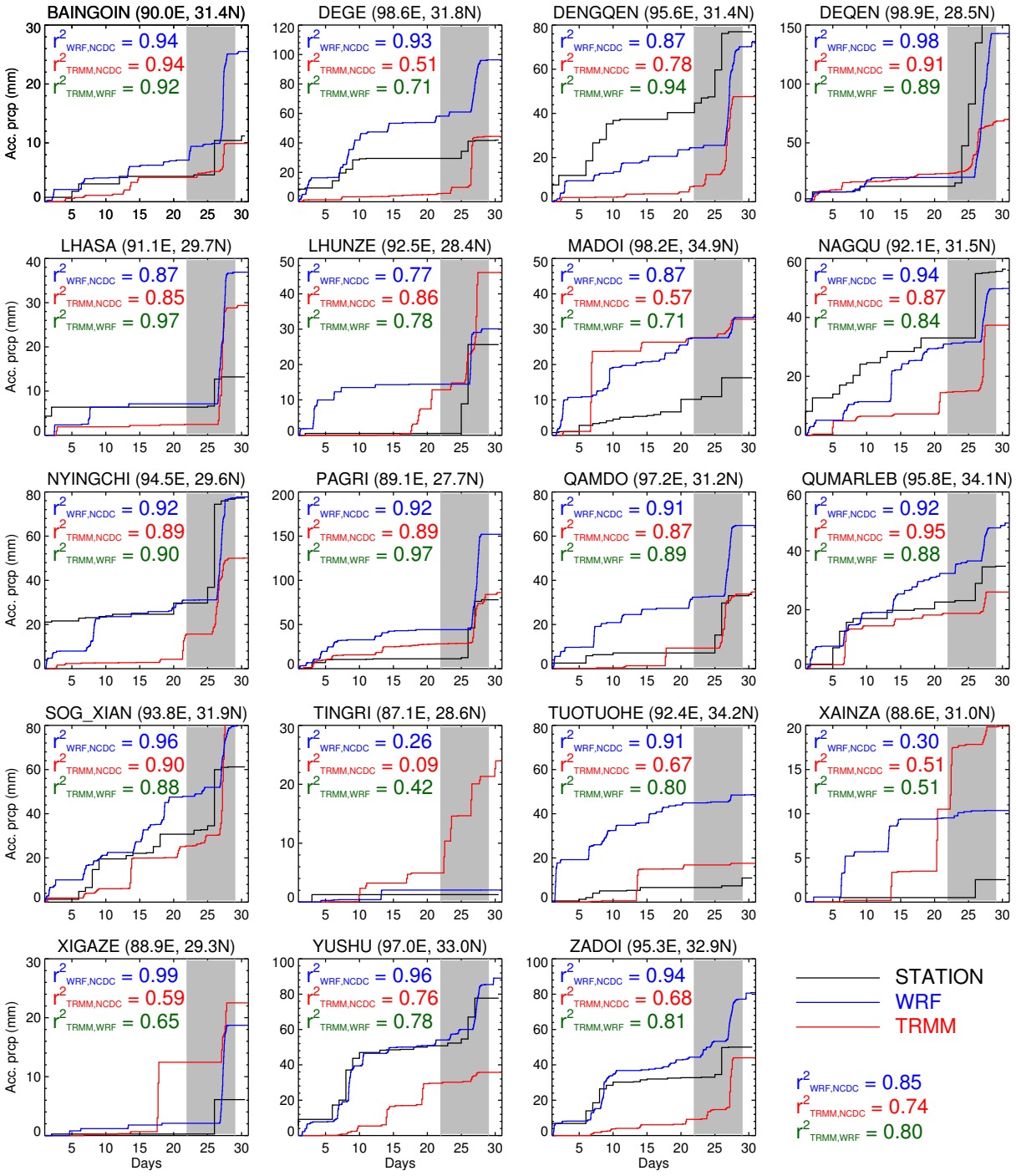

Fig. 11. Time series of daily precipitation amounts accumulated during October 2008 observed at weather stations, by TRMM and predicted by the one-month WRF10 simulation. Explained variances (r^2) are given for each pair of the three data sets and each station, as well as the mean r^2 for all stations. X-axis values are the days in October, the grey band marks the one-week focus period 22–28 October 2008.

resolution. Bookhagen and Strecker (2008) analysed orographic precipitation along the eastern Andes, showing that only TRMM 2B31 data, which has a high spatial resolution of about 5 km is able to depict the small-scale orographic influence on precipitation. However, these data are not applicable to single events due to low temporal sampling rates (about one acquisition per day). Our findings are generally consistent with the results from other studies (e.g., Caldwell et al., 2009; Bromwich et al., 2005).

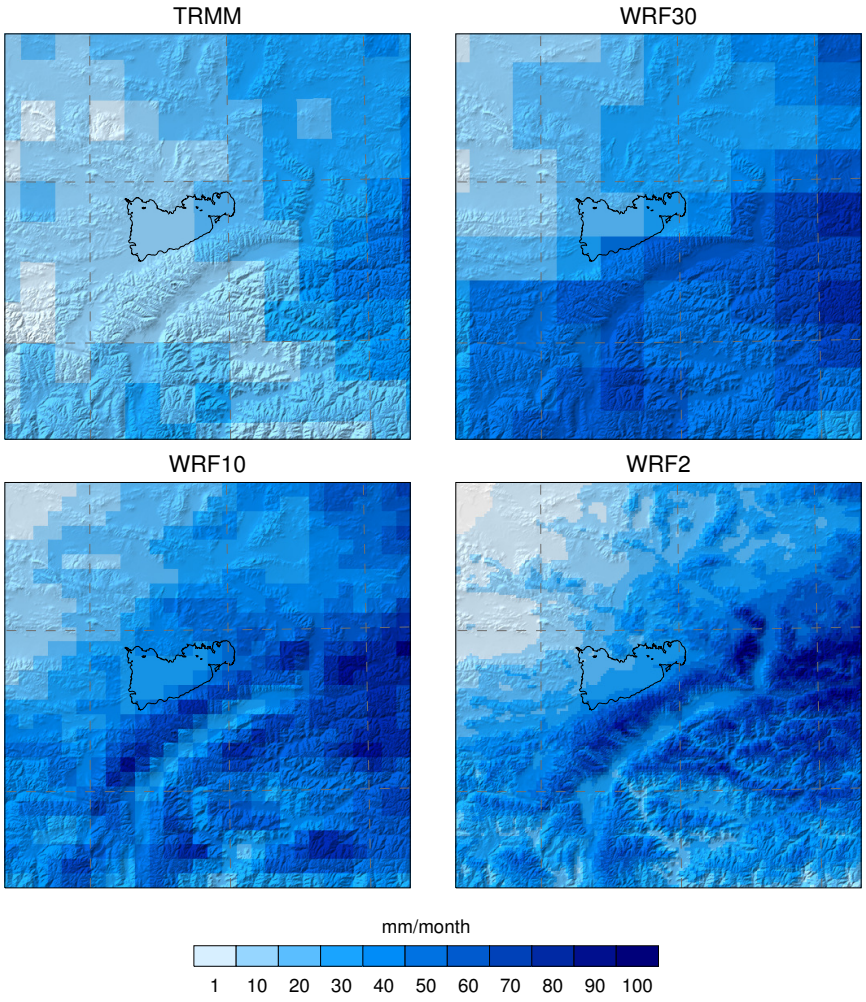

Fig. 12. Spatial distributions of precipitation amounts in October 2008 observed by TRMM and predicted by the one-month WRF30, WRF10 and WRF2 simulations on the SD.

5 Conclusion

Our study reveals that there is nothing like an optimal model strategy applicable for the high-altitude TiP, its fringing high-mountain areas of extremely complex topography and the low-altitude land and sea regions from which much of the precipitation on the TiP is originating. The choice of the physical parameterisation scheme will thus be always a compromise depending on the specific purpose of a model simulation.

Many other model configurations could have been proposed and tested, but the comparatively small sensitivity to the physical parameterisation schemes on the TiP suggests that further investigation should also focus on the models response to the forcing data sets providing the initial and boundary conditions.

In this study we do not apply bias correction for precipitation, thus keeping the model results physically consistent, and the errors caused by the different elements of the experimental design traceable. Bias correction is only valid if observational data are accurate, which is not the case for current observation methods available on the TiP. New remote sensing approaches will probably improve the situation as e.g. Bookhagen and Strecker (2008) could demonstrate for orographic precipitation detected by the TRMM 2B31 data set. However, the same authors also discussed the limitations of this data set, in particular the low sampling frequency of about one overpass per day.

Our study demonstrates the high importance of orographic precipitation, which is well captured as assessed on a qualitative basis. However, the problem of the orographic bias remains unsolved since reliable observational data are still missing.

The results presented in this paper are relevant for anyone interested in carrying out a regional atmospheric reanalysis employing a NWP model. The benefits of NWP models over usual gridded precipitation products are obvious: e.g. high resolution in time and space, flexibility and reproducibility.

The WRF model showed good accuracy in simulating snow- and rainfall on the TiP for a one-month simulation period. Our results encourage further investigations over longer simulation periods, and should also include further atmospheric variables.

Many hydrological analyses and applications like rainfall-runoff modelling or the analysis of flood events require not only precipitation accumulated over weeks and months but also precipitation rates at daily or even hourly intervals. Thus, our study offers a process-oriented alternative for retrieving precipitation fields of high spatio-temporal resolution in regions like the TiP, where other data sources are limited.

With the exception of the ground observations at the Nam Co research station, all data sets and the WRF model used in this study are available free of charge to the scientific community. This recent melioration in data accessibility represents a great improvement and will offer many possibilities for future atmospheric, hydrological and glaciological research.

Acknowledgements. This work is supported by the German Research Foundation (DFG) Priority Programme 1372, "Tibetan Plateau: Formation – Climate – Ecosystems" under the codes SCHE 750/4-1, SCHE 750/4-2. The authors wish to thank the three anonymous referees that reviewed the manuscript and made very useful comments and critics. We wish to warmly thank our colleagues that helped to improve the quality of the manuscript, the staff of the Nam Co research station for providing the data used in this study. We also made use of TRMM data provided by the GSFC DAAC and MODIS products distributed by the Land Processes Distributed Active Archive Center (LP DAAC), located at the US Geological Survey (USGS) Earth Resources Observation and Science (EROS) Center (lpdaac.usgs.gov).

Edited by: R. Uijlenhoet

References

Appel, E. and Mosbrugger, V.: Tibetan Plateau: Formation – Climate – Ecosystems: TiP, Science Plan For A Priority Programme, Tech. rep., 2006.

Betts, A. K. and Miller, M. J.: A new convective adjustment scheme. Part II: Single column tests using GATE wave, BOMEX, and arctic air–mass data sets, Q. J. Roy. Meteor. Soc., 112, 693–709, 1986.

Bolch, T., Yao, T., Kang, S., Buchroithner, M. F., Scherer, D., Maussion, F., Huintjes, E., and Schneider, C.: A glacier inventory for the western Nyainqentanglha Range and the Nam Co Basin, Tibet, and glacier changes 1976–2009, The Cryosphere, 4, 419–433, doi:10.5194/tc-4-419-2010, 2010.

Bookhagen, B. and Strecker, M. R.: Orographic barriers, high-resolution TRMM rainfall, and relief variations along the eastern Andes, Geophys. Res. Lett., 35, L06403, doi:10.1029/2007GL032011, 2008

Box, J. E., Bromwich, D. H., and Bai, L.-S.: Greenland ice sheet surface mass balance for 1991–2000: Application of Polar MM5 mesoscale model and in-situ data, J. Geophys. Res., 109, D16105, doi:10.1029/2003JD004451, 2004.

Box, J. E., Bromwich, D. H., Veenhuis, B. A., Bai, L.-S., Stroeve, J. C., Rogers, J. C., Steffen, K., Haran, T., and Wang, S.-H.: Greenland ice sheet surface mass balance variability (1988–2004) from calibrated polar MM5 output, J. Climate, 19, 2783–2800, 2006.

Braun, S. A. and Tao, W. K: Sensitivity of High-Resolution Simulations of Hurricane Bob (1991) to Planetary Boundary Layer Parameterizations, Mon. Weather Rev., 128, 3941–3961, 2000.

Bromwich, D. H., Bai, L. H., and Bjarnason, G. G.: High-resolution regional climate simulations over Iceland using Polar MM5, Mon. Weather Rev., 2005(133), 3527–3547, 2005.

Bukovsky, M. S. and Karoly, D. J.: Precipitation Simulations Using WRF as a Nested Regional Climate Model, J. Appl. Meterol. Clim., 48, 2152–2159, doi:10.1175/2009JAMC2186.1, 2009

Caldwell, P., Chin, H.-N. S., Bader, D. C., and Bala, G.: Evaluation of a WRF dynamical downscaling simulation over California, Climatic Change, 95, 499–521, doi:10.1007/s10584-009-9583-5, 2009.

Chen, F. and Dudhia, J.: Coupling an advanced land surface-hydrology model with the Penn State-NCAR MM5 modeling system, Part I: model implementation and sensitivity, Mon. Weather Rev., 129, 569–585, 2001.

Chen, J., Li, C., and He, G.: A diagnostic analysis of the impact of complex terrain in the eastern Tibetan plateau, China, on a severe storm, Arct. Antarct. Alp. Res., 39, 699–707, 2007.

Dudhia, J.: Numerical study of convection observed during the winter monsoon experiment using a mesoscale two-dimensional model, J. Atmos. Sci., 46, 3077–3107, 1989.

Fowler, H. J., Blenkinsop, S., and Tebaldi, C.: Linking climate change modelling to impacts studies: recent advances in downscaling techniques for hydrological modelling, Int. J. Climatol., 27, 1547–1578, doi:10.1002/joc.1556, 2007

Frauenfeld, O., Zhang, T., and Serreze, M.: Climate change and variability using European Centre for Medium-Range Weather Forecasts reanalysis (ERA-40) temperatures on the Tibetan Plateau, J. Geophys. Res.-Atmos., 110, D02101, doi:10.1029/2004JD005230, 2005.

Gao, Y., Tang, M., Luo, S., Shen, Z., and Li, C.: Some aspects of recent research on the qinghai-xizang plateau meteorology, B. Am. Meteorol. Soc., 62, 31–35, 1981.

Goodison, B., Louie, P., and Yang, D.: WMO solid precipitation measurement intercomparison, 1998.

Grell, G. and Devenyi, D.: A generalized approach to parameterizing convection combining ensemble and data assimilation techniques, Geophys. Res. Lett., 29(14), 1693, doi:10.1029/2002GL015311, 2002.

Haginoya, S., Fujii, H., Kuwagata, T., Xu, J., Ishigooka, Y., Kang, S., and Zhang, Y.: Air-Lake Interaction Features Found in Heat and Water Exchanges over Nam Co on the Tibetan Plateau, Sola, 5, 172–175, 2009.

Hahn, D. and Manabe, S.: Role of mountains in south asian monsoon circulation, J. Atmos. Sci., 32, 1515–1541, 1975.

Hall, D. K., Riggs, G. A., and Salomonson, V. V.: MODIS/Terra Snow Cover Daily L3 Global 500 m Grid V005, 22–29 October 2008, Boulder, Colorado USA: National Snow and Ice Data Center, Digital media., 2006.

Harris, L. M. and Durran, D. R.: An Idealized Comparison of

One-Way and Two-Way Grid Nesting, Mon. Weather Rev., 138, 2174–2187, doi:10.1175/2010MWR3080.1, 2010.

Hong, S. Y., Noh Y., and Dudhia, J.: A new vertical diffusion package with an explicit treatment of entrainment processes, Mon. Weather Rev., 134, 2318–2341, 2006.

Huffman, G. J., Adler, R. F., Bolvin, D. T., Gu, G., Nelkin, E. J., Bowman, K. P., Hong, Y., Stocker, E. F., and Wolff, D. B.: The TRMM Multisatellite Precipitation Analysis (TMPA): Quasi-Global, Multiyear, Combined-Sensor Precipitation Estimates at Fine Scales, J. Hydrometeor., 8, 38-54, doi:10.1175/JHM560.1, 2007.

IMD: Cyclonic Storm, RASHMI: A preliminary Report, available at: http://www.imd.gov.in/section/nhac/dynamic/cycRashmi.pdf, last access: 8 June 2011, 2008.

Janjic, Z. I.: The step-mountain eta coordinate model: further developments of the con- vection, viscous sublayer and turbulence closure schemes, Mon. Weather Rev., 122, 927–945, 1994.

Janjic, Z. I.: Nonsingular Implementation of the Mellor-Yamada Level 2.5 Scheme in the NCEP Meso model, Tech. Rep., 437, 2002.

Kain, J. and Fritsch, J.: A one-dimensional entraining detraining plume model and its application in convective parameterization, J. Atmos. Sci., 47, 2784–2802, 1990.

Kang, S., Xu, Y., You, Q., Fluegel, W., Pepin, N., and Yao, T.: Review of climate and cryospheric change in the Tibetan Plateau, Environ. Res. Lett., 5, 015101, doi:10.1088/1748-9326/5/1/015101, 2010

Koo, M.–S., Hong, S.–Y., and Kim, J.: An Evaluation of the Tropical Rainfall Measuring Mission (TRMM) Multi–Satellite Precipitation Analysis (TMPA) Data over South Korea, J. Atmos. Sci, 45, 265–282, 2009

Krause, P., Biskop, S., Helmschrot, J., Flügel, W.-A., Kang, S., and Gao, T.: Hydrological system analysis and modelling of the Nam Co basin in Tibet, Adv. Geosci., 27, 29–36, doi:10.5194/adgeo-27-29-2010, 2010.

Laprise, R., de Elia, R., Caya, D., Biner, S., Lucas-Picher, P., Diaconescu, E., Leduc, M., Alexandru, A., and Separovic, L.: Challenging some tenets of Regional Climate Modelling, Meteorol. Atmos. Phys., 100, 3–22, doi:10.1007/s00703-008-0292-9, 2008

Leung, L. and Qian, Y.: The sensitivity of precipitation and snowpack simulations to model resolution via nesting in regions of complex terrain, J. Hydrometeorol., 4, 1025–1043, 2003.

Li, M., Ma, Y., Hu, Z., Ishikawa, H., and Oku, Y.: Snow distribution over the Namco lake area of the Tibetan Plateau, Hydrol. Earth Syst. Sci., 13, 2023–2030, doi:10.5194/hess-13-2023-2009, 2009.

Liu, J., Wang, S., Yu, S., Yang, D., and Zhang, L.: Climate warming and growth of high-elevation inland lakes on the Tibetan Plateau, Global Planet. Change, 67, 209–217, doi:10.1016/j.gloplacha.2009.03.010, 2009.

Lo, J. C., Yang, Z., Pielke, Sr., and Roger, A.: Assessment of three dynamical climate downscaling methods using the Weather Research and Forecasting (WRF) model, J. Geophys. Res.-Atmos., 113, D09112, doi:10.1029/2007JD009216, 2008

Ma, L., Zhang, T., Frauenfeld, O. W., Ye, B., Yang, D., and Qin, D.: Evaluation of precipitation from the ERA-40, NCEP-1, and NCEP-2 Reanalyses and CMAP-1, CMAP-2, and GPCP-2 with ground-based measurements in China, J. Geophys. Res.-Atmos., 114, D09105, doi:10.1029/2008JD011178, 2009.

Mlawer, E., Taubman, S., Brown, P., Iacono, M., and Clough, S.: Radiative transfer for inhomogeneous atmospheres: RRTM, a validated correlated-k model for the longwave, J. Geophys. Res.-Atmos., 102, 16663–16682, 1997.

Mukhopadhyay, P., Taraphdar, S., Goswami, B. N., and Krishna Kumar, K.: Indian summer monsoon precipitation climatology in a high resolution regional climate model: Impact of convective parameterization on systematic biases, Weather Forecast., 25, 369–387, 2009.

Pleim, J. E: A combined local and non-local closure model for the atmospheric boundary layer. Part 1: Model description and testing, J. Appl. Meteor. Clim., 46, 1383–1395, 2007.

Pleim, J. E. and Xiu, A.: Development and testing of a surface flux and planetary boundary layer model for application in mesoscale models, J. Appl. Meteor., 34, 16–32, 1995.

Rakesh, V., Singh, R., Pal, P. K., and Joshi, P. C.: Sensitivity of mesoscale model forecast during a satellite launch to different cumulus parameterization schemes in MM5, Pure Appl. Geophys., 164, 1617–1637, doi:10.1007/s00024-007-0245-0, 2007.

Sato, T., Yoshikane, T., Satoh, M., Miltra, H., and Fujinami, H.: Resolution Dependency of the Diurnal Cycle of Convective Clouds over the Tibetan Plateau in a Mesoscale Model, J. Meteorol. Soc. Jpn., 86, 17–31, 2008.

Shi, Y. and Liu, S.: Estimation on the response of glaciers in China to the global warming in the 21st century, Chinese Sci. Bull., 45, 668–672, 2000.

Skamarock, W. C., Klemp, J. B., Dudhia, J., Gill, D. O., Barker, D. M., Duda, M. G., Huang, X.-Y., Wang, W., and Powers, J. G.: A Description of the Advanced Research WRF Version 3, Tech. rep., 2008.

Smirnova, T., Brown, J., Benjamin, S., and Kim, D.: Parameterization of cold-season processes in the MAPS land-surface scheme, J. Geophys. Res.-Atmos., 105, 4077–4086, 2000.

Tao, W., Simpson, J., Baker, D., Braun, S., Chou, M., Ferrier, B., Johnson, D., Khain, A., Lang, S., Lynn, B., Shie, C., Starr, D., Sui, C., Wang, Y., and Wetzel, P.: Microphysics, radiation and surface processes in the Goddard Cumulus Ensemble (GCE) model, Meteorol. Atmos. Phys., 82, 97–137, doi:10.1007/s00703-001-0594-7, 2003.

Thompson, G., Field, P. R., Rasmussen, R. M., and Hall, W. D.: Explicit Forecasts of Winter Precipitation Using an Improved Bulk Microphysics Scheme. Part II: implementation of a New Snow Parameterization, Mon. Weather Rev., 136, 5095–5115, doi:10.1175/2008MWR2387.1, 2008.

Wang, X., Xie, H., and Liang, T.: Evaluation of MODIS snow cover and cloud mask and its application in Northern Xinjiang, China, Remote Sens. Environ., 112, 1497–1513, doi:10.1016/j.rse.2007.05.016, 2008.

Wilks, D. S.: Statistical Methods in the Atmospheric Sciences – An Introduction, vol. 59 of International Geophysics Series, Academic Press, 1995.

Wu, Y. and Zhu, L.: The response of lake-glacier variations to climate change in Nam Co Catchment, central Tibetan Plateau, during 1970–2000, J. Geogr. Sci., 18, 177–189, doi:10.1007/s11442-008-0177-3, 2008.

Yang, M. and Tung, Q.: Evaluation of rainfall forecasts over Taiwan by four cumulus parameterization schemes, J. Meteorol. Soc. Jpn., 81, 1163–1183, 2003.

Yao, T., Pu, J., Lu, A., Wang, Y., and Yu, W.: Recent glacial retreat

and its impact on hydrological processes on the tibetan plateau, China, and sorrounding regions, Arct. Antarct. Alp. Res., 39, 642–650, 2007.

Yin, Z.-Y., Zhang, X., Liu, X., Colella, M., and Chen, X.: An assessment of the biases of satellite rainfall estimates over the Tibetan Plateau and correction methods based on topographic analysis, J. Hydrometeorol., 9, 301–326, doi:10.1175/2007JHM903.1, 2008.

Zaengl, G.: To what extent does increased model resolution improve simulated precipitation fields? A case study of two north-Alpine heavy-rainfall events, Meteorol. Z., 16, 571–580, 2007.

Paper II

Precipitation seasonality and variability over the Tibetan Plateau as resolved by the High Asia Reanalysis

Maussion, F., Scherer, D., Mölg, T., Collier, E., Curio, J. and Finkelnburg, R. (2014): Precipitation seasonality and variability over the Tibetan Plateau as resolved by the High Asia Reanalysis, *Journal of Climate*, 27, 1910-1927, doi:10.1175/JCLI-D-13-00282.1

Status: Published

Own contribution:

- design of the study
- numerical simulations
- data preparation
- data analysis
- graphics and tables
- writing

Precipitation Seasonality and Variability over the Tibetan Plateau as Resolved by the High Asia Reanalysis*

FABIEN MAUSSION, DIETER SCHERER, THOMAS MÖLG, EMILY COLLIER,+ JULIA CURIO, AND ROMAN FINKELNBURG

Chair of Climatology, Technische Universität Berlin, Berlin, Germany

(Manuscript received 14 May 2013, in final form 4 October 2013)

ABSTRACT

Because of the scarcity of meteorological observations, the precipitation climate on the Tibetan Plateau and surrounding regions (TP) has been insufficiently documented so far. In this study, the characteristics and basic features of precipitation on the TP during an 11-yr period (2001–11) are described on monthly-to-annual time scales. For this purpose, a new high-resolution atmospheric dataset is analyzed, the High Asia Reanalysis (HAR), generated by dynamical downscaling of global analysis data using the Weather Research and Forecasting (WRF) model. The HAR precipitation data at 30- and 10-km resolutions are compared with both rain gauge observations and satellite-based precipitation estimates from the Tropical Rainfall Measurement Mission (TRMM). It is found that the HAR reproduces previously reported spatial patterns and seasonality of precipitation and that the high-resolution data add value regarding snowfall retrieval, precipitation frequency, and orographic precipitation. It is demonstrated that this process-based approach, despite some unavoidable shortcomings, can improve the understanding of the processes that lead to precipitation on the TP. Analysis focuses on precipitation amounts, type, seasonality, and interannual variability. Special attention is given to the links between the observed patterns and regional atmospheric circulation. As an example of an application of the HAR, a new classification of glaciers on the TP according to their accumulation regimes is proposed, which illustrates the strong spatial variability of precipitation seasonality. Finally, directions for future research are identified based on the HAR, which has the potential to be a useful dataset for climate, glaciological, and hydrological impact studies.

1. Introduction

The Tibetan Plateau and adjacent mountain ranges (TP)—Himalayas, Karakoram, Pamir, Kunlun, and Qilian Shan (cf. Fig. 1)—play a crucial role for downstream hydrology and water availability in Asia (Immerzeel et al. 2010). Rainfall, snowmelt, and, to a lesser extent, glaciers dominate the hydrological budget of the TP (Bookhagen and Burbank 2010), but the relative importance of these factors varies largely between regions and watersheds (Kaser et al. 2010). Most glaciers in the Himalayas (Bolch et al. 2012) or on the Tibetan Plateau (Yao et al. 2012) are retreating, but they show contrasting patterns of shrinkage (Kääb et al. 2012). Local factors (e.g., exposition, topography, and debris coverage) partly account for these differences, but spatial and temporal heterogeneity of climate and climate change (Palazzi et al. 2013) play a role that has yet to be quantified, especially in the regions where in situ measurements are nonexistent.

The TP climate is under the combined and competitive influences of the East Asian and South Asian monsoons (Webster et al. 1998) and of the westerlies (Schiemann et al. 2009). The role of the TP as a controlling factor for the Asian monsoon system and for atmospheric circulation at hemispheric scale has been studied for a long time (Hahn and Manabe 1975) and continues to be a key research topic (e.g., Molnar et al. 2010; Wu et al. 2012). While the mechanical and thermal effects of the highly elevated TP on global circulation patterns has received much attention, the strength and nature of the couplings between the various monsoon

Denotes Open Access content.

* Supplemental information related to this paper is available at the Journals Online website: http://dx.doi.org/10.1175/JCLI-D-13-00282.s1.

+ Additional affiliation: Department of Earth and Atmospheric Sciences, University of Alberta, Edmonton, Alberta, Canada.

Corresponding author address: Fabien Maussion, Technische Universität Berlin, Chair of Climatology, Rothenburgstr. 12, 12165 Berlin, Germany.
E-mail: fabien.maussion@tu-berlin.de

DOI: 10.1175/JCLI-D-13-00282.1

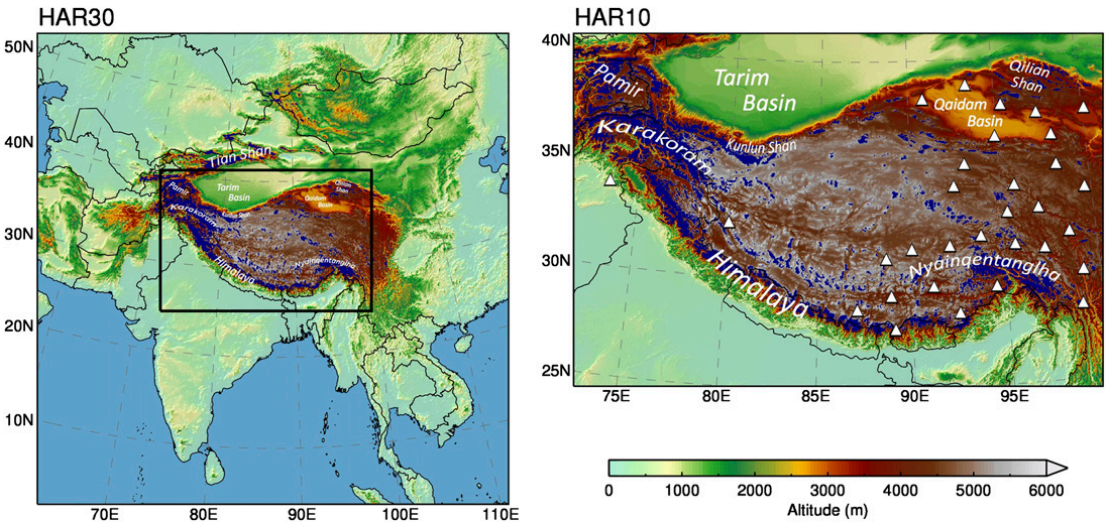

FIG. 1. Maps of the WRF model domains HAR30 (south-central Asia domain, 30-km resolution; 200 × 200 grid points) and HAR10 (High Asia domain, 10-km resolution; 270 × 180 grid points). Glacier outlines from the Randolph glacier inventory are drawn in blue, and the positions of the NCDC stations used for the validation are indicated by white triangles. Geographical locations mentioned in the text are indicated.

systems and the westerlies and especially their effects on TP precipitation variability remain less studied so far.

A substantial part of precipitation on the TP falls as snow. Spring TP snow cover has been proven to be a significant predictor for southwest Asian monsoon variability (Immerzeel and Bierkens 2010). The variability of snowfall frequency and intensity during spring/summer and related surface albedo conditions on glaciers also have a considerable impact on glacier mass balance. The timing and amount of snowfall in the early ablation (mass loss) season is a key process for the surface energy balance of glaciers and anomalous events (either dry or wet) initiate effects that can persist during the entire ablation season (e.g., Mölg et al. 2012; Yang et al. 2011, 2013). Glaciers on the TP are diverse in type regarding accumulation and ablation patterns, which are largely tied to precipitation amount and seasonality (Fujita 2008; Shi and Liu 2000).

The major reason for our lack of knowledge about the TP climate is the paucity of meteorological data. Permanent weather stations are scarce and confined to lower altitudes (Qin et al. 2009) and therefore are not representative of the high mountain climates. Global reanalysis datasets have coarse resolution that limits their representation of the mountainous topography. Of all climatological elements affected by topography, precipitation is probably the most complex and the most poorly represented by coarse-resolution grids (e.g., You et al. 2012; Bohner 2006).

Regional numerical weather prediction (NWP) models can be used to simulate precipitation fields and other meteorological variables at a high-spatiotemporal resolution. Longer time spans of years to decades can be simulated by NWP models by successive reinitialized model runs of shorter periods forced by large-scale observational datasets (e.g., Lo et al. 2008). In this study, we present a dataset generated using this method, that provides a tool to study atmosphere-related processes on the TP [the High Asia Reanalysis (HAR), described in section 2]. The HAR spans a period of more than 11 yr (October 2000–December 2011) and comprises two datasets with different spatial coverage and objectives: a domain of 30-km resolution including most parts of south and central Asia and a nested domain of 10-km resolution covering the TP and most parts of High Asia (Fig. 1). For simplicity, we use the acronym TP when referring to the Tibetan Plateau and surrounding mountain ranges as comprised in the 10-km-resolution High Asia domain.

The purpose of this study is twofold:

(i) describe the characteristics of precipitation (amount, type, seasonality, and variability) on the TP at monthly to annual time scales and obtain a more spatially detailed pattern than is possible from the few available observations (Fig. 1), as far as allowed by the accuracy and the resolution of the HAR and
(ii) provide some insights into the factors that lead to precipitation on the TP and propose perspectives for future research based on the HAR.

Producing accurate precipitation data using an atmospheric model is not trivial. Maussion et al. (2011, hereafter MA11) conducted a sensitivity analysis for a 1-month period during which strong rainfall and snowfall occurred on the TP and evaluated the model precipitation output

with (i) eight different physical parameterization schemes and (ii) several nesting and reinitialization configurations. No physical parameterization scheme outperformed the others for all the tests, but much effort went into choosing the model setup that performs best to produce the dataset presented in this study. In the first part of this paper, we assess the HAR precipitation output for the 11-yr period and evaluate its accuracy and potential errors. This evaluation is carried out by all available means; that is, by comparing the simulated precipitation with available surface and satellite observations but also by analyzing precipitation patterns and seasonality in the broader context of our current knowledge about precipitation in complex terrain and on the TP. The temporal resolution and extent of the HAR allows the analysis of processes from hourly to interannual time scales. In this study, we will not analyze diurnal cycles of precipitation or single stochastic weather events, although such aspects could also be addressed with the HAR dataset (see MA11).

In the following section, we describe the methods used to produce the HAR. The datasets used for the validation of the precipitation data are described in section 3. In section 4, we present and discuss the results. Section 5 shows an application example and provides a new map of glacier accumulation regimes based on precipitation seasonality. In section 6, we draw the conclusions of our study.

2. The High Asia Reanalysis dataset

To obtain gridded meteorological data at high-spatial and high-temporal resolutions, one general approach is to dynamically downscale a gridded global dataset that has been produced by data assimilation of a multitude of quality-controlled observations. Through data assimilation on the global scale, the resulting analysis or reanalysis dataset represents a physically consistent ''best guess'' of the state of the atmosphere at each time (usually at 6-h intervals). One of the basic requirements of our approach is that the downscaled data should represent as closely as possible the information that suitable observations would have delivered. This implies that the conditions at Earth's surface influencing atmospheric processes, particularly in the boundary layer, need to be described in sufficient spatial detail.

Lo et al. (2008) analyzed different dynamical downscaling methods and showed that consecutive reinitialized runs outperformed continuous long-term integrations with a single initialization, in particular when the reinitialization frequency was weekly instead of monthly. Other studies (e.g., von Storch et al. 2000) have successfully applied spectral nudging to continuous long-term integrations for dynamical downscaling, a technique that prevents the model from drifting away from the driving large-scale states while concurrently allowing the development of mesoscale processes. The major drawback of the latter method for our purposes is that no reinitialization takes place during which assimilated observations could possibly correct drifts in the land surface model or near-surface atmospheric variables.

MA11 tested different options for dynamical downscaling using reinitialization. Using almost the same domain as in this study, they showed for a test case that reinitialization sequences of daily runs outperformed weekly simulations. Based on these findings, we decided to follow a daily reinitialization strategy, which additionally prevents the land surface model from drifting away from the states provided by the analysis data. Several studies made use of this technique for regions of comparable environment (complex terrain and scarce observations): for example, Iceland (Bromwich et al. 2005), Greenland (Box et al. 2006), and the Arctic (Wilson et al. 2011).

The NWP model used to generate the HAR is the Advanced Research Weather Research and Forecasting model (WRF-ARW; Skamarock and Klemp 2008). The dataset consists of consecutive reinitialized model runs of 36-h time integration. Each run starts at 1200 UTC. The first 12 h from each run are discarded as spinup while the remaining 24 h of model output provide 1 day of the 11-yr-long time series. The model configuration used for the HAR is summarized in Table 1. The model is forced with the GFS operational model global tropospheric analyses [final analysis (FNL); dataset ds083.2], which are available every 6 h and have a spatial resolution of 1°. FNL data rely on numerous data sources, such as remote sensing data from Earth observing satellites assimilated together with surface and upper air reports from global observation networks. The data include pressure, geopotential height, temperature, dewpoint temperature, and wind direction and speed (National Centers for Environmental Prediction 2014). In the development phase of the HAR, the Interim European Centre for Medium-Range Weather Forecasts (ECMWF) Re-Analysis (ERA-Interim) dataset (Dee et al. 2011) was evaluated as a possible forcing dataset. We found that the accuracy of the HAR precipitation was improved when driven by FNL (Figs. S1–S3; see supplementary material). Moreover, initialization issues with ERA-Interim related to the treatment of snow cover in heavily glaciated grid cells[1] (Collier et al. 2013; Figs. S4–S6) and a summer cold bias on the TP further supported the choice of FNL.

[1] In ERA-Interim, snow depth is arbitrarily initialized at 10 m for grid cells with greater than 50% glacier coverage.

TABLE 1. HAR model strategy.

Map and grids	
Map projection	Lambert conformal
Center point of domain	30.0°N, 87.0°E
Number of vertical layers	28
Horizontal grid spacing	30 km and 10 km
Unstaggered grid points	200 × 200 and 270 × 180
Static geographical fields	U.S. Geological Survey (USGS) dataset at 10′ and 5′ resolution, glacier outlines from the RGI V1
Timing	
Simulation period	October 2000–September 2011
Time step	120 s and 40 s
Nesting strategy	
Nesting	Two-way nesting in cascade simulations
Forcing strategy	
Boundary conditions	National Centers for Environmental Prediction (NCEP) FNL from Global Forecast System (GFS) operational model global tropospheric analyses (1°, 6 hourly)
Sea surface temperature	NCEP Marine Modeling and Analysis Branch (MMAB) real-time global SST (RTG_SST) analysis (0.5°, daily)
Lake surface temperature	WRF model inland water module (avg_tsfc)
Initialization	Daily
Runs starting time	Daily, 1200 UTC
Runs duration	36 h
Spinup	12 h
Physical parameterization schemes	
Shortwave radiation	Dudhia scheme
Longwave radiation	Rapid Radiative Transfer Model (RRTM)
Cumulus parameterization	New Grell–Devenyi 3 sheme
Microphysics	Modified Thompson scheme
Land surface model	Noah land surface model (LSM)
PBL	Mellor–Yamada–Janjić turbulent kinetic energy (TKE)

In this study, a few minor setup changes with respect to MA11 were made, including upgrading the WRF model to version 3.3.1 and using the recently introduced inland water surface temperature initialization module. Since we expect the HAR dataset to be used as input data for hydrological and glaciological modeling, an adequate representation of ice-covered ground is important. Thus, we updated the original ice mask in the geographical land cover data with the Randolph glacier inventory, version 1.0 (RGI V1; Arendt et al. 2012). Since these modifications have a limited impact on the model output at regional scale (Collier et al. 2013), they will not be discussed here. The two-way nested cascading approach defined in MA11 has been followed here too. First the 10-km-resolution domain is run within the 30-km domain using the two-way nesting option, and then the 30-km-resolution domain is run alone to avoid inconsistencies due to the presence of the child domain. This allows us to consider the WRF model at 30 km (HAR30) and WRF model at 10 km (HAR10) as two different, complementary datasets.

Our approach using dynamical downscaling with short-term integration and daily reinitialization can be called ''regional reanalysis,'' following the ideas of, for example, Kanamitsu and Kanamaru (2007) or von Storch et al. (2000), who concluded that dynamical downscaling using spectral nudging may be seen as an indirect data assimilation technique. For the HAR we have not, however, performed data assimilation on the regional level, as is the case with ''true'' regional reanalyses like the North American Regional Reanalysis (NARR). Because of the scarcity of both surface observations and radio soundings as well as their inaccessibility, variational data assimilation is not possible for the TP. To our knowledge, such a comprehensive and process-based dataset is currently unique for the TP, and therefore the HAR is intended to fill a gap where other regional reanalyses are not available.

For the potential users of the dataset (atmospheric scientists, hydrologists, glaciologists, etc.), the WRF model output has been postprocessed for easy use. We provide separate data files per variable, per year, and per time aggregation (hourly, daily, monthly, and yearly), as well as vertically interpolated fields at standard pressure levels in addition to the model sigma levels. A webpage has been created for HAR users where the data can be downloaded (available at http://www.klima.tu-berlin.de/HAR). The range of applications of this dataset is rich and unexplored. So far, the HAR has been used by Mölg et al. (2012, 2014), who employed the HAR as input for a glacier energy and mass balance model; by Kropáček et al. (2013), who quantified the relation of air temperature and wind speed to the icing periods of large lakes on the plateau; and by Dietze et al. (2014), who analyzed sediment transport processes at four sites on the plateau.

We used the daily, monthly and yearly products from HAR30 and HAR10 (version 1) for this study. We consider the time span of October 2000–September 2011 but for simplicity we use the term ''decade'' for these 11 hydrological years. For the seasonality analyses we use the classical quarters: December–February (DJF), March–May (MAM), June–August (JJA), and September–November (SON). To avoid singularities we removed 10 and 5 grid points from the HAR30 and HAR10 domain boundaries, respectively. Unless specified otherwise, all figures and analysis are made using the original model grids.

3. Validation data and assessment methods

a. Weather stations

The HAR precipitation data are compared with rain gauge precipitation records from the ''Global Summary of the Day'' provided by the National Climatic Data Center (NCDC). We conduct our evaluation for the TP region. Thus, the weather stations selected for this study must satisfy two criteria: they are located within the HAR10 domain and are located above 2000 m MSL. We built monthly aggregated time series of precipitation rates (mm day^{-1}; day is abbreviated by d in figures) based on daily values and discarded months where less than 90% of the records were available. To ensure a correct reconstruction of the seasonal cycle at each station, we discarded the stations that did not include at least three valid months of each calendar month during the decade. After this filtering, 31 stations are left, of which 26 provide a gap-free time series, four contain a 1-month gap, and one has 51 valid months. The weather stations are not homogeneously distributed over the study region (Fig. 1), since they lie in more densely populated regions in the southern and eastern parts of the TP. In fact, some climatic precipitation regimes are not represented by this station population. To compare gridded precipitation data with the rain gauges, the nearest grid point is taken without interpolation (other interpolation methods—bilinear and cubic—did not change the results significantly). We use standard skill scores statistics for the assessment: mean deviation (MD; or mean bias), mean absolute deviation (MAD), and Pearson correlation coefficient r. For the daily precipitation occurrence statistics we use the Heidke skill score (HSS; Wilks 1995), computed from a contingency table (MA11, their Table 2). The HSS can only evaluate the detection or nondetection of discrete events; therefore, the tested events are defined as follows: precipitation exceeds a threshold T. The HSS indicates the capability of a simulation to be better or worse than a random simulation and ranges from -1 to 1 (1 for a perfect simulation and 0 for a random guess).

b. TRMM precipitation

Because of the uneven spatial distribution of the stations, we also compare the HAR precipitation output to precipitation estimates from the Tropical Rainfall Measuring Mission (TRMM). The TRMM precipitation estimates are derived from a combination of remote sensing observations calibrated against a large number of rain gauges on a monthly basis. In this study, the 3B42 (daily) and 3B43 (monthly) version 7 products are used (Huffman et al. 2007). The TRMM dataset covers the regions between 50°N and 50°S with a spatial resolution of 0.25°. It has been previously used to study convective activity on the TP (Yaodong et al. 2008) and in northern India (Medina et al. 2010), to study the diurnal cycle of precipitation over the TP (Zhou et al. 2008), and to validate atmospheric modeling studies (Chow and Chan 2009; MA11). The resolution of the TRMM 3B43 product (~28 km) allows a quantitative evaluation of HAR30 precipitation only.

As indicated by its name, TRMM was primarily designed for measuring tropical (i.e.: convective) rainfall. It has been shown that its accuracy on the TP is affected by sampling problems because of low grid resolution (Bookhagen and Strecker 2008; Yin et al. 2008). The authors of the latter study emphasize that TRMM performs poorly during winter, because of the presence of snow and ice over the TP (snow and ice on the ground scatter microwave energy in a similar fashion as ice crystals and raindrops in the atmosphere). Therefore, TRMM estimates in winter and more generally over the TP region should be analyzed with care.

Additionally, we used the 1998–2009 rainfall climatologies from Bookhagen and Burbank (2010). This dataset is processed from the TRMM 2B31 product and is a rainfall estimate at higher resolution than the TRMM 3B43 product (~5 km). Only the mean decadal climatologies are freely available, and they are computed for a slightly different period than the decade we consider. Therefore, we use the TRMM 2B31 dataset to qualitatively compare orographic precipitation with the HAR10 precipitation product.

4. Results and discussion

a. Seasonal climatologies at the synoptic scale

An overview of DJF and JJA climatologies derived from HAR30 is provided in Fig. 2. In DJF (left panel), a geopotential height (GPH) gradient produces strong westerly winds (Figs. 2c,e) over much of the domain (the GPH maximum, hidden by the color scale, is located at ~13°N). The winter monsoonal land to sea breeze (e.g., Qian and Lee 2000) characterizes the surface wind regime in the tropics (Arabian Sea, Bay of Bengal, and South China Sea; Fig. 2a). On the TP the westerlies dominate while in the north, surface winds are heterogeneous. The DJF season is mostly dry (Fig. 2a): precipitation occurs over land 1) in central Asia and western TP as a result of the orographic uplift of the westerly flow, 2) at coastal areas under moist sea-breeze flow (e.g., Vietnam, Malaysia, Sri Lanka), and 3) in southern China.

In JJA, the core Asian summer monsoons (ASM) season, the circulation patterns change dramatically.

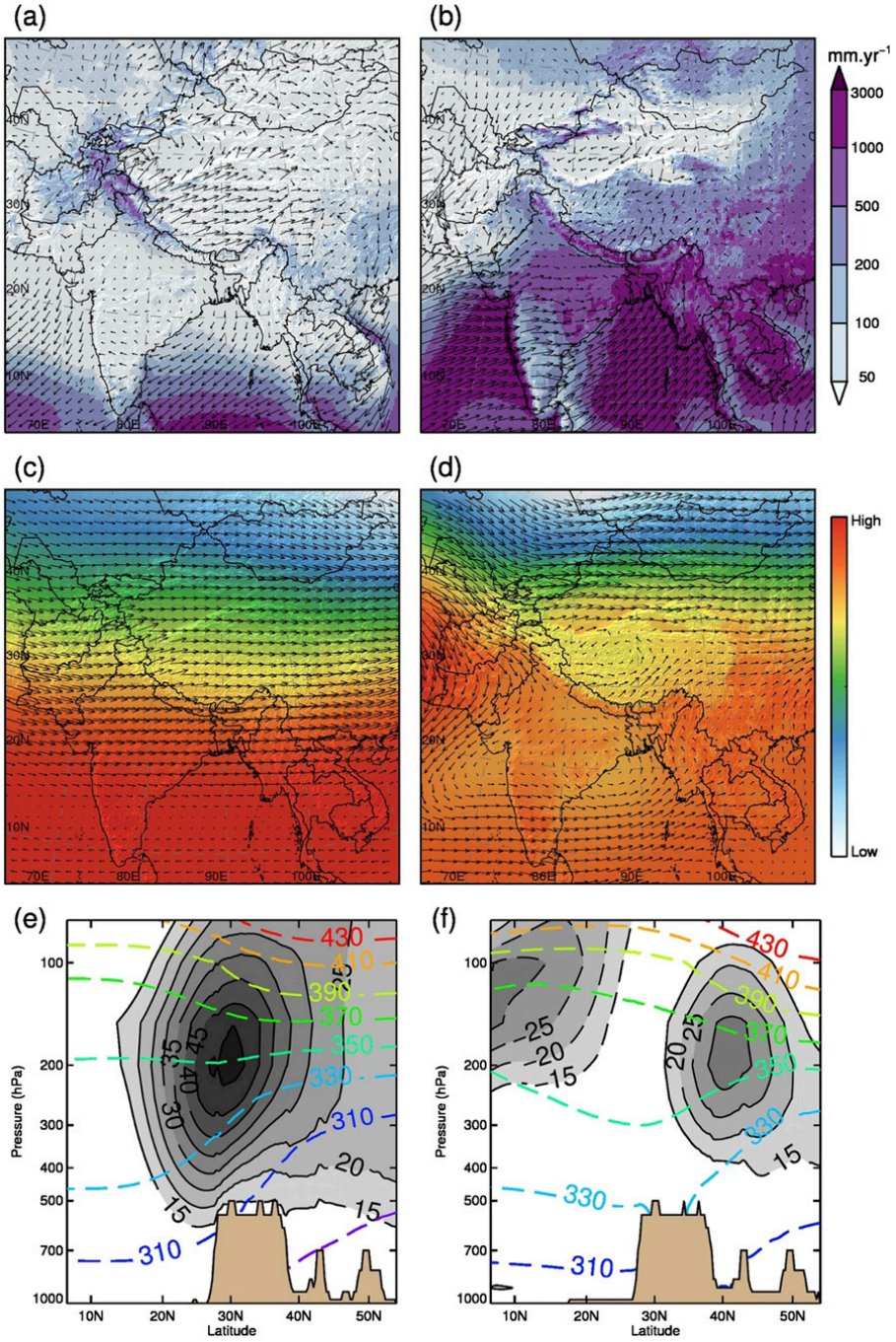

FIG. 2. Decadal (2001–11) seasonal means in the HAR30 dataset for (left) DJF and (right) JJA. (a),(b) Total precipitation and 10-m wind vectors (every fifth grid point). (c),(d) Geopotential height and horizontal wind vectors at the 500-hPa level. Note that the color scale represents a different range for winter (low: 5.24 km; high: 5.89 km) and summer (low: 5.67 km; high: 5.90 km). (e),(f) Horizontal wind speed ($m\,s^{-1}$; gray shades) and potential temperature (K; dashed color contours) along a latitude–pressure transect at 90°E. Dashed gray contours represent negative zonal wind.

The reversal of surface winds over oceans and coasts is characteristic of the monsoonal climate (Fig. 2b). The westerly flow is weaker and the main jet axis is shifted to the north (40°N; Fig. 2f) as a result of the summer hemisphere heating. Simultaneously, the tropical easterly jet forms in the upper troposphere. The warmest air in the free atmosphere is now located south of the TP as evident from the potential temperature field, as a result of both surface and convective heating. Two midtroposphere low pressure systems characterize the mean

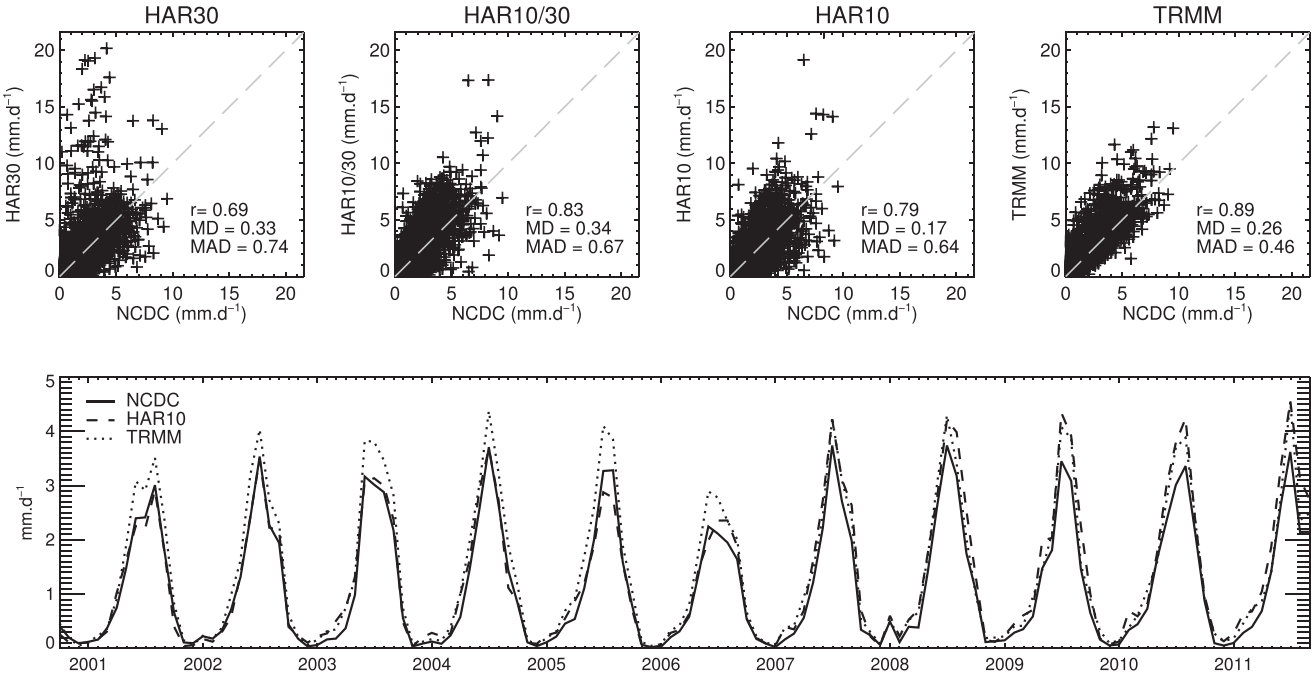

FIG. 3. Comparison of monthly precipitation rates (mm day^{-1}; 2001–11) with NCDC stations observations (31 stations; 4007 valid months). (top) Scatterplots of HAR30, HAR10/30, HAR10, and TRMM 3B43 and statistical scores r, MD (mm day^{-1}), and MAD (mm day^{-1}). HAR10/30 is constructed by spatially averaging HAR10 on the HAR30 grid. (bottom) Monthly precipitation time series (mm day^{-1}) averaged for all stations.

atmospheric circulation patterns at 500 hPa (Fig. 2d; Wang 2006): the monsoonal depression over India (which extends from the surface up to ~400 hPa) and the thermal low over the TP (confined to the TP boundary layer). Surface winds over the TP and partly over India follow the 500-hPa flow, with the exception of the Arabian Sea where surface winds are flowing in the opposite direction (they follow the Somali jet at ~850 hPa; not shown). The combined blocking effects of topography and of the Tibetan low seem to divide the 500-hPa westerly flow reaching the TP in a south and north stream. As a result of the ASM circulation, precipitation is observed at the Indian southwest coast, in Bangladesh, in the Indochinese peninsula, and in southeast China (Fig. 2b). The blocking effect of the Himalayas on the low-level atmospheric flow is clearly visible, as well as the orographically induced precipitation spells at the mountain ridges. The Pamir and Karakoram mountain ranges are mostly dry, but the Tien Shan is wetter than in DJF.

b. Comparison with observations

1) MONTHLY PRECIPITATION

We compare HAR and TRMM monthly precipitation with station observations in Fig. 3. The top panel shows the scatterplots and skill statistics for all stations and months. The results indicate an improvement between HAR30 and HAR10, as the former tends to overestimate precipitation and shows larger scatter. This confirms the findings of MA11 and other studies (e.g., Heikkila et al. 2011) that demonstrated the positive effect of higher resolution in complex terrain on simulated precipitation. The added value of higher resolution is also evident when spatially averaging the HAR10 dataset on the HAR30 grid (HAR10/30). The HAR10/30 still shows an improvement to HAR30 and has even slightly better correlation values than HAR10, while the other HAR10 scores remain better. The TRMM 3B43 product better explains the variance at the stations (higher correlation and lower MAD) but has a larger positive bias (MD).

Precipitation seasonality and interannual variability is well reproduced by the HAR (Fig. 3, bottom panel). Anomalous events on the TP, such as the driest year 2006 or the wet winter of 2008, are well represented. For the averaged time series, HAR10 is closer to observations than the TRMM 3B43 product (MD of 0.089 and 0.26 mm day^{-1} and MAD of 0.23 and 0.26 mm day^{-1}, respectively). However, the HAR diverges from the station data after 2007 in the summer months. The reasons for the disagreement are unclear, but the shift could be related to changes in the FNL assimilation system that occurred in 2007 (K. Manning 2013, personal communication). We compared HAR30 with the TRMM 3B43 product over the HAR30 domain and

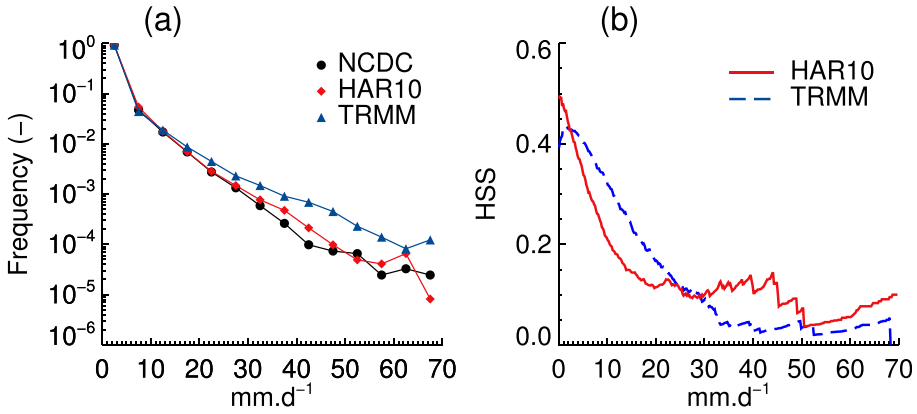

FIG. 4. (a) Histograms of daily precipitation amounts in the NCDC stations, HAR10, and TRMM data (note the logarithmic scale of the *y* axis) and (b) HSS for daily precipitation.

found that the statistical metrics are regular and constant throughout the decade, and no singularities could be detected (see Fig. S7 in the supplemental material). Similarly, we reproduced the analysis presented in Fig. 3 for all stations available in HAR10 (not only on the TP, thus doubling the number of stations) and found that (i) the updated scores confirms the results of Fig. 3 and (ii) the period 2007–11 does not appear to be singular (Fig. S8). Therefore, we argue that this shift either is only occurring on the TP or is an artefact resulting from the small number of stations used for the validation.

In Fig. S9 of the supplemental material, we present further validation analysis, this time by considering the mean seasonal cycle at each station location. Most stations have a characteristic summer precipitation regime but there are variations in both shape and magnitude that are captured by the HAR. It is worth noting that both TRMM and HAR show inconsistent deviations (positive or negative) at stations located close to each other. Since both datasets are produced with a spatially consistent methodology, these discrepancies are probably related to spatial sampling problems.

2) DAILY PRECIPITATION

One of the key objectives of the regional reanalysis is to represent past weather and therefore to be able to trace precipitation events (see MA11 for a day-by-day analysis of a severe precipitation event on the TP). Figure 4a shows the histograms of daily mean precipitation at the station locations for HAR10 and TRMM 3B42. The three histograms are close to each other for lower precipitation amounts (about 92% of all days are found in the 0–5 mm day^{-1} bin), but TRMM 3B42 overestimates the frequency of higher precipitation amounts (Zhou et al. 2008 also report that TRMM overestimates the frequency of precipitation in the diurnal variation). The HAR10 histogram is close to the stations, even for the extreme events. The HSSs of TRMM 3B42 and HAR10 are displayed in Fig. 4b. The HAR is closer to the stations for small thresholds, a feature that could be a result of the known problems of TRMM in detecting small raindrops and other issues related to irregular satellite overpasses (Kidd and Levizzani 2011). The HSSs decay rapidly for larger thresholds and faster for HAR10 than for TRMM 3B42. For higher amounts HAR10 performs better again, in accordance with the histograms presented in Fig. 4a.

c. *Precipitation over the TP and orography*

Figure 5a shows the decadal mean of HAR10 annual precipitation over the TP. There are large regional contrasts, from less than 50 mm yr^{-1} in the Tarim basin to more than 6000 mm yr^{-1} (35 grid points) in the southeast Himalayan foothills. As shown in Fig. 2b, the moist flow originating in Bay of Bengal is blocked by the Himalayas and redirected northwest following the range, generating an east–west precipitation gradient. The uplift caused by the Himalayan range generates an orographically induced "precipitation barrier," leaving the regions north of the range with drier air masses and less precipitation. On the TP, there is a clear southeast–northwest gradient, which is often attributed to the fact that most of the moisture is transported from the southeast by the monsoonal flow (e.g., Feng and Zhou 2012).

For completeness, we plotted TRMM 3B43 mean precipitation for the same period (Fig. 5b) and the 1998–2008 rainfall decadal mean from TRMM 2B31 (Fig. 5c). Similar features are observable in all three datasets: for example, the location of precipitation maxima, the gradients, the precipitation belt along the Himalayas, and the dry Tarim and Qaidam basins. However, HAR10 and TRMM 2B31 are more in agreement for detailed patterns such as the dry spell in the lee side of the

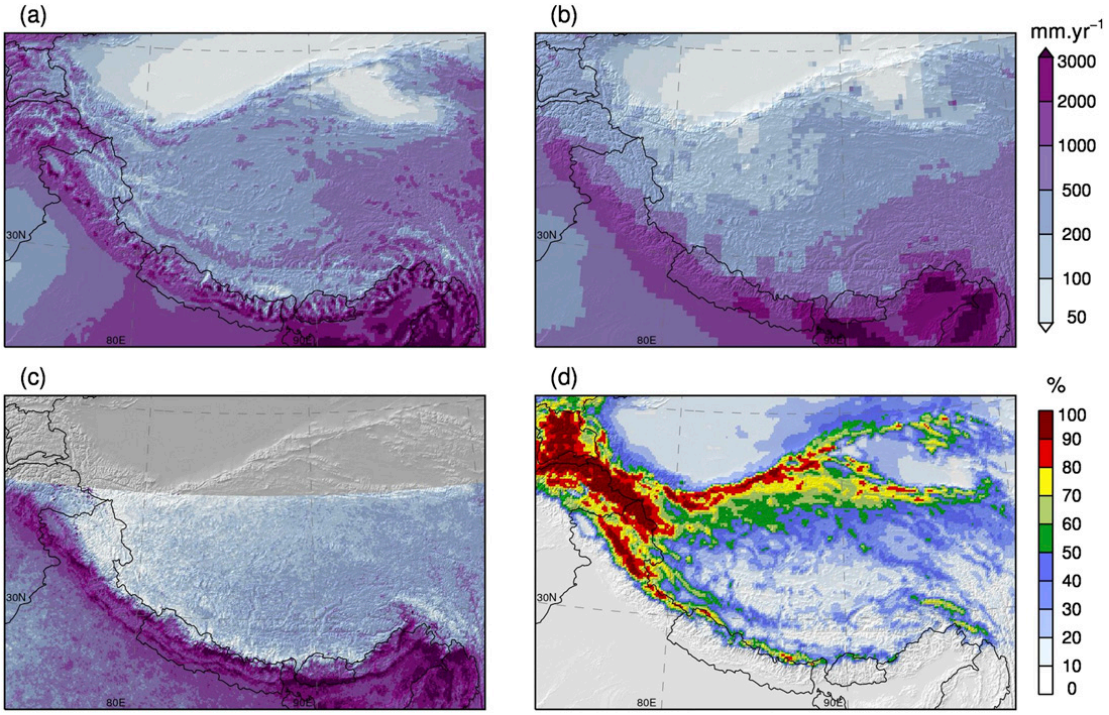

FIG. 5. Decadal means of annual precipitation for (a) HAR10 and (b) TRMM 3B43, (c) annual rainfall for TRMM 2B31, and (d) percentage of HAR10 precipitation falling as snow. Note that the decadal mean for TRMM 2B31 (1998–2008) covers a different period than HAR10 and TRMM 3B43 (2001–11).

Himalayas. The influence of orography is less pronounced in TRMM 3B43 on the TP, while it plays an obvious role in triggering precipitation in TRMM 2B31 and HAR10. The largest differences at regional scale between HAR10 and TRMM 3B43 are found in the Pamir and Karakoram regions and in northwestern Tibet. These regions experience mostly winter precipitation (Fig. 2a), with the majority falling as snow (Fig. 5d). The regions with large snowfall contribution to the total precipitation are the high mountains and the northwestern part of the TP, where temperatures are lower.

Interestingly, regions with larger discrepancies between TRMM and HAR10 correspond to areas with higher snowfall percentages. This is corroborated in Fig. 6, which shows the relative difference between TRMM 3B43 and HAR10 plotted against snowfall contribution at each grid point. There is a clear relationship between precipitation difference and snowfall, which is consistent with results of previous studies of possible TRMM detection errors of frozen precipitation (e.g., Yin et al. 2008). Although it is generally difficult to quantify the accuracy of the HAR snowfall data, there is support from studies in high mountains that the WRF model is able to reproduce observations (e.g., Mölg and Kaser 2011; Mölg and Scherer 2012). We repeat the analysis of Mölg and Scherer (2012) at one station location where snowfall information was available (Fig. S10 in the supplemental material) and found that the HAR captures well the phase of the precipitation compared with observations.

Bookhagen and Burbank (2010) suggested that two topographic classes can be defined along the Himalayas: either (i) the mean topography rises more or less steadily to an average elevation of 5 km (one-step topography) or (ii) it follows a two-step morphology in which the

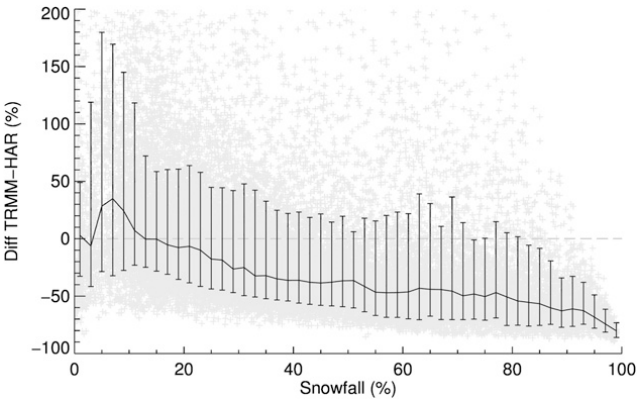

FIG. 6. Relative difference in annual precipitation between TRMM 3B43 and HAR10 with HAR10 as reference, as a function of annual snowfall fraction (%) in the HAR data. Each gray point represents one data point, and the curve represents 2%-wide binned median with 10% and 90% percentiles as error bars.

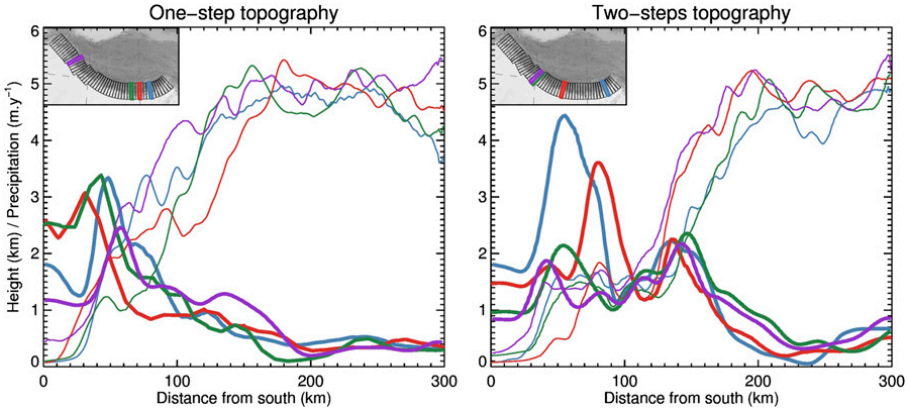

FIG. 7. Mean annual precipitation from HAR10 ($m\,yr^{-1}$; thick lines) and 30-km Shuttle Radar Topography Mission (SRTM30) topography (km; thin lines) along four 50-km-wide and 300-km-long south–north swaths. The swaths locations are indicated in the inset maps [swaths from Bookhagen and Burbank (2010)].

outer step corresponds to the Lesser Himalayas and the inner step to the Higher (Greater) Himalayas. The authors showed that precipitation in TRMM 2B31 mimics these two classes of topographic profiles. Such patterns are expected and known from the underlying processes of mountain–airflow interactions (e.g., Colle 2008). To evaluate HAR10 precipitation in this context, we computed the mean transect precipitation along several profiles and show examples of the two classes in Fig. 7. The HAR precipitation profiles follow similar features as the profiles in Bookhagen and Burbank (2010, their Fig. 7) but seem to slightly underestimate precipitation maxima, perhaps because of the coarser resolution of the HAR. This analysis underlines the importance of topography and snowfall for precipitation patterns on the TP and the added value of high-resolution modeling in this region.

Altogether, these results give confidence in the accuracy of the HAR with respect to the requirements of this study and indicate that it is free of a systematic precipitation error. Previous studies reported that the WRF model overestimates precipitation in mountainous terrain (e.g., Caldwell et al. 2009), but we find no evidence for this. Area averaged over the whole HAR10 domain, the model produces 15% more precipitation than TRMM 3B43 (734 versus 636 mm yr^{-1}, respectively), which we assume to be partly related to problems of TRMM snowfall retrievals.

d. Precipitation timing and seasonality on the TP

Figure 8 shows the contribution of each season to annual precipitation during the last decade. The Karakoram and Pamir regions form one coherent unit, with most precipitation falling in DJF and MAM and almost no precipitation in JJA. Precipitation in MAM shows two bands (north and south of the TP), indicating that these two spells have different origins. Most precipitation in the domain falls in JJA, especially in India and central TP but also in the northeasterly Qilian Mountains. In SON the patterns are fairly uniform, representing 10%–20% of the annual precipitation.

We analyze the seasonal cycle of precipitation in Fig. 9, this time by showing the contribution of each month to the annual precipitation, together with mean horizontal wind vectors at the 500-hPa level. With a height of approximately 5700 m, this level is a good indicator for the TP boundary layer flow. We start the description of the annual cycle in October, beginning of the hydrological year and end of the monsoon period. Low precipitation occurs in the southeast of the domain, and the winter precipitation season in the northwestern TP is starting. The seasonal cycle of precipitation in the northwest is tied to the location of the jet stream (Schiemann et al. 2008). Moisture is brought by southwesterly cyclones from the east of the Mediterranean and the Arabic Sea but under the stable winter conditions precipitation is mostly triggered by orography (e.g., Jiang 2003). From November to March, the 500-hPa zonal flow is constant and hardly perturbed by the mountains. The maximal winter precipitation intensity is reached in February. In March, the westerly jet starts to shift to the north, marking the beginning of the precipitation season in northern TP, which culminates in May–June. The first disturbances of the winter zonal flow occur in April, and the first indications for the formation of the Tibetan low appear in May. The center of this cyclonic system is not located in the south of the TP as one might expect because of stronger solar heating. Its location could be related to a combination of thermal and dynamical effects (Sugimoto and Ueno 2010).

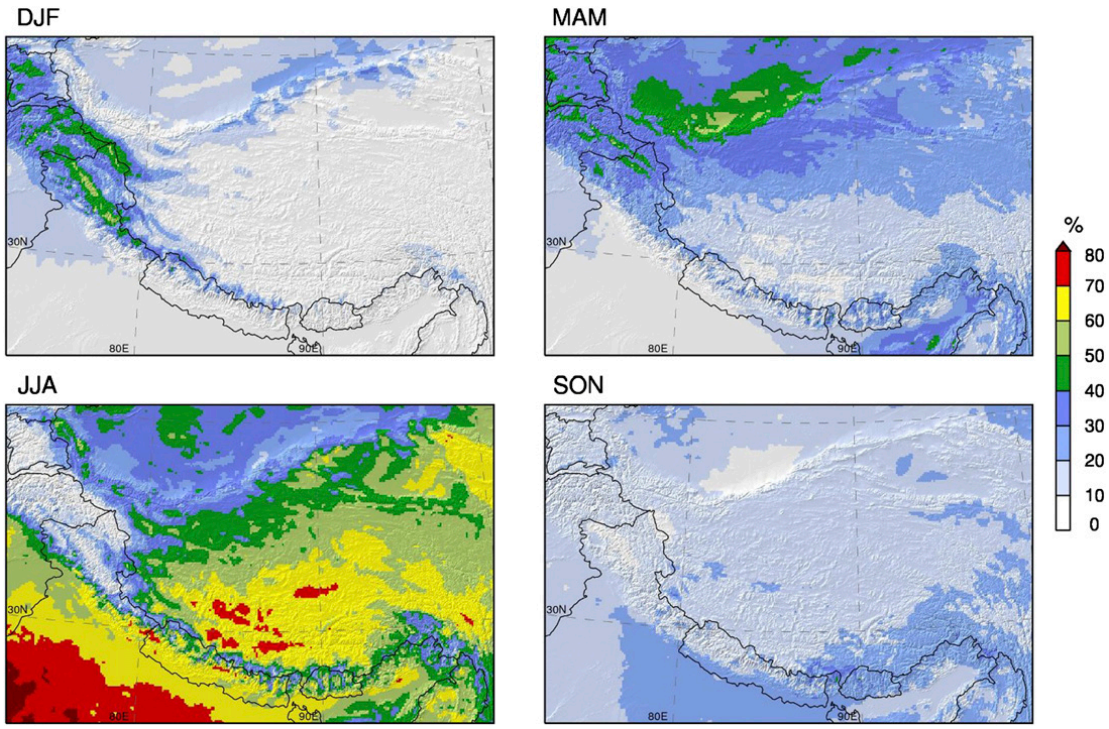

FIG. 8. Contribution (%) of DJF, MAM, JJA, and SON to the HAR10 mean annual precipitation.

The cyclonic circulation on the plateau is established months before the monsoonal circulation, characterized by a reversal of the flow south of the Himalayas. The circulation patterns on the TP during the transition phase (May–June) suggest a combined influence of southerly and westerly flows on precipitation on the TP. The circulation conditions remain stable in July and August, and the wet spell on the TP originates from its southern and eastern parts. There is an abrupt transition between the dry Pamir–Karakoram region and the wetter Pakistan lowlands. Finally, in September the Tibetan low decays and the remainder of the summer precipitation is evenly distributed over the TP.

e. *Precipitation frequency and role of convective precipitation*

Figure 10a shows the average number of precipitation days (>1 mm day^{-1}) per hydrological year. The number of precipitation days is related to precipitation amounts (cf. Fig. 5a), but this relationship is neither constant nor linear, as shown in Fig. 10c. As indicator for the occurrence of strong precipitation events, we count the smallest number of precipitation days needed to reach 50% of the yearly precipitation amounts (on average) and we divide it by the number of precipitation days shown in Fig. 10a to obtain Fig. 10b. A location with constant and regular precipitation days will then have a value of 50%, and a location with mostly light precipitation days but with a few strong precipitation events will have a lower value. We see in Fig. 10c that the number of days needed to reach 50% of the yearly precipitation is less dependent on the precipitation amount than precipitation frequency: it quickly reaches a value of approximately 25 days.

Most locations subject to strong precipitation events are located south of the TP. The most critical regions (where less than 15% of the precipitation days suffice to reach 50% of the annual precipitation amount) are not located in northeastern India, where most precipitation occurs, but in Pakistan and northwestern India, regions known to have experienced severe floods in the last decade (Webster et al. 2011) or cloud bursts (Kumar et al. 2012). On the plateau, Figs. 10a and 10b indicate less strong but more frequent precipitation events, in accordance with observational studies that documented the regularity of summer precipitation in central TP (Ueno et al. 2001) and a pronounced diurnal cycle related to frequent local convective activity (Liu et al. 2009).

The contribution of convective precipitation as diagnosed by the model physics to the annual precipitation is shown in Fig. 11. Precipitation is mostly convective in India, in the south ridge of the Himalayas and in large valleys, but barely any convection is triggered in higher mountains and in areas with frequent snowfall. Another large area of convective precipitation is found in central TP, in accordance with the results of several studies (e.g., Fu et al. 2006). Interestingly, the location of the center of the summer low pressure system on the TP (Fig. 9) does not match with the maximum occurrence

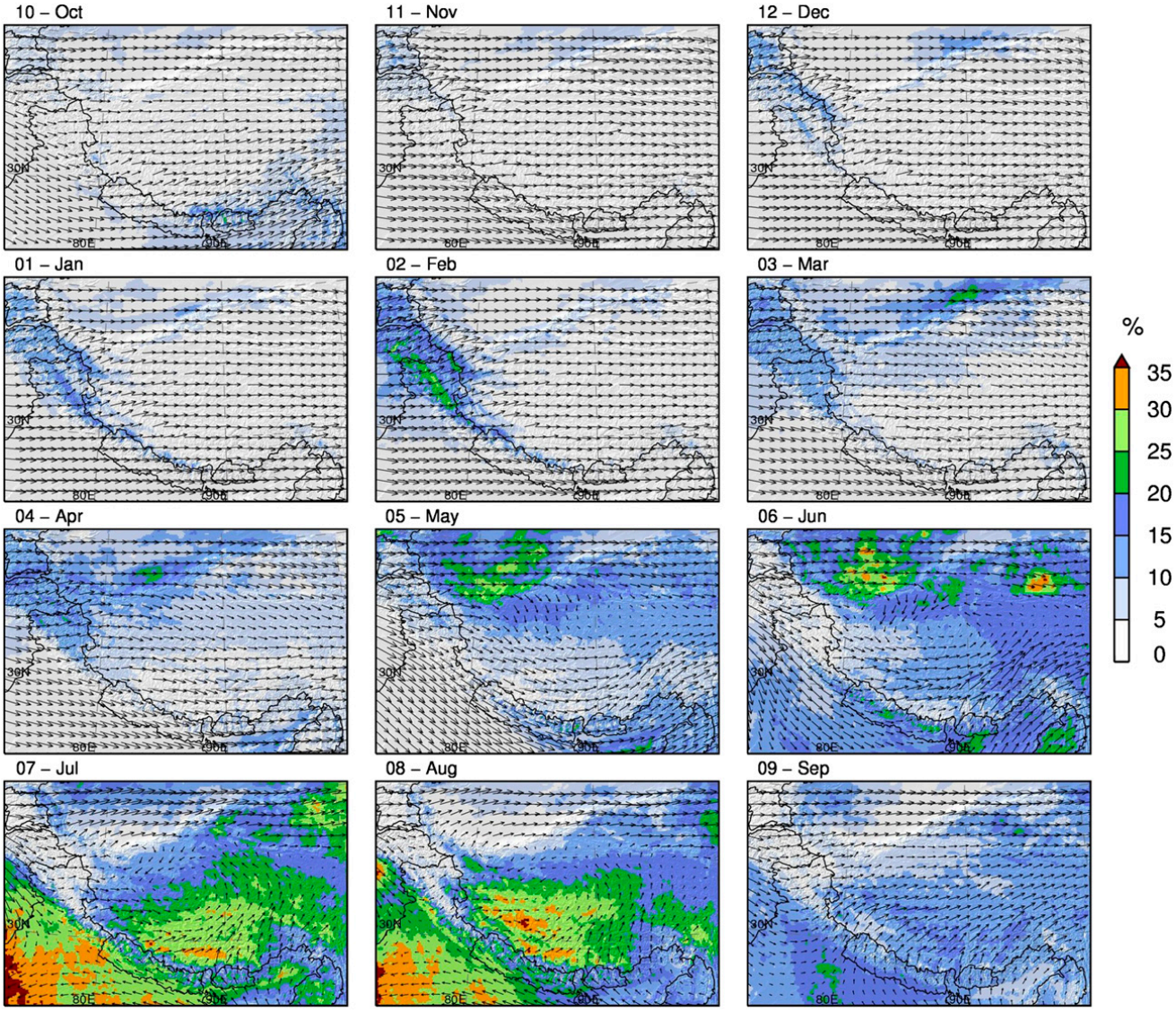

FIG. 9. Contribution (%) of each month to the HAR10 mean annual precipitation and mean monthly 500-hPa wind vectors (plotted every eighth grid point).

of convective precipitation, which is located more to the south. The location of the two areas of convective precipitation in Fig. 11 (central and eastern TP) matches well observations by Sugimoto and Ueno (2010, their Fig. 1).

f. Precipitation interannual variability

In addition to precipitation amount and regime, the variability of precipitation is important in characterizing a region's hydrological features. In Fig. 12, we describe interannual variability during the last decade considering hydrological years. We use the coefficient of variation c_v of annual precipitation, which is defined as the ratio between the standard deviation and the mean of precipitation. This metric provides more useful information than the standard deviation alone, since the latter is strongly related to precipitation amounts. The c_v is high in western and central TP and in northwestern India and is rather low in elevated areas and in the east (Fig. 12a). The relationship between the c_v and annual precipitation is shown in Fig. 12b. The c_v is, on average, only slightly related to precipitation for high amounts but much more for small amounts (e.g., Tarim and Qaidam basins). As proposed by Jurković and Pasarić (2013) based on the earlier work of Conrad (1941), we define the theoretical expected c_v as a decreasing hyperbolic function,

$$ec_v = \frac{B}{\overline{P} + C} + A, \tag{1}$$

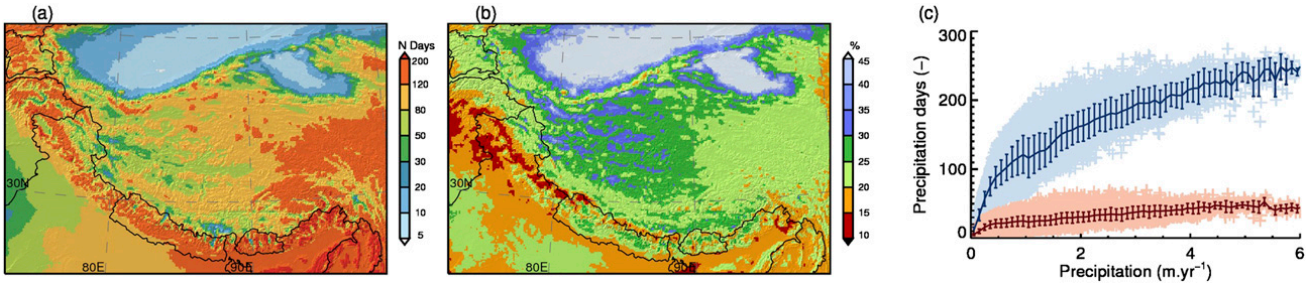

FIG. 10. Precipitation frequency and occurrence of large precipitation events. (a) Average number of precipitation days (>1 mm day^{-1}) per hydrological year (October–September). (b) Ratio (%) between the average number of days needed to reach 50% of the annual precipitation amount and the number of precipitation days per year. (c) Number of precipitation days (blue) and number of precipitation days needed to reach 50% of the annual precipitation amount (red) vs mean annual precipitation. The curves represent 0.1-m-wide binned means with $\pm 1\sigma$ error bars.

where $\overline{P}$ is the mean annual precipitation and A, B, and C are parameters to be obtained by least squares fitting. We obtain 17.17% for A, 5.99 m yr^{-1} for B, and 0.10 m yr^{-1} for C. Our constant A (representative of ec_v for high precipitation amounts) is similar to the one from Jurković and Pasarić (2013) of 15.37%. Unlike Jurković and Pasarić (2013), who computed ec_v for the whole globe, our ec_v is representative for the HAR10 region only. We use this theoretical curve to compute the c_v anomaly $c_v a$, which is defined as the difference between the c_v and the ec_v at each grid point. The resulting purple (brown) areas in Fig. 12c correspond to areas with higher (lesser) variability than "expected" in the domain. For instance, it appears that the relatively dry Qaidam basin has a high c_v but a negative $c_v a$, which means that it has a smaller interannual variability than expected from the annual precipitation amounts. Northwestern India and Pakistan show the strongest positive $c_v a$ (these regions correspond to the positive difference between the binned mean curve and the ec_v around 1 m yr^{-1} in Fig. 12b). The central and western TP also show more interannual variability than their neighboring TP areas.

In Fig. 13, we reproduce the analysis for the three precipitation seasons, DJF, MAM, and JJA. Precipitation in DJF has a spatially regular interannual variability, of about 20%–25%. The areas with higher variability are located at the southern edges of the Karakoram, where the influences of western disturbances that drive winter precipitation may be less continuous in this season. In MAM, the highest interannual variability is observable in the northwestern Tarim basin and, importantly, in the southeastern Himalayas (here the variability of the Indian summer monsoon onset probably accounts for a larger than average interannual variability of precipitation). The patterns of c_v and $c_v a$ in JJA resemble those of annual precipitation (Fig. 12c), which means that most of precipitation interannual variability is explained by summer precipitation variability.

5. An application example: Classification of glacier accumulation regimes

As discussed in the introduction, the TP hydrological cycle is strongly dependent on precipitation amounts and on seasonality. The works by Fujita (2008) and Mölg et al. (2012) emphasized the high sensitivity of glaciers on the TP to precipitation seasonality. Shi and Liu (2000) proposed a classification of the glaciers on the TP according to their continentality (maritime, subcontinental, and continental). Rupper and Roe (2008) proposed another grouping into three classes (western, eastern, and northern) according to the differences in spatial and temporal variability of the glaciers during the last glacial cycle.

In Fig. 14, we further propose a new classification based on precipitation seasonality, computed using an objective clustering approach. We used k-means clustering (e.g., Wilks 1995) to define five distinct classes that we named after the characteristics of their cluster centers. We recognize two dominant classes with winter (DJF) and summer (JJA) accumulation types and a third class with less elements having the maximum precipitation in MAM. Finally, we named two intermediate classes

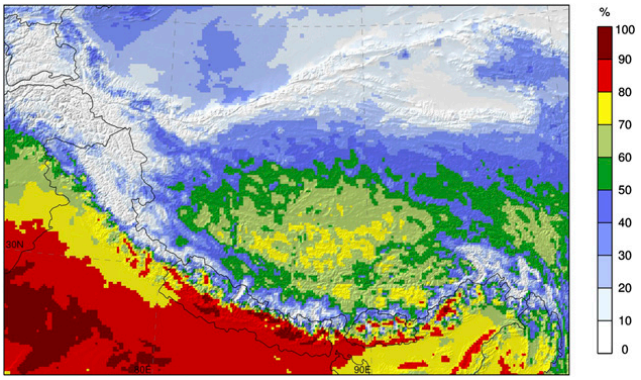

FIG. 11. Contribution (%) of convective precipitation to the total annual precipitation.

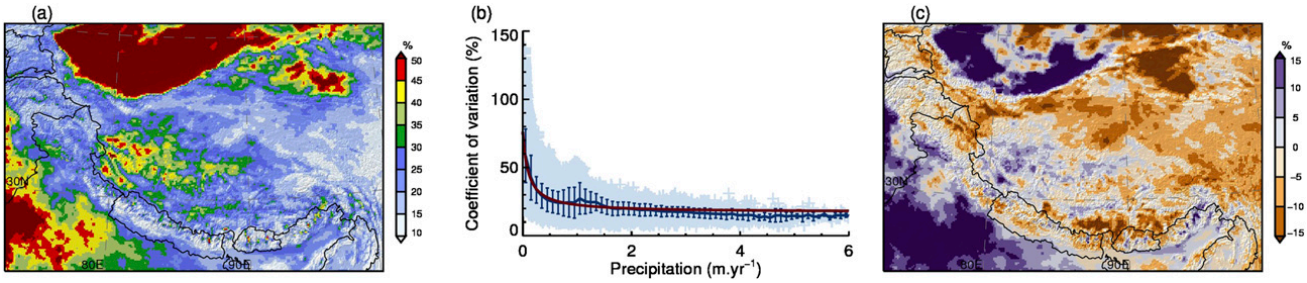

FIG. 12. Precipitation interannual variability for the 11 hydrological years (October 2000–September 2011). (a) Coefficient of variation (%) of annual precipitation. (b) Coefficient of variation vs annual precipitation. The blue curve represents 0.1-m-wide binned means with $\pm 1\sigma$ error bars. The red curve is the expected coefficient of variation obtained by fitting a hyperbolic curve to the data points [Eq. (1)]. (c) Anomaly of the coefficient of variation, defined as the difference between the coefficient of variation and the expected coefficient [red curve in (b)].

that tend to experience either winter (MAM/DJF) or summer (MAM/JJA) precipitation but with less pronounced centers. The mean seasonal cycles of each class are presented in Fig. 15. We recognize the three peaks of the DJF, MAM, and JJA classes and see that the two remaining classes have a less pronounced seasonality but different tendencies (MAM/DJF displays a February precipitation peak and precipitation almost all year-round; MAM/JJA experiences precipitation in MAM and JJA but less in winter). All classes but DJF have their minimum in November–December, while the DJF class has a minimum in June–July.

One striking feature is the clear difference between DJF (west) and JJA (central TP) regimes. The MAM cluster is mostly located in northern TP but a few glaciers can be found in southeast TP, together with a large region of mixed type glaciers, which correspond to the "maritime zone" defined by Shi and Liu (2000) or the "spring-accumulation type" zone proposed by Yang et al. (2013). Along the Himalayan range, we find glaciers of varying types over very short distances, which can be explained by the variability of precipitation regimes in the Himalayas. For example, Kansakar et al. (2004) identified as many as four different precipitation regimes for Nepal alone. The orientation of the glaciers and their location on the windward or lee side of the range also play a significant role, illustrating the importance of high spatial resolution in determining climatic influences on glaciers.

6. Conclusions

The TP precipitation regime is influenced by both the westerlies and the monsoons, as well as their interplay.

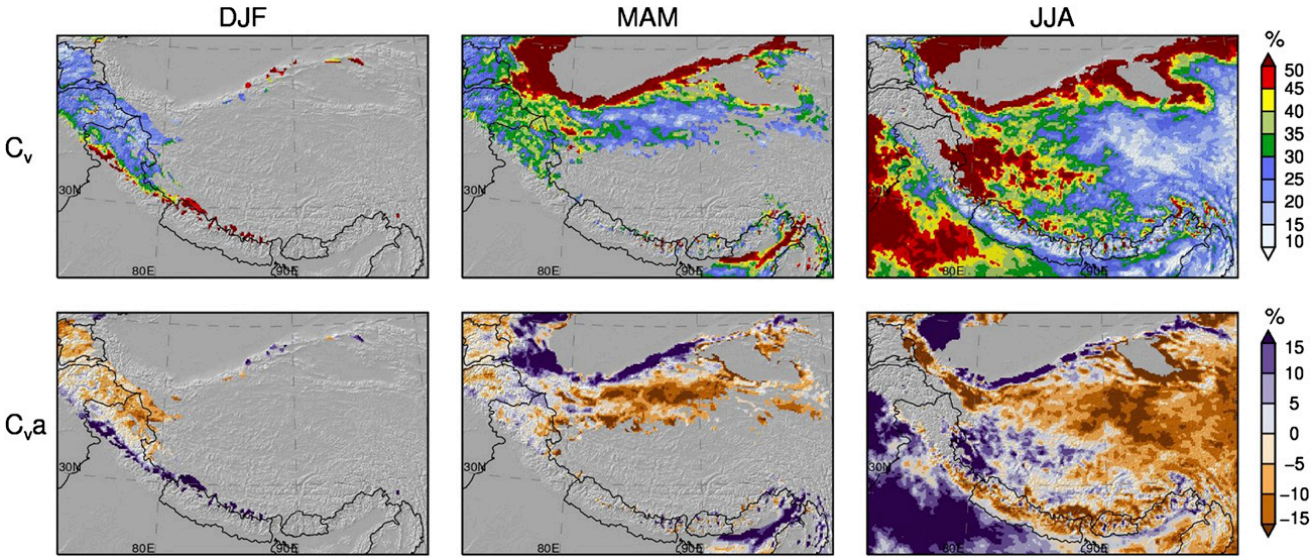

FIG. 13. Seasonal precipitation interannual variability for the 11 hydrological years (October 2000–September 2011). Coefficient of variation c_v and anomaly of the coefficient of variation c_va are shown, areas (i) where less than 25% of the annual precipitation occurs in the considered season and (ii) with less than 25-mm average seasonal precipitation are masked in gray. Precipitation in SON is too low and not presented here.

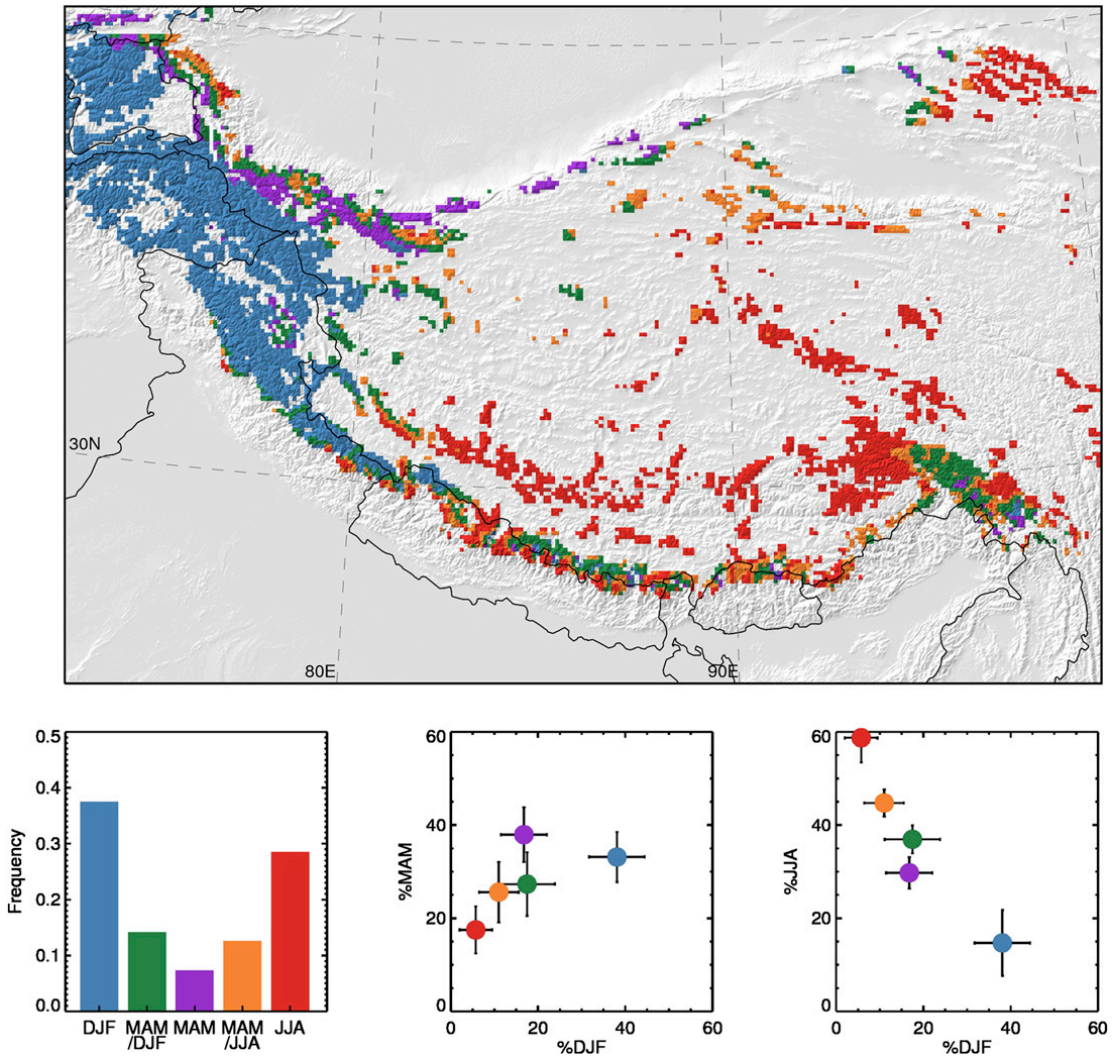

FIG. 14. Classification of glacier accumulation regimes according to precipitation seasonality. A *k*-means clustering algorithm is run on three input variables (percentage of precipitation falling in DJF, MAM, and JJA) and with five output clusters. We focus on glacierized grid points only. (bottom left) Histogram plot showing the relative occurrence of each class in the map with the color legend is described below. (bottom center),(bottom right) The clusters are named after their cluster centers characteristics. Since SON is a linear combination of the three other variables, it was not included in the clustering procedure.

The circulation dynamics create a complex puzzle for geophysicists or palaeoclimatologists attempting to reconstruct and understand the signals in various climate proxies. Furthermore, this task is made more difficult by our incomplete understanding of the present-day climate dynamics (e.g., Molnar et al. 2010). In this study, we did not attempt to explain and unravel all processes that drive precipitation on the TP, but we described the observed patterns and gave a framework for a better understanding of spatial and temporal variability. We showed that dynamical downscaling approaches like the HAR provide a way to resolve the full process chain of synoptic to regional dynamics for features such as precipitation and can provide details that are not represented in coarser datasets.

A crucial step was the evaluation of HAR precipitation in section 4. We demonstrated an improvement when increasing horizontal resolution from 30 to 10 km, quantitatively (by comparing to observations) as well as qualitatively (in the reproduction of documented orographic precipitation features). Further qualitative indices consolidated our confidence in the reliability of the HAR: for example, its realistic reproduction of both (i) the known relationship between the coefficient of variation and precipitation and (ii) the documented characteristics of precipitation on the TP (weak, frequent, and convective precipitation events). However, these considerations are qualitative and do not allow us to provide a quantitative uncertainty value of the HAR precipitation outputs. In this regard, integrated

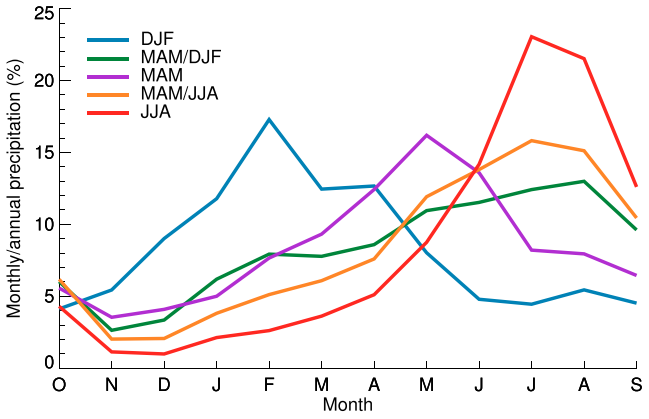

FIG. 15. Mean contribution of each month to annual precipitation for the five glacier clusters defined in Fig. 13.

approaches such as hydrological or glaciological modeling will aid evaluation at the basin scale. Furthermore, since validation and benchmarking are made difficult by scarce and imperfect observations, the new global precipitation measurement (GPM) system (Hou et al. 2014) or innovative cloud detection algorithms (Rüthrich et al. 2013) may help to improve the validation in the future.

In general, the annual cycle of precipitation on the TP is characterized by a winter precipitation regime in the west, a spring precipitation regime in northern and southern TP, and a summer precipitation regime elsewhere. This led some authors such as Shi (2002) to define the drivers of precipitation according to precipitation seasonality. In Fig. 1 of Shi (2002), the author draws a line along a southwest–northeast diagonal on the TP, symbolizing the limit between ''monsoonal precipitation'' and ''westerly precipitation.'' The use of these designations is interpreting ''synchronicity'' as ''causality.'' Our results do not contradict this view, as shown by the large domination of summertime precipitation on the TP. However, with a closer look at the seasonal cycle of precipitation on a monthly basis, we obtain more complex patterns than commonly assumed, especially on the central and northern TP, where spring precipitation represents a substantial part of the annual amounts. Recycling (moisture that originates and stays on the TP) could play a nonnegligible role in the TP hydrological cycle and should be quantified more precisely in the future. Recent studies that quantify moisture transport and provenance on the TP (e.g., Feng and Zhou 2012; Chen et al. 2012) focused on summer months and used atmospheric data from coarse-resolution global reanalysis. These studies could be complemented by similar approaches based on higher-resolution atmospheric datasets such as the HAR.

We identified regions with higher precipitation variability, either by analyzing the occurrence of strong precipitation events or by showing regional anomalies of the annual coefficient of variation. We see that both indicators are high for some regions: for example, in Pakistan and northwestern India. Located at the confluence zone of the westerly and monsoonal flows, this region may be more sensitive to variability of the synoptic atmospheric circulation. On the TP, precipitation days are of rather constant intensity during summer but the interannual variability in central and western TP is larger than in the neighboring TP regions. The drivers of interannual precipitation variability on the TP will be the subject of a future study.

Glaciers in different precipitation regimes will respond differently to changes in climate and shifts in precipitation seasonality. In this study, we proposed a new map of glacier accumulation regimes as one possible application for the HAR. Our analysis illustrates the high spatial variability of precipitation seasonality and provides a first approach for glacier energy and mass balance considerations. The map resulting from this cluster analysis emphasizes that glaciers on the TP cannot be considered as one entity with uniform mass balance sensitivity.

Acknowledgments. This work is supported by the German Federal Ministry of Education and Research (BMBF) Central Asia–Monsoon Dynamics and Geo-Ecosystems (CAME) program through the WET project (Variability and Trends in Water Balance Components of Benchmark Drainage Basins on the Tibetan Plateau) under the code 03G0804A and by the German Research Foundation (DFG) Priority Programme 1372, Tibetan Plateau: Formation–Climate–Ecosystems through the Dynamic Response of Glaciers on the Tibetan Plateau to Climate Change (DynRG-TiP) project under the codes SCHE 750/4-1, SCHE 750/4-2, and SCHE 750/4-3. Further support for TM came from the Alexander von Humboldt Foundation. We sincerely thank the developers of the WRF community model for providing such a comprehensive tool and B. Bookhagen for providing us the swaths locations and the TRMM 3B31 rainfall climatologies (available at http://www.geog.ucsb.edu/~bodo/TRMM/). All data analysis and graphics were realized with our own tools programmed in the IDL language and with the help of the Coyote IDL library. We made use of TRMM data provided by the GSFC DAAC and weather station data provided by the NCDC (available at http://www.ncdc.noaa.gov/oa/ncdc.html). We are grateful to three anonymous reviewers who made thoughtful comments and critics on an earlier version of this paper.

REFERENCES

Arendt, A., and Coauthors, 2012: Randolph glacier inventory [v1.0]: A dataset of global glacier outlines. Global Land Ice Measurements from Space Rep., 28 pp.

Bohner, J., 2006: General climatic controls and topoclimatic variations in Central and High Asia. *Boreas,* **35,** 279–295, doi:10.1111/j.1502-3885.2006.tb01158.x.

Bolch, T., and Coauthors, 2012: The state and fate of Himalayan glaciers. *Science,* **336,** 310–314, doi:10.1126/science.1215828.

Bookhagen, B., and M. R. Strecker, 2008: Orographic barriers, high-resolution TRMM rainfall, and relief variations along the eastern Andes. *Geophys. Res. Lett.,* **35,** L06403, doi:10.1029/2007GL032011.

——, and D. W. Burbank, 2010: Toward a complete Himalayan hydrological budget: Spatiotemporal distribution of snowmelt and rainfall and their impact on river discharge. *J. Geophys. Res.,* **115,** F03019, doi:10.1029/2009JF001426.

Box, J. E., and Coauthors, 2006: Greenland ice sheet surface mass balance variability (1988–2004) from calibrated Polar MM5 output. *J. Climate,* **19,** 2783–2800.

Bromwich, D. H., L. H. Bai, and G. G. Bjarnason, 2005: High-resolution regional climate simulations over Iceland using Polar MM5. *Mon. Wea. Rev.,* **133,** 3527–3547.

Caldwell, P., H.-N. S. Chin, D. C. Bader, and G. Bala, 2009: Evaluation of a WRF dynamical downscaling simulation over California. *Climatic Change,* **95** (3–4), 499–521, doi:10.1007/s10584-009-9583-5.

Chen, B., X.-D. Xu, S. Yang, and W. Zhang, 2012: On the origin and destination of atmospheric moisture and air mass over the Tibetan Plateau. *Theor. Appl. Climatol.,* **54,** doi:10.1007/s00704-012-0641-y.

Chow, K. C., and J. C. L. Chan, 2009: Diurnal variations of circulation and precipitation in the vicinity of the Tibetan Plateau in early summer. *Climate Dyn.,* **32,** 55–73, doi:10.1007/s00382-008-0374-x.

Colle, B. A., 2008: Two-dimensional idealized simulations of the impact of multiple windward ridges on orographic precipitation. *J. Atmos. Sci.,* **65,** 509–523.

Collier, E., T. Mölg, F. Maussion, D. Scherer, C. Mayer, and A. B. G. Bush, 2013: High-resolution interactive modelling of the mountain glacier–atmosphere interface: An application over the Karakoram. *Cryosphere,* **7,** 779–795, cp-10-91-2014/tc-7-779-2013.

Conrad, V., 1941: The variability of precipitation. *Mon. Wea. Rev.,* **69,** 5–11.

Dee, D. P., and Coauthors, 2011: The ERA-Interim reanalysis: Configuration and performance of the data assimilation system. *Quart. J. Roy. Meteor. Soc.,* **137,** 553–597, doi:10.1002/qj.828.

Dietze, E., and Coauthors, 2014: Sediment transport processes across the Tibetan Plateau inferred from robust grain-size end-members in lake sediments. *Climate* Past, **10,** 91–106, doi:10.5194/cp-10-91-2014.

Feng, L., and T. J. Zhou, 2012: Water vapor transport for summer precipitation over the Tibetan Plateau: Multidata set analysis. *J. Geophys. Res.,* **117,** D20114, doi:10.1029/2011JD017012.

Fu, Y., G. Liu, G. Wu, R. Yu, Y. Xu, Y. Wang, R. Li, and Q. Liu, 2006: Tower mast of precipitation over the central Tibetan Plateau summer. *Geophys. Res. Lett.,* **33,** L05802, doi:10.1029/2005GL024713.

Fujita, K., 2008: Effect of precipitation seasonality on climatic sensitivity of glacier mass balance. *Earth Planet. Sci. Lett.,* **276** (1–2), 14–19, doi:10.1016/j.epsl.2008.08.028.

Hahn, D., and S. Manabe, 1975: Role of mountains in South Asian monsoon circulation. *J. Atmos. Sci.,* **32,** 1515–1541.

Heikkila, U., A. Sandvik, and A. Sorteberg, 2011: Dynamical downscaling of ERA-40 in complex terrain using the WRF regional climate model. *Climate Dyn.,* **37** (7–8), 1551–1564, doi:10.1007/s00382-010-0928-6.

Hou, A. Y., and Coauthors, 2014: The Global Precipitation Measurement (GPM) mission. *Bull. Amer. Meteor. Soc.,* in press.

Huffman, G. J., and Coauthors, 2007: The TRMM Multisatellite Precipitation Analysis: Quasi-global, multiyear, combined sensor precipitation estimates at fine scale. *J. Hydrometeor.,* **8,** 38–55.

Immerzeel, W. W., and M. F. P. Bierkens, 2010: Seasonal prediction of monsoon rainfall in three Asian river basins: The importance of snow cover on the Tibetan Plateau. *Int. J. Climatol.,* **30,** 1835–1842, doi:10.1002/joc.2033.

——, L. P. H. van Beek, and M. F. P. Bierkens, 2010: Climate change will affect the Asian water towers. *Science,* **328,** 1382–1385.

Jiang, Q., 2003: Moist dynamics and orographic precipitation. *Tellus,* **55A,** 301–316, doi:10.1034/j.1600-0870.2003.00025.x.

Jurković, R. S., and Z. Pasarić, 2013: Spatial variability of annual precipitation using globally gridded data sets from 1951 to 2000. *Int. J. Climatol.,* **33,** 690–698, doi:10.1002/joc.3462.

Kääb, A., E. Berthier, C. Nuth, J. Gardelle, and Y. Arnaud, 2012: Contrasting patterns of early twenty-first-century glacier mass change in the Himalayas. *Nature,* **488,** 495–498, doi:10.1038/nature11324.

Kanamitsu, M., and H. Kanamaru, 2007: Fifty-seven-year California Reanalysis Downscaling at 10 km (CaRD10). Part I: System detail and validation with observations. *J. Climate,* **20,** 5553–5571.

Kansakar, S., D. M. Hannah, J. Gerrard, and G. Rees, 2004: Spatial pattern in the precipitation regime of Nepal. *Int. J. Climatol.,* **24,** 1645–1659, doi:10.1002/joc.1098.

Kaser, G., M. Grosshauser, and B. Marzeion, 2010: Contribution potential of glaciers to water availability in different climate regimes. *Proc. Natl. Acad. Sci. USA,* **107,** 20 223–20 227, doi:10.1073/pnas.1008162107.

Kidd, C., and V. Levizzani, 2011: Status of satellite precipitation retrievals. *Hydrol. Earth Syst. Sci.,* **15,** 1109–1116, doi:10.5194/hess-15-1109-2011.

Kropáček, J., F. Maussion, F. Chen, S. Hoerz, and V. Hochschild, 2013: Analysis of ice phenology of lakes on the Tibetan Plateau from MODIS data. *Cryosphere,* **7,** 287–301, doi:10.5194/tc-7-287-2013.

Kumar, M. S., M. S. Shekhar, S. S. V. S. R. Krishna, M. R. Bhutiyani, and A. Ganju, 2012: Numerical simulation of cloud burst event on August 05, 2010, over Leh using WRF mesoscale model. *Nat. Hazards,* **62,** 1261–1271, doi:10.1007/s11069-012-0145-1.

Liu, X., A. Bai, and C. Liu, 2009: Diurnal variations of summertime precipitation over the Tibetan Plateau in relation to orographically-induced regional circulations. *Environ. Res. Lett.,* **4,** 045203, doi:10.1088/1748-9326/4/4/045203.

Lo, J. C.-F., Z.-L. Yang, and R. A. Pielke Sr., 2008: Assessment of three dynamical climate downscaling methods using the Weather Research and Forecasting (WRF) model. *J. Geophys. Res.,* **113,** D09112, doi:10.1029/2007JD009216.

Maussion, F., D. Scherer, R. Finkelnburg, J. Richters, W. Yang, and T. Yao, 2011: WRF simulation of a precipitation event over the

Tibetan Plateau, China—An assessment using remote sensing and ground observations. *Hydrol. Earth Syst. Sci.,* **15,** 1795–1817, doi:10.5194/hess-15-1795-2011.

Medina, S., R. A. Houze Jr., A. Kumar, and D. Niyogi, 2010: Summer monsoon convection in the Himalayan region: Terrain and land cover effects. *Quart. J. Roy. Meteor. Soc.,* **136,** 593–616, doi:10.1002/qj.601.

Mölg, T., and G. Kaser, 2011: A new approach to resolving climate-cryosphere relations: Downscaling climate dynamics to glacier-scale mass and energy balance without statistical scale linking. *J. Geophys. Res.,* **116,** D16101, doi:10.1029/2011JD015669.

——, and D. Scherer, 2012: Retrieving important mass-balance model parameters from AWS measurements and high-resolution mesoscale atmospheric modeling. *J. Glaciol.,* **58,** 625–628, doi:10.3189/2012JoG11J258.

——, F. Maussion, W. Yang, and D. Scherer, 2012: The footprint of Asian monsoon dynamics in the mass and energy balance of a Tibetan glacier. *Cryosphere,* **6,** 1445–1461, doi:10.5194/tc-6-1445-2012.

——, ——, and D. Scherer, 2014: Mid-latitude westerlies as a driver of glacier variability in monsoonal High Asia. *Nat. Climate Change,* **4,** 68–73, doi:10.1038/nclimate2055.

Molnar, P., W. R. Boos, and D. S. Battisti, 2010: Orographic controls on climate and paleoclimate of Asia: Thermal and mechanical roles for the Tibetan Plateau. *Annu. Rev. Earth Planet. Sci.,* **38,** 77–102, doi:10.1146/annurev-earth-040809-152456.

National Centers for Environmental Prediction, cited 2014: NCEP ADP global upper air and surface weather observations (PREPBUFR format), May 1997—Continuing. National Center for Atmospheric Research Computational and Information Systems Laboratory Research Data Archive. [Available online at http://rda.ucar.edu/datasets/ds337.0.]

Palazzi, E., J. von Hardenberg, and A. Provenzale, 2013: Precipitation in the Hindu-Kush Karakoram Himalaya: Observations and future scenarios. *J. Geophys. Res. Atmos.,* **118,** 85–100, doi:10.1029/2012JD018697.

Qian, W., and D.-K. Lee, 2000: Seasonal march of Asian summer monsoon. *Int. J. Climatol.,* **20,** 1371–1386, doi:10.1002/1097-0088(200009)20:11<1371::AID-JOC538>3.0.CO;2-V.

Qin, J., K. Yang, S. Liang, and X. Guo, 2009: The altitudinal dependence of recent rapid warming over the Tibetan Plateau. *Climatic Change,* **97** (1–2), 321–327, doi:10.1007/s10584-009-9733-9.

Rupper, S., and G. Roe, 2008: Glacier changes and regional climate: A mass and energy balance approach. *J. Climate,* **21,** 5384–5401.

Rüthrich, F., B. Thies, C. Reudenbach, and J. Bendix, 2013: Cloud detection and analysis on the Tibetan Plateau using Meteosat and CloudSat. *J. Geophys. Res. Atmos.,* **118,** 10 082–10 099, doi:10.1002/jgrd.50790.

Schiemann, R., D. Luethi, P. L. Vidale, and C. Schaer, 2008: The precipitation climate of central Asia—Intercomparison of observational and numerical data sources in a remote semiarid region. *Int. J. Climatol.,* **28,** 295–314, doi:10.1002/joc.1532.

——, ——, and C. Schaer, 2009: Seasonality and interannual variability of the westerly jet in the Tibetan Plateau region. *J. Climate,* **22,** 2940–2957.

Shi, Y., 2002: Characteristics of late quaternary monsoonal glaciation on the Tibetan Plateau and in East Asia. *Quat. Int.,* **97–98,** 79–91, doi:10.1016/S1040-6182(02)00053-8.

——, and S. Liu, 2000: Estimation on the response of glaciers in china to the global warming in the 21st century. *Chin. Sci. Bull.,* **45,** 668–672.

Skamarock, W. C., and J. B. Klemp, 2008: A time-split nonhydrostatic atmospheric model for weather research and forecasting applications. *J. Comput. Phys.,* **227,** 3465–3485, doi:10.1016/j.jcp.2007.01.037.

Sugimoto, S., and K. Ueno, 2010: Formation of mesoscale convective systems over the eastern Tibetan Plateau affected by plateau-scale heating contrasts. *J. Geophys. Res.,* **115,** D16105, doi:10.1029/2009JD013609.

Ueno, K., H. Fujii, H. Yamada, and L. P. Liu, 2001: Weak and frequent monsoon precipitation over the Tibetan Plateau. *J. Meteor. Soc. Japan,* **79,** 419–434, doi:10.2151/jmsj.79.419.

von Storch, H., H. Langenberg, and F. Feser, 2000: A spectral nudging technique for dynamical downscaling purposes. *Mon. Wea. Rev.,* **128,** 3664–3673.

Wang, B., 2006: *The Asian Monsoon.* Springer-Praxis, 787 pp.

Webster, P. J., V. O. Magana, T. N. Palmer, J. Shukla, R. A. Tomas, M. Yanai, and T. Yasunari, 1998: Monsoons: Processes, predictability, and the prospects for prediction. *J. Geophys. Res.,* **103** (C7), 14 451–14 510.

——, V. E. Toma, and H. M. Kim, 2011: Were the 2010 Pakistan floods predictable? *Geophys. Res. Lett.,* **38,** L04806, doi:10.1029/2010GL046346.

Wilks, D. S., 1995: *Statistical Methods in the Atmospheric Sciences: An Introduction.* Academic Press, 467 pp.

Wilson, A. B., D. H. Bromwich, and K. M. Hines, 2011: Evaluation of polar WRF forecasts on the arctic system reanalysis domain: Surface and upper air analysis. *J. Geophys. Res.,* **116,** D11112, doi:10.1029/2010JD015013.

Wu, G., Y. Liu, B. He, Q. Bao, A. Duan, and F.-F. Jin, 2012: Thermal controls on the Asian summer monsoon. *Sci. Rep.,* **2,** 404, doi:10.1038/srep00404.

Yang, W., X. Guo, T. Yao, K. Yang, L. Zhao, S. Li, and M. Zhu, 2011: Summertime surface energy budget and ablation modeling in the ablation zone of a maritime Tibetan glacier. *J. Geophys. Res.,* **116,** D14116, doi:10.1029/2010JD015183.

——, T. Yao, X. Guo, M. Zhu, S. Li, and D. B. Kattel, 2013: Mass balance of a maritime glacier on the southeast Tibetan Plateau and its climatic sensitivity. *J. Geophys. Res. Atmos.,* **118,** 9579–9594, doi:10.1002/jgrd.50760.

Yao, T., and Coauthors, 2012: Different glacier status with atmospheric circulations in Tibetan Plateau and surroundings. *Nat. Climate Change,* **2,** 663–667, doi:10.1038/nclimate1580.

Yaodong, L., W. Yun, S. Yang, H. Liang, G. Shouting, and R. Fu, 2008: Characteristics of summer convective systems initiated over the Tibetan Plateau. Part I: Origin, track, development, and precipitation. *J. Appl. Meteor. Climatol.,* **47,** 2679–2695.

Yin, Z.-Y., X. Zhang, X. Liu, M. Colella, and X. Chen, 2008: An assessment of the biases of satellite rainfall estimates over the Tibetan Plateau and correction methods based on topographic analysis. *J. Hydrometeor.,* **9,** 301–326.

You, Q., K. Fraedrich, G. Ren, B. Ye, X. Meng, and S. Kang, 2012: Inconsistencies of precipitation in the eastern and central Tibetan Plateau between surface adjusted data and reanalysis. *Theor. Appl. Climatol.,* **109** (3–4), 485–496, doi:10.1007/s00704-012-0594-1.

Zhou, T., R. Yu, H. Chen, A. Dai, and Y. Pan, 2008: Summer precipitation frequency, intensity, and diurnal cycle over China: A comparison of satellite data with rain gauge observations. *J. Climate,* **21,** 3997–4010.

Supplemental information to

"Precipitation seasonality and variability over the Tibetan Plateau as resolved by the High Asia Reanalysis"

Maussion et al., Journal of Climate
DOI: 10.1175/JCLI-D-13-00282.1

1. Sensitivity experiments: ERA-Interim as forcing dataset

The ERA experiment is designed as follows:

Time period: four years (2002/03 and 2010/11).
Domain: HAR30
Forcing data: ERA-Interim (Dee et al., 2011), 0.75° resolution, 6-Hourly.
Model physics: unchanged

The validation is realized for seasonal means (DJF and JJA) using all NCDC stations available in the HAR30 domain.

1.1 Comparison with weather stations: precipitation

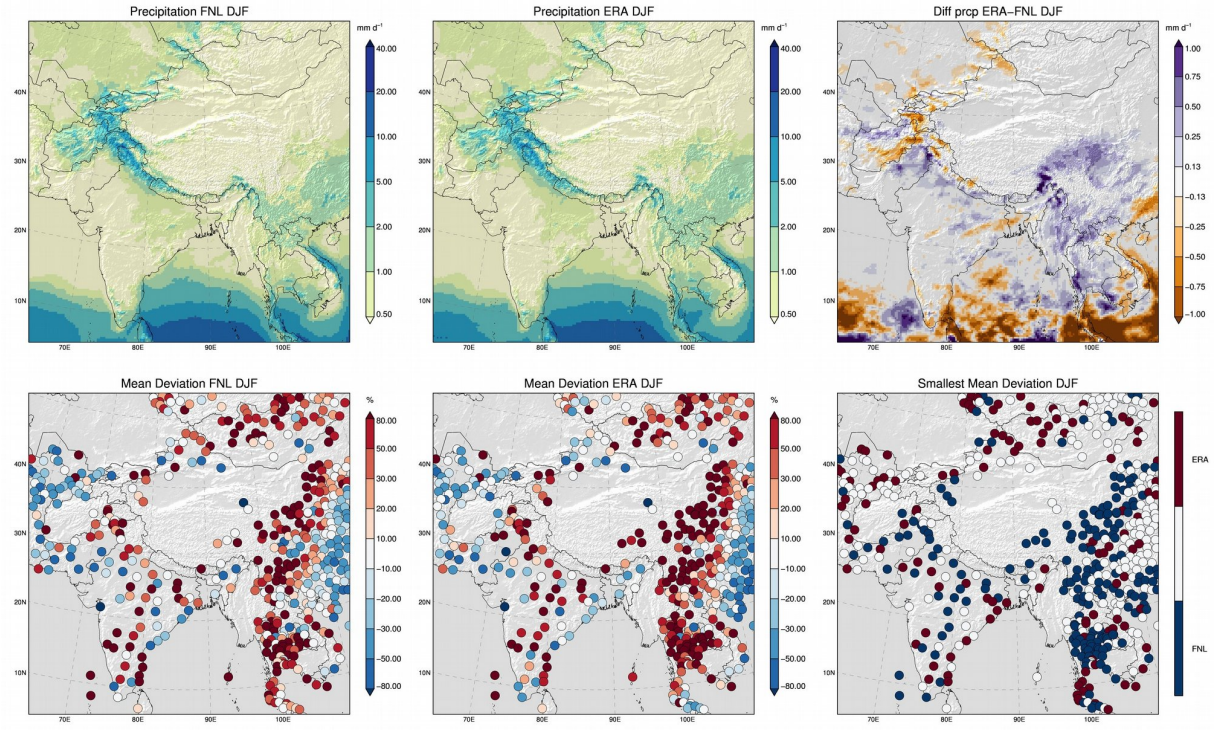

Figure S1: ***Upper panel:*** *4-yr averaged precipitation in winter (DJF) for FNL and ERA and their difference over the HAR30 domain.* ***Lower panel:*** *mean deviations (bias, %) at each station location for FNL and ERA, and closest dataset at each station (the closest dataset is indicated when one experiment outperforms the other with at least 10 % difference). In total, 628 stations are available for the validation. FNL has the smallest MD at 190 stations, ERA at 118. The patterns of precipitation (and therefore of biases) are very similar (e.g. south to north band of positive and then negative band over China), indicating that most of the differences are related to either WRF or the same errors in both global datasets. On the TP in winter, ERA is wetter than FNL, with the latter being closer to observations for the majority of stations.*

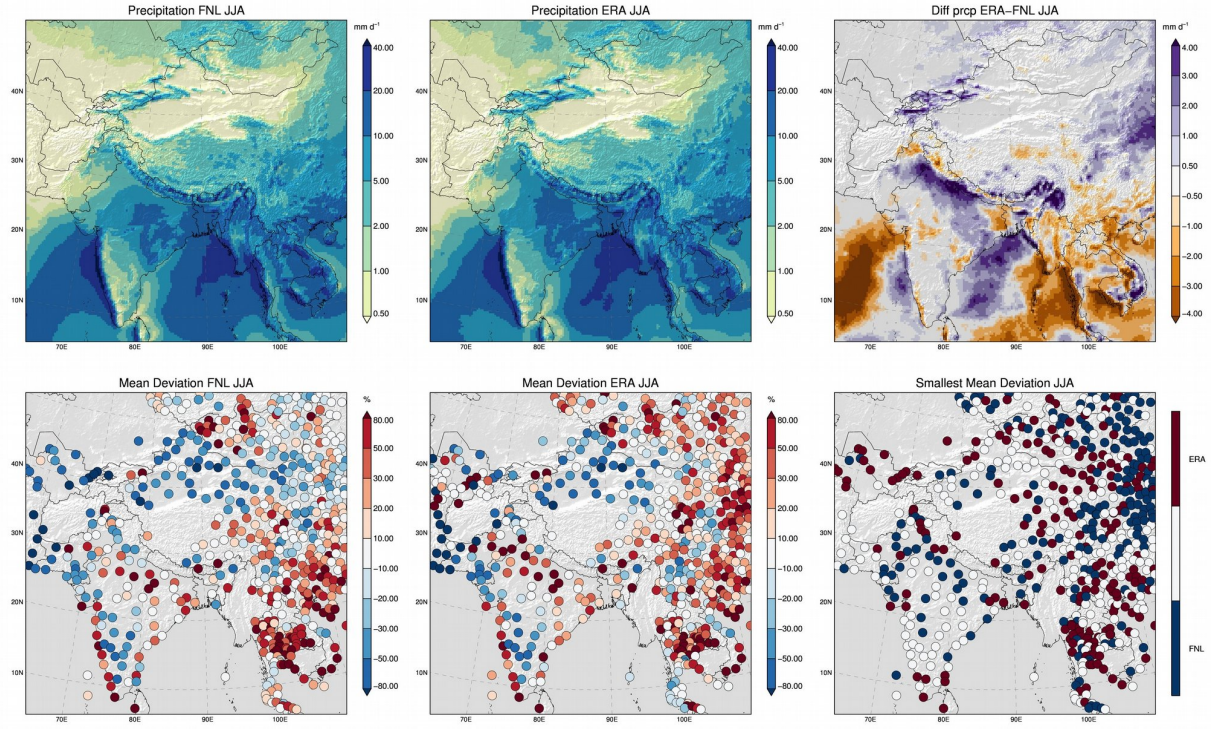

Figure S2: Same as Fig. S1 but for summer (JJA). FNL (ERA) has the smallest MD at 196 (185) stations. As for DJF, the patterns of biases in JJA are very similar, indicating that most of the differences are related to either WRF or the same errors in both global datasets. On the TP the performance of both forcing datasets is similar.

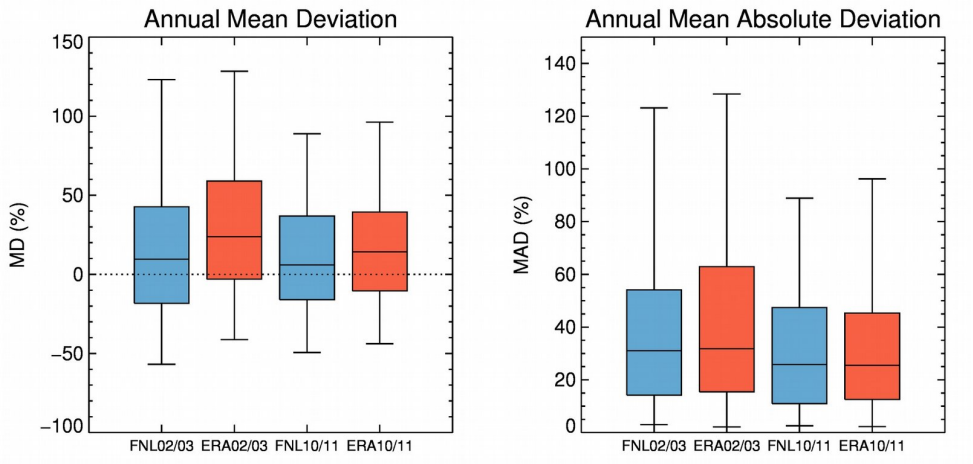

Figure S3: Box plots of Annual Mean (Absolute) Deviation for all stations over the HAR30 domain (628 stations) in % for FNL (blue) and ERA (red). The two periods (2002/03 and 2010/11) are plotted separately. The whiskers are drawn for the 05%, 25%, 50%, 75% and 95% percentiles. ERA has a marked positive bias on average, but in absolute value both datasets have comparable accuracies (FNL is slightly better).

1.2 Comparison with weather stations: temperature

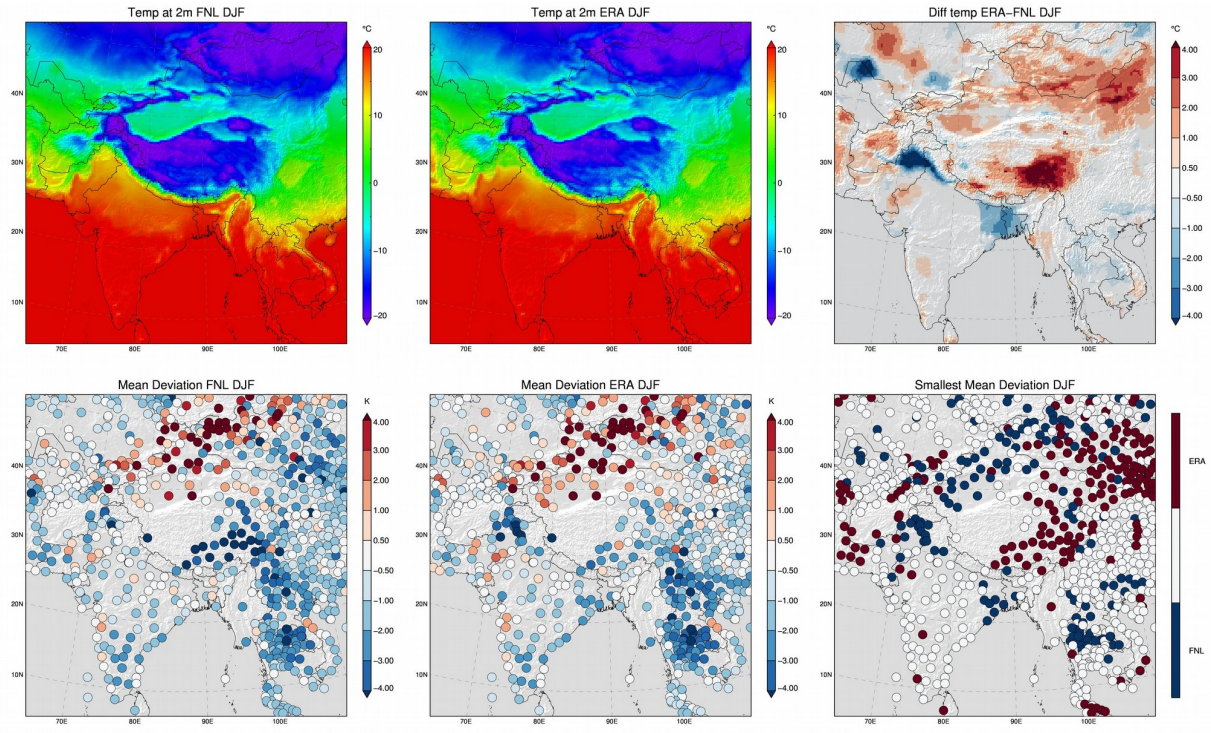

Figure S4: ***Upper panel:*** *4-yr averaged 2 m air temperature in winter (DJF) for FNL and ERA and their difference over the HAR30 domain.* ***Lower panel:*** *mean deviations (bias) at each station location for FNL and ERA, and closest dataset at each station (the closest dataset is indicated when one experiment outperforms the other with at least 0.5 K difference). In total, 747 stations are available for the validation. FNL (ERA) has the smallest MD at 150 (188) stations. The patterns of temperature biases are very similar (e.g. too cold over the TP and most parts of the Indochina peninsula, too warm in the north), indicating again that most of the differences are related to either WRF or the same errors in both global datasets. On the TP in winter, ERA is significantly warmer than FNL, and closer to observations.*

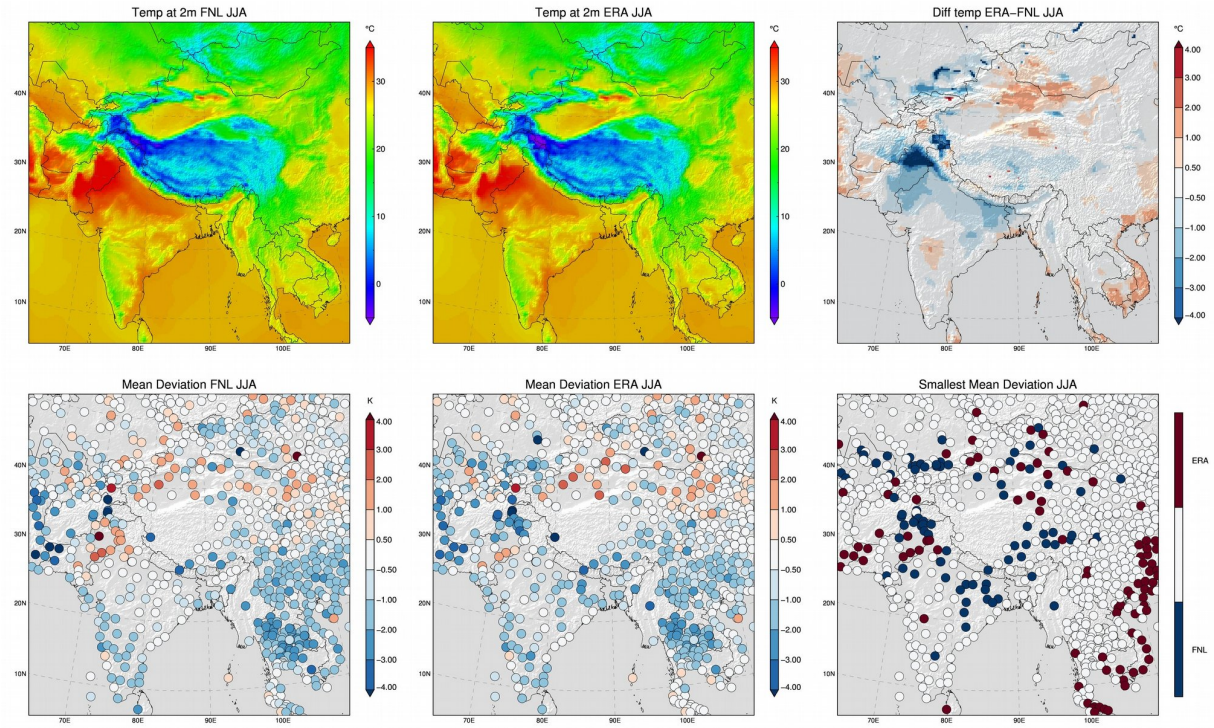

Figure S5: Same as Fig. S4 but for summer (JJA). FNL (ERA) has the smallest MD at 84 (93) stations. The differences between the datasets are smaller in summer than in winter. There is an obvious artefact in ERA over the Karakoram, which is due to the snow cover initialization in ERA land surface model for gridpoints with more than 50% glacier area (Collier et al, 2013). Another (unrelated) cold bias is visible in Pakistan and over the TP (approx 0.5 to 1 K).

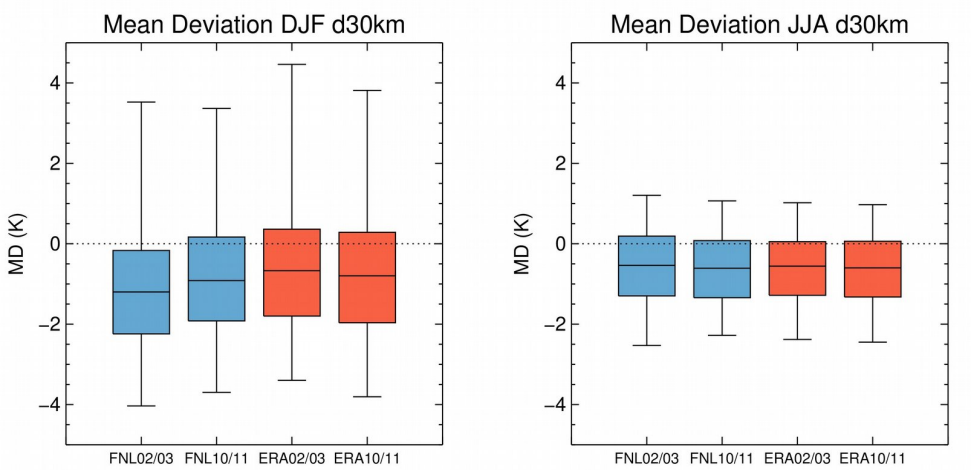

Figure S6: Box plots of Mean Deviation for all stations over the HAR30 domain (747 stations) in winter (DJF, left) and summer (JJA, right). The whiskers are drawn for the 05%, 25%, 50%, 75% and 95% percentiles. Temperatures are much closer to observations in summer. Again, the performances of both datasets are similar.

2. Supplementary validation of HAR data with TRMM

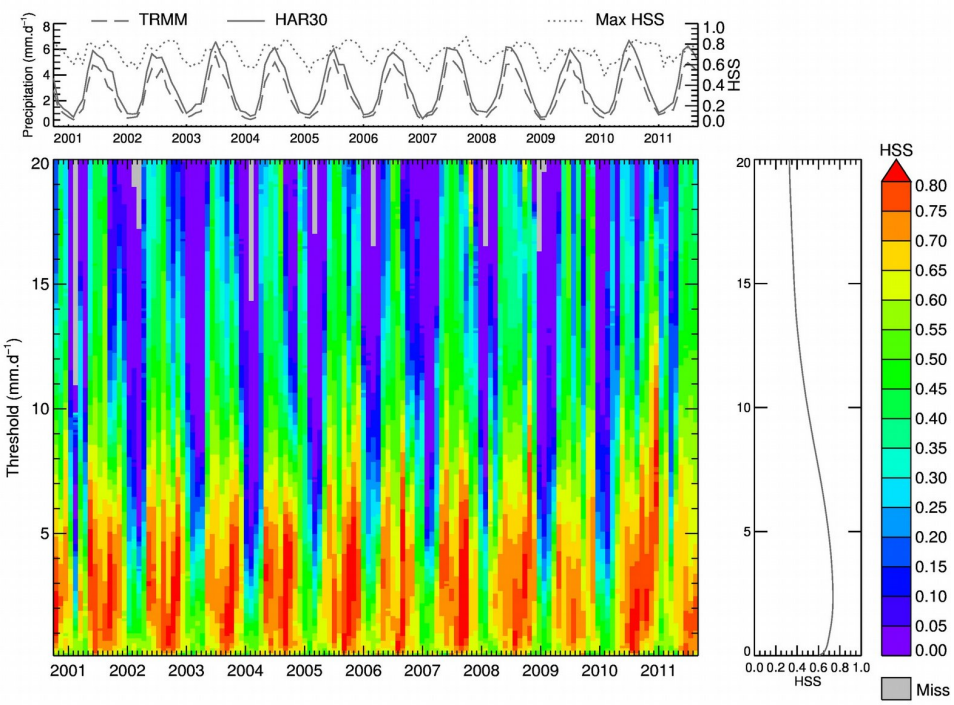

Figure S7: HSS of HAR30 for different months/thresholds using TRMM3B43 as reference in the full HAR30 domain (N=39990). The upper plot represents the spatially averaged monthly precipitation timeseries from HAR30 and TRMM3B43, together with the maximum HSS for all thresholds at a given month. The right plot represents the HSS evolution with varying thresholds for all pairs. Grey color occurs when no precipitation event was detected by TRMM3B43.

The objective of this domain-wide analysis is to detect potential systematic divergences or inconsistencies in the HAR dataset during the decade. TRMM3B43 and HAR30 are in good agreement for the spatial distribution of precipitation, as indicated by constant high scores for small thresholds. The best scores are reached during the summer months, when most of the precipitation is occurring. HAR30 predicts more precipitation than TRMM3B43, but the two datasets agree well on precipitation seasonality and variability. Seasonality aside, the scores are regular and constant throughout the decade and no singularities can be detected. There is no evident outlier or discrepancy, indicating that the HAR dataset is of constant quality.

3. Supplementary validation of HAR data with NCDC

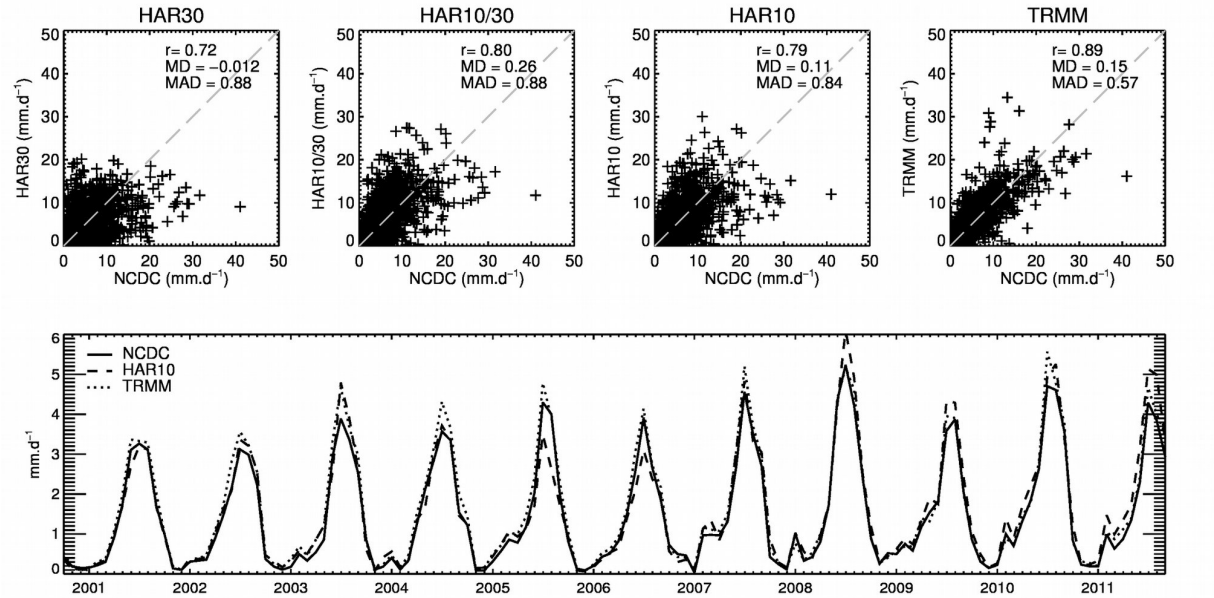

Figure S8: Same as Fig. 3 but with all stations in the HAR10 domain (71 stations, 8356 valid months)

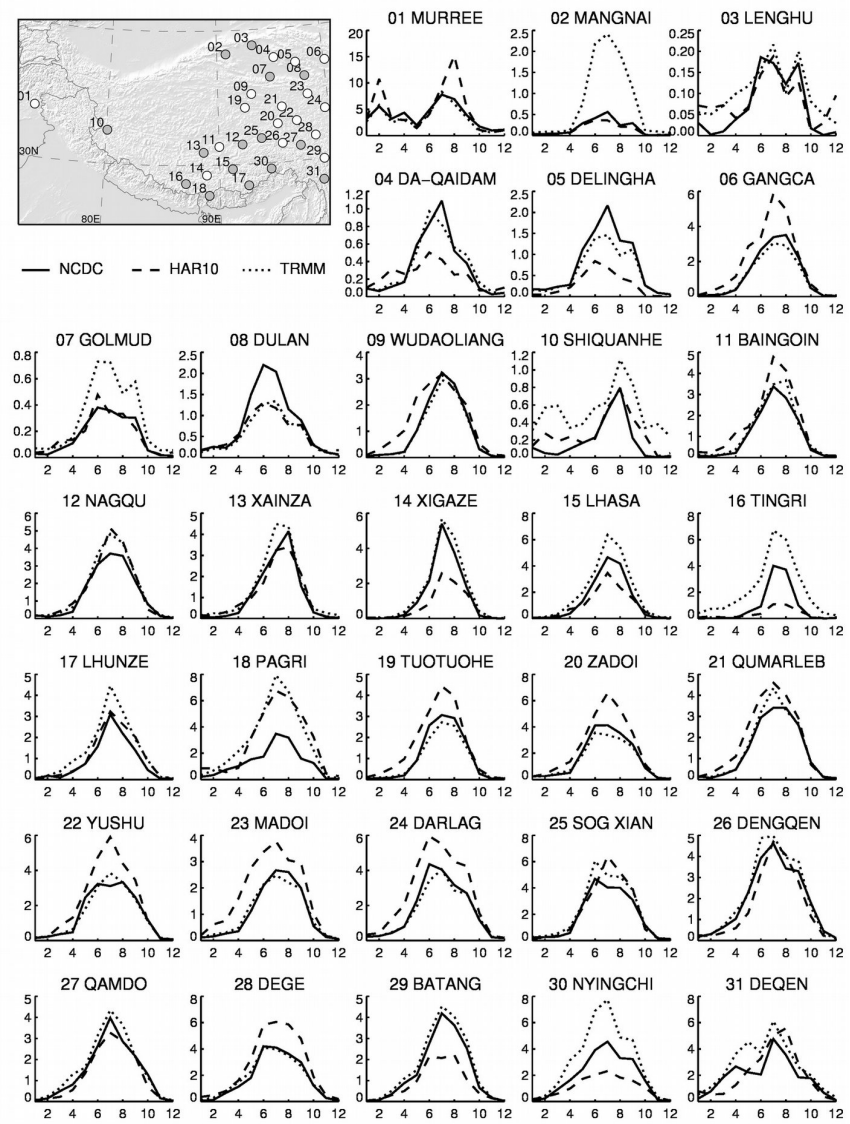

Figure S9: Mean decadal seasonal cycles of NCDC stations, TRMM3B43 and HAR10 (X-axis units: months, Y-axis units: mm d^{-1}). The map shows the station locations, with grey points when HAR10 is closer to observations, white points when TRMM3B43 is closer.

The majority of the stations exhibits a characterized summer precipitation regime but there are large variations in shape and in magnitude. The westernmost station, Murree (01), has two pronounced precipitation peaks. The second westernmost, Shiquanhe (10), has a less-pronounced winter precipitation mode that is captured by both TRMM3B43 and HAR10. The stations in the Qaidam Basin (02 to 08) are the driest, with substantial variations in shape. The stations in central TP have generally dry winters, but are different with respect to the length of the precipitation period or to the precipitation magnitude (see for example 16-Tingri and 21-Qumarleb). For 16 of the 31 stations, HAR10 is closer to observations than TRMM3B43.

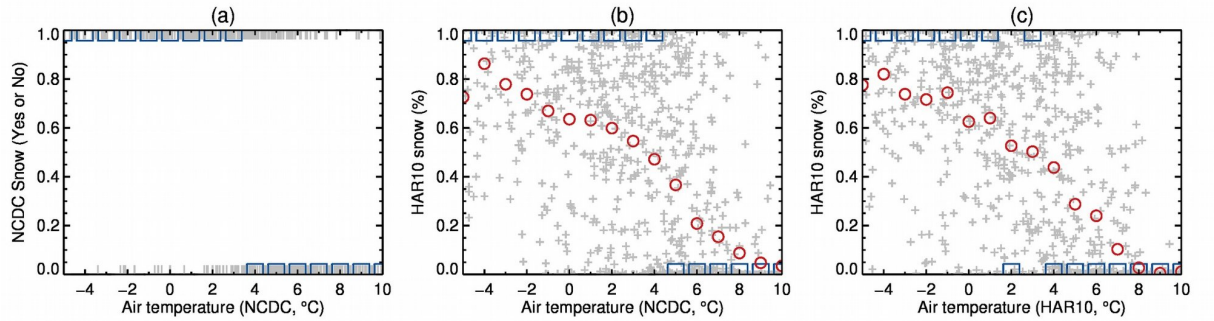

Figure S10: Snowfall as a function of air temperature at the station WUDAOLIANG (see Figure S9 for the station location). The elevation difference between the HAR10 grid elevation and the station is 47m.

*(a) **Daily** NCDC frozen precipitation flag (1 or 0) for precipitation days (> 1 mm d^{-1}) as a function of daily temperature measured at the station (grey crosses). 1°C sized binned modes (blue squares)*

*(b) **Daily** HAR10 frozen precipitation (%) for precipitation days (> 1 mm d^{-1}) as a function of daily temperature measured at the **station** (grey crosses). 1°C sized binned means (red circles) and modes (blue squares)*

*(c) **Daily** HAR10 frozen precipitation (%) for precipitation days (> 1 mm d^{-1}) as a function of **daily HAR10** air temperature (grey crosses). 1°C sized binned means (red circles) and modes (blue squares)*

Frozen precipitation is reported at the station for a wide range of temperatures and the mode (majority of reports) changes at 3°C. Snowfall from the HAR is given as percentage of total amounts and the mode (where the majority of days with > 50% snowfall) also changes at 3°C. The results are similar when plotted against NCDC temperature (b) or HAR10 Temperature (c).

Paper III

The footprint of Asian monsoon dynamics in the mass and energy balance of a Tibetan glacier

Mölg, T., **Maussion, F.**, Yang, W., and Scherer, D. (2012): The footprint of Asian monsoon dynamics in the mass and energy balance of a Tibetan glacier, *The Cryosphere*, 6, 1445-1461, doi:10.5194/tc-6-1445-2012

Status: Published.

Own contribution:

- field work
- station data acquisition/preparation
- atmospheric simulations
- contribution to analysis
- minor contribution to writing

The Cryosphere, 6, 1445–1461, 2012
www.the-cryosphere.net/6/1445/2012/
doi:10.5194/tc-6-1445-2012

The Cryosphere

The footprint of Asian monsoon dynamics in the mass and energy balance of a Tibetan glacier

T. Mölg[1], **F. Maussion**[1], **W. Yang**[2], **and D. Scherer**[1]

[1]Chair of Climatology, Technische Universität Berlin, Berlin, Germany
[2]Key Laboratory of Tibetan Environment Changes and Land Surface Processes, Institute of Tibetan Plateau Research, Chinese Academy of Sciences, Beijing, China

Correspondence to: T. Mölg (thomas.moelg@campus.tu-berlin.de)

Received: 26 June 2012 – Published in The Cryosphere Discuss.: 8 August 2012
Revised: 15 October 2012 – Accepted: 3 November 2012 – Published: 6 December 2012

Abstract. Determinations of glacier-wide mass and energy balance are still scarce for the remote mountains of the Tibetan Plateau, where field measurements are challenging. Here we run and evaluate a physical, distributed mass balance model for Zhadang Glacier (central Tibet, 30° N) based on in-situ measurements over 2009–2011 and an uncertainty estimate by Monte Carlo and ensemble strategies. The model application aims to provide the first quantification of how the Indian Summer Monsoon (ISM) impacts an entire glacier over the various stages of the monsoon's annual cycle. We find a strong and systematic ISM footprint on the interannual scale. Early (late) monsoon onset causes higher (lower) accumulation, and reduces (increases) the available energy for ablation primarily through changes in absorbed shortwave radiation. By contrast, only a weak footprint exists in the ISM cessation phase. Most striking though is the core monsoon season: local mass and energy balance variability is fully decoupled from the active/break cycle that defines large-scale atmospheric variability during the ISM. Our results demonstrate quantitatively that monsoon onset strongly affects the ablation season of glaciers in Tibet. However, we find no direct ISM impact on the glacier in the main monsoon season, which has not been acknowledged so far. This result also adds cryospheric evidence that, once the monsoon is in full swing, regional atmospheric variability prevails on the Tibetan Plateau in summer.

1 Introduction

Changes in the Asian monsoon climate and associated glacier responses have become predominant topics of climate research. Their importance is founded on, e.g. (i) the effect of monsoon activity on the livelihood of millions of people (e.g. Tao et al., 2004), (ii) the effect of glacier change on regional water supply and global sea level rise (Kaser et al., 2006, 2010), and (iii) the role of the monsoon in gobal teleconnections, which was discussed by Webster et al. (1998) and continues to be a research focus (e.g. Li et al., 2010; Park et al., 2010).

Understanding the direct influence of atmospheric conditions on glacier mass requires quantitative knowledge of the surface energy balance (SEB) and its relation to the mass balance (MB) of a glacier. Compared to mid and high latitudes, there are few detailed SEB/MB studies for the high Asian mountains. This scarcity was emphasized more than a decade ago by Fujita and Ageta (2000) and it has only slightly improved due to the difficulty of field data collection. A number of such studies are available for the Himalaya at the border region of Nepal and China (Kayastha et al., 1999; Aizen et al., 2002), including glacier-wide analyses. Other examined regions are the interior of the Tibetan Plateau in the Tanggula Mountains (Fujita and Ageta, 2000) and the plateau's north margin (Jiang et al., 2010), where distributed quantifications have been conducted, and the maritime southeast of the Tibetan Plateau, where point SEB studies were performed (Xie, 1994; Yang et al., 2011).

In the Nyainqêntanglha Mountains on the south-central plateau section, Caidong and Sorteberg (2010) modeled the

SEB/MB of Xibu Glacier. However, the authors themselves noted that their study only revealed basic features, since no direct measurements from the glacier were available. For Zhadang Glacier in the same mountain chain, Zhou et al. (2010) investigated the runoff variability in relation to local air temperature and precipitation and made conceptual SEB considerations. In this paper we calculate the glacier-wide SEB/MB of Zhadang Glacier in detail with the help of in-situ measurements. We therefore extend the knowledge of SEB/MB processes on the Tibetan Plateau, which meets the need to better understand the heterogeneous glacier changes on the plateau (e.g. Yao et al., 2012). However, we also pursue a specific application: to investigate the SEB/MB link to Asian monsoon dynamics. The study goals are therefore (i) to reveal the SEB/MB terms and their space–time variability; and (ii) to analyze these terms in relation to specific periods that reflect both intra- and interannual monsoon variability (the "monsoon footprint" on the glacier), since glacier fluctuations in the high Asian mountains have traditionally been linked to Asian summer monsoon conditions (e.g. Fujita and Ageta, 2000; Yang et al., 2011).

Our study is unique due to the *combination* of a multi-year data set (vs. single-season investigations), the use of distributed analysis (vs. point studies), and, most especially, the focus on the linkage of SEB/MB to multi-temporal monsoon dynamics (vs. focus on the monsoon onset, i.e. on inter-annual variability alone). Despite the heterogeneous glacier changes on the Tibetan Plateau, which result from interacting large-scale atmospheric flows and local relief factors (He et al., 2003; Fujita and Nuimura, 2011; Scherler et al., 2011), a common feature is the strong sensitivity to climatic conditions in summer (wet season). This was found by all previous SEB studies and stems from the regional climatic conditions, which show peaks in the annual air temperature and precipitation cycle at the same time. Of particular importance is the precipitation phase in response to air temperature variations (e.g. Kayastha et al., 1999; Fujita and Ageta, 2000; Caidong and Sorteberg, 2010), which has a double effect on MB through changes in accumulation by solid precipitation, and through changes in ablation by albedo. Thus, our goals build on the working hypothesis that local conditions in the monsoon season (boreal summer) govern the mass variability of Zhadang Glacier, which was also postulated from runoff observations downstream of the glacier (Kang et al., 2009; Zhou et al., 2010).

2 Methods, data basis and climatic setting

A physically-based SEB/MB model (Sect. 2.3) is the main tool employed in this study. The forcing data are mainly provided by on-site measurements (Sect. 2.1) and also partly by atmospheric model output (Sect. 2.2), while measurements not used for forcing serve to evaluate the MB model's performance. We rely on large-scale reanalysis and satellite data to distinguish between different phases of monsoon activity (Sect. 2.4).

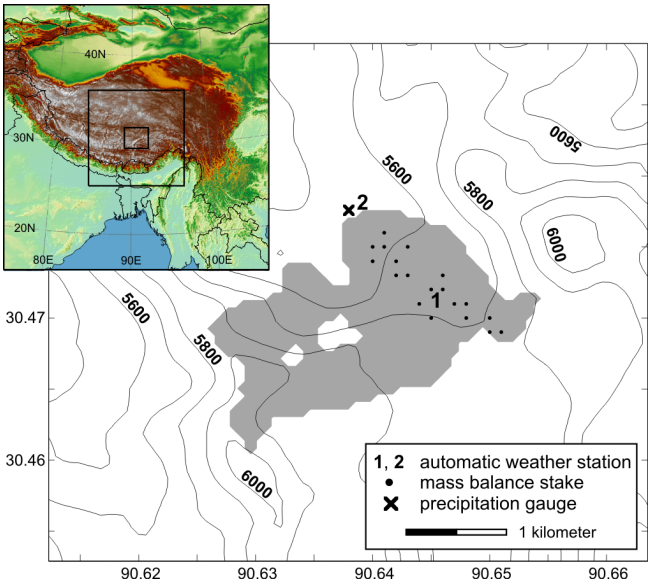

Fig. 1. Zhadang Glacier (grey shading) in the digital terrain model used for mass balance modeling. The locations of available measurements are indicated, and contours are in meters a.s.l. (100 m spacing). Note that the glacier is debris-free. The inlay shows the atmospheric model domain and the two nested domains as smaller rectangles (Maussion et al., 2011). Horizontal resolution increases towards the innermost domain that contains the Zhadang area: 30, 10, and 2 km grid spacing.

2.1 In-situ measurements

The pivotal observational data are the records from automatic weather station (AWS) 1 on Zhadang Glacier, which is situated at 5665 m in the ablation zone (Fig. 1). Characteristics and usage of available data are summarized in Table 1. AWS1 has been in operation since 2009, but unfortunately has two data gaps due to the extreme environment. However, three periods of sufficient data coverage exist for our study: 27 April–14 July 2009 (period 1), 1 October 2009–25 June 2010 (period 2), and 16 August 2010–15 September 2011 (period 3). This yields a total of 743 days, which is the time frame for the MB modeling and the analysis of the monsoon impact. All data were post-processed according to the instrument manuals, but also carefully screened following the procedure described in Mölg et al. (2009a) in order to detect and correct measurement errors. Basically, this procedure aims to identify periods when radiative sensor heating and/or riming of instruments may have occurred. Only 0.9 % of wind data and between 0 and 0.7 % of the other variables needed correction, which indicates high data quality.

Note that we use accumulation recorded by the sonic ranger (SR50) only for the months of October to April (Table 1), since air temperature (T_a) at AWS1 in the summer

Table 1. Measurement specifications for AWS1 located at 5665 m a.s.l. The height (depth) values refer to the initial distances to the surface on 27 April 2009. Last column indicates the usage for the mass balance modeling: forcing (F), parameter setting (P), or model evaluation (E). The two radiation components yield the measured albedo.

Variable	Instrument	Nominal accuracy	Usage
Air temperature (1.9 m)	Campbell CS215[a]	0.9 °C (−40 °C to +70 °C)	F
Relative humidity (1.9 m)	Campbell CS215[a]	4 % (0–100 %)	F
Wind speed (3.4 m)	Young 05103-45	0.3 m s^{-1}	F
Air pressure	TH Friedrichs DPI 740	0.15 hPa	F
Winter accumulation[b]	Campbell SR50	1 cm or 0.4 % to target	F
Incoming and reflected shortwave radiation	Campbell CS300	5 % (daily totals)	P
Surface height change	Campbell SR50	1 cm or 0.4 % to target	E
Glacier surface temperature	Campbell IRTS-P[c]	0.3 °C	E
Subsurface temperature (5.6 m)	Campbell TP107	0.3 °C	E
Subsurface temperature (9.6 m)	Campbell TP107	0.3 °C	P

[a] With ventilated radiation shield. [b] The months October to April. [c] Uses the principle of emitted radiation.

months clearly exceeds the melting point and therefore the SR50 does not capture the liquid fraction of precipitation. However, total precipitation is a required input for the model (Sect. 2.3). Further, subsurface temperature measurements at AWS1 were also performed at depths less than 5 m, but were obviously affected by radiative heating. Thus, we only use data from the initial depths of ≈ 5.6 and ≈ 9.6 m for MB model evaluation and lower boundary condition definition, respectively (Table 1). Regarding the latter, data from $\approx$ 9.6 m depth show an almost constant temperature of 268.6 K (standard deviation 0.06 K). We initialize the MB model after midnight on the first day of each of the three periods, and include measured surface temperature as well as data from the sensors at ≈ 3 and ≈ 1.5 m depth since the heating problem during night is minimal.

The time-dependent height of the T_a/relative humidity (RH) and wind speed sensors, as well as the depth of subsurface sensors, can be estimated from the SR50 record. Within period 3, however, surface height change is not available from 4 October 2010 to 30 June 2011 (68 % of period 3). This gap was filled with SR50 data from nearby AWS2 (Fig. 1), which has been operated since 2 October 2010 at 5566 m altitude (wind instrument from 21 May 2011 onward). AWS2 does not record ice ablation, as it is located slightly off the glacier margin on a moraine. Nevertheless, the data gap coincides with a period of weak ablation, which will be shown in the results section. Thus, we deem this correction to be a reasonable alternative to assuming a random sensor height. Wind speed and T_a/RH from AWS2 (same instruments as at AWS1) were also used to examine vertical gradients, but only for intervals when AWS1 and AWS2 sensor heights agreed within 0.2 m and when there was high enough wind speed for sufficient natural ventilation of the T_a/RH sensor (Georges and Kaser, 2002; $n = 1629$ h for wind; $n = 1340$ h for T_a/RH). We find no gradients in wind speed and RH, as differences are within the instrument accuracy. Typical T_a gradients were considered for defining MB model parameters (Sect. 2.3).

Finally, data from a precipitation gauge (Geonor T-200B; sensitivity ≤ 0.1 mm) at AWS2 between 22 May 2010 and 15 September 2011 are used to (i) constrain atmospheric model output (Sect. 2.2) and (ii) obtain winter precipitation for period 3 when SR50 data at AWS1 are unavailable. Also, several ablation stakes on Zhadang Glacier serve in the MB model evaluation. The locations of these measurement sites are presented in Fig. 1. Stake readings performed by personnel from the Institute of Tibetan Plateau Research are available for three intervals that overlap with each of the three model simulation periods once, as will be detailed in Sect. 3.1.

2.2 Atmospheric modeling

We run the Advanced Weather Research and Forecasting (WRF) numerical atmospheric model (Skamarock and Klemp, 2008) with a domain that covers a large part of Asia and the Northern Indian Ocean (Fig. 1) for the years 2009–2011. Multiple grid nesting in the parent domain yields a local-scale spatial resolution over Zhadang Glacier of 2 km (Fig. 1), which reproduces the real terrain altitude well (see below). All details of the model configuration are presented in Maussion et al. (2011), e.g. the grid structure (their Fig. 1) and the chosen model options and forcing strategy (their Table 1). We initialize WRF every day from the Global Forecast System's final analysis (Maussion et al., 2011), which differs from the traditional regional climate model approach where the model fields evolve over the entire simulation time. WRF output here, by contrast, is strongly constrained by the observed synoptic weather patterns and thus represents a regional atmospheric reanalysis.

Running WRF and producing a high-resolution reanalysis data set are part of a larger project, but for the present study we are only interested in the simulation of two variables that

are not available from measurements: local precipitation during the monsoon season and cloud cover fraction at Zhadang Glacier, both from the 2 km-resolution grid. The cloud cover is determined for a 50 km view field around AWS1 following the method of Mölg and Kaser (2011), which diagnoses saturated regions using the total condensate mixing ratio. Simulated precipitation is extracted from one of the four grid points surrounding AWS1 that has the least altitude difference (only 8 m). However, we constrain the WRF output with the ≈ 16 months of measurements from the precipitation gauge (Fig. 2a). Simulated precipitation shows an excellent correlation with the measured seasonal evolution ($r = 0.99$; Fig. 2a), a point that is vital for this study. Also, the simulated diurnal cycle in the summer monsoon months with the main and secondary maximum during night and early afternoon (Fig. 2b), respectively, agrees with observations on the Tibetan Plateau (Ueno et al., 2001). Thus, we have confidence in the simulated variability, but apply a scaling factor (K_{WRF}) of 0.56 for the amount of precipitation (Fig. 2a). This does not necessarily mean that WRF overestimates precipitation almost two-fold. Rather, it most likely reflects undercatch of the gauge (Goodison et al., 1998) or – since the scaled precipitation proves to be useful for the MB modeling (Sect. 3.1) – loss of snow on the glacier by wind drift, which has been observed during field work but is not resolved in the MB model. Both processes cannot be quantified at our site and are therefore absorbed by $K_{\mathrm{WRF}} < 1$. There is a detailed discussion in Sect. 3.3 about the influence of K_{WRF} on the results.

Figure 3 presents the time series of all local variables that are used to force the MB model, and indicates their source (measurement or WRF output). We will repeatedly refer to details of Fig. 3 later, but in general the plots nicely illustrate the local climatic setting with the coincidence of summertime peaks in air temperature and the moisture variables (Fig. 3a–d). In principle, the MB model could also be forced with atmospheric model output for the AWS1 grid cell alone, and in this context the modeling period could be extended as well. However, in this paper we attempt to use as many in-situ measurements as possible, so the study is limited to the three years 2009–2011 (Fig. 3).

2.3 SEB/MB modeling

The physical MB model is described in detail in Mölg et al. (2008, 2009a), thus we only give a brief summary. The model calculates the specific MB from mass gains by solid precipitation, surface water deposition and refreezing of liquid water in the snow pack, and from mass losses by surface melt, sublimation and subsurface melt. The following SEB equation lays the foundation for calculating these mass fluxes:

$$S\downarrow\cdot(1-\alpha)+L\downarrow+L\uparrow+\mathrm{QS}+\mathrm{QL}+\mathrm{QPRC}+\mathrm{QG}=F \quad (1)$$

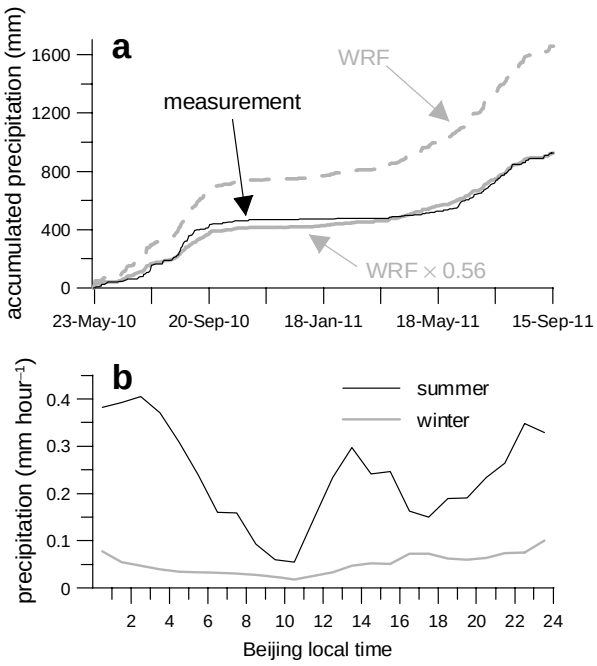

Fig. 2. Precipitation in the atmospheric model. **(a)** Accumulated precipitation between 22 May 2010 and 15 September 2011 at the precipitation gauge close to AWS2 (5566 m) and simulated at the associated WRF grid cell (5533 m). A scaling factor of 0.56 for WRF equals the total measured sum. **(b)** Mean diurnal cycle in WRF at the same grid cell for the summer (May–September) and winter (October–April) over 2009–2011.

These symbols signify incoming shortwave radiation ($S\downarrow$), broadband surface albedo (α), incoming and outgoing longwave radiation ($L\downarrow$ and $L\uparrow$), the turbulent sensible and latent heat fluxes (QS and QL), the heat flux from precipitation (QPRC), and the heat flux from the ground (QG). An energy flux has a positive (negative) sign when it induces an energy gain (sink) at the surface. The sum of these fluxes yields a resulting flux F, which represents the latent energy for melting (QM) if glacier surface temperature is 273.15 K. QG consists of fluxes of heat conduction (QC) and penetrating shortwave radiation (QPS), where the latter – owing to the energy conservation principle – is always an energy sink at the surface.

At the upper boundary, the model is forced hourly by the six variables shown in Fig. 3. Note that Fig. 3 presents daily means, while the hourly forcing naturally encompasses a greater range than visible in the figure (e.g. hourly T_{a} can rise to 10–15 °C in summer). As stated in Sects. 2.1 and 2.2, these inputs are provided by local measurements or atmospheric model output at one point on the glacier, and are distributed over the entire glacier using vertical gradients (see below) if the model is run in distributed mode. A fixed bottom temperature is prescribed at the lower boundary in the ice, which we chose at 9 m depth based on the measurements

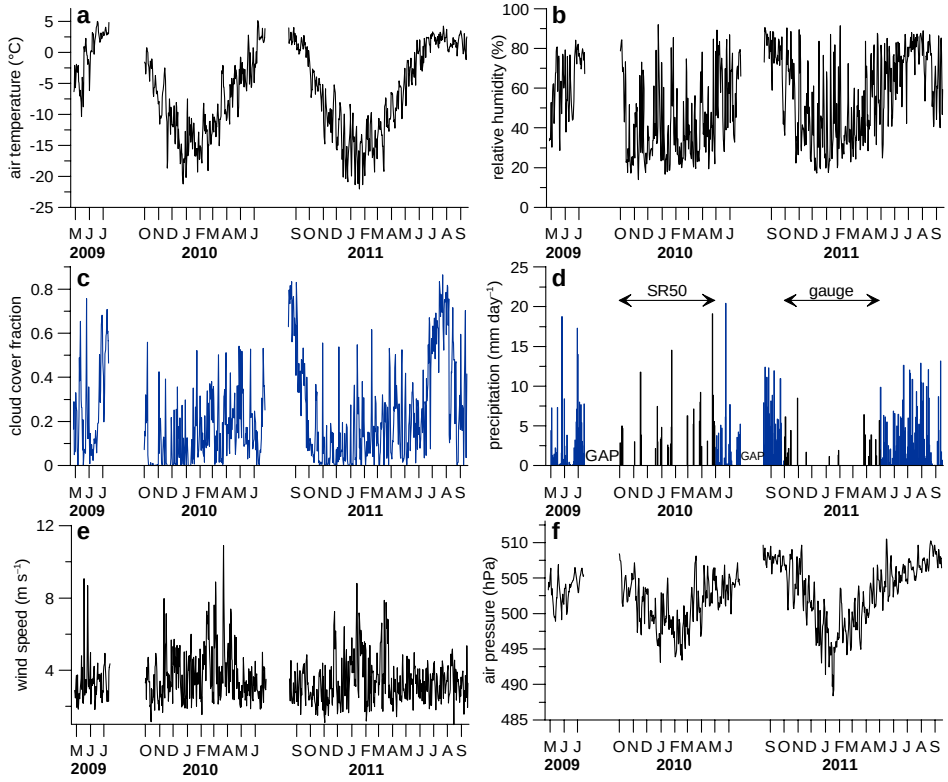

Fig. 3. Daily means of **(a)** air temperature, **(b)** relative humidity, **(c)** cloud cover fraction, **(e)** wind speed, **(f)** air pressure, and **(d)** daily sums of all-phase precipitation at AWS1 between 27 April 2009 and 15 September 2011. Ticks on the x-axes indicate the first day of the respective month, and black (blue) signifies measurements (atmospheric model output). In panel **(d)**, the data gaps due the measurement failure are indicated to distinguish them from zero precipitation, and the measurement source for surface accumulation in winter is indicated as well (SR50 or gauge). For consistency, SR50 derived precipitation (actual height) has been converted to w.e. values by a density of 200 kg m^{-3}.

in this region (Sect. 2.1). The remaining subsurface layers are at 0.1, 0.2, 0.3, 0.4, 0.5, 0.8, 1.4, 2, 3, 5, and 7 m depth, which yielded a stable solution in all runs. For these model layers the initial temperature profile is specified from the available subsurface measurements (Sect. 2.1) by linear interpolation. A digital terrain model at 60 m resolution (re-sampled from the Shuttle Radar Topography Mission; Rabus et al., 2003) and the 2009 glacier extent (Bolch et al., 2010) constitute the topographic boundary (Fig. 1). A concise overview of the MB model, to illustrate which atmospheric forcing variables affect each energy and mass flux in the model, is provided in Table 1 in Mölg et al. (2009a).

Since the last model version (Mölg et al., 2009a) we added a few new features based on published work: (i) the local air temperature gradient can vary between day and night/morning to better capture the effect of katabatic wind development (Petersen and Pellicciotti, 2011); (ii) snow settling and compaction is simulated from the viscous fluid assumption (Sturm and Holmgren, 1998), and together with refreezing can contribute to snow densification. Specifically, we use Eqs. (5)–(8) in Vionnet et al. (2012); (iii) the transition solid–liquid precipitation is specified by a temperature range using linear interpolation (e.g. Mölg and Scherer, 2012), instead of abruptly by one air temperature threshold; (iv) a second stability correction for stable conditions is available so the turbulence damping factor can be calculated from either equation 11 or 12 in Braithwaite (1995); (v) the energy flux from precipitation may be included in the SEB (standard equation; e.g. Bogan et al., 2003); and (vi) a second parameterization of $L\downarrow$ from air temperature, water vapor pressure and cloud cover (Klok and Oerlemans, 2002) provides an alternative to the original formulation (Mölg et al., 2009b).

In light of the main goal to unravel the "monsoon footprint" in the glacier SEB/MB, we also attempt to quantify the model uncertainty. Thus, we perform a Monte Carlo simulation consisting of 1000 realizations, in which all important model parameters, including the vertical gradients for extrapolation of meteorological conditions, as well as selected structural uncertainties, are varied (Appendix A). This simulation is conducted for one point at the location of AWS 1, since the computational expense for the distributed model is too large. From the point results we select three combinations of parameter settings that are maintained for running the full distributed MB model (Appendix A), i.e. the final ensemble size is 3. One of these combinations, henceforth called

reference run (REF), reflects the best match with the measured surface height change. The other two settings are used to spread the uncertainty range around REF (Appendix A). All error estimates in the remainder of the text are based on this method, unless otherwise noted. One advantage of the method is that the uncertainty does not simply increase with progressive simulation time like in classical sensitivity experiments where one parameter is changed and all others are held constant. Instead, in the present method the uncertainty range is mainly dependent on surface conditions (snow vs. ice), which is shown later in the model evaluation (Sect. 3.1) and in Appendix A.

2.4 Characterization of monsoon dynamics

The specific component of the Asian monsoon system that affects the Tibetan Plateau is the Indian Summer Monsoon (ISM) (Ding, 2007). To relate glacier energy/mass fluxes to the ISM we focus on (i) interannual variability associated with the monsoon onset and cessation, and (ii) intra-seasonal variability tied to the active/break cycle – both of which are typical oscillations in the monsoon dynamics (Webster et al., 1998; Ding, 2007). To characterize these dynamics we follow Prasad and Hayashi (2007) in identifying active and break periods of the ISM, since the authors showed that their method satisfies both precipitation- and circulation-based indices used in previous research. A horizontal wind shear index (HWSI) is defined as the difference in the 850 hPa zonal wind (from NCEP/NCAR reanalysis data: Kalnay et al., 1996) between a southern (5–15° N, 40–80° E) and northern region (20–30° N, 70–90° E). Active periods are defined as days with HWSI $> 1\sigma$ over 2009–2011, and break periods as days $> 1.5\,\sigma$ in the northern region's zonal wind (i.e. strong westerlies).

Figure 4a shows that establishment of the ISM circulation in the examined years occurred between 1 June (2011) and 21 June (2009), when the curves start to rise. The ISM ceased between 16 September (2011) and 19 October (2010), when the curves flatten. The former interval contains the mean onset date in terms of convection and rainfall in the Zhadang region (Webster et al., 1998). Thus, we define the yearly period of *monsoon onset* (*monsoon cessation*) from 1–21 June (16 September–19 October), which comprises the time windows used in the subsequent analysis (Sect. 3.4). Only two years are available for the analysis of the cessation period, as AWS data in 2011 ends before 16 September. However, both 2009 and 2010 contain the interval 1–19 October and cover the respective cessation dates (6 October in 2009 and 19 October in 2010).

Between 22 June and 15 September (*ISM core season*) the succession of active periods and the remaining non-active (weak and break) periods characterizes the intra-seasonal ISM variability (Prasad and Hayashi, 2007). Consequently, we have 105 active days and 39 non-active (weak/break) days during the core season in our data set. Amongst the non-active periods, 10 days can be classified as break days, which will also be considered in the analysis (Sect. 3.4). These amounts of days are typical of the active/break cycle in the monsoon region (Webster et al., 1998).

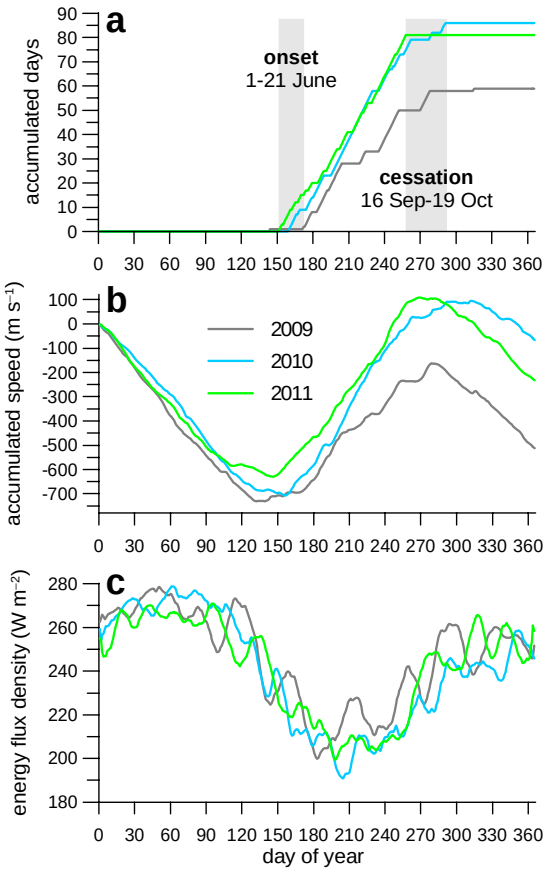

Fig. 4. (a) Accumulated active monsoon days, **(b)** accumulated horizontal wind shear index, and **(c)** top-of-atmosphere outgoing longwave radiation (14-day smooth) in the ISM region (65–105° E, 5–27.5° N; Ding, 2007) for 2009, 2010, and 2011.

Late monsoon onset and few active periods in 2009 (Fig. 4a) are in agreement with the weak cumulative strength of the ISM circulation in this year, as seen in Fig. 4b. To draw robust conclusions about monsoon activity, it is desirable to supplement the circulation index with a convection indicator (Wang and Fan, 1999), for which we extract top-of-atmosphere outgoing longwave radiation (Liebmann and Smith, 1996) over the ISM precipitation region. This second indicator yields the same result (Fig. 4c): 2010 and 2011 exceed 2009 in terms of ISM strength, which is particularly obvious from day 200–270 (ca. July–September) where 2009 shows markedly reduced convection (i.e. higher values in Fig. 4c than other years).

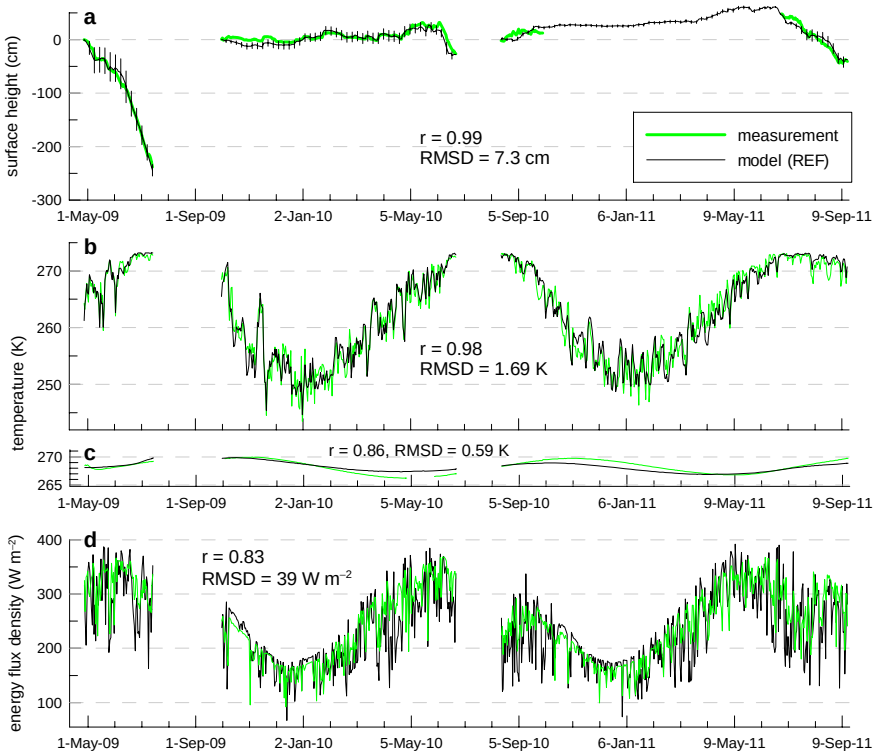

Fig. 5. Measurements versus MB model (REF run) at AWS1 with correlation and root-mean-square statistics. **(a)** Accumulated surface height change (error bars reflect model uncertainty as defined in Sect. 2.3), where every curve starts at 0 at the beginning of the periods; **(b)** glacier surface temperature; **(c)** subsurface temperature, whereas observed depth varies between start and end from 5.6–3.2 m in period 1, 5.3–5.1 m in period 2, and 4.4–4.1 m in period 3 (model values found by linear interpolation between layers; note a measurement gap within period 2 in May 2010); **(d)** global radiation. All data are daily mean values.

3 Results and discussion

3.1 MB model performance

We first evaluate the model at the point scale against observations at AWS1 in Fig. 5. The observations of a rather stable surface height during the winter months and surface lowering in summer are well reproduced (Fig. 5a). Regarding the latter, the model also captures the differential ablation between 2009 (strong) and 2011 (weak) well. Figure 5a also illustrates that the model uncertainty is greatest when snow cover is removed during periods of strong ablation (first half of the 2009 curve). This is a reasonable finding since modeling snow ablation, which is complicated by variable snow density and refreezing processes, is more difficult than modeling ice loss (e.g. Mölg et al., 2009a). The root-mean-square difference (RMSD) in Fig. 5a is only a tiny fraction of the observed amplitude (≈ 3 m), and the explained variance is very high.

A similarly-good performance is evident for glacier surface temperature (T_{sfc}), where the model captures the variability between 245–250 K mean daily T_{sfc} in winter and melting point in peak summer well (Fig. 5b). Measured T_{sfc} is based on emitted radiation (Table 1), which typically leads to uncertainties over glacier surface on the order of 2–2.5 K (e.g. Greuell and Smeets, 2001; Mölg et al., 2008). The RMSD in Fig. 5b, however, is below 2 K and corroborates the model. Moreover, the temperature variability in the subsurface (Fig. 5c) indicates that penetrating shortwave radiation is simulated reasonably well, since no systematic model bias is evident (Hoffman et al., 2008; Mölg et al., 2008). Finally we consider global radiation (an important driver of the SEB) in Fig. 5d, which shows good agreement for variability but a rather high RMSD. As soon as the two curves are a 5-day smooth, however, the RMSD drops below 10 % of the mean measured global radiation, and 10 % is indeed a more realistic estimate for measurement uncertainty in remote field places than the nominal accuracy (e.g. Michel et al., 2008). Thus, incoming shortwave radiation generated by the MB model can be interpreted reliably for means over five or more days, an averaging period always used in this study for the monsoon analysis.

To evaluate the distributed output of the model, we calculate the mean MB over the available ablation stakes as well as the associated gradient of the vertical balance profile (VBP) in Fig. 6a. Stake readings are available for three intervals, where the first one (June–July 2009) is contained in simulation period 1, and the third one (August–September 2010)

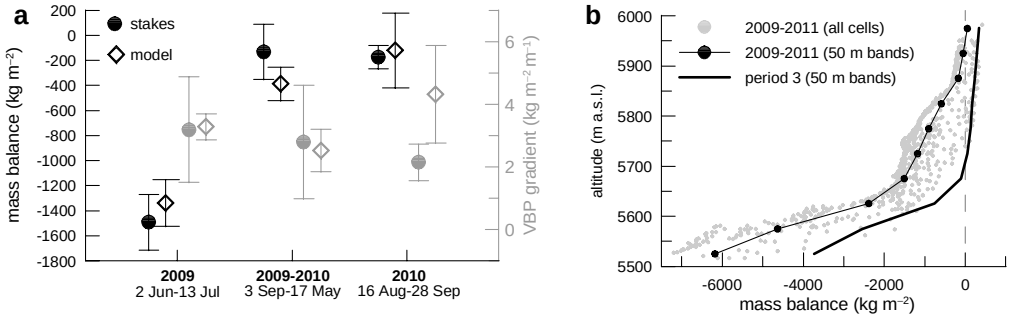

Fig. 6. (a) Mean mass balance (black) and vertical balance profile (VBP) gradient (grey) over the available ablation stakes (see Fig. 1) and the associated model locations (found by bi-linear interpolation) for the three intervals indicated at the bottom. Error bars are defined as 1σ for mass balance, and as 95 % confidence interval of the least-squares regression coefficient for the VBP gradient. **(b)** Modeled VBP over the entire simulation period (743 days) and period 3 (16 August 2010–15 September 2011). Model data in **(a)** and **(b)** are from the mean model (REF and two uncertainty settings, see Sect. 2.3).

in simulation period 3 except for the last 13 days in September 2010 (which are missing in the model). Since ablation late in September is usually small, we neglect these days. However, for the second interval of stake readings (3 September 2009–17 May 2010) the model is missing the entire month of September, since AWS data in period 2 starts on 1 October 2009. As ablation in early September can still be large, we run the MB model for September 2009 with only atmospheric model output as MB model forcing in order to better evaluate the results for the second interval (without September 2009, modeled MB has a positive bias). The only discrepancy in Fig. 6a concerns the VBP in the 2010 interval, where the model shows a higher gradient. However, there is agreement for the net mass flux in the same interval, which is most important as the area-integrated mass is of primary interest in this study. In all other cases, model and measurements agree within the error bounds (Fig. 6a), which gives us confidence that ablation processes are well simulated. Correlation coefficients between the single stakes and the associated model locations range between 0.5 and 0.81 in the three intervals of Fig. 6a (significant at 5 % based on a two-sided t-test), so the model also captures the basic structure of observed spatial variability. Note that strong mass loss in summer 2009 affected the entire ablation area (Fig. 6a), not only the AWS1 site (Fig. 5a).

3.2 SEB/MB characteristics

The altitudinal dependence of MB is shown in Fig. 6b, where areas of positive modeled MB are confined to elevations > 5750 m. The most notable feature of the VBP is the change in slope between 5600 and 5700 m. The only other distributed MB model study for a nearby region, which was also checked against stake measurements, is for Xiao Dongkemadi Glacier in the Tanggula Mountains for October 1992–September 1993. There, Fujita and Ageta (2000) also found steepening of the VBP around 5600 m; however, it occurs above the equilibrium-line altitude (ELA). If we examine only period 3, when ablation on Zhadang Glacier was rather weak (Figs. 5a and 6a), the "knee" in the VBP is also shifted along the x-axis and above the ELA (Fig. 6b). The single year studied by Fujita and Ageta (2000) was also characterized by weak ablation and a slightly positive glacier-wide MB. In the pure modeling study by Caidong and Sorteberg (2010), the steepening of the VBP occurs at ≈ 5800 m. These findings suggest that a dual VBP gradient is a robust feature of glaciers in the central Tibetan Plateau, and is more determined by altitude (weak above 5600–5800 m) than by the MB in a specific year. The result also fits with theoretical work, as the shape/gradient in Fig. 6b is almost a perfect mixture of the typical mid-latitude and subtropical VBP (Kaser, 2001). The explanation of the shape can be found in the energy fluxes: the VBP in Fig. 6b mimics the profile of QM (not shown), i.e. the energy available for melting diminishes clearly above 5700 m.

What processes drive the variability of the glacier-wide MB? In general (Fig. 7a; unit is $\mathrm{W\,m^{-2}}$), $S\downarrow$ (260.4) and $L\downarrow$ (200.9) dominate energy input, followed by QS (17.9), QC (4.5), and very small QPRC (0.2). Reflected shortwave radiation $S\uparrow$ (-187.7), $L\uparrow$ (-268.2), and QL (-10.9), QPS (-3.4), and QM (-13.7) are the energy sinks at the surface. A salient feature of the variability is the period of April–June both in 2010 and 2011, when $S\uparrow$ developed into an equally strong energy sink as $L\uparrow$ (i.e. when the two lower curves converge in Fig. 7a). The pattern was completely different in 2009, when anomalously low albedo weakened this process of energy removal. This, in combination with the highest $L\downarrow$ in the record, resulted in exceptionally high availability of melt energy in June–July 2009. Also noteworthy is a continuously negative QL on the monthly scale (Fig. 7a), which is not unexpected owing to the generally dry conditions in the central Tibetan Plateau.

The low reflectance of solar radiation in summer 2009 is clearly manifested in the MB components (Fig. 7b). First, surface melt is much higher than in the simulated months of

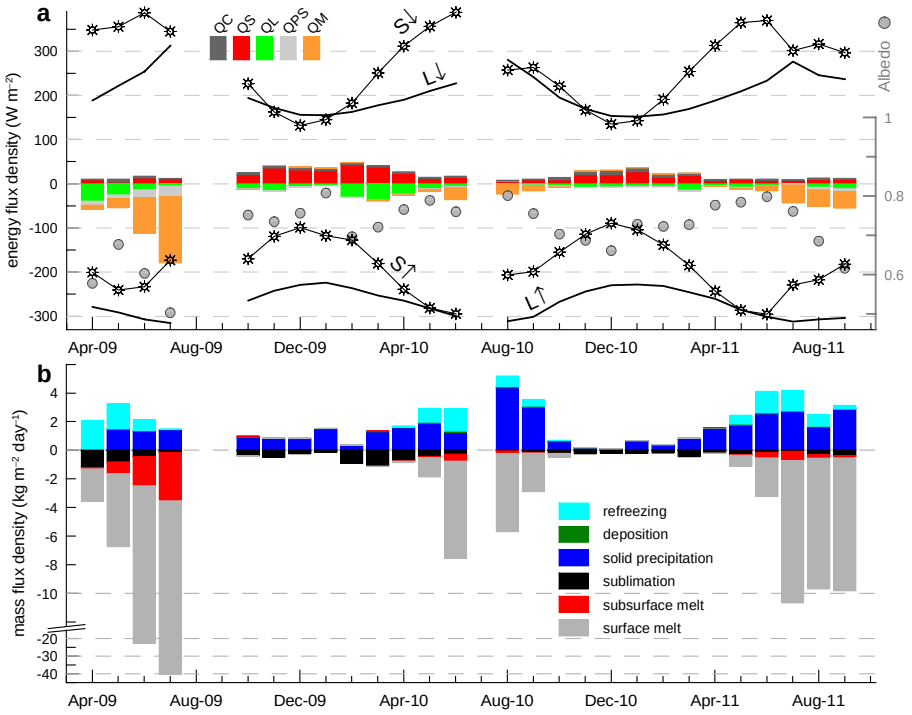

Fig. 7. Glacier-wide mean monthly **(a)** SEB components with surface radiation terms shown as lines, albedo as dots, and the remaining fluxes as bars (see Sect. 2.3 for abbreviations; precipitation heat flux is not shown as it is negligibly small) and **(b)** MB components from April 2009 to September 2011 in the REF run. Note the y-axis break and variable scaling in **(b)** due to large melt amounts in 2009.

the ablation seasons 2010 and 2011. Second, the high energy availability at the surface also caused more penetrating shortwave radiation and thus subsurface melt in 2009, which hardly occurs at other times. Due to the negative QL discussed above, sublimation is also evident in the MB record. It peaks in the months prior to monsoon onset (e.g. February–April 2010) when (i) T_{sfc} rises after the winter minimum (Fig. 5b) but the atmosphere remains rather dry, which favors a large surface-air vapor pressure gradient, and (ii) higher wind speeds (Fig. 3e) drive turbulence. Melting is absent from November–March, and in total 3.7 % of the modeled grid cell-scale melt happens at air temperatures below 0 °C. The latter was previously detected as a typical feature of glaciers in High Asia (e.g. Aizen et al., 2002). Refreezing of liquid water can occasionally be larger than accumulation by solid precipitation, generally in spring/early summer (Fig. 7b). This feature affirms previous statements that refreezing in the snow is an evident process on Asian high-altitude glaciers (Ageta and Fujita, 1996; Fujita and Ageta, 2000). On average, 13 % of surface melt refreezes, which is less than the 20 % obtained for Xiao Dongkemadi Glacier (Fujita and Ageta, 2000). The glacier-wide MB estimate from the REF run over the 743 modeled days ($-1.63 \times 10^3\,\mathrm{kg\,m^{-2}}$) is composed as follows (same unit): solid precipitation (1.02), refreezing (0.32), deposition (0.03), surface melt (-2.52), sublimation (-0.28), and subsurface melt (-0.20). The dominance of melt over sublimation at this site fits into the regional-scale pattern of ablation characteristics suggested by simplified MB modeling (Rupper and Roe, 2008).

We can also give two annual MB estimates for Zhadang Glacier, from 1 October to 30 September of the subsequent year for consistency with previous studies (Kang et al., 2009). Glacier-wide MB based on the model for 2009/2010 (2010/2011) is -154 ± 43 (-382 ± 41) $\mathrm{kg\,m^{-2}}$. The model data gap from 26 June to 15 August 2010 can be accounted for fairly reasonably, since the initial condition for period 3 on 16 August 2010 (based on observations) is a snow-free glacier (i.e. all the snow at the end of period 2 is assumed to be lost in the gap for the MB estimate). Still, 2009/2010 is more likely an over- rather than under-estimation, since ice may have also ablated in this gap. For 2010/2011, the model ends 15 days earlier in September 2011, which must be neglected. The values found here are within the range measured from 2005–2008, -1099 to 223 $\mathrm{kg\,m^{-2}}$ per year (Kang et al., 2009).

3.3 Sensitivity to processes and forcing

We performed sensitivity runs for the REF configuration in Table 2 because little is known about the importance of particular physical processes for the Tibetan glaciers. For these runs, certain structural components of the MB model (physical parameterizations) are deactivated, thus they differ from

Table 2. Sensitivity of glacier-wide MB over the entire simulation period (with respect to REF settings: -1.63×10^3 kg m^{-2}) to particular processes or (last four lines) changes in the forcing. Relative changes in parentheses. Winter (W) and summer (S) half years are defined as October–March and April–September, respectively.

Process	MB change (10^3 kg m^{-2})
no topographic shading	−0.193 (−12 %)
no stability correction for turbulence	−0.788 (−48 %)
no variation in surface roughness	−0.141 (−9 %)
no snow compaction/settling	−0.421 (−26 %)
no refreezing in snow	−0.199 (−12 %)
no subsurface melt	+0.339 (+21 %)
no penetrating shortwave radiation	−0.185 (−10 %)
$\Delta T_a = +1$ °C	−1.140 (−70 %); W: −0.053 (−3 %), S: −1.087 (−67 %)
$\Delta T_a = -1$ °C	+0.789 (+48 %); W: +0.034 (+2 %), S: +0.755 (+46 %)
precipitation: +10 %	+0.248 (+15 %); W: +0.015 (+1 %), S: +0.233 (+14 %)
precipitation: −10 %	−0.303 (−19 %); W: −0.017 (−1 %), S: −0.286 (−18 %)

usual sensitivity studies that change the value of one internal model parameter. From the calculations, we find little influence of using variable surface roughness lengths, while QPS, topographic shading and refreezing are on the order of the model uncertainty (0.21×10^3 kg m^{-2}). Also important are snow compaction/settling due to the resultant effects on snow density and subsurface melt. Suppressing the latter in the model leads to a saving of 0.34×10^3 kg m^{-2} in the MB, which is a higher absolute value than the subsurface melt term in the MB budget (-0.20×10^3 kg m^{-2}; see Sect. 3.2). This result indicates that the absence of subsurface melt has a feedback potential (mostly through the influence on snow depth and thus albedo). The strongest impact on MB is clearly from the stability correction of turbulent fluxes (Table 2). A strong feedback process also operates here, since the increase in absorbed shortwave radiation (5.3 W m^{-2}) from the initially turbulence-driven acceleration of snow ablation is eventually larger than the increase in the turbulent flux itself (ΔQS + ΔQL = 3.6 W m^{-2}). The stratification of the surface layer, on the other hand, reduces the strength of QS and QL to 54 % of their value in neutral conditions. Thus, not accounting for stability effects can lead to a strong negative MB bias, and Table 2 suggests that any physical MB model for Tibetan glaciers must include stability correction. Also, empirically-based models driven by T_a and precipitation alone should incorporate parameterizations of refreezing (e.g. Gardner et al., 2011) for Tibetan glaciers. Refreezing only shows an intermediate effect in Table 2, but due to the systematic seasonal importance in the MB (Fig. 7b) its neglect seems unwarranted as soon as seasonal variations are modeled and interpreted.

Furthermore we present in Table 2 classical, static MB sensitivity to constant changes in the two atmospheric forcings T_a and precipitation, using the typical perturbations of 1 °C and 10 %. First, in both T_a and precipitation perturbations, the MB change is hardly affected by conditions in winter. Hence, our study complements other evidence that the "summer accumulation type glaciers" of Asia are extremely sensitive to atmospheric conditions in the warm season, as discussed in the introduction. Second, the general MB sensitivity is calculated from Table 2 as the mean of absolute ΔMB for negative and positive perturbations before being converted to an annual value by multiplying with the factor 365/743, i.e. the number of days per year/days in model record. The annual value then amounts to (all units in the remaining paragraph in 10^3 kg m^{-2} = m w.e.) 0.47 per °C for the T_a perturbations, and to 0.14 per 10 % for the precipitation perturbations. These numbers can be compared to the few available studies that also employed identical perturbations to a glacier-wide, SEB-based MB model run over at least one year. A typical glacier in the European Alps (Klok and Oerlemans, 2002) seems to respond slightly stronger ($\approx$ 0.67 per °C and $\approx$ 0.17 per 10 %), while the extremely maritime and high-precipitation glaciers in New Zealand (Anderson et al., 2010) show a clearly higher sensitivity in the order of 2.0 per °C and 0.4 per 10 %. On the other hand, the high-altitude equatorial glaciers on Kilimanjaro (Mölg et al., 2009a) show a lower response in their dry climatic environment (0.24 per °C and 0.09 per 10 %) than Zhadang Glacier. Our calculations therefore support the generally accepted relation of increasing MB sensitivity as the climatic conditions become wetter and warmer (e.g. Fujita and Ageta, 2000).

Finally, we vary K_{WRF}, which is the only parameter used to scale MB model input (Sect. 2.2). This is done for period 1 as it relies entirely on scaled summer precipitation as input (Fig. 3d), shows the highest mass amplitude (Fig. 5a), and hence is most sensitive to the scaling. In concert with K_{WRF} we vary the density of solid precipitation, because (i) it is a free model parameter (Appendix A) and together with K_{WRF} determines the actual precipitation height, i.e. the variable that enters the MB model (Mölg and Scherer, 2012), and (ii) this procedure helps to explore the physically meaningful range of the scaling (see below). Multiplication of K_{WRF} by 1.25, 1.5 and 1.75 changes the glacier-wide MB in period 1

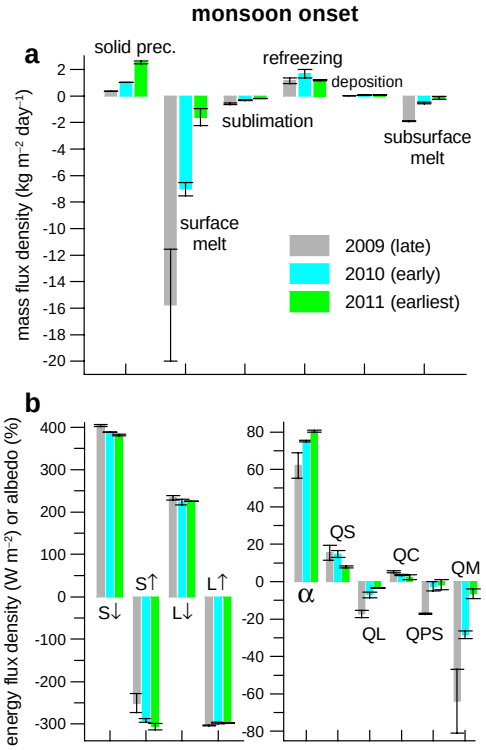

Fig. 8. Glacier-wide **(a)** MB and **(b)** SEB components during monsoon onset for 2009–2011. Error bars reflect model uncertainty as defined in Sect. 2.3. Note the different y-axis scaling in **(b)**.

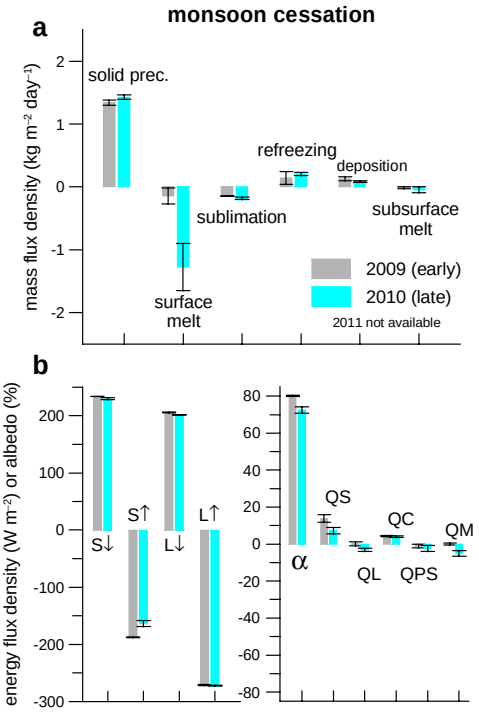

Fig. 9. Glacier-wide **(a)** MB and **(b)** SEB components during monsoon cessation for 2009–2010. Error bars reflect model uncertainty as defined in Sect. 2.3. Note the different y-axis scaling in **(b)**.

by 48, 96 and 143 kg m^{-2} (4, 7 and 11 %), respectively. The density of solid precipitation multiplied by the same factors increases from 225 to 281, 338 and 394 kg m^{-3}. Since values > 300 kg m^{-3} are rather unrealistic as seasonal mean (Table A1; Mölg and Scherer, 2012), we can certainly treat the $K_{\mathrm{WRF}} \cdot 1.75$ case as the upper sensitivity of the scaling approach. However, 143 kg m^{-2} is lower than the modeled uncertainty for period 1 (217 kg m^{-2}), so it can be ruled out that the scaling procedure alters the interpretation of MB model results.

3.4 Impact of monsoon variability

The final important question in this study is as follows: what is the role of the Asian monsoon in the SEB and MB processes discussed so far? We begin with the monsoon onset period 1–21 June. A series of systematic differences in the MB components, which are not affected by model error, is evident in Fig. 8a: the later the onset of the ISM, the (i) less accumulation by solid precipitation, (ii) more sublimation, (iii) more melt at the surface, and (iv) more subsurface melt as well. The overwhelming signal is the sharp increase in surface melt when the ISM commences late, as in 2009. Figure 8b sheds light on the underlying SEB processes. The stronger negative QL in 2009 drives intensified sublimation, and the higher latent energy flux of melting is clearly controlled by low albedo and reduced reflection of solar radiation. Thus, the timing of monsoon onset leaves a clear footprint on the glacier through the albedo effect, which leads to higher mass loss on the glacier the later the ISM is established in a particular year.

The monsoon cessation period from 1–16 October is the theme in Fig. 9. The clearest signal again concerns surface melt (Fig. 9a), however, this time in the opposite way: the presence of the monsoon coincides with both increased surface melt and slightly higher sublimation, and therefore with higher ablation on the glacier. Figure 9b illustrates that the higher melt amount is mainly a response to more absorbed shortwave energy. As differences in $S\downarrow$, $L\downarrow$, and solid precipitation are all small (Fig. 9), the higher albedo in 2009, and therefore the MB in the cessation period, seems to be mostly a delayed response to the snow cover evolution in the preceding core monsoon season: mean modeled snow depth on 1 October is 0.26 m higher in 2009 than in 2010. Thus, while it is difficult to elaborate the ISM impact during its cessation phase from only two years of data, the most important conclusion from Fig. 9 concerns the amplitude of the MB response, which is almost an order of magnitude smaller than during monsoon onset (cf. Fig. 8a). Hence, in general the ISM footprint at the end of the monsoon season is of little importance.

Figure 10 finally turns to the monsoon core season. The amplitude of mass fluxes (Fig. 10a) is comparable to the monsoon onset phase (Fig. 8a), but a series of systematic differences between active and non-active ISM days is not evident. Surface melt is higher during break periods than during active periods, but this difference does not hold for active versus non-active days (Fig. 10a). Solid precipitation, albedo and $L\downarrow$ are higher during non-active and break periods than on active monsoon days (Fig. 10), a surprising finding in the context of the core season given that monsoon air masses carry abundant moisture. We discuss this result in the paragraph below from three angles, but wish to first note that introducing a lead/lag of one or two days to the analysis in Fig. 10 for the monsoon/local SEB and MB relation does not change the results, since active and non-active periods occur as clusters of several consecutive rather than isolated days (Fig. 4a).

First, Prasad and Hayashi (2007) analyzed the synoptic structure of the intra-seasonal ISM variability in detail. Their Fig. 4 shows that convective centers are clearly shifted away from the main ISM precipitation region (defined by Ding, 2007, as 65–105° E, 5–27.5° N) during non-active periods, but little difference is evident over the Tibetan Plateau. An analysis of WRF output as well as satellite-based data (Fig. 11) supports the idea that the expected increase in precipitation during active monsoon days exists for the large-scale ISM area, but not for the Zhadang region. Thus, atmospheric variability over the ISM area does not seem to directly influence the Zhadang region. Second, Ueno et al. (2001) highlighted that precipitation on the Tibetan Plateau is dominated by weak but frequent events in the monsoon season that typically originate from mesoscale systems or local deep convective cells. Hence, the monsoon can be understood as the "background trigger", but local to mesoscale processes forced by the complex relief structure, as well as by the numerous lakes (e.g. Lake Nam Co close to the investigation site: Haginoya et al., 2009), modify the large-scale flow and cause a unique precipitation regime over the Tibetan Plateau. A recent study (Chen et al., 2012) also shows that one of the moisture source regions for the Tibetan Plateau in summer is situated on the plateau itself, and that local water recycling is evident in the same season. Third, it is well appreciated that mid-latitude flow impacts High Asia in the non-monsoon season, but less is known about mid-latitude intrusions during the monsoon. For instance, Ueno (2005) shows that mid-latitude flow anomalies affect the Tibetan Plateau as late as in mid May, so it cannot be ruled out that mid-latitude circulation also modifies ISM activity in the core season, especially when the monsoon onset occurs early. This should be investigated in more detail in future studies in the context of cryospheric changes in High Asia.

In summary, the moisture regime on the Tibetan Plateau during the ISM core season seems to be controlled by local and regional circulations, and/or by the fact that large-scale

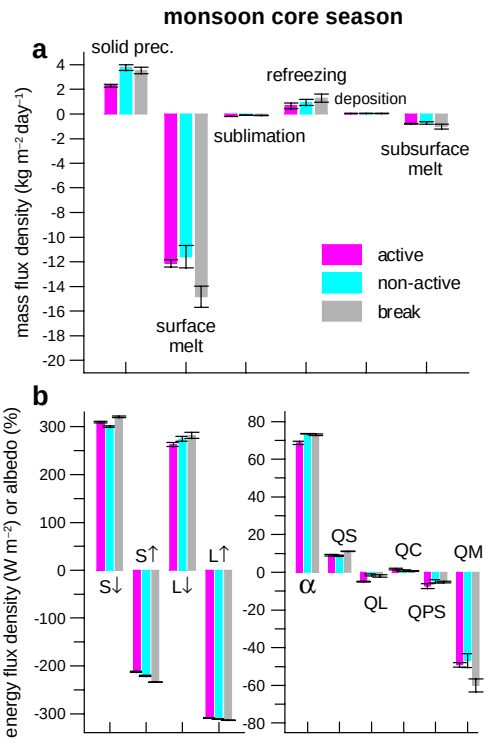

Fig. 10. Glacier-wide **(a)** MB and **(b)** SEB components in the monsoon core season for active, non-active, and break composites in 2009–2011. Error bars reflect model uncertainty as defined in Sect. 2.3. Note the different y-axis scaling in **(b)**.

ISM variability does not advance as far north as onto the central Tibetan Plateau. Therefore, local conditions may show a poor correlation to large-scale flow at this time of the year, e.g. as also found for measured precipitation at Lhasa from May to September (Caidong and Sorteberg, 2010). In this vein, local SEB and MB on Zhadang Glacier do not follow a systematic pattern in relation to large-scale ISM variability during the monsoon core season (Fig. 10).

4 Conclusions

Our state-of-the-art, distributed and physical mass balance model (Mölg et al., 2009a) reproduces the available measurements on Zhadang Glacier well, and a novel combination of the Monte Carlo and ensemble approaches allows for a reasonable time-varying estimate of model uncertainty. Model forcing is mainly based on field measurements, but also on output from high-resolution atmospheric modeling – a strategy that should become more common for data-sparse regions (e.g. Van Pelt et al., 2012). From the glacier model's output it is evident that interannual variability in mass balance has its physical origin in late spring/early summer, when the energy sink by reflected shortwave radiation is much weaker in high-ablation years than in other years. Affected

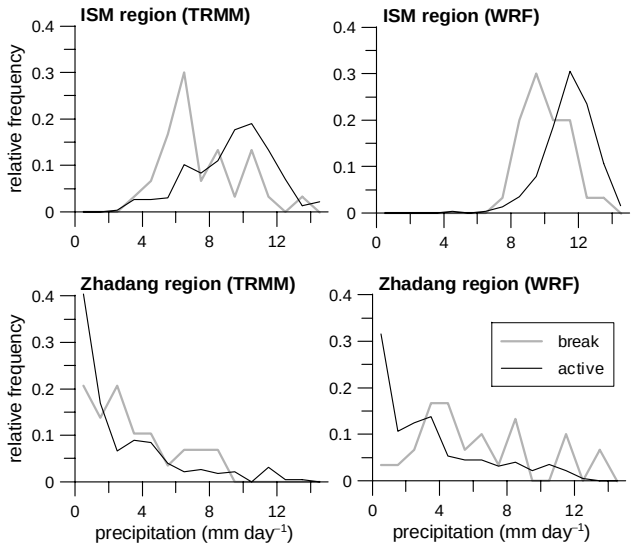

Fig. 11. Precipitation histograms in the ISM region (65–105° E, 5–27.5° N) and the region of Zhadang Glacier (90–91° E, 30–31° N) in the monsoon core season for active and break composites 2009–2011. Data are from (left) the Tropical Rainfall Measuring Mission satellite, product 3B42 (Huffman et al., 2007) and from (right) the WRF simulation (Sect. 2.2).

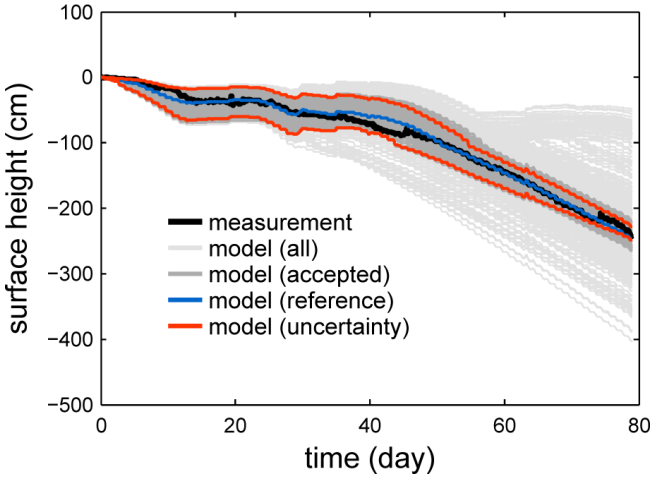

Fig. A1. Surface height change at AWS1 from 27 April to 14 July 2009, measurement versus 1000 model realizations.

mass and energy fluxes can differ by almost one order of magnitude between such contrasting circumstances.

This strong mechanism is closely linked to the onset period of the Indian Summer Monsoon from 1–21 June. Early (late) monsoon onset not only results in increased (decreased) accumulation, but through the albedo effect provides less (more) energy for surface melt, sublimation, and subsurface melt. This local footprint shows that Zhadang Glacier senses the monsoon dynamics in the onset period, which has a profound impact on interannual mass balance variability as well. In the monsoon cessation period during fall, however, the footprint on the glacier is relatively weak and also seems to be impacted by the snow cover evolution in the preceding core monsoon season. During the core season, we do not find any systematic relation in our data between monsoon dynamics and glacier mass/energy fluxes.

Coming back to the hypothesis from the introduction section, our results do confirm that the Asian monsoon has a vital impact on the glaciers of the Tibetan Plateau. However, results also demonstrate the need to differentiate in any hypothesis/research question between the phase of the monsoon, onset vs. intraseasonal variability. The present results show that in the core season of the monsoon, at least for 2009–2011, the glacier mass and energy budgets obey local-scale weather that is not related to large-scale circulation variability. Thus, local and regional meteorological systems seem to control atmospheric variability on the Tibetan Plateau from July to mid September (e.g. Ueno et al., 2001), which is corroborated here from a cryospheric viewpoint.

Appendix A

MB model uncertainty

For the free MB model parameters, values are assigned pseudo-randomly from either published ranges or ranges constrained by on-site measurements and atmospheric simulations (Table A1). Figure A1 shows the result for the first period of forcing data coverage. A total 450 of 1000 parameter combinations yield a root-mean-square difference (RMSD) $< 10\,\%$ of the measured amplitude and a deviation $< 10\,\%$ from the measurement at the final data point in the time series. These runs pass the test and therefore are "accepted" (dark grey in Fig. A1). Amongst them, the run with minimum RMSD (blue in Fig. A1) is the reference run (REF), while the two combinations that result in the largest positive and negative sum of the deviation from the measurement define the uncertainty (red). It is evident (Fig. A1) that uncertainty is larger for the first part of the period when snow is present (until day 51 in REF) and decreases afterwards. For the second and third period of data coverage, the criterion of 10 % is increased to 20 %, since the measured amplitude of surface height change is clearly smaller (see Fig. 5a); 65 and 62 parameter combinations pass the test in period 2 and 3, respectively. The 10–20 % criterions are greater than the nominal accuracy of the SR50, but in order to detect a robust monsoon footprint the aim is to avoid an underestimation of model uncertainty (thus we chose these rather large percentage criterions), and also provide space for uncertainty/error in the meteorological forcing data. Errors in the forcing data have been minimized as much as possible (Sects. 2.1 and 2.2) and are absorbed by the model parameters in our case. Even

Table A1. Free parameters in the MB model. Base value (V) and uncertainty (U) are from the literature, or constrained by on-site field measurements (meas. – Sect. 2.1) and atmospheric model output (atmo. – Sect. 2.2). For assumptions (assum.), the uncertainty is chosen to be relatively large (20 %). Bold parameters indicate structural uncertainty, others parametric uncertainty (e.g. Tatang et al., 1997). For the Monte Carlo simulation, values are assigned randomly from a uniform distribution, except for case 13 (normal distribution) since the authors provide uncertainty as one standard deviation (Gromke et al., 2011).

	Parameter(ization)	Value	References	Note
1	vertical air temperature gradient (night/morning: $>$ 21:00–13:00 local time)	$-0.0035\,\mathrm{K\,m^{-1}} \pm 10\,\%$	V + U: meas., Petersen and Pellicciotti (2011)	a
2	vertical air temperature gradient (day: $>$ 13:00–21:00 local time)	$-0.0095\,\mathrm{K\,m^{-1}} \pm 10\,\%$	V + U: meas., Petersen and Pellicciotti (2011)	a
3	vertical precipitation gradient	$+0.038 \pm 0.026\,\%\,\mathrm{m^{-1}}$	V: Li (1986), atmo.; U: atmo.	b
4	upper threshold for precipitation phase (all liquid above)	$6.5 \pm 0.5\,^{\circ}\mathrm{C}$	V + U: Fujita and Ageta (2000), Zhou et al. (2010), atmo.	
5	lower threshold for precipitation phase (all solid below)	$1 \pm 1\,^{\circ}\mathrm{C}$	V + U: Fujita and Ageta (2000), Zhou et al. (2010), atmo.	
6	**parameterization of $L\downarrow$**	n.a.	Mölg et al. (2009b) or Klok and Oerlemans (2002)	
7	layer thickness for surface temperature scheme	$0.5\,\mathrm{m} \pm 10\,\%$	V + U: Mölg et al. (2008)	
8	**parameterization of stable condition effect on turbulence**	n.a.	Eqs. (11) or (12) in Braithwaite (1995)	
9	clear-sky diffuse radiation fraction	$0.046 \pm 20\,\%$	V: Mölg et al. (2009b); U: assum.	
10	cloud effect in radiation scheme	$0.55 \pm 10\,\%$	V + U: Mölg et al. (2009b), meas.	
11	roughness length ice (momentum)	$1.7 \pm 1\,\mathrm{mm}$	V: Cullen et al. (2007); U: Brock et al. (2006)	c
12	roughness length ice (scalars)	$1.7 \pm 1\,\mathrm{mm}$	V: Cullen et al. (2007); U: Brock et al. (2006)	c
13	roughness length fresh snow	$0.24 \pm 0.05\,\mathrm{mm}$	V + U: Gromke et al. (2011)	c
14	roughness length aged snow (momentum)	$4 \pm 2.5\,\mathrm{mm}$	V + U: Brock et al. (2006)	c
15	roughness length aged snow (scalars)	$4 \pm 2.5\,\mathrm{mm}$	V + U: Brock et al. (2006)	c
16	density of solid precipitation	$250 \pm 50\,\mathrm{kg\,m^{-3}}$	V+U: Sicart et al. (2002), Mölg and Scherer (2012)	
17	initial snow depth	two- or threefold increase towards peak	V + U: assum.	d
18	initial snow density	$300\,\mathrm{kg\,m^{-3}} \pm 20\,\%$	V + U: assum.	
19	superimposed ice constant	$0.3 \pm 20\,\%$	V: Mölg et al. (2009a); U: assum.	
20	fraction of $S\downarrow \cdot(1-\alpha)$ absorbed in surface layer (ice)	$0.8 \pm 10\,\%$	V + U: Bintanja and van den Broeke (1995), Mölg et al. (2008)	
21	fraction of $S\downarrow \cdot(1-\alpha)$ absorbed in surface layer (snow)	$0.9 \pm 10\,\%$	V+U: Bintanja and van den Broeke (1995), Van As et al. (2005)	
22	extinction of penetrating shortwave radiation (ice)	$2.5\,\mathrm{m^{-1}} \pm 20\,\%$	V: Bintanja and van den Broeke (1995); U: assum.	
23	extinction of penetrating shortwave radiation (snow)	$17.1\,\mathrm{m^{-1}} \pm 20\,\%$	V: Bintanja and van den Broeke (1995); U: assum.	
24	fixed bottom temperature	$268.6 \pm 0.2\,\mathrm{K}$	V + U: meas.	e
25	ice albedo	0.3 ± 0.1	V + U: meas.	
26	fresh snow albedo	0.85 ± 0.03	V + U: meas.	
27	firn albedo	0.55 ± 0.05	V + U: meas.	f
28	albedo time scale	$6 \pm 3\,\mathrm{days}$	V + U: meas.	f
29	albedo depth scale	$8 \pm 6\,\mathrm{cm}$	V + U: meas.	f

[a] Determined from AWS1 vs. AWS2 data (Sect. 2.1). [b] The value 3.8 % per 100 m in the atmospheric model agrees well with the observations of Li (1986): 5 % per 100 m. Uncertainty is the 95 % confidence interval of the gradient in the atmospheric model output. [c] Several roughness lengths are specified because the MB model uses a scheme for space/time-varying roughness, which is described in Mölg et al. (2009a). [d] Between the measured initial snow depth at AWS1 and the highest altitude on the glacier in the digital terrain model; there are no measurements other than at AWS1, but field experience clearly suggests increasing snow depth with altitude. [e] 0.2 K is the amplitude of the measurements at that level (Sect. 2.1). [f] Optimal values of these three albedo scheme parameters are determined from measurements over period 2 (the only period with a reliable snow depth record), as described in Oerlemans and Knap (1998). The uncertainty reflects varying choice of the parameters that are held constant in the optimization procedure.

if the Monte Carlo simulation is done with the point model, vertical gradients influence the result due to the altitude difference between AWS1 and the associated grid cell in the digital terrain model (≈ 20 m). Also, these gradients clearly differ between the three chosen parameter combinations for the distributed runs (i.e. REF and two uncertainty settings), which allows us to capture uncertainty for the higher glacier reaches as well.

Acknowledgements. This work was supported by the Alexander von Humboldt Foundation (Thomas Mölg), by the German Research Foundation (DFG) Priority Programme 1372, "Tibetan Plateau: Formation – Climate – Ecosystems" within the DynRG-TiP ("Dynamic Response of Glaciers on the Tibetan Plateau to Climate Change") project under the codes SCHE 750/4-1, SCHE 750/4-2, SCHE 750/4-3, and by the German Federal Ministry of Education and Research (BMBF) Programme "Central Asia – Monsoon Dynamics and Geo-Ecosystems" (CAME) within the WET project ("Variability and Trends in Water Balance Components of Benchmark Drainage Basins on the Tibetan Plateau") under the code 03G0804A. We thank Eva Huintjes and Christoph Schneider, RWTH Aachen, for their active participation in field work and in AWS design questions, and for providing DEM and AWS2 data. We thank Tandong Yao, Shichang Kang, Guoshuai Zhang and the staff of the Nam Co monitoring station from the Institute of Tibetan Plateau Research, Chinese Academy of Sciences, for leading the glaciological measurements on Zhadang and for providing ablation stake and rain gauge data. We also thank the local Tibetan people for their assistance during field work.

Edited by: V. Radic

References

Ageta, Y. and Fujita, K.: Characteristics of mass balance of summer-accumulation type glaciers in the Himalayas and Tibetan Plateau, Z. Gletscherk. Glazialgeol., 32, 61–65, 1996.

Aizen, V. B., Aizen, E. M., and Nikitin, S. A.: Glacier regime on the northern slope of the Himalaya (Xixibangma glaciers), Quatern. Int., 97–98, 27–39, 2002.

Anderson, B., Mackintosh, A., Stumm, D., George, L., Kerr, T., Winter-Billington, A., and Fitzsimmons, S.: Climate sensitivity of a high-precipitation glacier in New Zealand, J. Glaciol., 56, 114–128, 2010.

Bintanja, R. and van den Broeke, M.: The surface energy balance of Antarctic snow and blue ice, J. Appl. Meteorol., 34, 902–926, 1995.

Bogan, T., Mohseni, O., and Stefan, H. G.: Stream temperature–equilibrium temperature relationship, Water Resour. Res., 39, 1245, doi:10.1029/2003WR002034, 2003.

Bolch, T., Yao, T., Kang, S., Buchroithner, M. F., Scherer, D., Maussion, F., Huintjes, E., and Schneider, C.: A glacier inventory for the western Nyainqentanglha Range and the Nam Co Basin, Tibet, and glacier changes 1976–2009, The Cryosphere, 4, 419–433, doi:10.5194/tc-4-419-2010, 2010.

Braithwaite, R. J.: Aerodynamic stability and turbulent sensible-heat flux over a melting ice surface, the Greenland ice sheet, J. Glaciol., 41, 562–571, 1995.

Brock, B. W., Willis, I. C., and Martin, M. J.: Measurement and parameterization of aerodynamic roughness length variations at Haut Glacier d'Arolla, Switzerland, J. Glaciol., 52, 281–297, 2006.

Caidong, C. and Sorteberg, A.: Modelled mass balance of Xibu glacier, Tibetan Plateau: sensitivity to climate change, J. Glaciol., 56, 235–248, 2010.

Chen, B., Xu, X. D., Yang, S., and Zhang, W.: On the origin and destination of atmospheric moisture and air mass over the Tibetan Plateau, Theoret. Appl. Climatol., 110, 423–435, doi:10.1007/s00704-012-0641y, 2012.

Cullen, N. J., Mölg, T., Kaser, G., Steffen, K., and Hardy, D. R.: Energy-balance model validation on the top of Kilimanjaro, Tanzania, using eddy covariance data, Ann. Glaciol., 46, 227–233, 2007.

Ding, Y.: The variability of the Asian Summer Monsoon, J. Meteorol. Soc. Jpn., 85B, 21–54, 2007.

Fujita, K. and Ageta, Y.: Effect of summer accumulation on glacier mass balance on the Tibetan Plateau revealed by mass-balance model, J. Glaciol., 46, 244–252, 2000.

Fujita, K. and Nuimura, T.: Spatially heterogeneous wastage of Himalayan glaciers, P. Natl. Acad. Sci. USA, 108, 14011–14014, 2011.

Gardner, A. S., Moholdt, G., Wouters, B., Wolken, G. J., Burgess, D. O., Sharp, M. J., Cogley, J. G., Braun, C., and Labine, C.: Sharply increased mass loss from glaciers and ice caps in the Canadian Arctic Archipelago, Nature, 473, 357–360, 2011.

Georges, C. and Kaser, G.: Ventilated and unventilated air temperature measurements for glacier-climate studies on a tropical high mountain site, J. Geophys. Res., 107, 4775, doi:10.1029/2002JD002503, 2002.

Greuell, W. and Smeets, P.: Variations with elevation in the surface energy balance on the Pasterze (Austria), J. Geophys. Res., 106, 31717–31727, 2001.

Goodison, B., Louie, P., and Yang, D.: WMO solid precipitation measurement intercomparison, 1998.

Gromke, C., Manes, C., Walter, B., Lehning, M., and Guala, M.: Aerodynamic roughness length of fresh snow, Bound.-Lay. Meteorol., 141, 21–34, 2011.

Haginoya, S., Fujii, H., Kuwagata, T., Xu, J., Ishigooka, Y., Kang, S., and Zhang, Y.: Air-lake interaction features found in heat and water exchanges over Nam Co on the Tibetan Plateau, SOLA, 5, 172–175, 2009.

He, Y., Zhang, Z., Theakstone, W. H., Chen, T., Yao, T., and Pang, H.: Changing features of the climate and glaciers in China's monsoonal temperate glacier region, J. Geophys. Res., 108, 4530, doi:10.1029/2002JD003365, 2003.

Hoffman, M. J., Fountain, A. G., and Liston, G. E.: Surface energy balance and melt thresholds over 11 years at Taylor Glacier, Antarctica, J. Geophys. Res., 113, F04014, doi:10.1029/2008JF001029, 2008.

Huffman, G. J., Adler, R. F., Bolvin, D. T., Gu, G., Nelkin, E. J., Bowman, K. P., Hong, Y., Stocker, E. F., and Wolff, D. B.: The TRMM Multi-satellite precipitation analysis: quasi-global, multi-year, combined-sensor precipitation estimates at fine scale,

J. Hydrometeorol., 8, 38–55, 2007.
Jiang, X., Wang, N. L., He, J. Q., Wu, X. B., and Song, G. J.: A distributed surface energy and mass balance model and its application to a mountain glacier in China, Chinese Sci. Bull., 55, 2079–2087, 2010.
Kalnay, E., Kanamitsu, M., Kistler, R., Collins, W., Deaven, D., Gandin, L., Iredell, M., Saha, S., White, G., Woollen, J., Zhu, Y., Leetmaa, A., Reynolds, R., Chelliah, M., Ebisuzaki, W., Higgins, W., Janowiak, J., Mo, K. C., Ropelewski, C., Wang, J., Jenne, R., and Joseph, D.: The NCEP/NCAR 40-year reanalysis project, Bull. Am. Meteorol. Soc., 77, 437–471, 1996.
Kang, S., Chen, F., Gao, T., Zhang, Y., Yang, W., Yu, W., and Yao, T.: Early onset of rainy season suppresses glacier melt: a case study on Zhadang glacier, Tibetan Plateau, J. Glaciol., 55, 755–758, 2009.
Kaser, G.: Glacier-climate interaction at low latitudes, J. Glaciol., 47, 195–204, 2001.
Kaser, G., Cogley, J. G., Dyurgerov, M. B., Meier, M. F., and Ohmura, A.: Mass balance of glaciers and ice caps: consensus estimates for 1961–2004, Geophys. Res. Lett., 33, L19501, doi:10.1029/2006GL027511, 2006.
Kaser, G., Großhauser, M., Marzeion, B.: Contribution potential of glaciers to water availability in different climate regimes, P. Natl. Acad. Sci. USA, 107, 20223–20227, 2010.
Kayastha, R. B., Ohata, T., and Ageta, Y.: Application of a mass balance model to a Himalayan glacier, J. Glaciol., 45, 559–567, 1999.
Klok, E. J. and Oerlemans, J.: Model study of the spatial distribution of the energy and mass balance of Morteratschgletscher, Switzerland, J. Glaciol., 48, 505–518, 2002.
Li, J.: The glaciers of Tibet, Science Press, Beijing, China, 1986.
Li, J., Wu, Z., Jiang, Z., and He, J.: Can global warming strengthen the East Asian Summer Monsoon?, J. Climate, 23, 6696–6705, 2010.
Liebmann, B. and Smith, C. A.: Description of a complete (interpolated) outgoing longwave radiation dataset, Bull. Am. Meteorol. Soc., 77, 1275–1277, 1996.
Maussion, F., Scherer, D., Finkelnburg, R., Richters, J., Yang, W., and Yao, T.: WRF simulation of a precipitation event over the Tibetan Plateau, China – an assessment using remote sensing and ground observations, Hydrol. Earth Syst. Sci., 15, 1795–1817, doi:10.5194/hess-15-1795-2011, 2011.
Michel, D., Philipona, R., Ruckstuhl, C., Vogt, R., and Vuilleumier, L.: Performance and uncertainty of CNR1 Net Radiometers during a one-year field comparison, J. Atmos. Ocean. Technol., 25, 442–451, 2008.
Mölg, T. and Kaser, G.: A new approach to resolving climate-cryosphere relations: downscaling climate dynamics to glacier-scale mass and energy balance without statistical scale linking, J. Geophys. Res., 116, D16101, doi:10.1029/2011JD015669, 2011.
Mölg, T. and Scherer, D.: Retrieving important mass-balance model parameters from AWS measurements and high-resolution mesoscale atmospheric modeling, J. Glaciol., 58, 625–628, 2012.
Mölg, T., Cullen, N. J., Hardy, D. R., Kaser, G., and Klok, E. J.: Mass balance of a slope glacier on Kilimanjaro and its sensitivity to climate, Int. J. Climatol., 28, 881–892, 2008.
Mölg, T., Cullen, N. J., Hardy, D. R., Winkler, M., and Kaser, G.: Quantifying climate change in the tropical midtroposphere over East Africa from glacier shrinkage on Kilimanjaro, J. Climate, 22, 4162–4181, 2009a.
Mölg, T., Cullen, N. J., and Kaser, G.: Solar radiation, cloudiness and longwave radiation over low-latitude glaciers: implications for mass balance modeling, J. Glaciol., 55, 292–302, 2009b.
Oerlemans, J. and Knap, W. H.: A 1 year record of global radiation and albedo in the ablation zone of Morteratschgletscher, Switzerland, J. Glaciol., 44, 231–238, 1998.
Park, H. S., Chiang, J. C. H., Lintner, B., and Zhang, G. J.: The delayed effect of major El Nino events on Indian Monsoon Rainfall, J. Climate, 23, 932–946, 2010.
Petersen, L. and Pellicciotti, F.: Spatial and temporal variability of air temperature on a melting glacier: atmospheric controls, extrapolation methods and their effect on melt modeling, Juncal Norte Glacier, Chile, J. Geophys. Res., 116, D23109, doi:10.1029/2011JD015842, 2011.
Prasad, V. S. and Hayashi, T.: Active, weak and break spells in the Indian summer monsoon, Meteorol. Atmos. Phys., 95, 53–61, 2007.
Rabus, B., Eineder, M., Roth, A., and Bamler, R.: The shuttle radar topography mission – a new class of digital elevation models acquired by spaceborne radar, J. Photogramm. Remote Sens., 57, 241–262, 2003.
Rupper, S. and Roe, G.: Glacier changes and regional climate: A mass and energy balance approach, J. Climate, 21, 5384–5401, 2008.
Scherler, D., Bookhagen, B., and Strecker, M. R.: Spatially variable response of Himalayan glaciers to climate change affected by debris cover, Nat. Geosci., 4, 156–159, 2011.
Sicart, J. E., Ribstein, P., Chazarin, J. P., and Berthier, E.: Solid precipitation on a tropical glacier in Bolivia measured with an ultrasonic depth gauge, Water Res. Res., 38, 1189, doi:10.1029/2002WR001402, 2002.
Skamarock, W. C. and Klemp, J. B.: A time-split nonhydrostatic atmospheric model for weather research and forecasting applications, J. Comput. Phys., 227, 3465–3485, 2008.
Sturm, M. and Holmgren, J.: Differences in compaction behavior of three climate classes of snow, Ann. Glaciol., 26, 125–130, 1998.
Tao, F., Yokozawa, M., Zhang, Z., Hayashi, Y., Grassl, H., and Fu, C.: Variability in climatology and agricultural production in China in association with the East Asian summer monsoon and El Niño Southern Oscillation, Clim. Res., 28, 23–30, 2004.
Tatang, M. A., Pan, W., Prinn, R. G., and McRae, G. J.: An efficient method for parametric uncertainty analysis of numerical geophysical models, J. Geophys. Res., 102, 21925–21932, 1997.
Ueno, K.: Synoptic conditions causing nonmonsoon snowfalls in the Tibetan Plateau, Geophys. Res. Lett., 32, L01811, doi:10.1029/2004GL021421, 2005.
Ueno, K., Fujii, H., Yamada, H., and Liu, L.: Weak and frequent monsoon precipitation over the Tibetan Plateau, J. Meteorol. Soc. Jpn., 79, 419–434, 2001.
Van As, D., van den Broeke, M. R., Reijmer, C., and van de Wal, R.: The summer surface energy balance of the high Antarctic plateau, Bound.-Lay. Meteorol., 115, 289–317, 2005.
van Pelt, W. J. J., Oerlemans, J., Reijmer, C. H., Pohjola, V. A., Pettersson, R., and van Angelen, J. H.: Simulating melt, runoff and refreezing on Nordenskiöldbreen, Svalbard, using a coupled snow and energy balance model, The Cryosphere, 6, 641–659, doi:10.5194/tc-6-641-2012, 2012.

Vionnet, V., Brun, E., Morin, S., Boone, A., Faroux, S., Le Moigne, P., Martin, E., and Willemet, J.-M.: The detailed snowpack scheme Crocus and its implementation in SURFEX v7.2, Geosci. Model Dev., 5, 773–791, doi:10.5194/gmd-5-773-2012, 2012.

Wang, B. and Fan, Z.: Choice of South Asian summer monsoon indices, Bull. Am. Meteorol. Soc., 80, 629–638, 1999.

Webster, P. J., Magaña, V. O., Palmer, T. N., Shukla, J., Tomas, R. A., Yanai, M., and Yasunari, T.: Monsoons: processes, predictability, and the prospects for prediction, J. Geophys. Res., 103, 14451–14510, 1998.

Xie, Y.: Autumn heat balance in the ablation area of Hailuogou Glacier, in: Glaciers and Environment on the Tibet Plateau (1), the Gongga Mountain, edited by: Xie, Z. and Kotlyakov, V. M., Science Press, Beijing, China, 1994.

Yang, W., Guo, X., Yao, T., Yang, K., Zhao, L., Li, S., and Zhu, M.: Summertime surface energy budget and ablation modeling in the ablation zone of a maritime Tibetan glacier, J. Geophys. Res., 116, D14116, doi:10.1029/2010JD015183, 2011.

Yao, T., Thompson, L., Yang, W., Yu, W., Gao, Y., Guo, X., Yang, X., Duan, K., Zhao, H., Xu, B., Pu, J., Lu, A., Xiang, Y., Kattel, D. B., and Joswiak, D.: Different glacier status with atmospheric circulations in Tibetan Plateau and surroundings, Nature Clim. Change, 2, 663–667, 2012.

Zhou, S., Kang, S., Gao, T., and Zhang, G.: Response of Zhadang Glacier runoff in Nam Co Basin, Tibet, to changes in air temperature and precipitation form, Chinese Sci. Bull., 55, 2103–2110, 2010.

Paper IV

Analysis of ice phenology of lakes on the Tibetan Plateau from MODIS data

Kropacek, J., **Maussion, F.**, Chen, F., Hoerz, S., and Hochschild, V. (2013): Analysis of ice phenology of lakes on the Tibetan Plateau from MODIS data, *The Cryosphere*, 7, 287-301, doi: 10.5194/tc-7-287-2013

Status: Published.

Own contribution:

- climate data acquisition/preparation
- figures 1 and 3, tables 4 and 5
- contribution to analysis and writing

The Cryosphere, 7, 287–301, 2013
www.the-cryosphere.net/7/287/2013/
doi:10.5194/tc-7-287-2013

The Cryosphere Open Access

Analysis of ice phenology of lakes on the Tibetan Plateau from MODIS data

J. Kropáček[1,2], F. Maussion[3], F. Chen[4], S. Hoerz[2], and V. Hochschild[2]

[1]Institute for Cartography, Dresden University of Technology, Helmholzstr. 10, 01069 Dresden, Germany
[2]Department of Geography, University of Tuebingen, Ruemelinstr. 19–23, 72070 Tuebingen, Germany
[3]Institut für Ökologie, Technische Universität Berlin, Rothenburgstr. 12, 12165 Berlin, Germany
[4]Institute of Tibetan Plateau Research (ITP), Chinese Academy of Sciences (CAS), 18 Shuangqing Rd., Beijing 100085, China

Correspondence to: J. Kropáček (jan.kropacek@tu-dresden.de)

Received: 5 April 2012 – Published in The Cryosphere Discuss.: 21 May 2012
Revised: 7 January 2013 – Accepted: 14 January 2013 – Published: 15 February 2013

Abstract. The Tibetan Plateau includes a large system of endorheic (closed basin) lakes. Lake ice phenology, i.e. the timing of freeze-up and break-up and the duration of the ice cover may provide valuable information about climate variations in this region. The ice phenology of 59 large lakes on the Tibetan Plateau was derived from Moderate Resolution Imaging Spectroradiometer (MODIS) 8-day composite data for the period from 2001 to 2010. Ice cover duration appears to have a high variability in the studied region due to both climatic and local factors. Mean values for the duration of ice cover were calculated for three groups of lakes defined by clustering, resulting in relatively compact geographic regions. In each group several lakes showed anomalies in ice cover duration in the studied period. Possible reasons for such anomalous behaviour are discussed. Furthermore, many lakes do not freeze up completely during some seasons. This was confirmed by inspection of high resolution optical data. Mild winter seasons, large water volume and/or high salinity are the most likely explanations. Trends in the ice cover duration derived by linear regression for all the studied lakes show a high variation in space. A correlation of ice phenology variables with parameters describing climatic and local conditions showed a high thermal dependency of the ice regime. It appears that the freeze-up tends to be more thermally determined than break-up for the studied lakes.

1 Introduction

The Tibetan Plateau (TP) was identified as one of the most sensitive regions in the world to changes in climate (Liu and Chen, 2000). At the same time, because of its unique properties, the TP has a strong impact on the global climate system, acting as a large heat source and moisture sink during the summer (Ueno et al., 2001; Hsu and Liu, 2003; Sato and Kimura, 2007). It impacts the monsoon circulation as a barrier to zonal and meridional air motion (e.g. Kurzbach et al., 1993; Barry, 2008). Recently, many studies have been focusing on various aspects of climate change impact on the TP, yet our knowledge of its mechanisms and regional variations is still limited. An unbiased analysis of the impact of the changing climate on the TP is often hindered by lack of ground measurements. Sparseness of meteorological stations, rough conditions, and difficult accessibility call for the use of remote sensing methods. Variations in climate in this area are reflected by several phenomena that are well documented by satellite records such as snow distribution (Shreve et al., 2009; Xu et al., 2009; Kropáček et al., 2010), changes in glacier extent (Ye et al., 2006, Bolch et al., 2010), and fluctuations in lake area (Bianduo et al., 2009), which can therefore be seen as climate indicators.

An important indicator of changes in climate derived from satellite data is lake ice phenology. This has been proved by a number of recent studies on regional (Ruosteenoja, 1986; Barry and Maslanik, 1993; Duguay et al., 2006; Che et al., 2009) and global scales (Walsh et al., 1998; Magnuson at al.,

2000). Interannual variation in lake ice phenology allows estimates of local climatic variability (Walsh et al., 1998). The lakes on the TP are distributed mainly in the central and western part, while meteorological stations are concentrated in the eastern part of the plateau (Liu and Chen, 2000). Derivation of lake ice phenology of Tibetan lakes could therefore fill a gap in our knowledge about the impact of climate change in this remote region.

1.1 Lake ice phenology

Ice phenology deals with periodic formation and decay of ice cover over water bodies and changes in its timing as a result of seasonal and interannual variations in climate. Formation of ice cover affects water bodies in high latitudes and altitudes, where the temperature during cold season falls below 0 °C for a sufficiently long time period. Appearance of ice is initiated when the lake surface water temperature falls below 0 °C. The date when detectable ice appears is referred to as the Freeze Onset (FO) in this study. The ice formation usually begins along the shore of shallow bays. Ice growth, especially during the formation of a new thin ice, can be interrupted by strong wind events. The date of the end of the freeze-up period, when the lake is fully ice-covered, is denoted as Freeze-up date (FU). An increase in temperature of the air above and the water below the ice in spring leads to a thinning of ice, eventually resulting in the ice breaking up. Appearance of a detectable ice-free water surface, after which no more total freeze-up occurs, is called Break-up date (BU). Further deterioration of ice leads to an eventual disappearance of ice, denoted as Water Clean of Ice (WCI).

Since there are discrepancies in the definition of variables describing the duration of lake ice cover, a comparison of ice phenology records for different regions is often biased (Brown and Duguay, 2010). Here we use two variables describing the duration of ice cover: Duration of Ice cover (DI), which results from subtraction of the WCI and FO, and Duration of Complete Ice cover (DCI), which is defined as the period between BU and FU. Many lakes on the plateau freeze up as late as January or February. A freeze-up in December or November is counted as ice cover for the following year for sake of simplicity, since it belongs to the same ice cycle. The choice of lake-ice phenology variables as a climate indicator varies among authors. Liston and Hall (1995) suggest that FU and BU, together with maximum ice thickness, are useful indicators of regional climate change, while Latifovic and Pouliot (2007) use the end of freeze-up and the end of break-up in their analysis of lake ice phenology in Canada instead; however, their choice was influenced by the availability of comparable in situ data.

1.2 Factors influencing the lake ice phenology

Sensitivity of lake phenology to climate variables has been investigated by several authors, where it was proved that BU/FU are highly sensitive to changes in air temperature. Using the results of a numerical simulation, a delay of as much as 4 weeks in freeze-up and break-up dates has been found by Liston and Hall (1995) for St Mary Lake in Canada in reaction to an increase in air temperature of 4 °C. They also attribute a sensitivity of ice phenology to a decrease in wind speed, which amounts to 2 weeks delay for Great Slave Lake in Canada. Air temperature has been suggested to be the most significant factor influencing the ice phenology, for instance by Livingstone (1997) and Kouraev et al. (2007). Analysis of ice phenology of numerous lakes and rivers in the Northern Hemisphere showed that a 1 °C change in mean air temperature corresponds to a change of about 5 days in the duration of the ice cover season (Skinner, 1993; Magnuson et al., 2000). However Weyhenmeyer et al. (2004) suggested that the relationship between temperature and break-up date is non-linear, leading to more sensitive reactions of ice break-up date, and to temperature changes in cold regions; however, it is not only temperature that determines the ice regime of lakes. There are several factors that affect both the duration of ice cover and the timing of ice phenology events, which can be divided into local and climatic factors. Apart from temperature, climate-related factors include wind speed, radiation and snow cover, the latter acting as an insulating layer. The absence of snow cover thus results in thicker ice cover, and leads in turn to later break-up (Kouraev et al., 2007). Local factors that are related to the ice regime of lakes are: lake bathymetry, salinity, altitude, shape of the shoreline, and lake area. The relative importance of particular factors for the lake-ice regime can be assessed using numerical models. For instance, Ménard et al. (2002) showed by using a one-dimensional thermodynamic lake ice model that lake depth is a determinant factor of freeze-up date for Canadian lakes.

1.3 Effects of lake ice phenology on local or regional climate

While the lake ice phenology is impacted by climate change, the lake ice regime can in turn influence the local or even the regional climate. Freeze-up and break-up processes lead to an abrupt change of lake surface properties (e.g. albedo, roughness), affecting mass and energy exchange between the lake water and atmosphere. The lakes basically act as heat sinks in summer and heat sources in autumn and winter (Wilson, 1977). The relatively cool/warm air above the lake will inhibit/enhance convection in summer/winter. The variations in ice phenology affect the amount of on-lake evaporation, since the lake-ice blocks the water–air interface, and sublimation does not compensate this effect.

A deep lake, such as Nam Co, can supply a large amount of heat energy to the atmosphere in the post-monsoon period (Haginoya et al., 2009). Air masses passing over a large, relatively warmer open-water area during winter can lead to heavy snow fall on the downwind shore. This so-called lake effect is well-known in the case of the large

Lurentinan Great Lakes (Eichenlaub, 1970). For the TP, lake effect has been described in the case of Nam Co, which is a large saline lake in the central part of the plateau (Li et al., 2009), and has been analysed by remote sensing data by Kropáček et al. (2010). This exchange process is obviously interrupted by lake freeze-up when no more warmer open-water is available. The relationship between lake freeze-up and lake-effect-determined snow cover in Nam Co Basin has been compared on time series of optical satellite and passive microwave data by Kropáček et al. (2011a).

1.4 Objectives

So far, little attention has been paid to the ice regime of lakes on the TP in comparison with high latitude lakes in other regions. The comprehensive analysis of Northern Hemisphere lake ice cover as a response to changing temperature presented by both Magnuson et al. (2000) and Dibike et al. (2011) (based on ground observations and modelling approaches, respectively), do not include the TP. Analysis of the ice regime of two large lakes on the TP has been carried out so far: the Qinghai Lake on the NE margin of the TP by Che et al. (2009) using data from a passive microwave satellite instrument, and Nam Co in the central TP by Ye et al. (2011), using a combination of passive microwave and optical satellite data. An overview of lake ice phenology of at least the largest lakes on the TP is, to our knowledge, still missing.

Ground observations of lake ice phenology on the remote TP with harsh winter conditions are not available. Such cost-intensive observations are furthermore complicated in the case of large lakes, where the surface of the whole lake cannot be observed from a shore station (Walker and Davey, 1993). The number of such stations is globally decreasing, for instance in Canada, decreasing from 140 sites in mid-1970's to less than 20 sites by the end of the 1990's. Obviously the analysis of lake ice phenology on the TP has to rely on satellite observations. This study is focused on the derivation of the time series of lake ice phenology events from MODIS 8-day snow composites, for a representative group of lakes on the TP, allowing for the calculation of the duration of the ice cover period. The relation of ice phenology to (i) local factors and to (ii) climate variables is analysed in order to assess the potential of ice phenology as a proxy for climate variability. Additionally, trends in duration of the ice cover in the period from 2001 to 2010 for the studied lakes are derived.

2 Study area

The TP has a mean elevation exceeding 4500 m a.s.l. and it is bordered by the high mountain ranges Karakorum and the Himalayas in the south and by Kunlun Shan in the north, extending to a length of several hundreds of kilometers. The

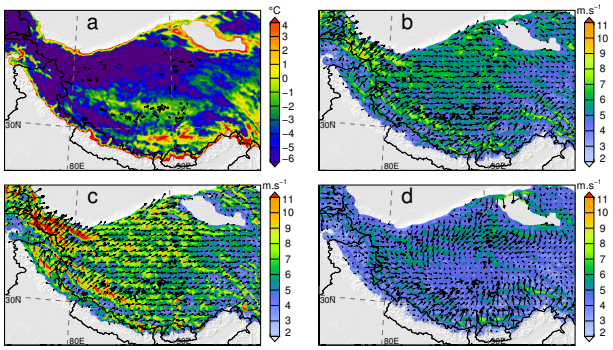

Fig. 1. Climate properties of the Tibetan Plateau for the period 2001–2010: **(a)** annual mean 2 m temperature, **(b)** annual mean 10 m wind speed, **(c)** mean 10 m wind speed for December, January and February, **(d)** mean 10 m wind speed for June, July and August. Data points below 3000 m a.s.l. have been masked out for clarity. Flow arrows are shown for every 7-th model grid point and indicate average wind direction and wind speed. See Sect. 3.4 for details on the reanalysed climate data set.

climate of the study region is under the influence of the westerlies in winter and the Asian monsoons in summer, and is characterized by wet summers and cold, dry winters. The most relevant climate parameters for this study are given in Fig. 1, which shows air temperature and wind speed/direction on the TP. The mean annual air temperature for 2001–2010 (Fig. 1a) features an evident dependency on orography, but also a negative gradient from south-east to north-west. The central and southern part of the TP have a mean annual temperature between 0 and 5 °C, dropping to far below 0 °C in the north-western part of the plateau. Only in the south, around Lhasa, does the mean annual temperature exceed 5 °C.

The climate of the TP is typical with a pronounced air circulation pattern driven by both the westerlies and the monsoon. Figure 1b, c and d shows, respectively, the mean 10 m wind speed and direction for 2001–2010. Wind speed is also strongly controlled by orography, with significantly higher wind velocities on mountain ridges. The dominant surface wind direction is west–east for most parts of the TP, which is owing to the prevailing influence of the westerlies in winter, with high velocities and a constant flow pattern. During the summer months the picture is different, with lower wind velocity and a cyclonic circulation forming in the low levels of the atmosphere and at the surface. This well-known low-pressure system is linked to the summer plateau heating and associated air updraft (Gao et al., 1981).

Analysis of meteorological records over the last decades reveals that both temperature and precipitation show an increasing trend (Liu and Chen, 2000; Xu et al., 2008). This general climate trend appears to feature some regional differences across the TP. The south-eastern part of TP becomes warmer and wetter, the south-western part follows the same

trend but with smaller amplitude, while the north-eastern part of the TP turns warmer and drier (Niu et al., 2004).

There are a large number of lakes on the TP differing in size, salinity, altitude and shape. Putting the limit of the minimum area to 0.1 km^2, their number reaches almost 6880, covering a total area of around 43 000 km^2, out of which 1260 lakes exceed 1 km^2 (Jiang et al., 2008). This makes the TP one of the largest lake systems in the world, unique in the high-elevation conditions. There are 7 lakes larger than 500 km^2 distributed mainly in the SW part of the plateau, out of which 4 exceed 1000 km^2. So far, there is little known about the bathymetry of even the largest lakes (Wang et al., 2010).

Most of the lakes on the TP are brackish or saline. An overview of salinity in three classes is presented by the "Map of the Lakes and Glaciers on the Tibetan Plateau" (Yao, 2007), while zoning of Tibetan lakes according to their hydrochemical type is described in Zheng and Liu (2009). Additionally, several figures on salinity of the Tibetan lakes are dispersed in literature. Nevertheless, a comprehensive data set describing the salinity of lakes on the TP is not available. Salinity, in the context of limnology, represents the total sum of ions dissolved in water. Most of the lakes on the TP represent a termini of inland drainage basins and are therefore salty. Only a few lakes, e.g. Taro Co in the SW part of the plateau, are through-flow lakes containing freshwater (salinity $< 3\,g\,L^{-1}$). Lakes in highly arid basins with little surface inflow may become hypersaline, which is, for instance, the case of Chabyer Caka (Zabuye Lake) with salinity of its surface brine reaching up to 425 $g\,L^{-1}$ (Zheng and Liu, 2009), or Lagkor Co in the SW part of the plateau. Average salinity of five hydrochemical zones defined by Zheng and Liu (2009) ranges from 135 to 352 $g\,L^{-1}$. Such high salinity indeed influences the freezing temperature of the lake water. The magnitude of the freezing point depression decreases with an increase of salinity. This in turn leads to a shortening of the ice cover period of salty lakes in comparison with freshwater lakes under the same conditions, i.e. climate, elevation, etc.

Levels and extent of lakes on the TP experienced high oscillations as a reaction to changes in climate conditions in the past (Zhang et al., 2011; Phan et al., 2012; Kropáček et al., 2011b). Furthermore, the lake shore may have shifted by even hundreds of meters during the last 40 yr (Bianduo et al., 2009; Kropáček et al., 2011b). These oscillations were related to an increased runoff, owing to the retreat of mountain glaciers, according to Yao et al. (2007), who analysed several catchments in Tibet. There is a lot of confusion in the terminology, caused by parallel usage of several versions of names for the same lake. Often more than two versions are used in Tibetan, while different transcriptions from Tibetan (often via Chinese) increase the confusion. Here, we decided to adhere to a convention introduced by the Map of the lakes and glaciers on the TP (Yao, 2007) compiled by the Institute of TP Research, Chinese Academy of Science (ITP, CAS).

3 Data and methods

3.1 MODIS instrument and data description

The study area features favourably low cloud cover during winter and spring periods, and the data acquisitions by optical instruments are not hindered by polar darkness, as is the case for instances of high-latitude Canadian lakes (Howell et al., 2009). Furthermore, the medium resolution optical data, which have spatial resolution in the order of several hundred meters, allow for derivation of ice phenology for tens of lakes on the TP. This is in contrast to passive microwave data, with spatial resolutions in the order of tens of kilometers, which are useful only for the largest lakes (Che et al., 2009). In this study, we used MODIS data for the derivation of lake ice phenology of Tibetan lakes.

The Moderate Resolution Imaging Spectroradiometer (MODIS) instrument is carried by two polar orbiting satellites, Terra and Aqua. The system is able to acquire data of the entire Earth's surface every 1 to 2 days in 36 spectral bands by both Terra (in the morning) and Aqua satellites (in the afternoon). In order to keep the data amounts at a reasonable level in this study we used the MODIS snow product MYD10A2 (Hall et al., 2007) instead of primary spectral bands. This product has a resolution of 500 m and is a composite classification image over an 8-day period, based on a Normalized Difference Snow Index (NDSI) and several other criteria tests that minimize the impact of cloud cover. The classification scheme matches the needs of this study as it contains the following five classes: Snow, No snow, Lake, Ice and Cloud.

3.2 Derivation of ice phenology dates from the MODIS 8-day composite data

The frozen lake surface is represented by classes Ice and Snow in the MODIS 8-day composites. We adopted the percentage of pixels classified as class water as a measure for the frozen status of the lake. This approach provides more accurate estimates than querying the number of pixels belonging to classes Ice and Snow, since it accounts better for missregistrations between MODIS scenes. For practical reasons, a threshold for the ice/water extent had to be set in order to detect the ice phenology dates. Factors 5 % and 95 % for the area of open water were chosen as thresholds for the identification of the ice phenology events in order to exclude the influence of noise. Such absolute thresholds would be sensitive to various disturbing effects. Instead we used an adaptive approach. The data set was first divided by a median into two parts: one below median corresponding to frozen lake, and the other one with the values above median corresponding to unfrozen conditions. In the next step, mean values were calculated from both data sets. The thresholds 5 % and 95 % were then applied to the range limited by these calculated mean values, instead of the whole range 0–100 %.

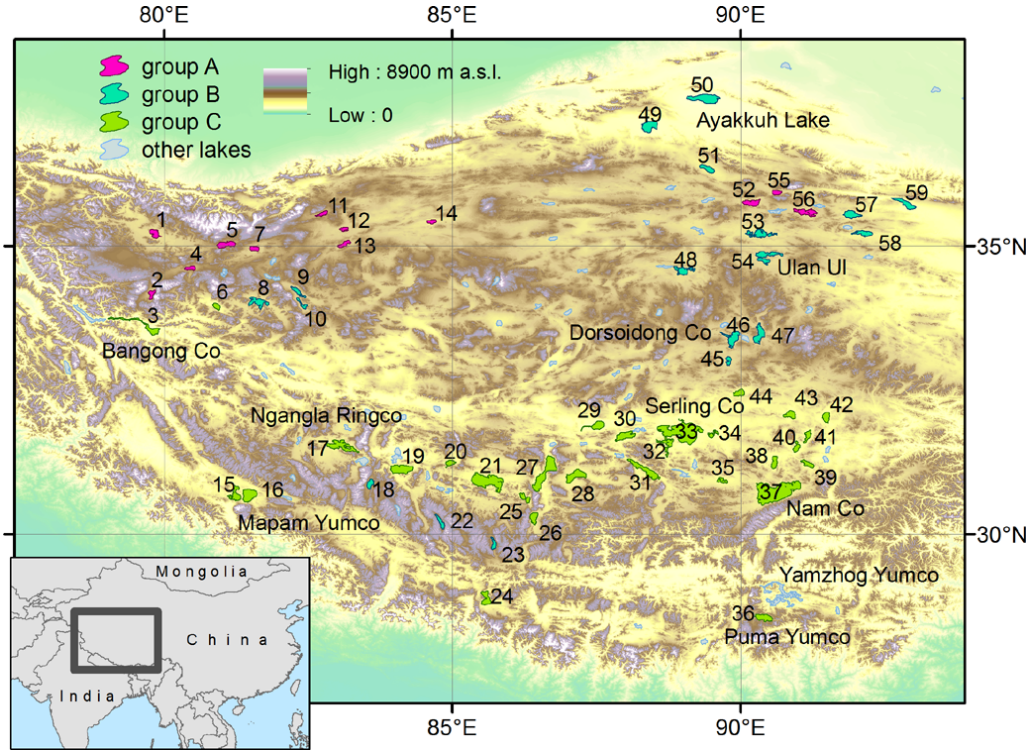

Fig. 2. Studied lakes are divided into three groups labeled as A, B and C: Group A: 1 Aksayqin, 2 Chem Co, 4 Longmu Co, 5 Gozha Co, 7 Bamgdog Co, 11 North Heishi, 12 Jianshui, 13 Bairab, 14 Yang, 52 Lixi'Oidaim Co, 55 Taiyang, 56 Hoh Xil Lake; Group B: 8 Lumaqangdong Co, 9 Memar Co, 10 Aru Co, 18 Palung Co, 22 Geysa Co, 23 Dajia Co, 45 Yaggain Canco, 46 Dorsoidong Co, 47 Migriggyangzham Co, 48 Dogai Coring, 49 Aqqik Kol, 50 Ayakkuh Lake, 51 Jingyu, 53 Xijir Ulan Lake, 54 Ulan Ul Lake, 57 Huiten Nur, 58 Dorge Co and 59 Hoh Sai Lake; Group C: 3 Bangong Co, 6 Geyze Caka, 15 Langa Co, 16 Mapam Yumco, 17 Ngangla Ringco, 19 Taro Co, 20 Dawa Co, 21 Zhari Namco, 24 Paiku Co, 25 Monco Bunnyi, 26 Xuru Co, 27 Tangra Yumco, 28 Ngangzi Co, 29 Dogze Co, 30 Urru Co, 31 Gyaring Co, 32 Co Ngoin, 33 Serling Co, 34 Pangkog Co, 35 Ringco Ogma, 36 Puma Yumco, 37 Nam Co, 38 Bam Co, 39 Npen Co, 40 Pung Co, 41 Dung Co, 42 Co Nag, 43 Zige Tangco, 44 Kyebxang Co.

This helped us to suppress the influence of mixed pixels and remaining discrepancies between the used lake outlines and the real shorelines.

For the extraction of ice phenology events from MODIS data, all lakes larger than 100 km^2 were selected. This resulted in 65 lakes that are well-distributed over the TP (Fig. 2). Out of this group, 6 lakes (Yinmar, Yamzhog Yumco, Nau Co, Chabyer Caka and Ringinyububu Co) had to be sorted out, since their histograms were too noisy for a reliable extraction of ice phenology. For instance, the Yamzhog Yumco has a highly complex tentacle-like shape that results in an extremely noisy signal. In order to account for regional differences in the ice regime of lakes in such a large area, the lakes were grouped by k-means clustering in a multi-dimensional space, defined by six variables (area, elevation, latitude, longitude, shape index, and mean temperature) into three groups denoted by abbreviations A, B and C respectively (see Fig. 2 and Table 1). These groups correspond to relatively geographically compact regions located in the north-west, north-east and south, respectively. This approach aims to select homogenous groups in terms of factors affecting ice phenology. Unfortunately, for further important factors, e.g. water volume and salinity, no comprehensive data was available. Mean monthly values of temperature and wind speed for each group (Fig. 3) show a clear seasonality of both the variables and differences in temperature amongst the groups. All three groups have maximum wind speed in February that corresponds roughly to the freeze-up period.

Table 1. Average values of basic characteristics and ice phenology for each lake group. Duration of complete ice cover (DCI) and duration of ice cover (DI) in days calculated as a mean value for each of the three groups over the period from 2001 to 2010 and standard deviations (σ) of both variables, which is a measure of variation of ice cover duration amongst the lakes in each group.

Group	Mean elev. (m a.s.l.)	Mean temp. (°C)	Mean area (km^2)	DCI (days)	σDCI	DI (days)	σDI
A	4925.5	−8.4	146.9	149	47.4	209	42.4
B	4780.0	−5.4	235.0	109	61.2	159	70.1
C	4600.0	−1.2	401.2	72	42.7	126	38.2

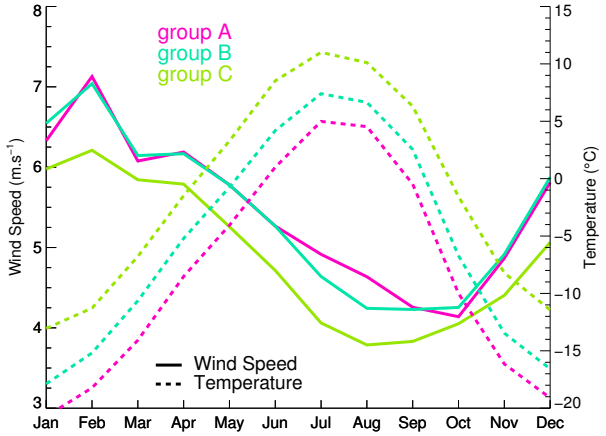

Fig. 3. Mean monthly values of 2 m air temperature and 10 m wind speed averaged for each lake group based on reanalysed climate data (see Sect. 3.4 for details) for the period 2001–2010. Both variables have a marked seasonality.

In order to get a regional overview of the ice regime on the TP, mean values of DI and DCI, phenology dates and trends for these groups were calculated and compared.

For definition of the spatial extents of the lakes we used Global Lakes and Wetlands Database – GLWD (Lehner and Döll, 2004), which is a global data set created as a combination of various available sources. The shorelines from the GLWD were checked against the MODIS images. In some instances, a certain amount of manual editing of the shoreline had to be involved, i.e. shifts or shape adjustments. In order to account for small variations of the lake shapes caused by mixed pixels, a mean image was calculated from MODIS images covering the autumn period after the monsoon and before the lake freeze-up. This image, which shows in one layer spatial variations of shape between single acquisitions, was used as a base layer for adjustments of the vector data. Another source of the size variation is probably a shoreline displacement connected to the lake volume/size oscillations (Bianduo et al., 2009; Wu and Zhu, 2008; Kropáček et al., 2011b) during the study period. These variations usually do not exceed the pixel size of MODIS.

In the next step, histograms were extracted from all MODIS images in the time series separately for each lake. Graphs of the percentage of open water area were constructed for the whole time period. The ice phenology events were then identified automatically as intersections of the curve representing open water with thresholds 5 % and 95 %. It was observed that multiple intersections with thresholds occur during the freeze-up and break-up period. This can occur owing to ice retreat caused by wind events and refreezing during the break-up period, or by cloud cover not accounted for by the 8-day compositing approach. Another reason is the presence of noise in the time series induced by classification uncertainty. The magnitude of the noise is given by variation of the water curve during the summer period, when it is not due to cloud cover.

In order to identify correctly the FU in case of multiple intersections of the open water curve with the threshold, which is mainly owing to noise, a point that has been set well-before possible early freeze up was used. The first threshold crossing was searched for from this point. Analogously, all the other ice phenology dates were identified (Fig. 4). Since the points of the open water have 8-day sampling, the exact day of each ice phenology date was obtained as a linear interpolation of the first point below and above the threshold. All identified points representing the ice phenology dates were plotted together with the open water curve for a visual check.

3.3 Validation of open water area derived from MODIS 8-days composites

The accuracy of the derivation of the open water area for a lake from the MODIS 8-day composites was estimated by a comparison with a number of reference satellite images (Fig. 5). These images cover various phases of freeze-up and break-up processes and are from various satellite sensors, including Envisat/ASAR (Advanced Synthetic Aperture Radar, wide swath mode data), Landsat, TerraSAR-X (Synthetic Aperture Radar) and SPOT (System for Earth Observation). For each validation image, a percentage of the open water area was derived and compared with the water curve from MODIS 8-day data, which was interpolated for each day. A time difference in days between each point representing the validation image and a corresponding point on the interpolated curve with the same percentage of open water was derived. An overall accuracy was then calculated as a root mean square error of these time differences in days. An RMS error equal to 9.6 days was obtained from twenty validation images for Nam Co. A mean time difference as low as 1.2 days proves that there is no systematic error in the open water area estimation.

3.4 Correlation of the lake phenology with the local and climate factors

In an attempt to identify the main drivers of the ice regime of the study area, the extracted ice phenology data was compared with data describing local and climate factors. The local factors, which were possible to describe by available data, were: latitude, longitude, elevation, area and shape. Latitude and longitude were retrieved from the GLWD using automatically generated centroids of lake polygons. The centroids were manually shifted inside the lake in several cases where they fell outside the lake polygons, owing to the concave shape of the shore. Lake altitude was identified in the Shuttle Radar Topography Mission (SRTM) digital elevation model using the edited centroids. A simple shape index was defined as a ratio between perimeter and area, which can be easily

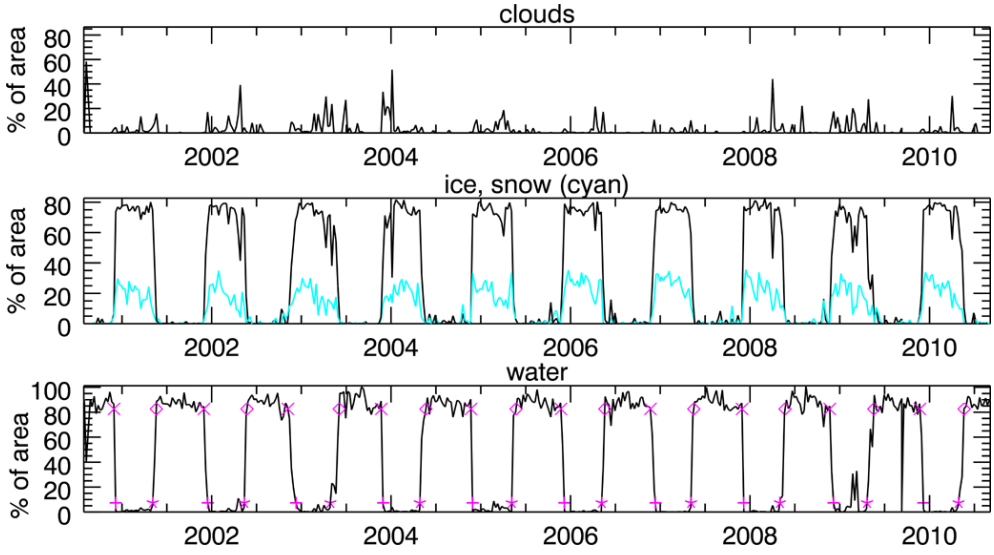

Fig. 4. An example of curves for open water (below), ice and snow (middle) and clouds (above), derived from MODIS 8-days composite data for Dorsoidong Co. The identified lake ice phenology events are marked with symbols: "x" for FO, "+" for FU, "*" for BU and "◊" for WCI. The noise in the total ice cover is often caused by confusion with clouds, which are actually rare in the winter period on the TP.

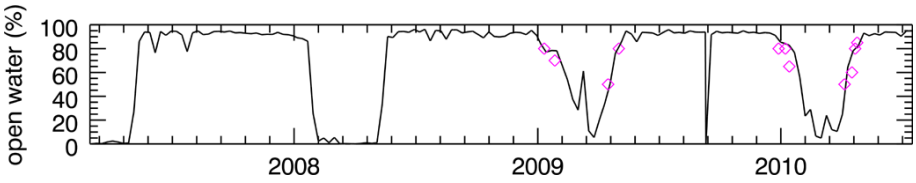

Fig. 5. Validation of the time series representing the area of open water for Nam Co, derived from MODIS 8-day composite data by comparing the open water curve with points representing the area of open water extracted from high-resolution satellite images (Landsat, Envisat/ASAR, TerraSAR-X and SPOT).

retrieved from the GIS layer of lakes. This index describes shape complexity of the shore. Lakes with a complex shape are likely to have a lower depth and, as a consequence, a lower thermal inertia in comparison with a rounded lake of the same size. Lakes with high shape index are likely to provide more shallow bays where the freeze-up usually starts. In addition, the parameter lake area itself is a proxy of the lake volume and is related to the thermal inertia of the lake.

For characterization of the climate for the selected lakes it is not possible to simply rely on measurements of nearby ground meteorological stations, because of their sparseness. The density of stations decreases towards the west, leaving the whole western part of the plateau with some five stations. To our knowledge, only Nam Co and Gyaring Co have a ground meteorological station located in the immediate vicinity of its lake shore. Instead we rely on a climate data set generated with the Advanced Weather Research and Forecasting (WRF) numerical atmospheric model (Skamarock and Klemp, 2008). Two-way grid nesting in the parent domain (30 km spatial resolution) yields to a regional-scale spatial resolution over the TP of 10 km (Fig. 1). All details of the model configuration are presented in Maussion et al. (2011). The 10 yr data set (2001–2010) is composed by consecutive model runs, reinitialized every day using data from the Global Forecast System's final analysis. The model is strongly constrained by the observed synoptic weather patterns and thus represents a regional atmospheric reanalysis.

Other studies successfully made use of this modelling technique for other regions of comparable characteristics (complex terrain, scarce observations), for example Iceland (Bromwich et al., 2005) or Greenland (Box et al., 2006). Producing a high-resolution reanalysis data set is part of a larger project (Maussion et al., 2012). For the present study we use time series of daily and monthly averages of hourly values for two variables (2 m air temperature and 10 m wind speed). A validation effort using 84 weather stations located within the 10 km domain, showed a good match between the measured and the simulated daily mean temperature (mean bias of −0.91 K, Root Mean Square Deviation (RMSD) of 2.74 K and coefficient of determination (r^2) of 0.92). Wind speed was validated for monthly means owing to its high variability. Direct comparison with observations is difficult because of the altitude difference between station and model grid points, but the inter-annual and annual variability of wind

speed are well-reproduced by the model with an r^2 of 0.44. Contours of mean temperature, wind speed and wind direction on the TP are shown in Fig. 1. Based on the reanalysed data, the mean annual temperature was identified for each lake. In addition we derived a thawing index as the cumulative temperatures above 0 °C, and the freezing index as below 0 °C days. These two variables characterize the temperature in periods that affect ice thawing and ice melting respectively. Correlation coefficients were calculated between variables describing ice phenology and those describing the local and climate factors (see Table 3).

4 Results and discussion

The lake ice phenology for 59 lakes on the TP has been extracted from the time series of MODIS 8-day composites for the period from 2001 to 2010. This allowed us to get an overview of the regional differences in ice regime over the TP (Fig. 6). There is a remarkable difference in the ice cover duration in terms of both DCI and DI amongst the studied lake groups (Table 1). The groups resulting from k-means clustering form well-defined geographical regions (Fig. 1). Group C in the south features the lowest values for both DCI and DI, while group A, containing mainly lakes in the north-west of the plateau, has the highest values for DCI and DI. The ice cover duration for group A is roughly two-times greater than group C. Owing to these high differences in ice cover duration amongst the groups, any general figures for the whole TP would not be representative. Statistical significance of the differences in DCI and DI amongst all three groups was checked by ANOVA (Analysis of variance between groups) test (F-value = 13.8, P-value = 0.001 for DCI and F-value = 9.2, P-value = 0.001 for DI). There is a high variation in both the DCI and DI in each group (Table 1). Grouping of the lakes into a higher number of clusters (four and five) using K-means clustering resulted in spatially heterogeneous regions and moreover did not lead to a decreased variation in ice phenology variables in the groups.

For several lakes it was not possible to extract the ice phenology because of a high level of noise in the signal obtained from the MODIS 8-day composites. This was most likely to be owing/attributed to the effect of mixed pixels. This effect impacts to a greater degree smaller lakes and lakes with complex shape. Since the lower limit of the used method, in terms of lake size, is shape dependant, it would be difficult to set a threshold of certain minimal lake size as a clear limitation of the method. In the case of some lakes, open water was misclassified as class land in the MODIS 8-day composites, which can be probably explained by a high sediment load in the water, for instance in the Ulan Ul Lake.

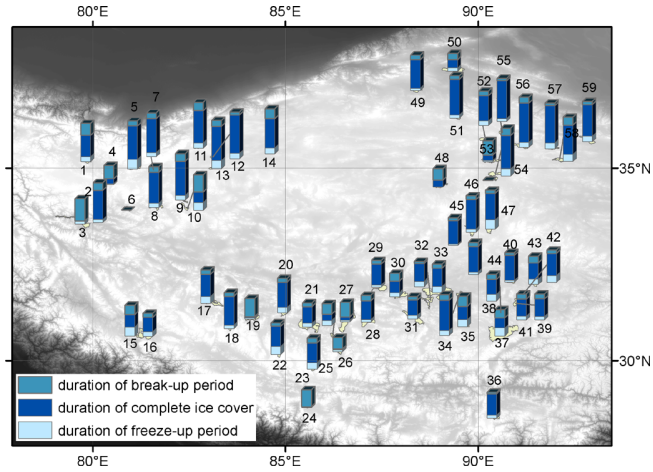

Fig. 6. Ice cover duration for the studied lakes on the TP showing duration of freeze-up period, duration of complete ice cover (DCI) and duration of break-up period as heights of the respectively coloured sections of bar symbols, whereas the total size of the bar represents the duration of ice cover (DI).

4.1 Validation of the no complete freeze-up events

It appears that there was no complete freeze-up in some years for several lakes. This may be surprising in an area with a harsh climate and with a long period of temperatures below 0 °C. This occurs also in the case of some large lakes like, for instance, Taro Co. In order to exclude the possibility that the phenomena is only random noise in the data, quick-looks of Landsat scenes were checked for the presence of open water in the relevant periods. The presence of open water during usual ice-on season was confirmed in this way for a number of lakes (see Table 2).

4.2 Results for the three groups

4.2.1 Group A

The main characteristics of this group are high elevation, low mean annual temperature, and relatively small size. This cluster contains only twelve lakes, which are located mainly in the very western part of the TP bordered from the north by the Kunlun Mts. (Fig. 2, Appendix A). Three lakes are located further in the east, somewhat separated from the main group surrounded by lakes of the group B. The reason why these lakes belong to the group A instead of the group B is a low mean-annual temperature (Lixi'Oidaim Co: −7.4 °C, Taiyang: −7.6 °C and Hoh Xil: −8.3 °C) when comparing to the mean value for the group B: −5.4 °C. The ice regime of lakes in this group is determined by cold continental climate that is reflected by a long ice cover period: DCI 149 and DI 209 days (Table 1). Longmu Co has a remarkably short duration of ice cover, both in terms of DI and DCI, and in some seasons it did not freeze-up completely, while the longest ice

Table 2. Validation of the no complete freeze-up events detected by MODIS data for selected lakes by Landsat data. Percentage of ice cover was determined from available Landsat images falling to the period of usual ice cover determined for the particular region.

Lake name (region)	Ice Cover from Landsat, Dates (% of ice cover from Landsat TM and ETM+)	Mean FU from MODIS (region)	Mean BU from MODIS (region)	Seasons of no complete freeze-up from MODIS
Taro Co (C)	6/2/09 (40 %), 15/2/2009 (60 %), 3/3/2009 (60 %), 2/2/10 (30 %), 18/2/10 (80 %), 6/3/10 (90 %)	18 Jan (7 Jan)	24 Jan (15 Apr)	2003–2005, 2008–2010
Tangra Yumco (C)	11/02/2010 (5 %), 27/02/2010 (40 %), 15/03/2010 (40 %)	21 Jan (7 Jan)	6 Feb (15 Apr)	2003, 2005–2007, 2009–2010
Nam Co (C)	5/2/2001 (70 %), 26/4/2001 (60 %)	13 Feb (27 Dec)	4 Apr (29 Mar)	2001, 2009
Xijir Ulan (B)	16/3/2001 (20 %), 19/3/2002 (20 %), 23/3/2003 (20 %), 23/2/2005 (20 %)	29 Dec (7 Dec)	25 Jan (18 Apr)	2001–2003, 2005–2006
Bangoing Co (C)	22/2/2004 (0 %), 7/1/2005 (60 %), 28/3/2005 (0 %), 2/3/2010 (10 %)	(8 Dec)	(14 Apr)	2001–2010

cover was observed by the Hoh Xil Lake. The anomaly of Longmu Co is not easy to explain since it is one of the highest lakes of the group and its mean temperature is not exceptionally high. The mean trend in the ice cover duration is 2.6 and 1.4 days yr^{-1} for DCI and DI, respectively (Table 3). Nevertheless, there is a high variation of the trend in this group (Appendix B). The mean trend in DCI is also strongly influenced by the high trend of the two lakes Aksayqin and North Heishi, with extremely low values of DCI in 2001 and 2003.

Table 3. Trends in days yr^{-1} in duration of both DCI and freezing period DI in the period from 2001 to 2010 for each group. The corresponding standard deviations of trends gives an idea about the variation of trends in each group.

Group	Trend DCI	Trend DI	σ trend DCI	σ trend DI
A	2.6	1.4	5.9	3.5
B	−0.2	1.7	4.9	4.8
C	−1.1	−1.6	3.1	2.1

4.2.2 Group B

This group contains in total eighteen lakes, out of which five are larger than 300 km^2 (Fig. 2, Appendix A). The lakes are mostly located in the northern part of the plateau. This group includes also three lakes in the west and another three lakes in the south-west surrounded by group A and C, respectively. This inclusion is due to their high elevation and low mean annual temperature. On average, lakes in this group feature a relatively long ice cover period (DCI 109 days and DI 159 days). There is a high variation of both DCI and DI (Table 1), which is influenced by a large variation of elevation (Appendix B) and a large range of latitude. Lake Ayakkuh features remarkably short mean DI of 88.3 days in comparison with the average DI of the group, mainly due to its low elevation (4161 m a.s.l.). Lakes Xijir Ulan, Yaggain Canco and Dogai Coring did not freeze up completely during the seasons 2001 and 2002. The mean trend in duration of lake ice period is negative in terms of DCI, but positive in terms of DI (Table 3), and amounts for −0.2 and 1.7 days yr^{-1}, respectively; however, there is again a high variation in both the DI and DCI in this group (Table 3). Four lakes in this region appear to have a rapid increase in the ice cover duration in terms of the DI: Dogai Coring, Xijir Ulan, Ayakkuh Lake and Yaggain Canco. All of these lakes have also a high variation in ice cover duration (Appendix B). In the case of Dogai Coring, Xijir Ulan and Yaggain Canco, both the increasing trend and the high variation are strongly impacted by the occurrence of no freeze-up events in the studied period.

4.2.3 Group C

Lakes of this group, which can be characterized by a low elevation and a high mean annual temperature (Table 1), are distributed approximately along the parallel 31° N in the south of the Tibetan Plateau (Fig. 2). This cluster contains twenty nine lakes, which is the highest number of all the three groups (Appendix C), including many of the largest lakes on the TP, e.g. Serling Co, Nam Co, Zhari Namco, Ngangla Ringco, Tangra Yumco and Taro Co. Except for Mapam Yumco, La'nga Co, Paiku Co and Puma Yumco, all lakes are in the central part of the plateau north from the Gangdise and Nyainqentanglha Mts., which act as a barrier to the monsoon circulation. The lakes Bangong Co and Geyze Caka are located in the western part of the plateau. The lake ice cover in this region, with an average DCI of 72 days and a DI of 126 days, is the shortest of the three regions. A number

of lakes in this group, e.g. Taro Co, Tangra Yumco, Paiku Co, Xuru Co, Monco Bunyi, Dajia Co, Bam Co, Npen Co in and Ringco Ogma, did not freeze up completely in some years. Gyeze Caka did not freeze-up completely during the whole period from 2001 to 2010, and there are no signs of it freezing up before, which could be due to its hypersalinity ("caka" means "salty lake" in Tibetan). Another interesting lake in this group is Tangra Yumco, which is regarded as the deepest lake on the TP (Wang et al., 2010). It is divided into a northern and a southern part by a narrow strait. The northern part freezes over later or not at all, as seen on Landsat images (for instance on 31 March 2007, 27 February 2008 and 15 March 2010). This is obviously caused by heat accumulation in the northern part that reaches a depth of 214 m, which is approximately 100 m deeper than the southern part (Wang et al., 2010). In the case of Taro Co, the influence of high salinity on this effect can be excluded since this lake, while having an outlet towards Chabyer Caka, is a fresh water lake (Wang et al., 2002). The DI of lakes in this region varies from 59.2 days (Paiku Co) to 204.8 days (Pangkog Co). In the case of Paiku Co it was only in 2008 that it froze over completely. Pangkog Co, which is located immediately to the east of Serling Co, is, with an altitude of 4529 m a.s.l., the third lowest lake in the group. A possible explanation of its long ice cover would be its relatively small size of 100.7 km^2 combined with its low depth. Mean trend in ice cover duration of this group is -1.1 and -1.6 days yr^{-1} in DCI and DI, respectively, with a relatively low variation (Table 3).

4.3 Trends in duration of ice cover for the three groups

Trends in DCI and DI for all regions were calculated as mean values of trends in each group. Statistical significance of trends in both DCI and DI are given in Appendices A, B and C. The mean values for each group are listed together with the corresponding standard deviations in Table 3. The statistical significance test by means of ANOVA (F-value = 3.45, P-value = 0.038 for trend in DCI and F-value = 0.05, P-value = 0.95 for DI) revealed that the groups do not differ in terms of mean trend. The standard deviations reveal the magnitude of differences in the behaviour of lakes in each group. The especially high standard deviation in the case of group B suggests that there is a strong influence from the local factors on the ice regime of these lakes. There are differences between the trend in DCI and the trend in DI for the same region, which reflects variation in duration of the freeze-up and break-up periods and it is also highly influenced by no complete freeze-up events. The differences in duration of the freeze-up and break-up periods may be caused by snow fall and wind events, insulating effect of snow cover slowing up the break-up, changes in albedo, etc. It has to be noted that the variations of ice cover duration of all groups exceed the calculated trend (Table 3), meaning that even if the lakes were grouped with respect to the factors influencing their ice regime, there are large differences in the behaviour of single lakes in each group. It is not easy to identify the reason for this; however, this may be owing to some local factors, for instance a feedback effect of snow cover.

Table 4. Correlation of ice cover duration (DCI – duration of complete ice cover and DI – duration of ice cover) and ice phenology dates with climate and local parameters calculated for all 59 studied lakes. Statistically significant values at the level of significance 0.02 are bold.

	DCI	DI	FO	FU	BU	WCI
longitude	0.16	0.18	**−0.30**	0.09	0.02	**−0.63**
latitude	**0.49**	**0.44**	**−0.45**	**0.33**	0.12	**−0.63**
altitude	0.40	**0.43**	−0.25	0.20	0.16	**0.65**
mean temp.	**−0.63**	**−0.70**	**0.61**	**−0.48**	**−0.35**	**0.64**
thawing index	**−0.63**	**−0.69**	**0.60**	**−0.48**	**−0.35**	**0.67**
freezing index	**−0.62**	**−0.69**	**0.60**	**−0.48**	**−0.34**	**0.61**
perimeter/area	0.29	0.27	**−0.37**	0.24	0.17	−0.09
area	**−0.34**	−0.27	**0.35**	−0.26	−0.07	0.06

4.4 Correlation of ice phenology variables with climatic and local parameters

Statistical analysis of the dependency of ice phenology variables on climatic and local parameters was carried out for all 59 studied lakes (Table 4). In order to assess the sensitivity of the analysis to lake selection and to suppress the influence of noise introduced by mixed pixels, which obviously play a more important role in the case of smaller lakes, the same analysis was repeated for lakes larger than 300 km^2 (18 lakes in total, Table 5). Results of the analysis showed that there is a high correlation between ice cover duration (DCI and DI) and temperature and both the thawing and freezing indices. The correlation coefficient, which is 0.62 to 0.63 for all lakes, increases up to 0.82 when selecting lakes larger than 300 km^2. This confirms a high thermal determination of lake phenology reported by many studies for a number of lakes worldwide (Ruosteenoja, 1986; Manguson et al., 2000; Latifovic and Puoliot, 2007). It is likely that the dependency of ice phenology on thermal variables would be even higher if the freezing point depression caused by salinity could have been taken into account. It appears that the correlation with the three variables based on temperature is higher for FO and WCI than for FU and BU. This suggests that the FO and WCI are more thermally determined. Surprisingly there is only a little difference in dependency of freeze-up and break-up events on the freezing and thawing indices. It appears that for the large lakes there is a high dependency of ice phenology on the shape index. The strikingly lower value for all lakes, including many smaller lakes around 100 km^2, is likely to be due to the generalized lake outlines in the lake database, which affects the reliability of the calculated shape index.

High correlation of ice cover duration ($r = 0.46$ for DCI and $r = 0.45$ for DI of the group of the large lakes) with latitude is in fact related to a decrease in temperature and irradiation towards the north. There is probably no strong driver

Table 5. Correlation of ice cover duration (DCI – duration of complete ice cover and DI – duration of ice cover) and ice phenology dates with climate and local parameters calculated for lakes larger than 300 km^2 (18 largest lakes). Statistically significant values at the level of significance 0.02 are bold.

	DCI	DI	FO	FU	BU	WCI
longitude	0.28	0.29	−0.33	0.18	0.11	**−0.63**
latitude	0.46	0.45	**−0.63**	0.52	0.16	**−0.63**
altitude	**0.75**	**0.73**	−0.54	0.36	0.31	0.50
mean temp.	**−0.80**	**−0.81**	**0.85**	**−0.73**	−0.47	**0.64**
thawing index	**−0.74**	**−0.75**	**0.81**	**−0.72**	−0.46	**0.66**
freezing index	**−0.82**	**−0.83**	**0.85**	**−0.73**	−0.47	**0.61**
perimeter/area	**0.79**	0.49	−0.49	0.43	0.26	−0.05
area	−0.32	−0.27	0.31	−0.07	0.14	−0.08

of the ice regime, which would lead to an east–west gradient in ice phenology, since only a weak correlation was revealed between the ice phenology variables and longitude. The ice cover duration appears to change with altitude, owing to a decrease in temperature connected to a decrease in air pressure, which can be expressed by temperature lapse rate. The selection of the large lakes leads to a significant increase in dependency of ice cover duration to altitude. This could have been likely caused by an inaccuracy in determination of lake ice phenology dates for smaller lakes with noisy time series of the satellite data classifications.

While there is no significant correlation of ice phenology variables with the perimeter/area index for all lakes, there is a strong correlation for the selected large lakes achieving $r = 0.79$ in the case of duration of complete ice cover (DCI). This shows that the shape complexity significantly affects the ice phenology, in particular, the freeze-up process providing shallow bays for the development of early ice. On the contrary, the break-up process seems to be largely unaffected by the shape complexity, even in the case of the large lakes. For the parameter area, a statistically significant correlation was found only in the case of DCI and FO (for the 18 largest lakes). This suggests that the studied lakes with a large area do not always have a large volume and thermal capacity.

The analysis revealed much higher dependency of FO and WCI to the climate and local parameters than in the cases of FU and BU. This can be caused by two factors. Either wind or the local conditions can lead to a higher variation in FU and BU, but do not affect the FO and WCI in the same way; alternatively, the spatial variation of BU and FU is purely caused by systematically higher inaccuracy in BU and FU estimation. Irrespective of the reason, the FO and WCI (respective DI as their difference) derived from MODIS 8-day snow composites appears to be a better indicator for changes in climate on the TP. While comparing the correlation of BU and FU with temperature, it is the FU that appears to be more thermally determined, which contradicts findings of Duguay et al. (2006), who found the BU to be a more robust indicator of climate oscillations than FU in the case of Canadian lakes. It seems that apart from temperature, there are some important factors that influence the break-up on the TP. Wind disturbances during the freeze-up period, marked by the maximum wind speed for all three groups in February (Fig. 3), are thus likely to have a lower impact on the freeze-up process than the insulating effect of snow cover on the break-up process in the case of Tibetan lakes.

5 Conclusions

Ice phenology was derived for 59 lakes on the TP from MODIS 8-day composite data. The obtained results imply that despite some influence of local settings, e.g. salinity, shape or wind exposure, the ice phenology of the Tibetan lakes is to a high degree determined by climate, especially the air temperature, which is in agreement with results from other cold regions in the world. This suggests that changes in the ice phenology of Tibetan lakes can indicate variations in regional climate. This is highly valuable since the area is only sparsely covered by ground observations, and at the same time plays an important role in regional and global climate. The ice phenology of the studied lakes, averaged over the acquisition period, features a high variation both in the lake groups and when comparing them, which reflects differences in geographical position (altitude and latitude) and local settings, e.g. shape complexity and salinity. This study showed that a number of Tibetan lakes do not freeze up completely during some winter seasons. This interesting phenomenon and its consequences for local climate, including snow cover regime, should have proper attention paid to it in further research. Both of the variables, used as a measure of duration of the ice cover, DI and DCI, can be used as climate indicators, although DI appeared to be more stable in terms of variation in two of the three regions than DCI. Additionally, the estimation of DCI is hindered when the lakes do not freeze up completely. It can be thus concluded that DI allows for a more reliable characterization of the ice regime from MODIS 8-days composites for lakes on the TP. Furthermore, it appears that FO is more thermally determined than BU in the case of the studied lakes.

The available time series of MODIS data allowed us to derive a trend in ice cover duration for the studied lakes, which appeared to be highly variable over the TP. The high variation remains even after grouping the lakes by clustering in a multi-dimensional space defined by relevant climatic and local variables. These facts, together with the relatively short evaluation period of ten years, would make any general conclusion about a trend in ice phenology on the TP dubious. Even though this study confirmed the usefulness of lake ice phenology as a climate indicator, the extraction of a significant trend for the assessment of changes in climate on the TP requires a longer time series of observations. The high variation of the trend amongst the lakes also points out the fact that whenever ice phenology will be used as a proxy of climate change on the TP, proper care has to be paid to the selection of a representative sample of lakes.

Appendix A

Table A1. Ice phenology of the lakes in group A.

Name	Elevation (m a.s.l.)	Label Fig. 1	Trend in DCI	f-test DCI	Trend in DI	f-test DFP	Mean DCI (days)	σ of DCI	Mean DI (days)	σ DI	Mean FO	Mean FU	Mean BU	Mean WCI
Aksayqin	4844	1	10.5	4.3	2.1	3.2	106.3	57.1	192.2	12.1	8 Nov	3 Dec	20 Mar	19 May
Bairab	4960	13	−0.4	0.0	0.7	0.2	169.7	37.1	241.0	14.6	23 Oct	3 Dec	22 May	21 Jun
Bamgdog Co	4904	7	2.6	1.2	2.8	3.0	169.1	21.6	219.8	16.3	4 Nov	25 Nov	14 May	11 Jun
Chem Co	4961	2	0.2	0.0	−1.4	1.6	145.3	19.7	197.4	10.6	13 Nov	28 Nov	22 Apr	30 May
Gozha Co	5080	5	2.4	2.0	2.0	0.9	165.6	16.3	240.9	19.0	9 Nov	28 Dec	12 Jun	8 Jul
Hoh Xil Lake	4886	56	−6.2	3.5	2.5	2.6	195.0	34.0	249.9	15.5	20 Oct	15 Nov	29 May	27 Jun
Jianshui	4889	12	−2.1	0.6	−3.5	7.4	190.9	24.3	230.9	15.1	21 Oct	17 Nov	26 May	9 Jun
Lixi'Oidaim Co	4870	52	7.5	25.6	7.2	11.5	124.7	25.9	171.6	28.5	15 Nov	9 Dec	12 Apr	5 May
Longmu Co	5004	4	−3.6	0.1	7.5	9.9	24.1	32.3	94.9	30.5	11 Jan	16 Jan	9 Feb	16 Apr
N. Heishi	5049	11	12.9	7.7	−1.0	0.9	160.2	55.7	228.6	9.1	5 Nov	2 Dec	11 May	22 Jun
Taiyang	4881	55	−0.6	0.2	−2.8	6.2	188.2	13.1	213.6	12.9	16 Nov	30 Nov	7 Jun	18 Jun
Yang	4778	14	8.3	3.9	0.0	0.0	146.1	62.7	224.4	16.6	29 Oct	27 Nov	22 Apr	10 Jun

Appendix B

Table B1. Ice phenology of the lakes in group B.

Name	Elevation (m a.s.l.)	Label Fig. 1	Trend in DCI	f-test DCI	Trend in DI	f-test DFP	Mean DCI (days)	σ of DCI	Mean DI (days)	σ DI	Mean FO	Mean FU	Mean BU	Mean WCI
Aqqik Kol	4251	49	2.4	4.6	1.2	2.2	140.6	12.3	176.4	8.0	16 Nov	28 Nov	18 Apr	11 May
Aru Co	4937	10	−1.2	0.0	−0.2	0.0	51.8	52.9	176.5	21.7	16 Nov	26 Dec	16 Feb	11 May
Ayakkuh Lake	3876	50	4.6	9.6	4.0	14.1	41.5	18.9	88.3	15.0	16 Dec	3 Jan	14 Feb	15 Mar
Dajia Co	5145	23	−3.4	0.9	−0.4	0.0	97.4	44.0	155.8	31.0	29 Nov	31 Dec	8 Apr	4 May
Dogai Coring	4818	48	2.5	0.5	7.3	3.4	33.4	30.7	90.8	40.8	31 Dec	1 Jan	4 Feb	1 Apr
Dorge Co	4688	58	1.9	0.3	−0.1	0.0	144.8	29.1	221.9	9.4	17 Oct	22 Nov	17 Apr	27 May
Dorsoidong Co	4929	46	−0.9	1.8	−0.6	0.3	146.9	6.5	180.8	10.4	22 Nov	7 Dec	3 May	22 May
Geysa Co	5198	22	−7.9	9.6	3.8	1.2	101.1	40.7	156.0	31.9	6 Dec	16 Jan	27 Apr	12 May
Hoh Sai Lake	4475	59	−1.2	4.3	−0.4	0.1	156.6	6.0	199.5	11.0	4 Nov	2 Dec	8 May	23 May
Huiten Nur	4753	57	−1.6	1.9	1.2	0.3	184.9	10.9	228.0	19.6	25 Oct	24 Nov	28 May	10 Jun
Jingyu	4713	51	3.3	3.0	−0.4	0.3	176.9	18.9	211.1	7.1	7 Nov	23 Nov	20 May	7 Jun
Lamaqang-dong Co	4812	8	−1.6	2.8	−0.4	0.1	153.3	9.7	204.6	14.8	15 Nov	8 Dec	10 May	7 Jun
Memar Co	4920	9	−0.7	0.2	−0.3	0.0	169.1	15.0	232.8	13.2	26 Oct	19 Nov	8 May	16 Jun
Migrig-gyangzham Co	4935	47	−4.3	2.4	−1.9	1.9	131.5	27.0	194.2	13.4	18 Nov	4 Jan	16 May	31 May
Palung Co	5101	18	−2.0	1.2	−1.5	0.6	144.3	16.9	179.9	17.2	16 Nov	3 Dec	27 Apr	15 May
Ulan Ul Lake	4855	54	3.4	0.7	−0.3	0.0	166.0	35.9	237.9	14.2	21 Oct	26 Nov	11 May	16 Jun
Xijir Ulan Lake	4772	53	−5.5	0.2	13.1	6.0	26.7	36.7	102.8	60.3	24 Dec	29 Dec	25 Jan	6 Apr
Yaggain Canco	4872	45	8.9	12.5	15.5	21.6	117.0	51.3	136.8	55.0	1 Dec	6 Dec	2 Apr	17 Apr

Appendix C

Table C1. Ice phenology of the lakes in group C.

Name	Elevation (m a.s.l.)	Label Fig. 1	Trend in DCI	f-test DCI	Trend in DI	f-test DFP	Mean DCI (days)	σ of DCI	Mean DI (days)	σ DI	Mean FO	Mean FU	Mean BU	Mean WCI
Bam Co	4560	38	−5.2	1.7	−0.6	0.2	73.3	41.6	132.2	12.2	6 Dec	9 Jan	22 Mar	17 Apr
Bangong Co	4239	3	0.0	0.0	1.0	0.3	0.0	0.0	125.4	15.6	17 Dec	1 Jan	1 Jan	21 Apr
Co Nag	4585	42	−4.1	3.0	−3.5	2.4	80.7	23.8	140.9	22.5	14 Nov	11 Dec	2 Mar	4 Apr
Co Ngoin	4563	32	1.1	0.1	−2.9	0.8	89.3	26.8	126.0	28.8	29 Nov	26 Dec	25 Mar	4 Apr
Dawa Co	4623	20	0.7	1.5	−2.1	1.6	124.8	5.3	172.3	15.5	12 Nov	10 Dec	14 Apr	4 May
Dogze Co	4465	29	−0.7	0.6	−1.7	3.1	104.6	7.7	132.2	9.7	6 Dec	16 Dec	31 Mar	18 Apr
Dung Co	4551	41	−4.5	8.0	−5.3	7.8	110.0	19.2	160.5	22.7	4 Nov	8 Dec	28 Mar	14 Apr
Geyze Caka	4525	6	0.0	0.0	−0.6	0.0	0.0	0.0	0.0	0.0	00 Jan	00 Jan	00 Jan	00 Jan
Gyaring Co	4649	31	−0.6	0.1	−1.2	1.8	76.0	21.0	113.2	8.8	30 Dec	18 Jan	4 Apr	22 Apr
Kyebxang Co	4615	44	−1.7	6.2	−2.1	16.9	127.2	7.8	161.6	7.7	22 Nov	6 Dec	13 Apr	3 May
Langa Co	4570	15	−0.2	0.0	2.1	0.5	60.8	35.1	154.3	25.5	10 Dec	25 Jan	27 Mar	13 May
Mapam Yumco	4585	16	−5.6	8.6	−4.2	10.9	71.6	23.5	114.9	16.7	9 Jan	2 Feb	15 Apr	5 May
Monco Bunnyi	4684	25	10.7	7.0	−0.1	0.0	30.6	37.3	106.8	21.4	24 Dec	17 Jan	17 Feb	10 Apr
Nam Co	4724	37	0.4	0.0	−3.2	13.1	50.3	29.4	130.8	12.4	4 Jan	13 Feb	4 Apr	15 May
Ngangla Ringco	4716	17	−0.7	0.6	−1.0	0.3	109.2	8.3	167.0	16.9	18 Nov	24 Dec	12 Apr	4 May
Ngangzi Co	4685	28	−1.2	0.6	−1.2	2.2	92.3	13.3	132.6	8.1	26 Nov	9 Dec	11 Mar	8 Apr
Npen Co	4666	39	−2.7	14.9	2.8	2.4	84.7	31.3	130.5	17.8	22 Dec	10 Jan	5 Apr	1 May
Paiku Co	4580	24	0.0	0.0	−4.0	2.1	3.8	12.0	59.5	26.7	3 Feb	6 Jan	10 Jan	4 Apr
Pangkog Co	4527	34	−0.8	1.1	−5.6	22.9	150.5	6.9	204.8	19.8	23 Oct	17 Nov	17 Apr	16 May
Puma Yumco	5013	36	−3.3	1.2	−1.1	1.5	106.0	27.6	128.2	8.7	28 Dec	12 Jan	28 Apr	6 May
Pung Co	4529	40	−2.7	0.7	−2.9	3.8	87.9	28.8	128.3	15.2	8 Dec	25 Dec	23 Mar	16 Apr
Ringco Ogma	4656	35	−5.7	1.3	−3.9	6.0	65.8	50.1	152.6	18.0	25 Nov	30 Dec	6 Mar	27 Apr
Serling Co	4539	33	−1.7	3.4	−3.0	9.4	91.3	9.5	142.0	12.5	4 Dec	3 Jan	5 Apr	25 Apr
Tangra Yumco	4535	27	3.0	2.3	−1.9	2.1	16.0	21.9	95.1	12.4	13 Jan	21 Jan	6 Feb	18 Apr
Taro Co	4567	19	−2.5	4.6	0.2	0.0	6.0	8.9	102.4	10.9	12 Jan	18 Jan	24 Jan	24 Apr
Urru Co	4554	30	−1.6	0.3	0.1	0.0	57.0	23.8	116.4	7.9	31 Dec	20 Jan	18 Mar	26 Apr
Xuru Co	4714	26	0.0	0.0	1.2	0.4	5.2	8.6	69.1	15.9	1 Feb	9 Feb	15 Feb	12 Apr
Zhari Namco	4612	21	0.8	0.5	−0.1	0.0	83.3	9.4	121.8	7.8	16 Dec	4 Jan	29 Mar	17 Apr
Zige Tangco	4568	43	−3.0	31.8	−2.4	28.7	123.7	10.1	145.6	8.3	1 Dec	10 Dec	13 Apr	26 Apr

Acknowledgements. This work has been carried out within the frame of the German Research Foundation (DFG) Priority Programme 1372, "Tibetan Plateau: Formation – Climate – Ecosystems" under the codes BU 949/20-13, SCHE 750/4-3. This study was supported by the National Natural Science Foundation of China (No. 41001033). The MODIS data were gratefully provided by the National Snow and Ice Data Center (NSIDC). We would like to thank two anonymous referees for providing detailed and useful comments that improved the revised version of the manuscript.

Edited by: T. Zhang

References

Barry, R. G.: Mountain Weather and Climate, Cambridge University Press, Cambridge, UK, ISBN 978-0-521-86295-0, 506 pp., 2008.

Barry, R. G. and Maslanik, J. A.: Monitoring lake freeze-up/break-up as a climate index, Glaciol. data rep., GD-25, 66–79, 1993.

Bianduo, Bianbaciren, Li, L., Wang, W., and Zhaxiyangzong: The response of lake change to climate fluctuation in north Qinghai-Tibet Plateau in last 30 years, J. Geogr. Sci., 19, 131–142, 2009.

Bolch, T., Yao, T., Kang, S., Buchroithner, M. F., Scherer, D., Maussion, F., Huintjes, E., and Schneider, C.: A glacier inventory for the western Nyainqentanglha Range and the Nam Co Basin, Tibet, and glacier changes 1976–2009, The Cryosphere, 4, 419–433, doi:10.5194/tc-4-419-2010, 2010.

Box, J. E., Bromwich, D. H., Veenhuis, B. A., Bai, L.-S., Stroeve, J. C., Rogers, J. C., Steffen, K., Haran, T., and Wang, S.-H.: Greenland ice sheet surface mass balance variability (1988–2004) from calibrated polar MM5 output, J. Climate, 19, 2783–2800, 2006.

Bromwich, D. H., Bai, L. H., and Bjarnason, G. G.: High-resolution regional climate simulations over Iceland using Polar MM5, Mon. Weather Rev., 133, 3527—3547, 2005.

Brown, L. C. and Duguay, C. R.: The response and role of ice cover in lake-climate interactions, Prog. Phys. Geog., 34, 671–704, doi:10.1177/0309133310375653, 2010.

Che, T., Li, X., and Jin, R.: Monitoring the frozen duration of Qinghai Lake using satellite passive microwave remote sensing low frequency data, Chinese Science Bulletin, 54, 2294–2299, 2009.

Dibike, Y., Prowse, T., Saloranta, T., and Ahmed, A.: Response of Northern Hemisphere lake-ice cover and lake-water thermal structure patterns to a changing climate, Hydrol. Process, 25, 2942–2953, 2011.

Duguay, C. R., Prowse, T. D., Bonsal, B. R., Brown, R. D., Lacroix, M. P., and Ménard, P.: Recent trends in Canadian lake ice cover,

Hydrol. Process, 20, 781–801, 2006.
Eichenlaub, V. L.: Lake effect snowfall to the lee of the Great Lakes: Its role in Michigan, B. Am. Meteorol. Soc., 51, 403–412, 1970.
Gao, Y., Tang, M., Luo, S., Shen, Z., and Li, C.: Some aspects of recent research on the qinghai-xizang plateau meteorology, B. Am. Meteorol. Soc., 62, 31–35, 1981.
Haginoya, S., Fujii, H., Kuwagata, T., Xu, J., Ishigooka, Y., Kang, S., and Zhang, Y.: Air-lake interaction features found in heat and water exchanges over Nam Co on the Tibetan Plateau, Sci. Online Lett. Atmos., 5, 172–175, 2009.
Hall, D. K., Riggs, G. A., and Salomonson, V. V.: updated weekly. MODIS/Aqua Snow Cover 8-Day L3 Global 500 m Grid V005, [list the dates of the data used], Boulder, Colorado USA: National Snow and Ice Data Center, Digital media, 2007.
Howell, S. E. L., Brown, L. C., Kang, K. K., and Duguay, C. R.: Variability in ice phenology on Great Bear Lake and Great Slave Lake, Northwest Territories, Canada, from SeaWinds/QuikSCAT: 2000–2006, Remote Sens. Environ., 113, 816–834, doi:10.1016/j.rse.2008.12.007, 2009.
Hsu, H. H. and Liu, X.: Relationship between the Tibetan Plateau heating and East Asian summer monsoon rainfall, Geophys. Res. Lett., 30, D2066, doi:10.1029/2003GL017909, 2003.
Jiang, Q., Fang, H., and Zhang, J.: Dynamic changes of lakes and the geo-mechanism in Tibet based on RS and GIS technology, Remote Sensing of the Environment: 16th National Symposium on Remote Sensing of China, edited by: Tong, Q., Proceedings of the SPIE, Vol. 7123, 71230S–71230S-8, 2008.
Kouraev, A. V., Semovski, S. V., Shimaraev, M. N., Mognard, N. M., Legrésy, B., and Rémy, F.: The ice regime of Lake Baikal from historical and satellite data: Relationship to air temperature, dynamical, and other factors, Limnol. Oceanogr., 52, 1268–1286, 2007.
Kropacek, J., Feng, C., Alle, M., Kang, S., and Hochschild, V.: Temporal and Spatial Aspects of Snow Distribution in the Nam Co Basin on the Tibetan Plateau from MODIS Data, Remote Sens., 2, 2700–2712, 2010.
Kropáček, J., Chen, F., Hoerz, S., and Hochschild, V.: Analysis of Icing Cycle and Snow Distribution in a Basin on the Tibetan Plateau from Passive Microwave and Optical Data, proceedings of the 31st Annual EARSeL Symposium 2011, Prague, Czech Republic, May–June 2011a.
Kropáček, J., Braun, A., Kang, S., Feng, C., Ye, Q., and Hochschild, V.: Analysis of lake level changes of Nam Co in Central Tibet by synergy of satellite altimetry and evaluation of optical satellite imagery, Int. J. Appl. Earth Obs., 17, 3–11, 2011b.
Kutzbach, J. E., Prell, W. L., and Ruddiman, W. F.: Sensitivity of Eurasian Climate to Surface Uplift of the Tibetan Plateau, J. Geol., 101, 177–190, 1993.
Latifovic, R. and Pouliot, D.: Analysis of climate change impacts on lake ice phenology in Canada using the historical satellite data record, Remote Sens. Environ., 106, 492–507, 2007.
Lehner, B. and Döll, P.: Development and validation of a global database of lakes, reservoirs and wetlands, J. Hydrol., 296, 1–22, 2004.
Li, M., Ma, Y., Hu, Z., Ishikawa, H., and Oku, Y.: Snow distribution over the Namco lake area of the Tibetan Plateau, Hydrol. Earth Syst. Sci., 13, 2023–2030, doi:10.5194/hess-13-2023-2009, 2009.
Liston, G. E. and Hall, D. K.: Sensitivity of lake freeze-up and break-up to climate change: a physically based modeling study, Ann. Glaciol., 21, 387–393, 1995.
Livingstone, D. M.: Break-up dates of alpine lakes as proxy data for local and regional mean surface air temperatures, Climatic Change, 37, 407–439, 1997.
Liu, X. D. and Chen, B. D.: Climatic warming in the Tibetan Plateau during recent decades, Int. J. Climatol., 20, 1729–1742, 2000.
Magnuson, J. J., Robertson, D. M., Benson, B. J., Wynne, R. H., Livingstone, D. M., Arai, T., Assel, R. A., Barry, R. G., Card, V., Kuusisto, E., Granin, N. G., Prowse, T. D., Stewart, K. M., and Vuglinski, V. S.: Historical trends in lake and river ice cover in the Northern Hemisphere, Science, 289, 1743–1746, 2000.
Maussion, F., Scherer, D., Finkelnburg, R., Richters, J., Yang, W., and Yao, T.: WRF simulation of a precipitation event over the Tibetan Plateau, China – an assessment using remote sensing and ground observations, Hydrol. Earth Syst. Sci., 15, 1795–1817, doi:10.5194/hess-15-1795-2011, 2011.
Maussion, F., Curio, J., Finkelnburg, R., Mölg, T., and Scherer, D.: A decadal regional atmospheric reanalysis dataset for central Asia and the Tibetan Plateau – examples of applications in hydrology and glaciology, Geophysical Research Abstracts, Vol. 14, EGU2012-3412-1, EGU General Assembly, 2012.
Ménard, P., Duguay, C. R., Flato, G. M., and Rouse, W. R.: Simulation of ice phenology on Great Slave Lake, Northwest Territories, Canada, Hydrol. Process, 16, 3691–3706, 2002.
Niu, T., Chen, L., and Zhou, Z.: The characteristics of climate change over the Tibetan Plateau in the last 40 years and the detection of climatic jumps, Adv. Atmos. Sci., 21, 193–203, doi:10.1007/BF02915705, 2004.
Phan, V. H., Lindenbergh, R., and Menenti, M.: ICESat derived elevation changes of Tibetan lakes between 2003 and 2009, Int. J. Appl. Earth Obs.,17, 12–22 doi:10.1016/j.jag.2011.09.015, 2012.
Ruosteenoja, K.: The date of break-up of lake ice as a climatic index, Geophysica, 22, 89–99, 1986.
Sato, T. and Kimura, F.: How does the Tibetan Plateau affect the transition of Indian monsoon rainfall?, Mon. Weather Rev., 135, 2006–2015, 2007.
Shreve, C., Okin, G., and Painter, T.: Indices for estimating fractional snow cover in the western Tibetan Plateau, J. Glaciol., 55, 737–745, 2009.
Skamarock, W. C. and Klemp, J. B.: A time-split nonhydrostatic atmospheric model for weather research and forecasting applications, J. Comput. Phys., 227, 3465–3485, 2008.
Skinner, W. R.: Lake Ice Conditions as a Cryospheric Indicator for Detecting Climate Variability in Canada, Proc. of Snow Watch '92, WDC-A Glaciological Data Report, 25, 204–240, 1993.
Ueno, K., Fujii, H., Yamada, H., and Liu, L. P.: Seasonal heating of the Tibetan Plateau and its effects on the evolution of the Asian summer monsoon, J. Meteorol. Soc. Jpn., 79, 419–434, 2001.
Walker, A. E. and Davey, M. R.: Observation of Great Slave Lake ice freeze-up and break-up processes using passive microwave satellite data, 16th Proceedings of the Canadian Symposium on Remote Sensing, 7–10 June, Sherbrooke, Quebec, Canada, 233–238, 1993.
Walsh, S., Vavrus, S., Foley, J., Fisher, V., Wynne, R., and Lenters, J.: Global patterns of lake ice phenology and climate: Model simulations and observations, J. Geophys. Res., 103, 28825–28837,

doi:10.1029/98JD02275, 1998.

Wang, J., Peng, P., Ma, Q., and Zhu, L.: Modern limnological features of Tangra Yumco and Zhari Namco, Tibetan Plateau, Journal of Lake Science, 4, 629–632, 2010.

Wang, R. L., Scarpitta, S. C., Zhang, S. C., and Zheng, M. P.: Later Pleistocene/Holocene climate conditions of Qinghai-Xizhang Plateau (Tibet) based on carbon and oxygen stable isotopes of Zabuye Lake sediments based on carbon, Earth Planet. Sc. Lett., 203, 461–477, 2002.

Weyhenmeyer, G. A., Meili, M., and Livingstone, D. M.: Nonlinear temperature response of lake ice breakup, Geophys. Res. Lett., 31, L07203, doi:10.1029/2004GL019530, 2004.

Wilson, J.: Effect of Lake Ontario on precipitation, Mon. Weather Rev., 105, 207–214, 1977.

Wu, Y. and Zhu, L.: The response of lake-glacier variations to climate change in Nam Co Catchment, central Tibetan Plateau, during 1970–2000, J. Geogr. Sci., 18, 177–189, 2008.

Xu, L., Niu, R., Zhao, Y., Li, J., and Wu, T.: Snow cover mapping over the Tibetan Plateau with MODIS and ASTER data, Proc. SPIE 2009, 7471, doi:10.1117/12.836457, 2009.

Xu, Z. X., Gong, T. L., and Li, J. Y.: Decadal trend of climate in the Tibetan Plateau-regional temperature and precipitation, Hydrol. Process., 22, 3056–3065, 2008.

Yao, T.: Map of glaciers and lakes on the Tibetan Plateau and adjoining region, 1:2 000 000, Xi'an Cartographic Publishing House, Xi'an, China, 2007.

Yao, T., Pu, J., Lu, A., Wang, Y., and Yu, W.: Recent glacial retreat and its impact on hydrological processes on the Tibetan Plateau, China, and surrounding regions, Arct. Antarct. Alp. Res., 39, 642–650, 2007.

Ye, Q., Kang, S., Chen, F., and Wang, J.: Monitoring glacier variations on Geladandong mountain, central Tibetan Plateau, from 1969 to 2002 using remote-sensing and GIS technologies, J. Glaciol., 52, 537–545, 2006.

Ye, Q., Wei, Q., Hochschild, V., and Duguay, C. R.: Integrated observations of lake ice at Nam Co on the Tibetan Plateau from 2001 to 2009, Geoscience and Remote Sensing Symposium (IGARSS), 2011 IEEE International, 24–29 July 2011, Vancouver, 3217–3220, doi:10.1109/IGARSS.2011.6049904, 2011.

Zhang, G., Xie, H., Kang, S., Yi, D., and Ackley, S. F.: Monitoring lake level changes on the Tibetan Plateau using ICESat altimetry data (2003–2009), Remote Sens. Environ., 115, 1733–1742, 2011a.

Paper V

A glacier inventory for the western Nyainqentanglha Range and Nam Co Basin, Tibet, and glacier changes 1976–2009

Bolch, T., Yao, T., Kang, S., Buchroithner, M. F., Scherer, D., **Maussion, F.**, Huintjes, E., and Schneider, C. (2010): A glacier inventory for the western Nyainqentanglha Range and Nam Co Basin, Tibet, and glacier changes 1976–2009, *The Cryosphere*, 4, 419-433, doi:10.5194/tc-4-419-2010

Status: Published.

Own contribution:

- TP climate literature review
- minor contribution to analysis and writing (Sections 1 and 5.2)

The Cryosphere, 4, 419–433, 2010
www.the-cryosphere.net/4/419/2010/
doi:10.5194/tc-4-419-2010

The Cryosphere

A glacier inventory for the western Nyainqentanglha Range and the Nam Co Basin, Tibet, and glacier changes 1976–2009

T. Bolch[1,5], T. Yao[2], S. Kang[2], M. F. Buchroithner[1], D. Scherer[3], F. Maussion[3], E. Huintjes[4], and C. Schneider[4]

[1]Institut für Kartographie, Technische Universität Dresden, Dresden, Germany
[2]Institute of Tibetan Plateau Research, Chinese Academy of Sciences, Beijing, China
[3]Institut für Ökologie, Technische Universität Berlin, Berlin, Germany
[4]Geographisches Institut, RWTH Aachen University, Aachen, Germany
[5]Geographisches Institut, Universität Zürich, Zürich, Switzerland

Received: 5 March 2010 – Published in The Cryosphere Discuss.: 1 April 2010
Revised: 22 July 2010 – Accepted: 15 September 2010 – Published: 29 September 2010

Abstract. The western Nyainqentanglha Range is located in the south-eastern centre of the Tibetan Plateau. Its north-western slopes drain into Lake Nam Co. The region is of special interest for glacio-climatological research as it is influenced by both the continental climate of Central Asia and the Indian Monsoon system, and situated at the transition zone between temperate and subcontinental glaciers. A glacier inventory for the whole mountain range was generated for the year around 2001 using automated remote sensing and GIS techniques based on Landsat ETM+ and SRTM3 DEM data. Glacier change analysis was based on data from Hexagon KH-9 and Landsat MSS (both 1976), Metric Camera (1984), and Landsat TM/ETM+ (1991, 2001, 2005, 2009). Manual adjustment was especially necessary for delineating the debris-covered glaciers and the glaciers on the panchromatic Hexagon data. In the years around 2001 the whole mountain range contained about 960 glaciers covering an area of $795.6 \pm 22.3\,km^2$ while the ice in the drainage basin of Nam Co covered $198.1 \pm 5.6\,km^2$. The median elevation of the glaciers was about 5800 m with the majority terminating around 5600 m. Five glaciers with debris-covered tongues terminated lower than 5200 m. The glacier area decreased by $-6.1 \pm 3\%$ between 1976 and 2001. This is less than reported in previous studies based on the 1970s topographic maps and Landsat data from 2000. Glaciers continued to shrink during the period 2001–2009. No advancing glaciers were detected. Detailed length measurements for five glaciers indicated a retreat of around 10 m per year (1976–2009). Ice cover is higher south-east of the mountain ridge which reflects the windward direction to the monsoon. The temperature increase during the ablation period was probably the main driver of glacier wastage, but the complex glacier-climate interactions need further investigation.

Correspondence to: T. Bolch
(tobias.bolch@geo.uzh.ch)

1 Introduction

Often described as Asia's "water tower", the Tibetan Plateau (TiP) is the source area of many major rivers (e.g. Brahmaputra, Ganges, Huang He, Indus, Mekong, Yangtze). Glaciers on the TiP are characteristic elements of its natural environment and are contributing to its water resources (Immerzeel et al., 2010). TiP's climate showed a significant temperature increase since the mid 1950s latest (Liu and Chen, 2000; Frauenfeld et al., 2005; Kang et al., 2010), accompanied by an increase of the average precipitation (Zhao et al., 2004; Chen et al., 2009; Liu et al., 2009). The glaciers receded almost throughout the entire Tibetan Plateau during recent decades (Ding et al., 2006; Ye et al., 2006; Xiao et al., 2007; Li et al., 2008). Glacier shrinkage is also reported for the western Nyainqentanglha Range in particular (Kang et al., 2007a; Yao et al., 2007; Wu and Zhu 2008; Frauenfelder and Kääb, 2009). These studies are based on the comparison of satellite data with data from 1970s topographic maps. Frauenfelder and Kääb (2009) found uncertainties and location errors with this older data which is also available in the database of the GLIMS (Global Land Ice Measurements from Space) initiative (Li, 2003). Recently started glacier mass balance measurements on Zhadang Glacier show negative mass balance values of about −1000 mm w.e. per year

Published by Copernicus Publications on behalf of the European Geosciences Union.

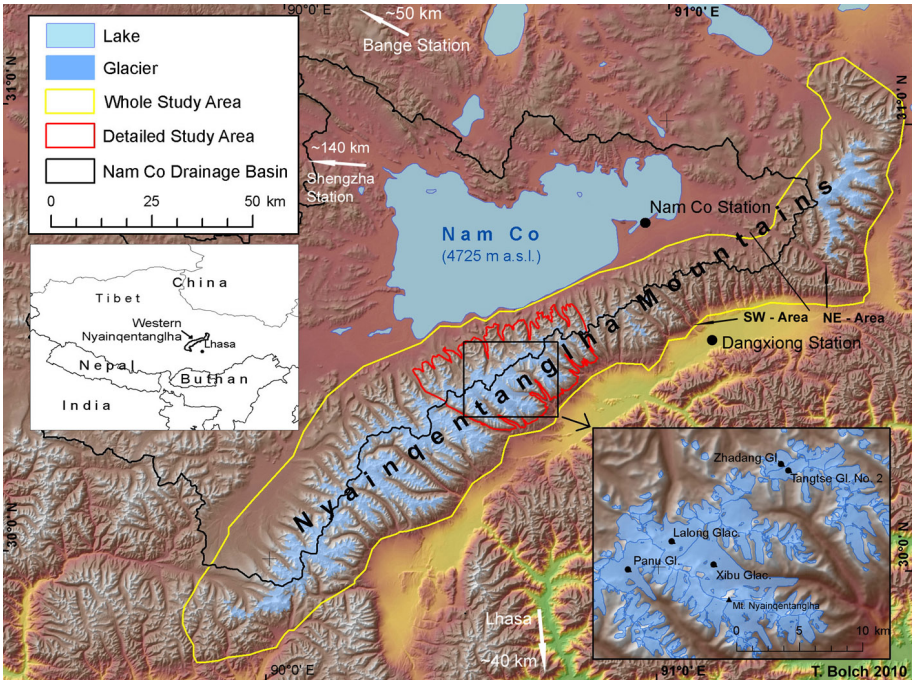

Fig. 1. Overview of the study area including the location of the climate stations (see Fig. 2) and the five glaciers studied in detail.

since 2005 except for a slightly positive balance in 2008 (Kang et al., 2009). Glacier wastage has not only caused an increase in river runoff from the plateau but also rising lake levels which are flooding pastures (Yao et al., 2007). There is a concern about an increasing threat from natural hazards such as landslides and glacial lake outburst floods (Ma et al., 2004), and decreasing water resources in the long run. These issues pose a need for evaluating the existing studies, and also for continuous glacier monitoring in this area.

Multi-temporal and multi-spectral satellite data are ideal to study and monitor glacier changes simultaneously over larger areas in remote mountainous terrain as they allow automated glacier mapping. A simple but robust method is the application of ratio images using one visible or near infrared and one short-wave infrared band (Bolch and Kamp, 2006; Paul et al., 2002). The earliest imagery suitable for automated mapping is available since the launch of Landsat TM in 1982. The availability of digital elevation models allows to split contiguous ice masses into their drainage basins, and to obtain characteristic topographic variables of the glaciers (e.g., minimum, maximum, median elevation, slope, aspect) automatically (Schiefer et al., 2008; Paul et al., 2009; Bolch et al., 2010). Declassified imagery from the US American intelligence satellite missions such as Corona KH-4, Corona KH-4B and Hexagon KH-9, the first images of which are available from the early 1960s, is ideal to extend the analysis back in time (Bolch et al., 2008; Narama et al., 2010; Surazakov and Aizen, 2010).

To our knowledge there is no study published addressing all glaciers and their changes in the western Nyainqentanglha Range for more than two points in time. Therefore, the aims of this study are:

1. to generate a recent glacier inventory for the whole mountain range, and to provide information on the general glacier characteristics,
2. to evaluate the data accuracy from the 1970s based on the topographic maps using declassified imagery,
3. to analyse glacier changes from 1976 to 2009,
4. to analyse glacier variability in detail for a subset of glaciers,
5. to discuss possible climatic drivers for glacier changes.

2 Study region, regional climate and glaciers

The western Nyainqentanglha Range, situated in the southeastern centre of the TiP (Fig. 1), represents a SW-NE striking high-mountain range of approx. 230 km in length with heights between some 5000 and 7162 m (Mount Nyainqentanglha). The region is under the complex influence of both the continental climate of Central Asia and the Indian Monsoon system with prevailing western winds in the dry season and winds from eastern direction during the wet season (Kang et al., 2009). The main mountain ridge is both

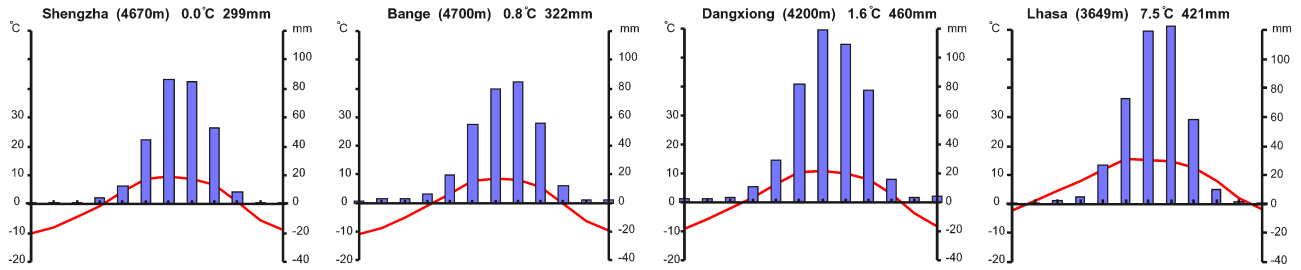

Fig. 2. Climate diagrams of Shengzha (also: Xainza), Bange (also: Bamgoin), Damxiong (also: Damxung), and Lhasa. The values are based on the period 1971–2000. Data source: National Climate Center of the Chinese Meteorological Administration; for the location of the climate stations see Fig. 1.

a water and climate divide. The SE exposed area is situated windward to the summer Monsoon and drains into the Yangbajain-Damxung Valley and subsequently into the Tsangpo-Brahmaputra River (cf. Yao, 2008). The north-western slope drains into Lake Nam (Nam Co, 4725 m, Fig. 1), Tibet's largest salt water lake with noticeable variations in size since the Last Glacial Maximum (Schütt et al., 2008), and also since 1970. From 1970 until 2006 the lake expanded its area by more than 50 km^2 (Liu et al., 2010).

Relatively little is known about the regional mountain climate above 5000 m because of its high elevation and the lack of long-term observational data (Kang et al., 2010). However, assumptions can be made by analysing data from the nearest meteorological stations (e.g. Shengzha, Bange, Danxiong, Lhasa – Fig. 2, and Amdo, for the location see Fig. 1 and Miehe et al., 2001), and the recent installation of observational instruments on Zhadang Glacier and the nearby Nam Co station (You et al., 2007). Amdo, situated at 4820 m, about 220 km in the NE, is currently the highest permanent climate station on the TiP (Liu et al., 2009). The mean annual air temperature at this station is −3.0 °C. Mean annual precipitation at the meteorological station Danxiong situated east of the Nyainqentanglha Range is 460 mm, and thus higher than the measured precipitation west of the mountain range (about 300 mm at the stations Shengzha and Bange) (Fig. 2). The annual precipitation measured at the Nam Co station (4725 m) was 415 mm during the past three years (Zhang et al., 2008). Caidong and Sortenberg (2010) estimate a vertical increase in precipitation of 5% per 100 m, and estimate annual precipitation values between 700 mm and more than 900 mm for Xibu Glacier situated close to Mt. Nyainqentanglha (see Fig. 1). A numerical modelling study also reports a SE-NW decrease of annual precipitation (Böhner, 2006), as the mountain range is a barrier for the summer monsoon. However, the climate is characterised by a strong seasonality in both temperature and precipitation. Only little precipitation is measured at the long-term meteorological stations, the Nam Co station and also estimated for Xibu Glacier (Caidong and Sortenberg, 2010) during the months November until March, while about 90% of mean annual precipitation is measured in the warm season from June to September (Fig. 2). Summer temperatures on Zhadang Glacier, at an elevation of about 5600 m, observed by Kang et al. (2009) are ranging between 0.35 and 1 °C. Following Sato (2001), summer mean temperatures are expected to be around 3 °C at the same elevation, illustrating the cooling effect of glaciated areas. Winter temperatures usually remain below −15 °C at this altitude.

Glaciers on the TiP are roughly classified into continental or subpolar and maritime or temperate glaciers (Huang, 1990). Continental type glaciers with little precipitation and cold ice are widely distributed from the central to the arid north-western plateau, while the maritime type with high monsoon precipitation and a temperate ice body is limited to the humid south-eastern region (Fujita et al., 1996; Fujita and Ageta, 2000). The snow-line elevation increases from about 4800 m in the humid south-eastern part to over 6200 m in the extremely continental north-eastern parts of the TiP (Shi et al., 1980). Measurements at Zhadang Glacier since 2005 indicate polythermal characteristics and an equilibrium line altitude (ELA) situated at about 5800 m (unpublished data). In the transitional zone between continental and maritime glaciers, the location of the western Nyainqentanglha Range, polythermal glaciers with both cold and temperate ice within the glacier body are common (Shi and Liu, 2000). These glaciers are located in a continental summer-precipitation climate with the maximum of annual accumulation and ablation occurring simultaneously in summer (Ageta and Fujita, 1996; Kang et al., 2009). Superimposed ice and internal accumulation play an important role in glacier mass balance as it prevents mass loss during the ablation season due to the retention of meltwater (Ageta and Fujita, 1996; Fujita et al., 2007). Additionally, monsoonal summer snowfall leads to increasing surface albedo and largely restrains ablation. These glaciers can therefore maintain their mass even under arid conditions with strong solar radiation (Fujita and Ageta, 2000; Kang et al., 2009).

3 Data and methods

3.1 Data

The main source for the glacier inventory was Landsat TM/ETM+ scenes from different years (Table 1). The scenes were available from USGS (United States Geological Survey, http://glovis.usgs.gov/) and are orthorectified automatically by USGS using the SRTM3 DEM (level 1T). These scenes matched well our non-differential GPS-data (horizontal shift < 30 m). No DGPS data were available for this study. We selected a Landsat ETM+ scene from 2001 as reference. For the ETM+ scenes almost no horizontal shift was observed, whereas the TM scenes had small systematic shifts of 15 to 20 m. For the time ~1990, we found only one scene from 1991 at GLCF (Global Landcover Facility, www.landcover.org, correction level "geocover"; Tucker et al., 2004) with some seasonal snow cover.

Fortunately, the main area of interest around Mt. Nyainqentanglha and Zhadang Glacier is located in the centre of the ETM+ scenes, almost not affected by scanline errors present in ETM+ images since early summer 2003 ("SLC-off" scenes which have data gaps). Nevertheless, we had to use several SLC-off scenes for each year due to different snow conditions, cloud cover and the data gaps. A typical scene is shown in Fig. 3.

We utilized panchromatic Hexagon KH-9 data (resolution ~8 m, footprint ~120 by 240 km^2) from 1976 to extend the coverage back in time and to evaluate the existing data from the Chinese Glacier Inventory (CGI; Li, 2003). Most glaciers were identifiable on the Hexagon scene, except of some smaller high-altitude glaciers, due to low contrast and snow cover. Hence, we used Landsat MSS data from the same year as a secondary source. Unfortunately, this scene also showed partly higher seasonal snow cover. Additional information was provided by Corona data from 1970 with a resolution of 4 m, and by Space Shuttle Metric Camera (MC) imagery (Konecny et al., 1984) from the year 1984 with a resolution of ~20 m. Table 1 provides an overview of the utilized scenes.

We co-registered the scenes to the USGS scene from 2001, if the shift exceeded 15 m. The Hexagon, Corona, and Metric Camera data had to be orthorectified, since no terrain correction had been applied to these data yet. The ETM+ images were pan-sharpened for visual checking and improvement. We orthorectified and co-registered the KH-9, MC and KH-4B imagery in a two-step approach using ERDAS Imagine software: The projective transformation was performed based on ground control points (GCPs) and the SRTM3-DEM, followed by a spline adjustment. In total, we used 95 GCPs for the KH-9, 25 GCPs for KH-4, and 39 for the MC imagery.

Since no detailed DEM was available for the study area, we needed a suitable DEM not only for the orthorectification but also for the calculation of glacier parameters and the separation of the glaciers into their drainage basins. Therefore, we downloaded and tested the void-filled SRTM3 data (90 m resolution) from the Consortium for Spatial Information – Consultative Group for International Agriculture Research (CSI – CGIAR), version 4 (http://srtm.csi.cgiar.org/) and the ASTER GDEM (30 m resolution). The registration of the ASTER GDEM turned out to be suitable as it matched the reference USGS Landsat scene with a deviation of less than 30 m. The main disadvantage is that it contains artificial sinks and peaks, and does not accurately represent rock walls due to problems in image matching in steep or snow covered terrain (Kääb, 2001; Kamp et al., 2005; Toutin, 2008). The SRTM DEM, acquired in February 2000 is known to be of good height accuracy (Berry et al., 2007; Falorni et al., 2005), and has also the advantage that it is more accurate in areas of low optical contrast. The horizontal shift was less than one pixel to the USGS Landsat reference scene.

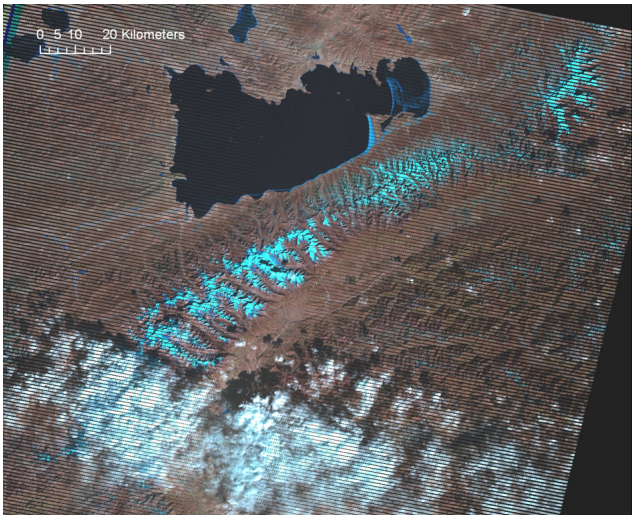

Fig. 3. Typical situation of a Landsat scene (ETM+ SLC-off from 18 January 2006): Part of the study area is suitable for glacier mapping, while seasonal snow hampers correct mapping in the NE region, and clouds covers the SW region. The region of highest interest in the center is not affected by scanline errors of the SLC scene.

3.2 Glacier identification

We applied a semi-automated approach using the TM3/TM5 band ratio to produce glacier outlines using Landsat TM/ETM+ imagery. This method is most appropriate for glacier mapping in larger study areas following the recommendations for the compilation of glacier inventories (Paul et al., 2009; Racoviteanu et al., 2009) and previous experience (Bolch and Kamp, 2006; Bolch et al., 2010). In addition, a 3 by 3 median filter was applied which only marginally alters the glacier size but eliminates isolated pixels. These are usually misclassified pixels due to debris or boulders on the glacier (Paul et al., 2002). We visually checked glacier

Table 1. Utilized space imagery.

Date	Satellite and Sensor	Path/Row	Spatial Resolution	Spectral Bands	Source	Suitability of scene	Utilisation
21 Nov 1970	Corona KH-4B		~ 4 m, stereo	1 PAN	USGS[1]		Additional information for glacier identification
7 Jan 1976	Hexagon KH-9		~ 8 m, stereo	1 PAN	USGS[1]	Seasonal snow on NE part	Glacier inventory ~1976 for whole study area
7 Dec 1976	Landsat MSS	148/039 148/039	79 m	3 VIS, 1 NIR	GLCF[2]	Seasonal snow on NE part	Glacier inventory ~1976 for whole study area
23 Nov 1984	Space Shuttle Metric Camera		~ 16 m, stereo	1 VIS	DLR[3]	Seasonal snow on glaciers	Additional information for selected glaciers
14 Sep 1991	Landsat TM	138/039	30/120 m	3 VIS, 1 NIR, 2 SWIR, 1 TIR	GLCF[2]	Seasonal snow on glaciers	Additional Information for selected glaciers.
17 Nov 2000	Landsat ETM+	138/039	15/30/60 m	1 PAN, 3 VIS, 1 NIR, 2 SWIR, 1 TIR	USGS[1]	Seasonal snow on NE part	Glacier inventory ~2001, additional information
2 May 2001	Landsat ETM+	138/039	15/30/60 m	1 PAN, 3 VIS, 1 NIR, 2 SWIR, 1 TIR	USGS[1]	Seasonal snow on NE part	Glacier inventory ~ 2001, additional information
6 Dec 2001	Landsat ETM+	138/039	15/30/60 m	1 PAN, 3 VIS, 1 NIR, 2 SWIR, 1 TIR	USGS[1]	Seasonal snow on NE part	Glacier inventory ~2001, whole study area
20 Jan 2001	Terra ASTER		15/30 m, stereo	2 VIS, NIR, TIR	USGS[1]		Glacier inventory ~2001 additional information
7 Oct 2005	Landsat ETM+, SLCoff	138/039	15/30/60 m	1 PAN, 3 VIS, 1 NIR, 2 SWIR, 1 TIR	USGS[1]		Additional information for selected glaciers
18 Jan 2006	Landsat ETM+, SLCoff	138/039	15/30/60 m	1 PAN, 3 VIS, 1 NIR, 2 SWIR, 1 TIR	USGS[1]		Additional information for selected glaciers
1 Aug 2007	Landsat ETM+, SLCoff	138/038	15/30/60 m	1 PAN, 3 VIS, 1 NIR, 2 SWIR, 1 TIR	USGS[1]		Glacier inventory NE part
6 Jan 2008	Landsat ETM+, SLCoff	138/039	15/30/60 m	1 PAN, 3 VIS, 1 NIR, 2 SWIR, 1 TIR	USGS[1]	some seasonal snow	Glacier inventory ~ 2009 NE part and detailed study area
19 Jun 2009	Landsat ETM+, SLCoff	138/039	15/30/60 m	1 PAN, 3 VIS, 1 NIR, 2 SWIR, 1 TIR	USGS[1]	Some clouds	Glacier inventory ~2009 NE part and detailed study area
21 Jul 2009	Landsat ETM+, SLCoff	138/039	15/30/60 m	1 PAN, 3 VIS, 1 NIR, 2 SWIR, 1 TIR	USGS[1]	Some clouds	Glacier inventory ~2009 NE part and detailed study area
15 Sep 2009	Landsat TM	138/039	30/120 m	3 VIS, 1 NIR, 2 SWIR, 1 TIR	USGS[1]	Some clouds	Glacier inventory ~2009 NE part and detailed study area

[1] United States Geological Survey (www.glovis.usgs.gov), [2] Global Landcover Facility (www.landcover.org), [3] Deutsches Zentrum für Luft und Raumfahrt (www.dlr.de)

Fig. 4. Terminus of debris-covered Xibu Glacier; Corona, year 1970 **(A)**, Hexagon, 1976 **(B)**, Landsat ETM+, 5-4-3-pan, 2009 **(C)**.

polygons derived from the ratio method for gross errors, and manually improved them where necessary. Debris-covered ice, proglacial lakes, seasonal snow and, for the SLC-off scenes, data gaps represented major sources of misclassified areas. The termini of some debris-covered glaciers were hardly identifiable by Landsat imagery. Here, we used the ETM+ pan-sharpened image to identify the most likely margin. The higher resolution Hexagon and Corona imagery (Fig. 4) helped in this process. Signs of movements, supraglacial ponds or creeks beginning at the end of the terminus are typical indicators which helped to determine the most likely position of the termini.

According to the recommendations to obtain a global glacier coverage for the time around the year 2000 (Paul et al., 2009), we generated an baseline inventory for the whole southern mountain range based on the Landsat ETM+ scene from the 6 December 2001 in the first step. In case of cast shadow and higher seasonal snow cover we used the other scenes from 2001 and 2000 as additional information. High seasonal snow hampered the correct mapping of the glaciers in the northern part. We had to use the three scenes from 2009 to map glaciers in this area due to clouds and the data gaps from the scan line error. The northernmost glaciers had to be mapped based on a 2007 scene from another row. Finally, full spatial coverage was obtained. We manually adjusted the 2001 outlines to the situation in 1976 based on the Hexagon and MSS data. No multi-temporal inventory could be generated for the north-eastern part of the mountain range (see Fig. 1) due to snow cover on both the Hexagon and the MSS data. The 2009 inventory for the detailed study area was generated semi-automatically as described above. The minimum size of mapped glaciers to be included in the inventory was set to 0.01 km^2. However, the comparison of glacier areas was restricted to those larger 0.1 km^2 as seasonal snow on at least one of the utilized scenes hampered the correct delineation, thus high errors would have been introduced. We could not find a single glacier that advanced between 1976 and 2001. Hence, we clipped all glaciers to the 1976 extend. The use of this mask ensured that the upper glacier boundary and the margins of the nunataks were kept constant, and no error was introduced due to varying seasonal snow cover or different ice divides.

3.3 Glacier inventory and change analysis

The contiguous ice masses were divided into their drainage basins in order to obtain a glacier inventory. We followed the automated approach presented by Bolch et al. (2010), and derived the basins based on hydrological analysis within a one-kilometre-buffer around each glacier. The SRTM3 DEM was suitable to detect flow divides also on ice fields. The main drawback, however, was the location of some steep mountain crests. They differed sometimes by approximately one pixel (90 m) from the location in the satellite imagery. An additional error occurred when smaller glaciers, connected in parts of the accumulation area, are close to larger ones so that no basin was generated automatically. Hence, we manually improved the basins based on the satellite imagery. This method was superior to the fully manual method as many ice divides were calculated accurately by the automatic method.

An identification number was assigned to each glacier based on the 1976 extends. We treated all ice masses as a single glacier also in cases where glaciers separated from each other in order to allow subsequent change analysis. The following characteristic parameters were obtained for each glacier and the years 1976 and 2001 based on the SRTM3 DEM: hypsography, minimum, maximum and median elevation, mean slope, and aspect. The SRTM3 DEM matches well with the 2001 outlines. No DEM representing the 1976 conditions were available. Hence, slight biases especially with the hypsography of 1976 occur.

Five selected glaciers (Panu, Lalong, Xibu, Zhadang, and Tangtse Glacier No. 2, Fig. 1) were studied in detail. The selection is based on existing studies that could be used for comparison (Kang et al., 2007a). The glaciers are exposed to different aspects but are not representative for the entire mountain range due to their relatively large size. We manually adjusted the outlines for the additional years 1991 and 2005, and for Xibu and Lalong Glacier for the additional year 1984. High seasonal snow cover on the Metric Camera

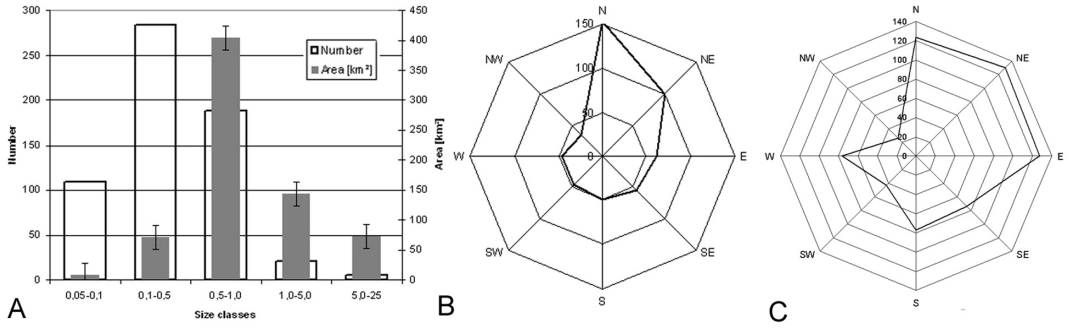

Fig. 5. Diagram showing the number and area covered for different size classes **(A)**, aspect of the glaciers – **(B)**: number, **(C)**: area).

data hampered the correct delineation of the other glaciers for 1984.

3.4 Error estimation

The potential error of the multi-temporal analysis mainly arises from positional and mapping errors. Visual checks of (almost) stable landforms like mountain peaks or lateral moraines on the co-registered imagery resulted in a mean horizontal shift of one pixel or less for the TM scenes (< 30 m), and less than half a pixel for the ETM+ scenes (< 15 m). Some ETM+ scenes from the USGS matched perfectly. Co-registration error of the Hexagon image was higher due to the more complex image geometry. The error was about two pixels (< 20 m) for the detailed study area, and could be up to four (< 40 m) at the outer part of the imagery where fewer tie points (TPs) were collected. Uncertainty of glacier mapping depends on the resolution of the utilised imagery and the conditions at the time of the acquisition (especially seasonal snow). Under best conditions an accuracy of less than half a pixel can be achieved. We estimated the uncertainty by the buffer method suggested by Bolch et al. (2010) and Granshaw and Fountain (2006). We have chosen a buffer size of 10 m for the Hexagon image, and 7.5 m for the ETM+ images. This led into an uncertainty of the mapped glacier area of 3.5% for the Hexagon imagery, and 2.8% for the ETM+ images on average. These uncertainties are within the range of previous accuracy estimates (Paul et al., 2002; Bolch and Kamp, 2006).

4 Results

4.1 Glacier characteristics

The whole mountain range contains almost 1000 glaciers according to our inventory. However, glacier counts are vague and depend on the purpose; e.g. contiguous ice masses can be counted as single entities, or can be subdivided into multiple glaciers as we did where parts of the ice masses cross ridges. Glaciers of the whole western Nyainqentanglha Range cover an area of about 800 km^2, while slightly more than 100 km^2 are situated in the north-eastern section, which was not further investigated. Ice coverage of the detailed study area and of the Nam Co drainage basin is slightly less than 200 km^2 each (Table 2). Glaciers draining into Nam Co are almost all situated at the north-western slope of the south-western part of the western Nyainqentanglha Range, except three small ones with an area of about 0.3 km^2 which are situated in the north-eastern section, and five glaciers ($\sim$1.3 km^2) below mountain peaks not within the main range. The mean glacier size in the Nam Co drainage basin (year 2001) is about 0.64 km^2, while the glaciers south east of the main ridge are on average about 0.88 km^2 in size.

Table 2. Number and ice covered area of the study regions based on the glacier inventory. See Fig. 1 for the regions.

Region	Number of glaciers	Area (km^2)	Year of utilized images
Whole Mountain range	963	795.6 ± 22.3	2001 (SW), 2007/2009 (NE)
NE section	141	103.2 ± 2.9	2009
SW section	822	692.3 ± 19.4	2001
Nam Co drainage basin	305	198.1 ± 5.6	2001
Detailed study area	308	194.5 ± 5.5	2001

The highest number of glaciers can be found in the size class 0.1–0.5 km^2, whereas glaciers between 0.5–1.0 km^2 cover the largest area (Fig. 5a). Most glaciers are facing north while the east sector has a similar ice covered area as the northern sector (Fig. 5b and c). Hence, the east facing glaciers are on average the largest. This is in line with the fact that the ice cover east (windward to the summer monsoon) of the main ridge of the Nyainqentanglha range is more than twice as large as the western part ($\sim$494 km^2 to $\sim$196 km^2).

Median elevation of the glaciers, which is a suitable and widely used estimation for the long-term ELA based on topographic data (Braithwaite and Raper, 2010), is situated at around 5820 m. The majority of the glaciers terminate

Table 3. Characteristics of the glaciers investigated in detail based on the 2001 extents.

Glacier	GLIMS ID/WGI ID*	Area (km^2)	Length (km)	Aspect	H med[1] (m a.s.l.)	H min[2] (m a.s.l.)	H max[3] (m a.s.l.)	Debris-covered tongue
Zhadang	G090633E30476N/ 5Z225D0003	2.48	2.7	NE	5710	5500	6095	No
Tangse No. 2	G090647E30462N/ 5O270C0086	2.96	2.1	SW	5785	5600	6080	No
Lalong	G090540E30424N/ 5Z225D0022	10.29	3.6	NW	5890	5340	6650	Few medial moraines
Xibu	G090601E30395N/ 5O270C0065	23.35	9.3	E	5815	5160	7090	Yes
Panu	G090521E30384N/ 5O270C0044	12.88	5.3	SE	5850	5335	6365	Few medial moraines

* ID number of the GLIMS data base (Li 2003, www.glims.org) and the World Glacier Inventory (www.wgms.ch), [1] median elevation, [2] minimum elevation, [3] maximum elevation

at around 5600 m. Only five glaciers terminate lower than 5200 m, with the lowest elevation at 5130 m. These glaciers all have debris-covered tongues. We have identified 29 glaciers with significant debris cover. Overall area covered by debris was about 20 km^2 (∼3% of the whole ice cover). Most of the debris-covered glaciers are situated in the outer south western part and around Mt. Nyainqentanglha below high and steep rock walls such as Xibu Glacier. These glaciers are typically large valley glaciers (average size about 4.4 km^2). Characteristics of Xibu and the four other glaciers investigated in detail are shown in Table 3.

4.2 Glacier shrinkage/recession

Ice cover in the south-western study area diminished by about $-42\,km^2$ ($\sim -5.7\%$) in the period 1976–2001 (Table 4). Percentage loss and rate for Nam Co drainage basin and the detailed study area around Mt. Nyainqentanghla were in a similar range but slightly higher for the first, and lower for the latter. Shrinkage of the glaciers situated south-east of the main ridge was about $-29.5\,km^2$ ($\sim -5.5\%$). Glaciers with debris-covered tongues lost about $-4.5\,km^2$ ($\sim -3.4\%$). The shrinkage rate for the period 2001–2009 was higher than for 1976–2001 but not statistically significant given the higher error term. However, visual checks and detailed analysis confirmed ongoing glacier shrinkage and retreat between 2001 and 2009 (Fig. 6 and Table 4). The overall number of glaciers remained almost unchanged. Disappearance of very few glaciers was compensated through disintegration of others. Disappeared glaciers were small and situated at relatively low altitudes.

Analysis of the relative area change against the initial glacier area indicated greater relative loss for smaller glaciers. However, there was a large scatter, especially for smaller ones, and in all size classes there are glaciers, which did not shrink (Fig. 7a). Absolute area loss was higher for larger glaciers (Fig. 7c). Glaciers in the size classes $< 0.5\,km^2$ and $> 5.0\,km^2$ lost both almost $-7\,km^2$ of ice, which is $\sim -11.4\%$ of their initial glacier size for the first size class but only $\sim -3.3\%$ for the latter. Glaciers with lower median elevation tended to lose relatively more area than higher elevation glaciers (Fig. 7b).

Analysis of the glacier hypsography showed that ice coverage above 6000 m remains almost unchanged while the highest absolute ice loss occured between 5500 and 5700 m

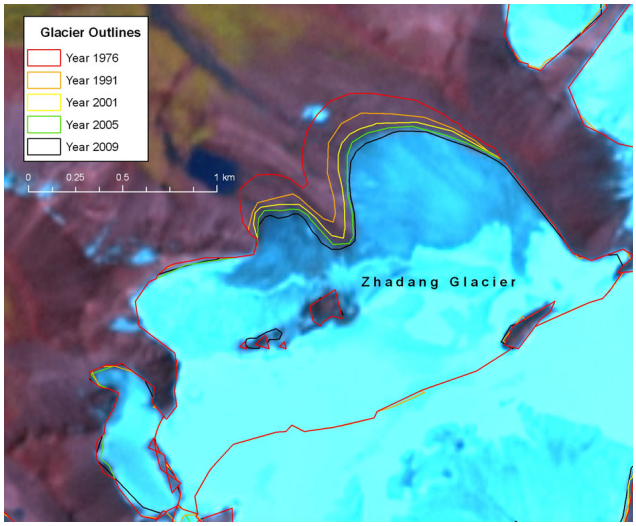

Fig. 6. Area changes of Zhadang Glacier (1976–2009).

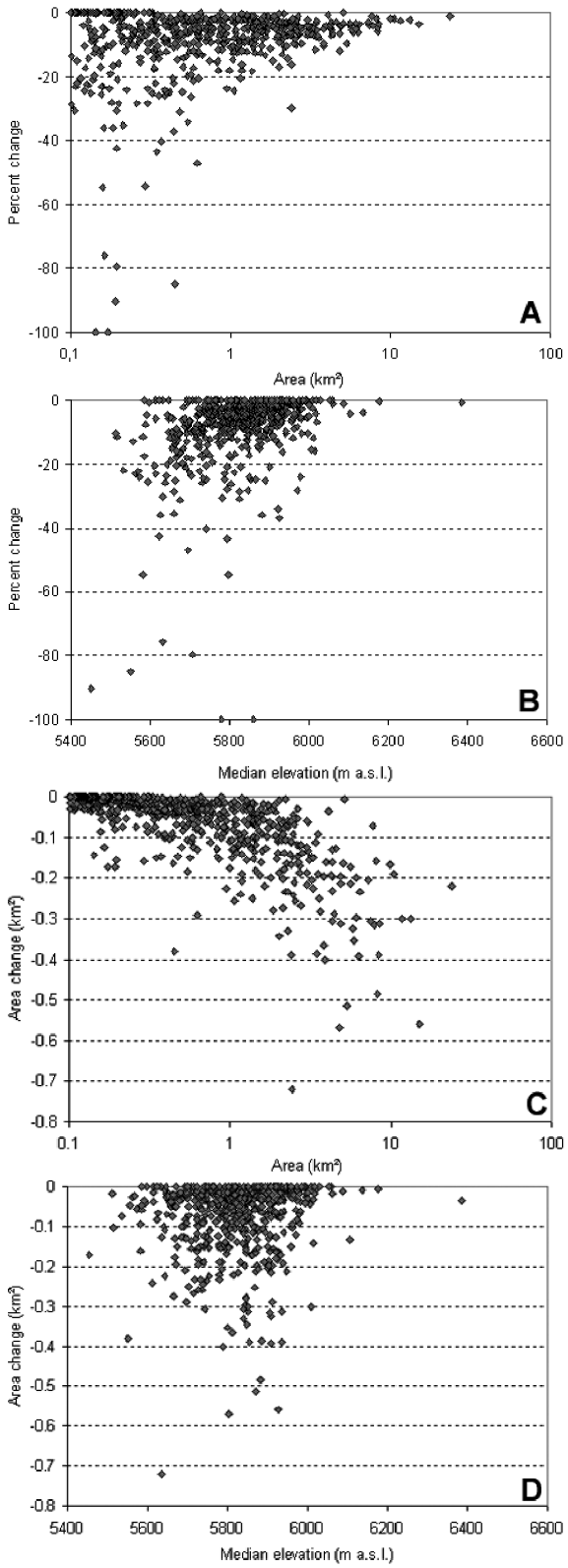

Fig. 7. Relative change in glacier area 1976–2001 versus initial glacier area **(A)** and median elevation **(B)**, absolute change in glacier area 1976–2001 versus initial glacier area **(C)** and median elevation **(D)**.

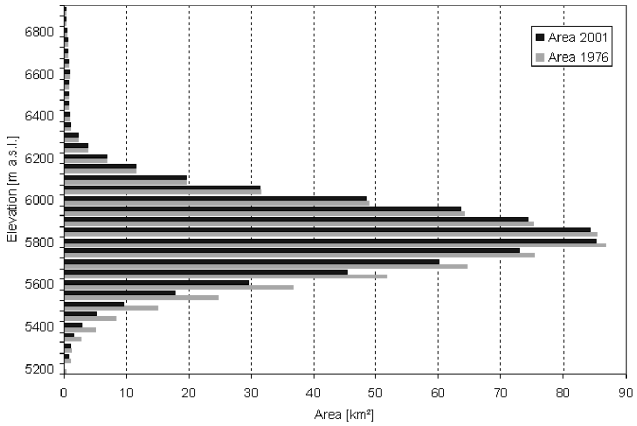

Fig. 8. Changes in glacier hypsometry 1976–2001; each bar represents an elevation interval of 50 m.

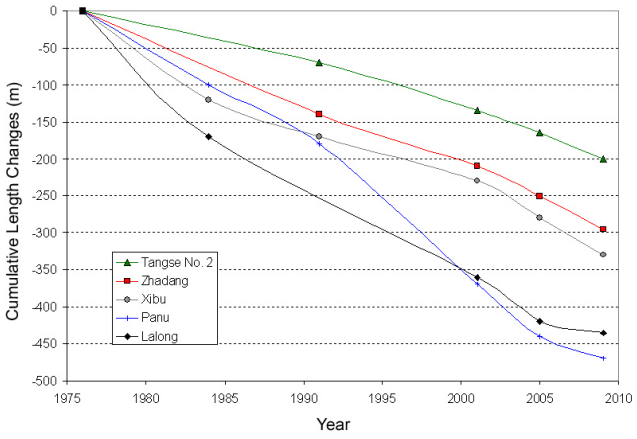

Fig. 9. Cumulative length change of the five glaciers studied in detail.

(Fig. 8). Median elevation increased by 9 m while the average minimum elevation of the glaciers rose about 15 m from 5671 to 5686 m.

A detailed analysis of the five selected glaciers confirmed the above mentioned tendencies. All glaciers decreased continuously, both in area and length throughout all investigated periods (Table 5, Fig. 9). Minimum elevation increased on average about 30 m between 1976 and 2001 with the highest value (75 m) for Lalong Glacier. The tongue of this glacier terminates in a comparatively steep valley. The rate of area loss was significantly higher for three glaciers in the period 2001–2009 compared to 1976–2001, whereas the rate was similar for Panu Glacier, and an opposite tendency could be found for Lalong Glacier. Length changes showed similar characteristics. Absolute area loss varied between $-0.24\,km^2$ (Tangtse Glacier No. 2, one of the smallest glaciers) and $-0.44\,km^2$ (Xibu Glacier, the largest one) for 1976–2009, while percentage loss was highest for Zhadang Glacier (-14.2%, the smallest glacier studied), and lowest

Table 4. Change in glacier area 1976-2001-2009.

	Area [km^2]			1976–2001			2001–2009			1976–2009		
	1976	2001	2009	Δa [km^2]	Δa [%]	Δa/yr [%]	Δa [km^2]	Δa [%]	Δa/yr [%]	Δa [km^2]	Δa [%]	Δa/yr [%]
South-Western Region	734.1 ± 25.7	692.4 ± 19.4	n.a.	−41.7 ± 22.4	−5.7 ± 3.1	−0.23 ± 0.12	n.a.	n.a.	n.a.	n.a.	n.a.	n.a.
Nam Co Drainage Basin	212.5 ± 7.4	198.1 ± 5.5	n.a.	−14.4 ± 6.5	−6.8 ± 3.1	−0.27 ± 0.12	n.a.	n.a.	n.a.	n.a.	n.a.	n.a.
Glaciers south-east of the main ridge	504.8 ± 17.7	475.3 ± 13.3	n.a.	−29.5 ± 13.3	−5.8 ± 2.6	−0.23 ± 0.12	n.a.	n.a.	n.a.	n.a.	n.a.	n.a.
Detailed study area	207.1 ± 7.2	194.5 ± 5.5	186.6 ± 5.4	−12.6 ± 6.4	−6.1 ± 3.1	−0.24 ± 0.12	−7.8 ± 5.4	−4.0 ± 2.8	−0.50 ± 0.34	−20.5 ± 6.4	−9.9 ± 3.1	−0.3 ± 0.10

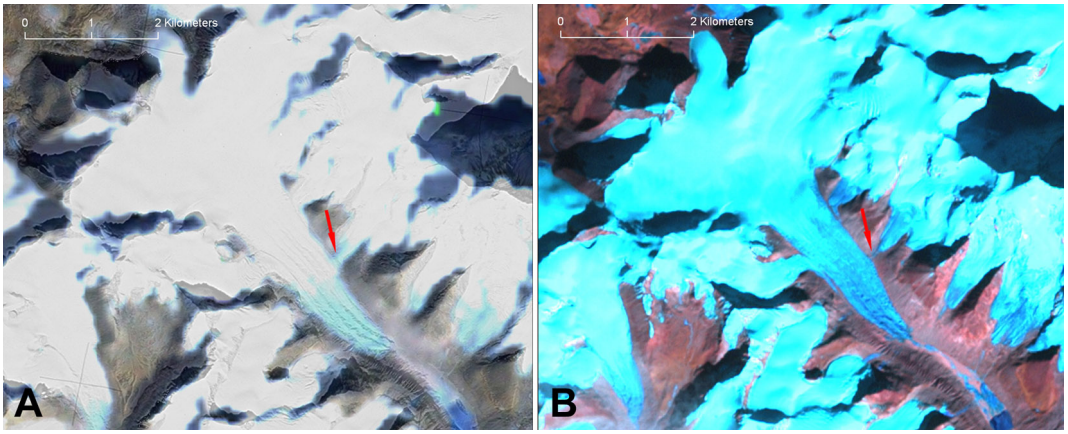

Fig. 10. Panu Glacier 1976 – merge of Landsat MSS and Hexagon **(A)** and 2001 – Landsat ETM+, 5-4-3-PAN **(B)**. The arrow indicates the separation of one tributary glacier between 1976 and 2001.

for Xibu Glacier (−1.9%). There was a slight tendency that retreat rates 1976–1991 were higher than those from 1991 to 2001, but lower than those from 2001 to 2009. One glacier contributing to the main Panu Glacier in 1976 separated from it before 2001 (Fig. 10).

5 Discussion

5.1 Glacier changes

Spaceborne imagery enabled us setting up a glacier inventory of the western Nyaingentanglha Range, and to trace back changes in glacier extension over a period of more than 40 years. This represents the longest time series over which a change detection of the glacier coverage has been performed for the study region until present. The study found glacier shrinkage and retreat in the western Nyainqentanglha Range between 1976 and 2009 of about -9.9 ± 3.1%. The slightly higher glacier shrinkage in Nam Co drainage basin compared to the whole study area and the glaciers east of the main ridge are most likely due to smaller average glacier size in the Nam Co basin. The relatively low shrinkage of the debris-covered glaciers is an indication of the insulation effect of the debris cover. However, their area loss was not significantly lower than of the other glaciers of the study area of similar size. Analysing the glacier hypsography indicated that a rise of the ELA above 5850 m will cause increased area loss as the

Table 5. Length and area changes for five selected glaciers. The uncertainty is estimated to be about 3%.

Zhadang Glac.	Area (km^2)	Δa abs. (km^2)	Δa rel. (km^2)	Rate (%/yr)	Retreat (m)	Rate (m/yr)
1976	2.75					
1991	2.56	−0.19	−6.9%	−0.46%	140	9.3
2001	2.48	−0.08	−3.1%	−0.31%	70	7.0
2005	2.41	−0.07	−2.8%	−0.71%	40	10.0
2009	2.36	−0.05	−2.1%	−0.52%	45	11.3
1976–2001		−0.27	−9.8%	−0.39%	210	8.4
2001–2009		−0.12	−4.8%	−0.60%	85	10.6
1976–2009		−0.39	−14.2%	−0.43%	295	8.9
Tangse No. 2	Area (km^2)	Δa abs. (km^2)	Δa rel. (km^2)	Rate (%/yr)	Retreat (m)	Rate (m/yr)
1976	3.13					
1991	3.02	−0.11	−3.5%	−0.23%	70	4.7
2001	2.96	−0.06	−2.0%	−0.20%	65	6.5
2005	2.95	−0.01	−0.3%	−0.08%	30	7.5
2009	2.89	−0.06	−2.0%	−0.51%	35	8.8
1976–2001		−0.17	−5.4%	−0.22%	135	5.4
2001–2009		−0.07	−2.4%	−0.30%	65	8.1
1976–2009		−0.24	−7.7%	−0.23%	200	6.1
Lalong Glac.	Area (km^2)	Δa abs. (km^2)	Δa rel. (km^2)	Rate (%/yr)	Retreat (m)	Rate (m/yr)
1976	10.5					
1984	10.43	−0.07	−0.7%	−0.08%	170	21.3
2001	10.29	−0.14	−1.3%	−0.08%	190	11.9
2005	10.25	−0.04	−0.4%	−0.10%	60	15.0
2009	10.21	−0.04	−0.4%	−0.10%	30	7.5
1976–2001		−0.21	−2.0%	−0.08%	360	14.4
2001–2009		−0.05	−0.5%	−0.06%	90	11.3
1976–2009		−0.26	−2.5%	−0.08%	450	13.6
Xibu Glac.	Area (km^2)	Δa abs. (km^2)	Δa rel. (km^2)	Rate (%/yr)	Retreat (m)	Rate (m/yr)
1976	23.55					
1984	23.43	−0.12	−0.5%	−0.06%	120	15.0
1991	23.39	−0.04	−0.2%	−0.02%	50	7.1
2001	23.35	−0.04	−0.2%	−0.02%	60	6.0
2005	23.04	−0.5	−2.1%	−0.33%	50	12.5
2009	22.90	−0.14	−0.6%	−0.15%	50	12.5
1976–2001		−0.2	−0.9%	−0.03%	230	9.2
2001–2009		−0.36	−1.5%	−0.24%	100	12.5
1976–2009		−0.44	−1.9%	−0.07%	330	10.0
Panu Glac.	Area (km^2)	Δa abs. (km^2)	Δa rel. (km^2)	Rate (%/yr)	Retreat (m)	Rate (m/yr)
1976	13.18					
1984	13.16	−0.02	−0.2%	−0.02%	100	12.5
1991	13.01	−0.15	−1.1%	−0.16%	80	11.4
2001	12.88	−0.13	−1.0%	−0.06%	190	19.0
2005	12.86	−0.02	−0.2%	−0.04%	70	17.5
2009	12.78	−0.08	−0.6%	−0.16%	30	7.5
1976–2001		−0.3	−2.3%	−0.09%	370	14.8
2001–2009		−0.1	−0.8%	−0.10%	100	12.5
1976–2009		−0.38	−2.9%	−0.09%	470	14.2

largest portion of glacier coverage is in the range of 5750–5850 m.

Our results are in tendency in agreement with previous studies. Field measurements and analysis of topographic maps carried out for Gurenhekou Glacier, located in the southern part of the range, showed an increased termini retreat rate after 1970 (Pu et al., 2006). Analysis of five glaciers around Mt. Nyainqentanglha suggests that glacier termini have been retreating around $-10\,\mathrm{m\,a^{-1}}$ from 1970 to 2007, with a significantly higher rate (~ -39 m/a) for the debris-covered Xibu Glacier (Kang et al., 2007a). Our results for length changes reveal similar values to the previous studies but significantly lower rates for Xibu Glacier. Kang et al. (2007a) compared GPS data obtained in the field with the position of the terminus as shown in the Chinese topographic map (scale 1:100 000). Hence, taking into account that usually the debris cover would reduce the retreat of the tongue, it is likely that this comparably high value can be attributed to wrong glacier delineation in the map.

Previous glacier change studies for the Nam Co basin showed a glacier area decrease by -15.4% from 1970 to 2000 (Yao et al., 2007; Wu and Zhu, 2008), while Frauenfelder and Kääb (2009) found an area decrease of $\sim -20\%$ for the SE side of the Nyainqentanglha Range in a similar period. This study, however, results in lower values for glacier area changes to previous studies for a similar time period. One explanation for the differences could be that Yao et al. (2007) and Wu and Zhu (2008) used mainly data from the Chinese Glacier Inventory (CGI) (Li, 2003). This inventory also used the Chinese topographic maps, which are based on aerial images acquired in the early 1970s, and were published in the 1970s and 1980s. Main reasons for the deviations to our data are probably different interpretation of debris-cover and seasonal snow on the utilized aerial images, which is known to be one of the major problems of maps (Bhambri and Bolch, 2009), as well as glacier shrinkage since the 1970s. Frauenfelder and Kääb (2009) used Corona imagery to validate the data from the CGI and found errors in georeferencing, which can be confirmed by this study. They omitted glaciers with obvious errors from the CGI for their change analysis but did not correct the remaining glaciers. Hence, the reason of the difference to our data is likely due to the inaccurate 1970s data. The quality of the CGI and Chinese topographic maps can hardly be evaluated if the original imagery is not available. Declassified imagery from the 1970s therefore provides a good opportunity for validation and to further improve the data from the CGI. Hexagon KH-9 data is superior to Corona due to less image distortion and larger footprints. Slight differences of some automated derived ice divides to the former Chinese Glacier Inventory led to different length and absolute areas for some glaciers, e.g. Zhadang Glacier (Chen et al., 2009). The terrain of the ice divide is almost flat in these cases. Further investigations, e.g. based on higher resolution DEMs, are required to identify the correct surface divide. However, the automated method is reproducible and this uncertainty does not affect the results of our study as we kept the ice divides constant for our analysis.

Our results indicate that glacier changes in the western Nyainqentanglha Range are similar to the average changes for whole China (-5.5% since the 1960s; Li et al., 2008). The recent acceleration of the retreat can also be found in most parts of the TiP (Kang et al., 2010). Values might be slightly but not significantly lower in other areas of central and western Tibet, e.g., the Geladanong Mountains about 500 km to the north of the study area (Ye et al., 2006; -4.8% between 1969 and 2002). Glacier shrinkage in Tibet south of the study area seems to be higher: Zhou et al., 2009 found a $\sim -5\%$ decrease between 1990 and 2005 in Nianchu River basin. However, these data can only show tendencies as different time periods and size classes are compared.

5.2 Climatic considerations

The significantly larger ice cover east of the main ridge of the Nyainqentanglha Range wind-ward to the summer monsoon is an indication that precipitation is higher in this region than leeward of the main ridge. However, the values of the glacier change rates are comparable, which indicates similar dominant influence of long-term regional climate variability in the study area. The reported temperature increase since the 1950s varies between 0.3 K per decade for the station Lhasa, which was shown to be representative for a larger region (Liu and Chen, 2000). A recent study using similar data also revealed a general warming trend, especially in winter months (You et al., 2010). The trend coefficient for the station Lhasa was 0.44 K/10a (winter months, dry season) and 0.23 K/10a (summer months, wet season) for 1955–2005 (Caidong and Sortenberg, 2010). The stations adjacent to the Nyainqentanglha Range and Amdo station had similar tendencies (Chen et al., 2009; Liu et al., 2009). Liu and Chen (2000) assumed a higher temperature increase in higher elevations. In contrast, Qin et al. (2009) showed, by using remote sensing data, that this altitudinal dependency may not be that pronounced, and levels out at elevations higher than 5000 m. The changes in air temperature were accompanied by an increase of precipitation due to variations in monsoonal activity. Liu et al. (2009) analysed data of the station Amdo, and recorded multi-year oscillations in precipitation from 1965 to the mid-1990s, followed by a trend to increasing precipitation since 1995. The July precipitation even slightly decreased until the mid 1990s (Thomas and Chen, 2002). Annual precipitation in the last decade was 50.6 mm (about 12%) above the average annual mean during the period 1965–1994. The same tendency was observed by Shi et al. (2006), Kang et al. (2007b), and Chen et al. (2009) for the stations adjacent to our study region. Pan evaporation showed stable or slightly increasing values until the mid 1990s (Thomas and Chen, 2002) and a decrease thereafter (Liu et al., 2010).

Linking the presented glacier area and length changes to the above summarized climate variations is not straightforward, mainly because (a) the glacier changes are only indirect signals and depend especially on glacier response times, (b) the availability of the climate data in the study area and especially at the altitude range of the glacier occurrence is very scarce.

The present knowledge on the response of polythermal, summer-accumulation type glaciers to climate changes at different time scales is still limited. Glacier size, shape, motion, and the local topography also influence the glacier response. On average, the response time can possibly be several decades (Naito et al., 2001). The summer-accumulation-type glaciers are more vulnerable to temperature increase than winter accumulation type glaciers (Fujita and Ageta, 2000; Fujita, 2008). Hence, it can be assumed that the observed warming in the wet season is the major driver for glacier changes. This is also confirmed by a recent modelling study on Xibu Glacier. The change in summer temperature was found to be more important than precipitation changes or the changes in winter (dry season) temperature even although the increase of winter temperature was found to be significantly higher than in summer (Caidong and Sortenberg, 2010). Changes in the summer temperature affect both the glacier melt and the snow line altitude. The latter has an important effect on the melt due to albedo changes.

Precipitation seasonality also plays an important role. For example, the early onset of wet season may suppress glacier melt during summer, and can lead into positive mass balance values (Kang et al., 2009). The presented glacier shrinkage may reflect the time prior to 1990 with slightly decreasing summer precipitation, but slightly increasing evaporation and temperature when considering the response time of the glacier. The recent trend since the mid 1990s with a stronger temperature increase but also slightly increasing precipitation and evaporation may not yet be reflected in our data. Taking the importance of the temperature variations for the glacier mass balance into account, it is likely that glaciers will continue to shrink even though some positive mass balance years occur in between. However, recent mass balance measurements on Zhadang Glacier are mostly negative (Kang et al., 2009). So far, we are not able to quantify the importance of the specific climate elements to the glacier changes since availability of climate data in the study area is insufficient. Especially the influence of solar radiation and sublimation needs further investigation. Ongoing investigations (e.g. direct mass balance measurements, meteorological energy balance measurements on Zhadang Glacier and at Nam Co station, acquisition of gridded climate data, and geodetic estimates of glacier mass changes by DEM differencing) will continuously improve the data base in the near future, and will help to adjust existing glacier models to the specific situation in the study area. The availability of the presented glacier outlines are of high importance for model validation and hence also for the investigation of climate change. Lake level variations of Nam Co are another source for model validation since glacier run-off is influenced by glacier variability (Yao et al., 2007; Wu and Zhu, 2008; Liu et al., 2010).

6 Conclusions

This study demonstrated the scientific value of detailed multi-temporal remote sensing analyses of glacier changes for regions that do not have sufficient observational data records. Our approach and the availability of precise orthorectified Landsat scenes allow repeated monitoring in the study area without costs for data every three to five years, if retreat rates remain unchanged. Future efforts to continue this time series will be minor as glacier drainage divides are already generated. Next steps will involve automated mapping of the debris-covered parts of glaciers. The availability of different optical satellite imagery from earlier years, especially the low cost Hexagon KH-9 from the 1970s and Landsat TM scenes from the 1980s and 1990s is of high value for glacier investigations. This allows evaluating existing data or glacier outlines from older topographic maps and deriving multi-temporal glacier inventories dating back several decades. The main drawback for some regions might be the unavailability of suitable scenes. However, in our study area characterised by continental climate little snow cover and clouds throughout the year facilitates the generation of multi-temporal glacier inventories. The Chinese Glacier Inventory from the 1970 is a valuable source of information but the data contains inaccuracies and geolocation errors. The use of different satellite data revealed a continuous glacier shrinkage of about $-9.9 \pm 3.1\%$ from 1976 until 2009. These values are lower than previously published results, which can be mainly attributed to the uncertainties of glacier delineations based on the Chinese topographic maps. The five glaciers investigated in detail showed an average retreat of about -10 m/a from 1976 until 2009. No glaciers advanced in the investigated periods. The larger ice cover of the south-eastern side of the Nyainqentanglha Range reflects the location windward to the summer monsoon. Short-term variations in the glacier mass balance were also driven by monsoonal variations. The main cause of long-term glacier wastage, however, was likely the increase in air temperature during the wet season. However, the complex glacier-climate interactions need to be further investigated.

Acknowledgements. The work is supported by the German Research Foundation (Deutsche Forschungsgemeinschaft, DFG) within the Tibetan Plateau (TiP) Priority Programme under the codes BU 949/20-1, SCHE 750/4-1, and SCHN 680/3-1. The authors are grateful to the German Aero Space Center (Deutsches Zentrum für Luft- und Raumfahrt, DLR) for providing the Metric Camera data at no cost. We thank Volker Hochschild, Jan Kropacek (both Universität Tübingen, Germany), Wolfgang Flügel, and Peter Krause (both Universität Jena, Germany) for the cooperation.

The valuable comments of Mauri Pelto, Adina Racoviteanu, an anonymous reviewer, and the scientific editor Andreas Kääb considerably helped to improve the quality of this contribution.

Edited by: A. Kääb

References

Ageta, Y. and Fujita, K.: Characteristics of mass balance of summer-accumulation type glaciers in the Himalayas and Tibetan Plateau, Z. Gletscherkd. Glazialgeol., 32, 61–65, 1996.

Berry, P. A. M., Garlick, J. D., and Smith, R. G.: Near-global validation of the SRTM DEM using satellite radar altimetry, Remote Sens. Environ., 106, 17–27, 2007.

Bhambri, R. and Bolch, T.: Glacier Mapping: A Review with special reference to the Indian Himalayas, Prog. Phys. Geog., 33(5), 672–704, 2009.

Böhner, J.: General climatic controls and topoclimatic variations of Central and High Asia, Boreas, 35(2), 279–295, 2006.

Bolch, T., Buchroithner, M. F., Pieczonka, T., and Kunert, A.: Planimetric and volumetric Glacier changes in Khumbu Himalaya since 1962 using Corona, Landsat TM and ASTER data, J. Glaciol., 54(187), 592–600, 2008.

Bolch, T. and Kamp, U.: Glacier Mapping in High Mountains using DEMs, Landsat and ASTER Data, Grazer Schriften der Geographie und Raumforschung, 41, Proc. 8th Int. Symp. on High Mountain Remote Sensing Cartography, 20–27 March 2005, La Paz, Bolivia, 13–24, 2006.

Bolch, T., Menounos, B., and Wheate, R. D.: Landsat-based inventory of glaciers in western Canada, 1985–2005, Remote Sens. Environ., 114(1), 127–137, 2010.

Braithwaite, R. J. and Raper, S. C. B.: Estimating equilibrium-line altitude (ELA) from glacier inventory data, A. Glaciol., 50, 127–132, 2010.

Caidong, C. and Sorteberg, A.: Modelled mass balance of Xibu glacier, Tibetan Plateau: sensitivity to climate change, J. Glaciol., 56(196), 235–248, 2010.

Chen, F., Kang, S., Zhang, J., and You, Q.: Glaciers and lake change in response to climate change in the Nam Co Basin, Tibet, (in Chinese with English abstract), J. Mt. Sci., 27(6), 641–647, 2009.

Ding, Y., Liu, S., Li, J., and Shangguan, D.: The retreat of glaciers in response to recent climate warming in western China, Ann. Glaciol., 43, 97–105, 2006.

Falorni, G., Teles, V., Vivoni, E. R., Bras, R. L., and Amartunga, K. S.: Analysis and characterization of the vertical accuracy of digital elevation models fro m the Shuttle Radar Topography Mission, J. Geophys. Res., 110, F02005, doi:10.1029/2003JF000113, 2005.

Frauenfeld, O. W., Zhang, T., and Serreze, M. C.: Climate change and variability using European Centre for Medium-Range Weather Forecasts reanalysis (ERA-40) temperatures on the Tibetian Plateau, J. Geophys. Res., 110, D02101, doi:10.1029/2004JD005230, 2005.

Frauenfelder, R. and Kääb, A.: Glacier mapping from multitemporal optical remote sensing data within the Brahmaputra river basin, Proc. 33rd int. Symposium on Remote Sensing of Environment, 4–8 May 2009, Stresa, Italy, Tucson, Arizona, International Center of Remote Sensing of Environment, Paper 299, 4 pp., 2009.

Fujita, K.: Influence of precipitation seasonality on glacier mass balance and its sensitivity to climate change, Ann. Glaciol., 48, 88–92, 2008.

Fujita, K. and Ageta, Y.: Effect of summer accumulation on glacier mass balance on the Tibetan Plateau revealed by mass-balance model, J. Glaciol., 46(153), 244–252, 2000.

Fujita, K., Ohta, T., and Ageta, Y.: Characteristics and climatic sensitivities of runoff from a cold-type glacier on the Tibetan Plateau, Hydrol. Process., 21, 282–289, 2007.

Fujita, K., Seko, K., Ageta, Y., Pu, J., and Yao, T.: Superimposed ice in glacier mass balance on the Tibetan Plateau, J. Glaciol., 42(142), 454–460, 1996.

Granshaw, F. D. and Fountain, A. G.: Glacier change (1958-1998) in the North Cascades National Park Complex, Washington, USA, J. Glaciol., 52(177), 251–256, 2006.

Huang, M.: On the temperature distribution of glaciers in China, J. Glaciol., 36(123), 210–216, 1990.

Immerzeel, W., van Beek, L. P., and Bierkens, M. F.: Climate change will affect the Asian water towers: Science, 328, 1382–1385, 2010.

Kääb, A.: Monitoring high-mountain terrain deformation from repeated air- and spaceborne opitcal data: examples using digital aerial imagery and ASTER data, J. Photogr. Remote Sens., 57, 39–52, 2001.

Kamp, U., Bolch, T., and Olsenholler, J.: Geomorphometry of Cerro Sillajhuay, Chile/Bolivia: comparison of DEMs derived from ASTER remote sensing data and contour maps, Geocarto International, 20(1), 23–34, 2005.

Kang, S., Chen, F., Ye, Q., Jing, Z., Qin, D., and Ren, J.: Glacier retreating dramatically on Mt. Nyainqêntanglha during the last 40 years. (In Chinese with English summary), J. Glaciol. Geocryol., 29(6), 869–873, 2007a.

Kang, S., Qin, D., Ren, J., Zhang, Y., Kaspari, S., Mayewski, P. A., and Hou, S.: Annual accumulation in the Mt. Nyainqentanglha ice core, southern Tibetan plateau, China: Relationships to atmospheric circulation over Asia, Arct. Antarct. Alp. Res., 39, 663–670, 2007b.

Kang, S., Chen, F., Gao, T., Zhang, Y., Yang, W., Yu, W., and Yao, T.: Early onset of rainy season suppresses glacier melt: a case study on Zhadang glacier, Tibetan Plateau, J. Glaciol., 55(192), 755–758, 2009.

Kang, S., Wei, X., You, Q., Flügel, W., Pepin, N., and Yao, T.: Review of climate and cryospheric change in the Tibetan Plateau, Environ. Res. Lett., 5, 015101, doi:10.1088/1748-9326/5/1/015101, 2010.

Konecny, G., Reynolds, M., and Schroeder, M.: Mapping from Space: The Metric Camera experiment, Science, 225(4658), 167–169, 1984.

Li, X.: GLIMS Glacier Database, Boulder, CO, National Snow and Ice Data Center/World Data Center for Glaciology, Digital Media, 2003.

Li, X., Cheng, G., Jin, H., Kang, E., Che, T., Jin, R., Wu, L., Nan, Z., Wang, J., and Shen, Y.: Cryospheric change in China, Global Planet. Change, 62(3–4), 210–218, 2008.

Liu, J., Wang, S., Yu, S., Yang, D., and Zhang, L.: Climate warming and growth of high-elevation inland lakes on the Tibetan Plateau, Global Planet. Change, 67, 209–217, 2009.

Liu, J., Kang, S., Gong, T., and Lu, A.: Growth of a high-elevation large inland lake, associated with climate change and permafrost

degradation in Tibet, Hydrol. Earth Syst. Sci., 14, 481–489, doi:10.5194/hess-14-481-2010, 2010.

Liu, X. and Chen, B.: Climatic warming in the Tibetan Plateau during recent decades, Int. J. Climatol., 20(14), 1729–1742, 2000.

Ma, D., Tu, J., Cui, P., and Lu, R.: Approach to Mountain Hazards in Tibet, China, J. Mt. Sci., 1(2), 143–154, 2004.

Miehe, G., Winiger, M., Böhner, J., and Zhang, Y.: The climatic diagram map of High Asia, Purpose and concepts, Erdkunde, 55, 94–97, 2001.

Narama, C., Kääb, A., Duishonakunov, M., and Abdrakhmatov, K.: Spatial variability of recent glacier area changes in the Tien Shan Mountains, Central Asia, using Corona (1970), Landsat (2000), and ALOS (2007) satellite data, Global Planet. Change, 71(1–2), 42–54, 2010.

Naito, N., Ageta, Y., Nakawo, M., and Waddington, E. D.: Response sensitivities of a summer-accumulation type glacier to climate changes indicated with a glacier fluctuation model, B. Glaciol. Res., 18, 1–8, 2001.

Paul, F. R., Barry, R. G., Cogley, J. G., Frey, H., Haeberli, W., Ohmura, A., Ommanney, C. S. L., Raup, B., Rivera, A., and Zemp, M.: Recommendations for the compilation of glacier inventory data from digital sources, Ann. Glaciol., 50(53), 119–126, 2009.

Paul, F. A., Kääb, A., Maisch, M., Kellenberger, T., and Haeberli, W.: The new remote sensing derived Swiss Glacier Inventory: I. Methods, Ann. Glaciol., 34, 355–361, 2002.

Pu, J., Yao, T., and Tian, L.: Change of the Gurenhekou Glacier in Yangbajain Area, Nyainqêntanglha Range, J. Glaciol. Geocryol., 28(6), 861–864, 2006.

Qin, J., Yang, K., Liang, S., and Guo, X.: The altitudinal dependence of recent rapid warming over the Tibetan Plateau, Climatic Change, 97(1–2), 321–327, 2009.

Racoviteanu, A. E., Paul, F., Raup, B., Khalsa, S. J. S., and Armstrong, R.: Challenges and recommendations in mapping of glacier parameters from space: results of the 2008 Global Land Ice Measurements from Space (GLIMS) workshop, Boulder, Colorado, USA, Ann. Glaciol., 50, 53–69, 2009.

Sato, T.: Spatial and temporal variations of frozen ground and snow cover in the eastern part of the Tibetan Plateau, J. Meteorol. Soc. Jpn., 79(1B), 519–534, 2001.

Schiefer, E., Menounos, B., and Wheate, R. D.: An inventory and morphometric analysis of British Columbia glaciers, Canada, J. Glaciol., 54(186), 551–560, 2008.

Schütt, B., Berking, J., Frechen, M., and Yi, C.: Late Pleistocene Lake Level Fluctuations of the Nam Co, Tibetan Plateau, China, Z. Geomorphol., Supplementary Issues, 52(2), 57–75, 2008.

Shi, Y., Hsieh, T., Chen, P., and Li, C. Distribution, features and variation of glaciers in China, IAHS Publ., 126, 111–116, 1980.

Shi, Y. and Liu, S.: Estimation on the response of glaciers in China to the global warming in the 21st century, Chinese Sci. Bull., 45(7), 668–672, 2000.

Shi, Y., Liu, S., Shangguan, D., Li, D., and Ye, B.: Peculiar phenomena regarding climatic and glacial variations on the Tibetan Plateau, Ann. Glaciol., 43, 106–110, 2006.

Surazakov, A. B. and Aizen, V. B.: Positional accuracy evaluation of declassified Hexagon KH-9 mapping camera imagery, Photogramm. Eng. Rem. S., 76(5), 603–608, 2010.

Thomas, A. and Chen, S.: Landwirtschaft und klimatische Trends im Yarlong Tsangpo-Tal, Tibet, Erdkunde, 56(4), 351–384, 2002.

Toutin, T.: ASTER DEMs for geomatic and geoscientific applications: a review, Int. J. Remote Sens., 29(7), 1855–1875, 2008.

Tucker, C., Grant, D., and Dykstra, J.: NASA's global orthorectified Landsat data set, Photogramm. Eng. Remote Sens., 70(3), 313–322, 2004.

Wu, Y. and Zhu, L.: The response of lake-glacier variations to climate change in Nam Co Catchment, central Tibetan Plateau, during 1970–2000, J. Geogr. Sci., 18(2), 177–189, 2008.

Xiao, C., Liu, S., Zhao, L., Wu, Q., Li, P., Liu, C., Zhang, Q., Ding, Y., Yao, T., Li, Z., and Pu, J.: Observed changes of cryosphere in China over the second half of the 20th century: an overview, Ann. Glaciol., 46, 382–390, 2007.

Yao, T.: Map of Glaciers and Lakes on the Tibetan Plateau and Adjoining Regions 1:2 000 000, Xian Cartographic Publishing House, 2008.

Yao, T., Pu, J., Lu, A., Wang, Y., and Yu, W.: Recent glacial retreat and its impact on hydrological processes on the Tibetan Plateau, China, and surrounding regions, Arct. Antarct. Alp. Res., 39(4), 642–650, 2007.

Ye, Q., Kang, S., Chen, F., and Wang, J.: Monitoring glacier variations on Geladandong Mountian, central Tibetan Plateau, from 1969 to 2002 using remote-sensing and GIS technologies, J. Glaciol., 52(179), 537–545, 2006.

You, Q., Kang, S., Tian, K., Liu, J., Li, C., and Zhang, Q.: Preliminary analysis on climatic features at Mt. Nyainqentanglha, Tibetan Plateau, (in Chinese with English abstract), J. Mt. Sci., 25(4), 497–504, 2007.

You, Q., Kang, S., Aguilar, E., Flügel, W., and Yan, Y.: Relationship between temperature trend magnitude, elevation and mean temperature in the Tibetan Plateau from homogenized surface stations and reanalysis data, Global Planet. Change, 71, 124–133, 2010.

Zhang, Y., Kang, S., and Li, M.: Climatic features at Nam Co station, Tibetan Plateau, Annual Report of Nam Co Station for Multisphere observation and Research, 3, 1–8, 2008.

Zhao, L., Ping, C., Yang, D., Cheng, G., Ding, Y., and Liu, S.: Changes of climate and seasonally frozen ground over the past 30 years in Qinghai-Xizang (Tibetan) Plateau, China, Global Planet. Change, 43, 19–31, 2004.

Zhou, C., Yang, W., Wu, L., and Liu, S.: Glacier changes from a new inventory, Nianchu river basin, Tibetan Plateau, Ann. Glaciol., 50(53), 87–92, 2009.

Appendices

Appendix A

Glaciological field studies at Zhadang Glacier (5500–6095 m), Tibetan Plateau

Maussion, F., Yang, W., Huintjes, E., Pieczonka, T., Scherer, D., Yao, T., Kang, S., Bolch, T., Buchroithner, M., and Schneider, C. (2011): Glaciological field studies at Zhadang Glacier (5500-6095m), Tibetan Plateau, *IASC Workshop on the use of automated measuring systems on glaciers - Extended abstracts and recommendations*, 62-68.

Non peer-reviewed document available online:
http://www.projects.science.uu.nl/iceclimate/workshop/documents/abstracts2011.pdf

Glaciological field studies at Zhadang Glacier (5500-6095 m), Tibetan Plateau

Fabien Maussion[1], Yang Wei[2], Eva Huintjes[3], Tino Pieczonka[4], Dieter Scherer[1], Tandong Yao[2], Shichang Kang[2], Tobias Bolch[4], Manfred Buchroithner[4] and Christoph Schneider[3]

[1] Institut für Ökologie, Technische Universität Berlin, Berlin, Germany
Email: fabien.maussion@tu-berlin.de
[2] Institute of Tibetan Plateau Research, Chinese Academy of Sciences, Beijing, China
[3] Geographisches Institut, RWTH Aachen University, Aachen, Germany
[4] Institut für Kartographie, Technische Universität Dresden, Dresden, Germany

Introduction

For historical and logistical reasons, meteorological observations on the Tibetan Plateau (TP) are scarce. It is even more true for mountain-regions, where glaciers have been observed intensively only since recent years. This lack of observations is problematic, regarding their importance for both local and regional ecosystems. Primarily, the Institute of Tibetan Plateau Research (ITP, Chinese Academy of Sciences) is dedicated to current glaciological observations on the TP.

Zhadang Glacier is a small valley glacier (2.48 km^2) located in the Nyainqentanglha Range, about 200 km North from Lhasa (see Fig. 1 and Bolch *et al.* (2010), for a comprehensive description of the study region and its glacier changes 1976-2009). The glacier is exposed to the northwest and drains into Lake Nam Co (4725 m a.s.l.), Tibet's largest salt water lake. The region is under the complex influence of both the continental climate of Central Asia and the Indian Monsoon system (Kang *et al.*, 2009), which leads to a climate characterised by a strong seasonality in both temperature and precipitation. Only little precipitation occurs during winter, while about 90% of mean annual precipitation is measured from June to September. Glaciers located in this continental summer precipitation climate, with the maximum of annual accumulation and ablation occurring simultaneously, are called summer accumulation type glaciers.

ITP operates two Automatic Weather Stations (AWS) since September 2005 in the area of Zhadang Glacier: one in the accumulation area of the glacier (5785 m a.s.l.) and the other in the valley (5400 m a.s.l.) in front of the glacier. Continuous measurements are supplemented by mass balance measurements applying the glaciological method. The installations have been complemented in May 2009 by Sino-German teams within the DynRG-TiP project (Link) with two AWS: one on the ablation zone of the glacier (5660 m a.s.l.) and one that has been relocated recently to the terminal moraine close to the glacier tongue (5550 m a.s.l.). Besides, two time-lapse cameras have been installed in May 2010 (Fig. 1). This makes Zhadang Glacier to be the one of the most sophisticated measurement

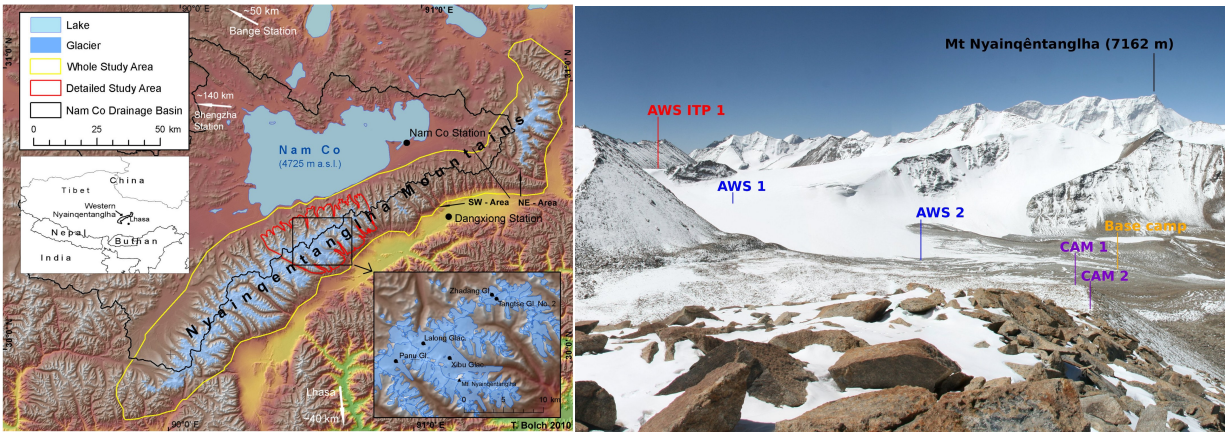

a. **b.**

Figure 1. a) Overview of the Nyainqentanglha Range, including a zoom into the Zhadang Glacier area (after Bolch *et al.*, 2010). b) Panorama of Zhadang Glacier, with locations of the AWS and camera installations (full panorama available online (Link))

sites on the TP. Here we focus on the recent DynRG-TiP AWS and camera installations.

Logistical aspects

The equipment and mechanical parts have been shipped from Germany to China a few months before our arrival. The Chinese customs allow a temporary import for a period of six months renewable only twice, and ask for a security deposit of about 20% of the ware value. Since our stations operate for a longer period, the deposit has been lost and the ware was officially imported to China in 2010. Some useful mechanical parts (tools, tubes, etc.) can be bought in Lhasa, but they are mostly of inferior quality or heavy.

We usually visit the glacier twice a year (May and September). However, this will no longer be necessary as the systems are now running stable. We expect that one campaign per year towards the end of the ablation season will be sufficient. Due to the high altitude two acclimatisation steps of three days each are necessary (Lhasa, 3650 m a.s.l. and Nam Co, 4740 m a.s.l) before being capable to go up to the base camp (5400 m a.s.l.), which is reached in a one day walk. Tibetan nomads are living in the valley from May to September and let their yaks graze. Without their support and the strength of their horses or yaks to carry our equipment, the ascension would be virtually impossible. However, the nomads are not always in favour of our activities: some of them are superstitious and recently our stations were held responsible for various capricious weather phenomena.

Automatic weather stations

The instruments (Tab. 1) were primarily mounted on a mast drilled into the ice to more than 2.5 m depth. Based on the mass balance measurements

Table 1. Sensor specifications.

Measured quantity	Instrument	Sample interval
Air temperature (2 heights)	CS215 (Campbell)	10 min
Relative humidity (2 heights)	CS215 (Campbell)	10 min
Air pressure	DPI740 (T. Friedrichs & Co)	10 min
Net radiation	NR-Lite (Campbell)	10 min
Solar radiation (up and down)	CS300 (Campbell)	10 min
Longwave radiation (up)	IRTS-P Apogee	10 min
Ice temperature (8 depths, down to 9 m)	107TP (Campbell)	10 min
Surface height	SR50 (Campbell)	10 min
Wind speed and direction	05103 (Young)	10 sec sample, 10 min storage
Wind (sonic anemometer)	Windmaster (Gill)	10 Hz sample, 10 min storage
Mast inclination (2D)	SCA121T (VTI Tech)	10 min

in previous years (about 1 m w.e. per year, Kang *et al.* (2009)) and our own estimation of the equilibrium line altitude, this seemed to be a reasonable choice. The high ablation in 2009, estimated to 2.5 m of ice, caused the fall of both stations around mid-July. Therefore, we changed to a tripod set-up and a separate mast for the sonic ranger (Campbell SR50) (Fig. 2). The stations was supposed to stay on their feet as the ice level decreases but for some reasons (extreme wind? debris within the ice?) the stations again fell over in summer 2010. ITP staff could re-erect them one month later. A construction with wider feet extent may have been more stable, but difficult to find in China. The SR50 structure inspired by Oerlemans *et al.* (2004) (three tubes of 5 m length, drilled inclined into the ice) proved to be very stable, but the inclined holes are difficult to drill properly using the steam drill.

The stations worked perfectly and had no data or power failures (radiation values are high also in winter and the batteries are recharged efficiently). Thanks to the inclinometer placed at the mast, it was easy to track all events of falling over. By this means valid measurement periods could be selected. The low-cost of the sensor is less of a problem than the provision of two extra slots on the data-logger (CR1000, Campbell). Nevertheless, this is really worthwhile considering the importance of the information on mast tilt. In order to measure the radiation budget we replaced the popular CNR1 from Kipp & Zonen by the cost-effective 4-sensor installation described in Table 1. The shortwave radiation measurements proved to be accurate. In contrast, the longwave radiation measurements were not satisfying for two reasons. The IRTS sensor shows high sensitivity to solar radiation and measured snow surface temperatures up to several K above the melting point during the day. Furthermore, incoming longwave radiation (obtained using the net radiation value subtracted from the three measured components) suffers from accuracy problems due to the different frequency responses of the various sensors. Two temperature and relative humidity (RH) probes are placed in a ventilated radiation

a. **b.**

Figure 2. a) The AWS 1 in autumn 2010 and our young Tibetan helper. b) The terrestrial camera system (placed in a waterproof box that is closed afterwards)

shield (THIES Clima GmbH). The ventilators are directly connected to two solar panels in an independent circuit. This has the strong advantage that the ventilator will not use the power of the battery and that the probes are efficiently ventilated during the day. However, there is the disadvantage that the probes are not ventilated at night. The solar panel voltage is sampled every 10 minutes to track the strength of ventilation. The effect of this ventilation strategy in comparison with permanent ventilation needs to be evaluated in more detail.

Terrestrial cameras

We installed two cameras on the glacier lateral moraine (Canon EOS D-60, objective of 28 mm focus, fixed aperture value of 7.1 and adaptive aperture time) taking three (recently changed to six) pictures a day of the glacier tongue area. The power supply for each camera and the camera timer, responsible for the triggering impulse, is ensured by a single 12 V battery recharged by a solar panel. Because both cameras (base of about 400 m with a base-to-height ratio of about 0.3) are operating simultaneously it is possible to compute glacier volume changes using stereoscopy. Therefore, 14 Ground Control Points (GCPs) were measured in the glacier forefield. As point locations we chose single boulders which are supposed to be stable over time. Even though one of the cameras was stolen in summer 2010, the second camera provided a dataset of high quality (animation available online (Link)). The pictures allow a rare insight into the meteorological and surface conditions of the glacier on a sub-daily basis, which is useful for AWS data processing, analysis and validation. For example, the image time series was analysed in order to produce a dataset of the timing and intensity of snow events which was used for the validation of the sonic ranger snowfall algorithm.

Data treatment

During winter, the tripod feet are covered by ice and snow and the system is very stable. Only standard corrections are necessary (RH for temperatures below zero using the values given by Campbell, interpolation of temperature and humidity at the 2 m height, sonic range correction for temperature). During summer, rapid snow events and follow-up melt may occur within hours. High wind speeds and surface changes make the station stagger.

Precipitation often occurs in the form of soft hail. All these surface conditions together seem to influence the quality of the signal of the sonic ranger. The quality flag provided by the sensor is useful for automatically filtering a large part of the invalid data. Nevertheless, the signal remains noisy (sometimes above the accuracy of 1 cm specified by the manufacturer) especially during precipitation events. The temperature correction is necessary to avoid artefacts, as the measured distance may "diminish" at the end of the day. This could falsely be interpreted as a snow event. In order to minimise this effect, a 3 h moving mean of top and bottom temperature sensors was used for the correction. Finally, a 3 h moving mean is applied to the sonic ranger data for noise reduction. A larger window size would increase the smoothing but would reduce the signal of the short and small (less than 10 cm) but frequent snow events of the summer season.

For the detection and quantification of snow events using sonic ranger data, several algorithms were compared and gave largely variable results (up to a factor 3 in the amounts). The main issue is that no validation can be made without a reference dataset. Using the information provided by the time-lapse camera as reference, one of the algorithms could objectively be selected. The 6 hourly snowfall amount is obtained as follows: if the mean surface height (snow depth) of the 6 h period is higher of at least 1 cm than the mean surface height of the previous 6 h, then a snow event occurred. The 6 h snowfall is given by the difference between the maximum and the minimum surface height during these 6 h.

Recommendations and conclusions

In this document, we presented the operation of two AWS and two cameras in the harsh environment of the TP. We addressed several topics such as logistics, instrumentation, mechanical construction and data treatment. In general, our field experiment is a success, but we also made several mistakes that we would like to share in the following list of recommendations. They are based on our own experience, and may be not entirely new or even be unsuitable for other environments.

- Despite the high altitude, ablation is very strong on glaciers of the central TP. The ablation season is short (June to mid-August) but intense. Therefore, AWS constructions based on stable tripods are recommended for altitude ranges below 6000 m a.s.l.

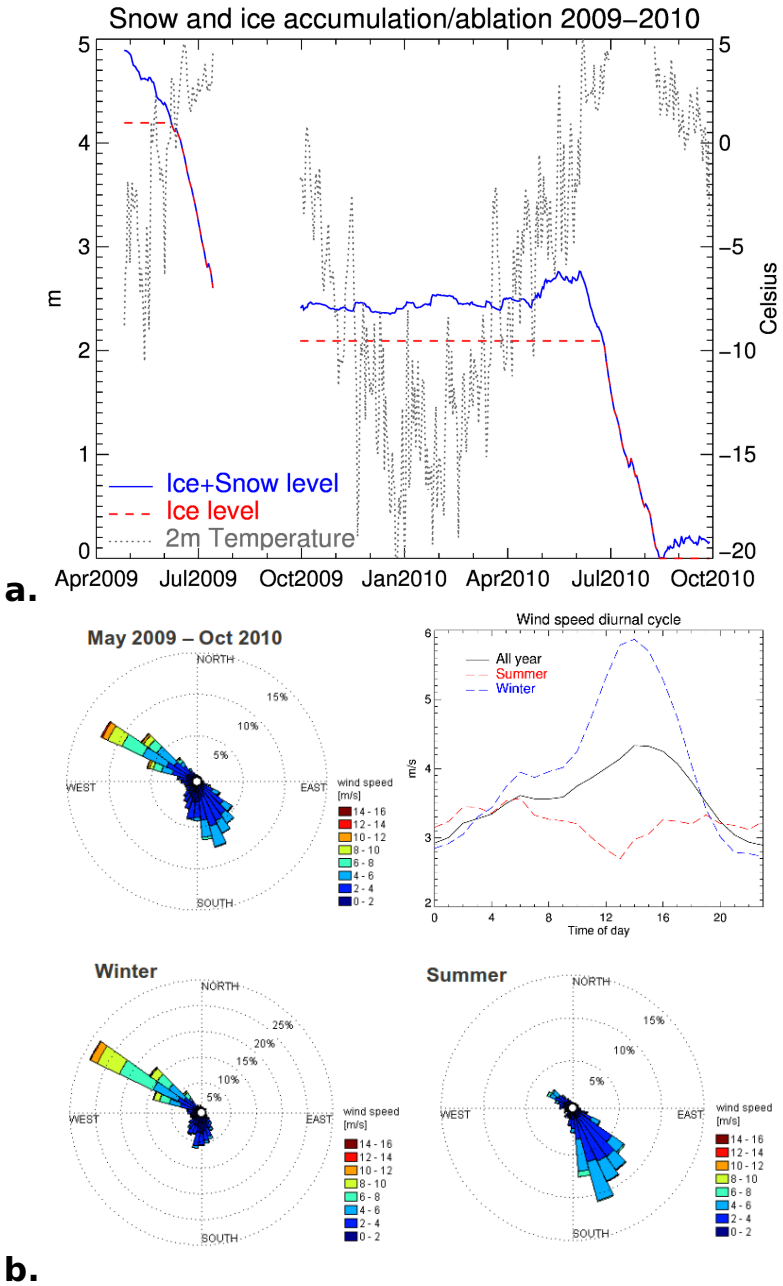

Figure 3. a) Daily means of snow accumulation and ablation at AWS 1 in 2009 and 2010 and air temperature. b) Wind roses and diurnal cycle of wind speed for the whole measurement period, winter season and summer season.

- The tripod should be as light and as bright as possible to resist the harsh weather conditions.
- A second system, installed next to the glacier, emerged as the safest way to ensure continuous data collection.
- Time-lapse cameras, besides the application for stereoscopy, are a useful tool to understand and observe surface and near-surface conditions of a glacier. Cost-effective systems are easily available for such purposes.
- The "daytime ventilation", radiation shield ventilators directly connected to independent dedicated solar panels, is an efficient way to ensure the

power supply of the instruments. The effect of this ventilation strategy on the temperature measurements especially during night is not yet quantified.

- If there are adequate financial resources, a direct measurement of all four radiation components using accurate sensors is a good solution to avoid complex and imperfect data post-processing.
- If there are enough slots available on the data-logger, the measurement of the tilt of the mast simplifies many aspects of data post-processing.
- The signal quality flag provided by the SR50 sensor provides useful information for efficient data filtering. There should be a memory slot reserved on the data logger for this number if ever possible.

The authors will be pleased to answer any further questions and are open to suggestions or comments regarding this list.

In the meantime, the efforts of measuring near surface meteorology on Zhadang Glacier have provided us with outstanding and unique data (see Fig. 3) that in the near future will allow accurate and state-of-the-art investigation of surface energy and mass exchange from a logistically difficult remote high altitude site.

Acknowledgements

The work is supported by the German Research Foundation (Deutsche Forschungsgemeinschaft, DFG) within the Tibetan Plateau (TiP) Priority Programme under the codes SCHE 750/4-1, SCHN 680/3-1, and BU 949/20-1. Many thanks to our colleagues from the ITP, from Germany and to our Tibetan helpers.

References

Bolch, T., T. Yao, S. Kang, M. Buchroithner, D. Scherer, F. Maussion and C. Schneider. 2010. A glacier inventory for the western nyainqentanglha range and nam co basin, tibet, and glacier changes 1976–2009. *The Cryosphere*, **4**, 419–433.

DynRG-TiP. Dynamic response of glaciers on the tibetan plateau to climate change (http://www.klima.tu-berlin.de/index.php?show=forschung_asien_tibet &lan=en). *DFG Priority Programme 1372*. "Tibetan Plateau: Formation, Climate Ecosystems (TiP)" (http://www.tip.uni-tuebingen.de).

Kang, S., F. Chen, T. Gao, Y. Zhang, W. Yang, W. Yu and T. Yao. 2009. Early onset of rainy season suppresses glacier melt: a case study on zhadang glacier, tibetan plateau. *J. Glaciol.*, **55**(192), 755–758.

Oerlemans, J., W. Boot, M. van den Broeke, C. Reijmer and R. van de Wal. 2004. Aws in the ablation zones of glaciers, workshop on the use of automatic weather stations on glaciers. In: Reijmer, C., editor, *Automatic weather stations on glaciers*, Proceedings of a workshop, 28-31 March 2004, Pontresina (Switzerland), pages 83–87. Institute for Marine and Atmospheric Research Utrecht (IMAU). http://www.projects.science.uu.nl/iceclimate/workshop/documents/aws_ab stracts.pdf.

One ablation season at zhadang glacier. *http://www.klima.tu-berlin.de/forschung/Asien/tibet/pics/one_season.gif.*

Panorama of zhadang glacier. *http://www.klima.tu-berlin.de/forschung/Asien/tibet/pics/panorama/zhadang_pano.html*.

Appendix B

Influence of the high-altitude Nam Co lake on local precipitation patterns

Summary. Lakes are important components of the climate system. The Tibetan Plateau, host of about 1260 lakes larger than 1 km^2, remains poorly studied in this regard. Large lakes like the Nam Co (1980 km^2 area, 4724 m a.s.l.) are expected to significantly influence their environment but this was rarely investigated using numerical modelling before. This document condenses the results of three modelling experiments using the Weather Research and Forecast (WRF) model. The experiments are designed to study the influence of the Nam Co lake on local precipitation patterns during four selected years (2002-03 and 2008-09). We investigate the influence of assimilating satellite-derived lake surface temperatures (ST) instead of using the standard WRF initialization approach. Furthermore, we run an idealized experiment where the Nam Co lake has been replaced by grasslands to quantify the influence of the presence of the lake on local precipitation spatio-temporal variability. We find that assimilating lake ST has a positive impact on the simulated cloud frequencies and precipitation patterns, especially during the months of August to December. The standard WRF approach proves to be an acceptable compromise for selected applications at regional scale but should be used carefully for hydrological impact studies. According to our simulations, the presence of the lake reduces precipitation averaged over the Nam Co drainage catchment of about 8%. This number becomes larger when considering the neighbouring regions on the eastern (lee) side of the lake. The effect of the lake is most notable in summer, when the colder surface inhibits convection. We also observe lake-effect snowfall events in Autumn. The influence of these events on yearly precipitation amounts is less significant.

Preamble: *the content of this document will be re-arranged into a manuscript that will be submitted for publication in a peer-reviewed journal in 2014. Foreseen co-authors: Rüthrich, F., Kropacek, J., Biskop, S. and D. Scherer. Foreseen journal: Theoretical and Applied Climatology. The document is organised around the nine graphics that provide the information needed to reach the conclusions stated here. To help the reader of this already lengthy thesis, the text is composed of key arguments and conclusions that should be sufficient to understand the figures and the results of the study.*

Introduction

Lakes have a strong influence on local climate. They interact with the atmosphere by exchanging moisture and thermal energy, and they have (among other characteristics) distinct heat capacity, surface albedo and roughness. The most observed effects of lakes are (i) the inhibition of convection in summer when the water is colder than surrounding land areas, and (ii) the initiation of precipitation in autumn/winter when the water is warmer and provides moisture and energy to the atmosphere (Wilson, 1977).

For weather forecast purposes and because of their remarkable effect on local climate, the lake-atmosphere interactions in the Great Lakes region (North America) have been intensively studied (e.g. Burnett et al., 2003; Kristovich and Spinar, 2004; Laird et al., 2009; Gula and Peltier, 2012). Also in Europe the role of lakes in a changing climate have been analysed using regional climate simulations (Samuelsson et al., 2010). So far, studies of lake-atmosphere interactions on the Tibetan Plateau (TP) have been mostly observational (Haginoya et al., 2009; Biermann et al., 2013; Kropacek et al., 2010). To our knowledge, two modelling case studies (over a short period of time) were conducted at Nam Co (Li et al., 2009; Gerken et al., 2013). In this study we analyse a four-years time period, thus we provide the first climatological investigation of lakes effect on the climate of the TP.

The TP hosts about 1260 lakes that exceed 1 km^2 in surface (Kropacek et al., 2013). The majority freeze in winter but the ice-phenology is highly variable both in space (between lakes) and in time (inter-annual variability). Icing period inter-annual variability could be correlated to autumn snow cover patterns on the lee side of lake Nam Co (Kropacek et al., 2010).

The Weather Research and Forecast (WRF) model is a widely used limited-area atmospheric model. There is no explicit treatment of the lakes in the model, therefore the lake ST must be either assimilated or obtained elsewhere. This is problematic at higher grid resolutions (from 1 to 10 km) when local characteristics such as land-cover become increasingly important. In the HAR 10 km domain, 316 grid-points are classified as inland water bodies (Fig. B.1).

Before version 3.3.1, WRF had no special handling of lake ST initialisation, leading to highly unrealistic conditions (Li et al., 2009; Maussion et al., 2011a). Since V 3.3.1, the "standard approach" in WRF[1] is to use information available from the large-scale input dataset: the

[1] we call it "standard" here but this initialisation technique still requires active changes to the default "out-of-the-box" configuration of WRF, which we believe to be problematic (especially for incoming users not aware of this potential problem)

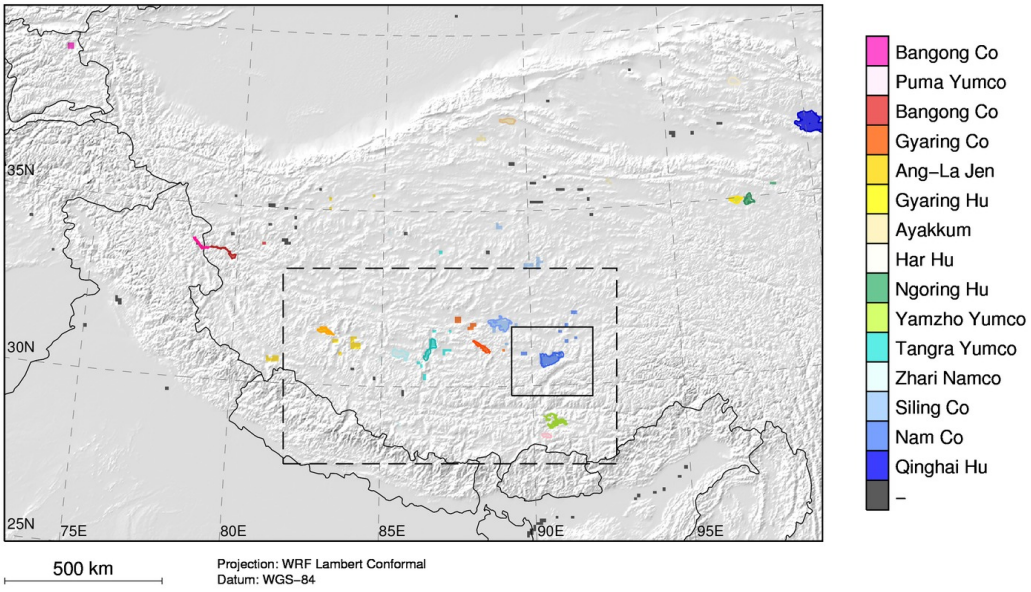

Figure B.1: Map of the HAR 10 km domain. Coloured grid points are classified by the model as inland water bodies: each colour refers to the corresponding lake from the ArcLake dataset. Grey grid points correspond to water bodies with no attributed lake. The dashed box delimits the region of interest shown in Fig. B.4, the black box delimits the Nam Co region.

surrounding land surface temperatures are averaged and the computed value is used to initialise (or update) lake ST on a daily basis. In this study we intend to test and analyse the validity of this approach.

The benefit of model-based approaches is that it is possible to run idealized simulation with modified boundary conditions. With the purpose of quantifying the effect of the lake on precipitation amounts and seasonality we also designed a sensitivity experiment where the Nam Co lake has been removed.

Data and methods

Lake surface temperatures

The observational dataset used in this study is the ArcLake dataset v2.0 (MacCallum and Merchant, 2011, 2012). This dataset contains observations of lake ST from the series of (Advanced) Along-Track Scanning Radiometers (ATSRs). ARC-Lake v2.0 data products cover the period 1991 to 2011. We use the CGREC9D time series datasets (spatially and temporally averaged daytime reconstructions, per-lake). For each lake and each day a surface temperature is provided, making this product particularly handy to use in automatized frameworks. The dataset focus is on large lakes (larger than 500 km^2) resulting in 263 target lakes worldwide out of which 15 are located in the HAR 10 km domain (Fig. B.1).

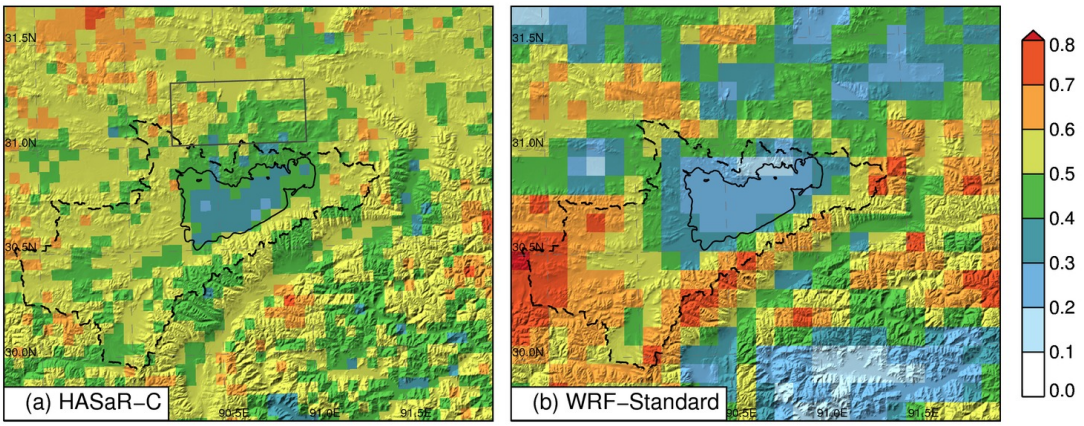

Figure B.2: Frequency of clouds occurrence in August at 16 H CST for **(a)** HASaR-C and **(b)** WRF. The Nam Co lake shore (black line) and Nam Co basin (black dashed line) are indicated, as well as the "Land area" (grey box, see text and Fig. B.6)

Cloud frequency

To evaluate cloud occurrences at Nam Co we use the "High Asia SAtellite Retrievals - Clouds" dataset (HASaR-C, Rüthrich et al., 2013). This dataset is generated using a novel gross-cloud retrieval method for the TiP using logistic regression models. It has a spatial resolution of 6 km and half-hourly temporal resolution for the period 1998–2008. Due to data gaps, this dataset is available for comparison during the years 2002-2003 only. We use monthly frequencies of cloud occurrence, for all months/hours with more than 80% available data. As an example, the cloud frequency at 16 H China Central Time (CST) at Nam Co is shown in Fig. B.2 (a). The equivalent cloud frequencies computed from the WRF model output are shown in Fig. B.2 (b). A grid box in the WRF model is classified as cloud when cloud water + ice mixing ratio exceeds a threshold value of 10^{-6} kg kg^{-1}.

Model experiments

The starting point of this study is the High Asia Reanalysis dataset (HAR). For the production of HAR, the WRF standard method was used to initialize lake ST every day. The surrounding land surface temperatures are averaged daily and the computed value is used to initialise (or update) lake ST on a daily basis. When the lake ST obtained this way falls below -3°C, the lake surface category is changed to "ice/snow" in the model.

To assess the validity of this approach, we conducted a new experiment (ArcLake) with assimilated lake ST. For this purpose, we developed a tool to automatically attribute a lake ST from the corresponding ArcLake to inland water bodies in the WRF domain. With this tool, all large water bodies become a measured lake ST (smaller isolated water bodies continue to be initialized with the standard method, see Fig. B.1). If the lake ST falls below 0.1°C, the lake

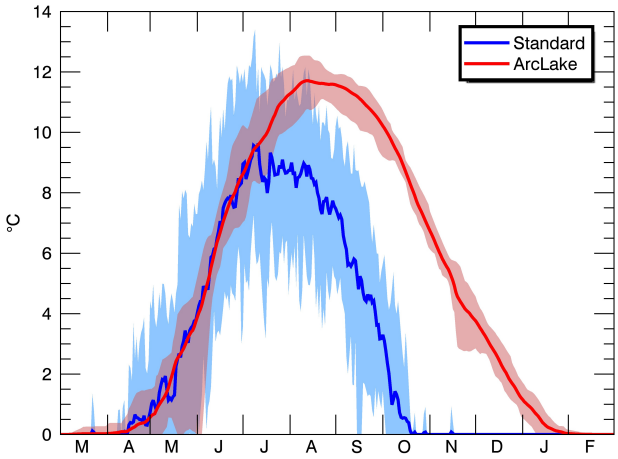

Figure B.3: Decadal mean of the Nam Co lake daily SST, according to the WRF Standard parametrization (blue) and to the ArcLake dataset (red). Shaded areas indicate the decadal minimum and maximum range.

surface category is changed to "frozen ground" in the model.

We chose to analyse a period of four years which is a compromise between computation effort and a sufficiently long time period to allow us build composites of for instance monthly values. The years 2002, 2003, 2008, 2009 were chosen because they are representative of the observed inter-annual variability (2003 and 2009 being rather average years, 2008 being a cold year and 2002 a warm year).

Results

Figure B.3 shows the decadal average of daily lake ST at Nam Co, from the HAR dataset (Standard) and from observations (ArcLake). The Standard method is close to observations in Spring, which means that the observed thawing date of the lake is closely related to the warming of the surrounding surface. In Summer and Autumn the two curves differ largely, since the thermal inertia of water and the increased energy supply from solar radiation are not considered by Standard. A cold bias in the FNL dataset can also contribute to the colder temperatures. The lake in Standard freezes much sooner (October) and the daily variability is (too) large. According to the ArcLake dataset, the lake freezes between January and February and thaws between March and May, in accordance with previous studies (Kropacek et al., 2010, 2013).

Which effect does this temperature discrepancy have on simulated precipitation? The differences in annual precipitation (percentage) between ArcLake and Standard are shown in Fig. B.4. Differences can reach more than 20% of annual precipitation in the close vicinity of the lake, 10 to 20% on the lee side (westerly wind directions largely dominate throughout the year,

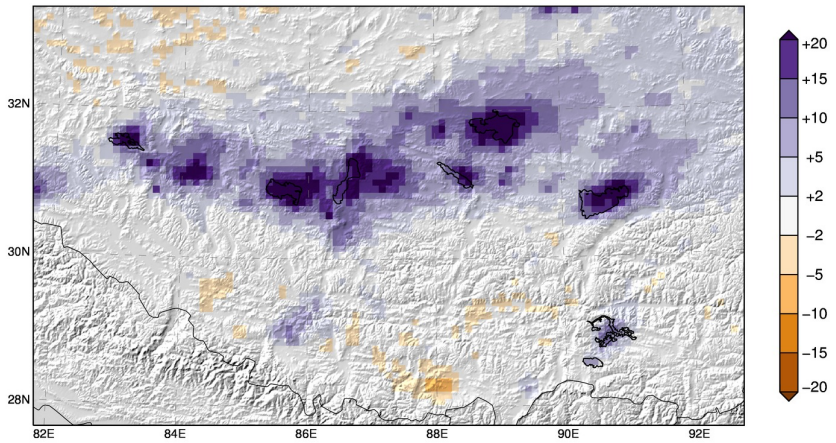

Figure B.4: Difference (%) in total annual precipitation between ArcLake and Standard over Central TP. Positive values indicate that there is more precipitation in ArcLake.

see Kropacek et al., 2013; Maussion et al., 2014), and smaller changes of 2% are observed a hundred kilometres away. Yearly averaged, ArcLake produces uniformly more precipitation, mostly between August and October, the other months showing no significant difference. The mechanisms leading to this increase in precipitation are analysed with more detail below.

Assimilating more realistic Lake ST does not necessarily imply that quantitative precipitation estimates from the model are more accurate. Unfortunately, observations on the TP are scarce, and no precipitation dataset has a sufficient accuracy to assess the benefits of Lake ST assimilation. Therefore, in a first approach, we compare cloud occurrence *over the lake surface* between the HASaR-C dataset and Standard and ArcLake experiments (Fig. B.5). The upper panel of the figure displays diurnal cycles of cloud frequencies (CF) in February (Fig. B.5 a) and August (Fig. B.5 b). There is a marked daily cycle of CF in February, with a minima at 11:00 and a maxima around 18:00 (solar time leads CST from about 2 hours in Tibet). The modelled cycle is really close to observations, with a slight underestimation which could be due to the empirical definition of clouds by the WRF model. In August the daily cycle is less pronounced, but there is a reduction of CF during the day which is more evident in WRF. The lower panel of the figure displays annual cycles of monthly CF at night time (00:00 to 03:00, Fig. B.5 c) and afternoon time (15:00 to 18:00, Fig. B.5 d). Observed and modelled CF follow similar variations throughout the year, again with a pronounced underestimation of WRF. Maximum CF is reached at night in summer and in the afternoon in spring. For all cases, ArcLake performs better than Standard, but the differences are moderate. These results indicate that it is appropriate to assimilate ArcLake temperatures in the WRF model.

The effect of the lake is best observable when comparing CF *over the lake surface* between ArcLake and NoLake (Fig. B.6 a). For comparison, we reproduce the same analysis with observed CF (Fig. B.6 b). Nevertheless, we have to use a trick: the "NoLake" area in the observations is replaced by a region of similar size close enough to the lake, see Fig. B.2. This may alter the results and is therefore not analysed quantitatively. The effect of the lake is largest at

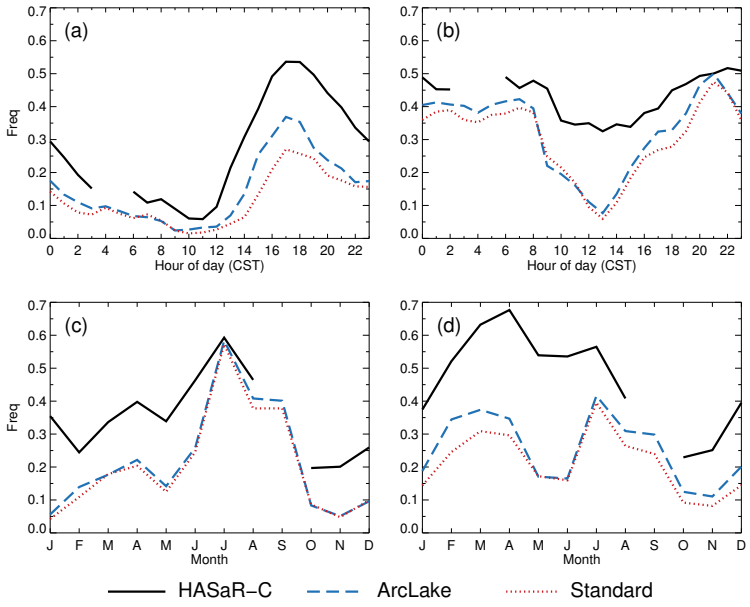

Figure B.5: Top: Daily cycle of cloud frequencies over the Nam Co lake in **(a)** February and **(b)** August. **Bottom**: monthly values of cloud frequencies over the Nam Co lake at (c) 00-03 H CST and (d) 15-18 H CST. Gaps in the observed time series indicate that sufficient cloud information is missing at that time.

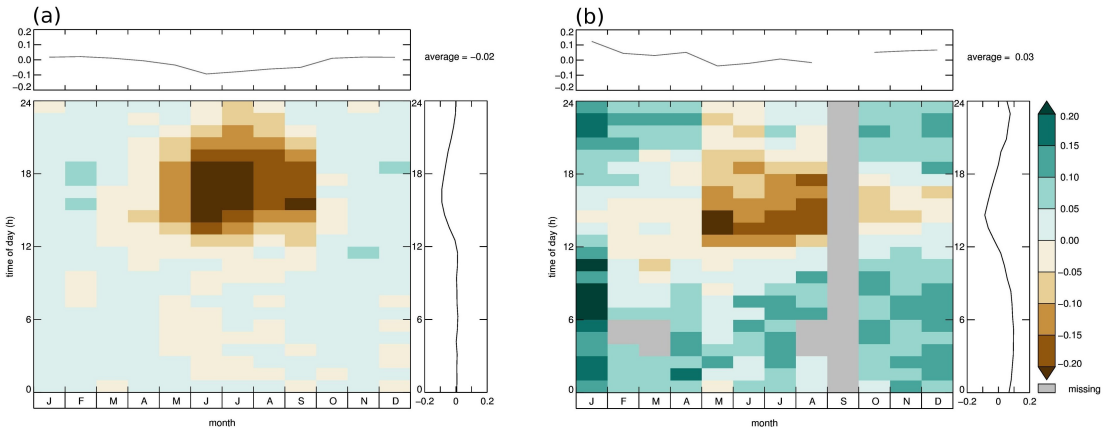

Figure B.6: Differences in cloud frequency for each month and time of day (CST). **(a)** Between ArcLake and NoLake over the lake surface. **(b)** In the HASaR-C dataset between the lake and land areas (grey box in Fig. B.2). Brown colours in summer indicate that there are less clouds over the lake than over land.

afternoon and in spring/summer. This is confirmed by observations, which also show a slight increase of CF at night and winter. This could be explained by fog (not resolved in WRF?) or by observational errors over the icy lake surface.

To assess the influence of the lake from the hydrological perspective we spatially average monthly precipitation over the Nam Co drainage basin for all three experiments (Fig. B.7). ArcLake produces more precipitation than Standard throughout the year, for a total increase of 7% in annual precipitation. The differences are largest in August and September, when the Standard Lake ST are too cold. From October to April, ArcLake produces more precipitation

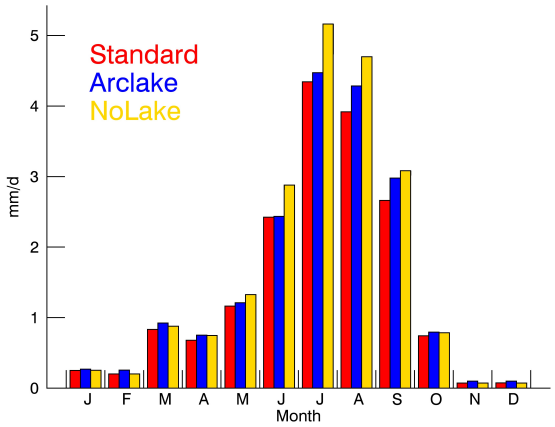

Figure B.7: Monthly precipitation (mm d^{-1}) averaged over the Nam Co basin for the three WRF experiments.

than the other experiments. The inhibition effect of the lake is best seen in June/July when NoLake produces noticeably more precipitation. Compared to NoLake, ArcLake reduces the basin-average precipitation by 8%. This result is interesting in the context of glacier extent on the Nyainqentanglha range (Paper V): there is a much larger area of ice on the south exposed ranged than to the north range flowing into the lake. In Paper V we argued that this difference could be due to rainshadow effects on the monsoonal moisture flow coming from the southeast in summer. Our results present an alternative explanation: the presence of the lake can be responsible for less precipitation on the northern side too.

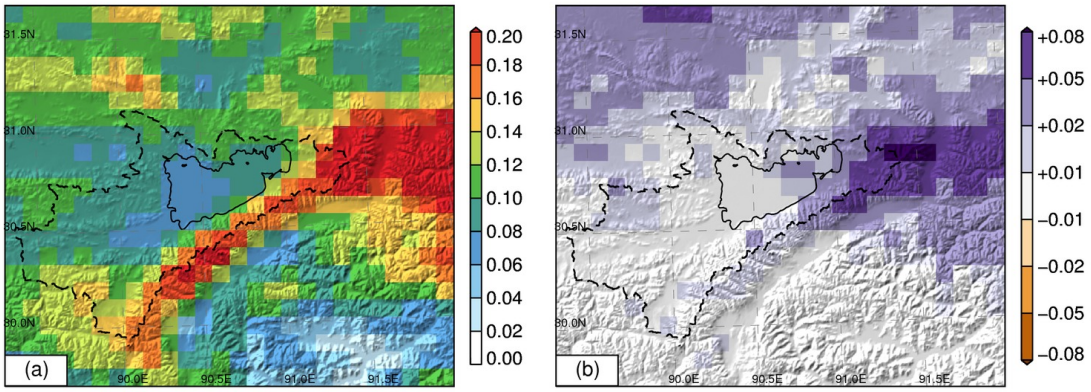

Figure B.8: (a) frequency of snowfall events (> 0.1 mm d^{-1}) during the October to December period for ArcLake. **(b)** Difference between ArcLake and Standard during the same period (positive values indicate that there are more snowfall events in ArcLake).

In Fig. B.8 a, we show the frequency of snowfall events from October to December at Nam Co. On Fig. B.8 b, we verify that the lake is responsible of a substantial part (about 50%) of the snowfall events. These are located on the lee side of the Nam Co lake. The events north of Nam Co are related to the neighbouring Silling Co lake (Fig. B.1).

Figure B.9: Panorama of the clouds surrounding the Nam Co lake in spring. The sky above the lake is cloud-free while small low-level convective clouds produce localized precipitation over land. Picture taken by the Author on the 2011.05.19 in late afternoon.

Conclusions

i. The Nam Co lake has a major influence on cloudiness, mostly in summer when the lake is cooler than surroundings. This is confirmed by both numerical simulations and observations (Figs. B.2, B.5 and B.6) and consolidates the results from previous studies. The panorama picture shown in Fig. B.9 is a "real-life" illustration of this effect.

ii. The lake ST obtained from surrounding land surface temperatures, without any consideration of the physical properties of the lake, are not realistic. This method leads to a much cooler lake than observed (Fig. B.3).

iii. From a) and b) it appears that the Standard lake ST lead to a substantial overestimation of the lake-related convective inhibition in summer (Fig. B.5) and therefore to an underestimation of precipitation.

iv. The lake in Standard freezes 3 to 4 months earlier than observed. This leads to a probable underestimation of lake-effect snowfall (Fig. B.8), but his could not yet be verified with ground truth data. A validation method based on MODIS data (Kropacek et al., 2010) is under consideration. The amounts of precipitation concerned by this modification are rather weak at the basin scale but expected to have a larger influence on longer time-scales (snow cover remains on the ground during winter) and for hydrological/glaciological applications where snowpack plays an important role.

v. The WRF model is able to reproduce the expected effect of the lake. Further processes such as land-see breeze (not shown here) are also correctly represented, illustrating the importance of accurate lake ST for atmospheric simulations. Therefore, we recommend to use either observations or an appropriate physically based lake ST model in the WRF model (and in similar atmospheric models). Without having tested it, we can advance with large confidence that using a climatological Lake ST instead of the standard WRF method would produce more realistic results in any case.

List of Figures

Bibliography

Adler, R. F., Huffman, G. J., Chang, A., Ferraro, R., Xie, P.-P., Janowiak, J., Rudolf, B., Schneider, U., Curtis, S., Bolvin, D., Gruber, A., Susskind, J., Arkin, P., and Nelkin, E.: The Version-2 Global Precipitation Climatology Project (GPCP) Monthly Precipitation Analysis (1979-Present), J. Hydrometeor, 4, 1147–1167, doi:10.1175/1525-7541(2003)004⟨1147:TVGPCP⟩2.0.CO;2, 2003.

Arakawa, A.: The cumulus parameterization problem: Past, present, and future, J. Climate., 17, 2493–2525, doi:10.1175/1520-0442(2004)017⟨2493:RATCPP⟩2.0.CO;2, 2004.

Becker, A., Finger, P., Meyer-Christoffer, A., Rudolf, B., Schamm, K., Schneider, U., and Ziese, M.: A description of the global land-surface precipitation data products of the Global Precipitation Climatology Centre with sample applications including centennial (trend) analysis from 1901–present, Earth System Science Data, 5, 71–99, doi:10.5194/essd-5-71-2013, URL http://www.earth-syst-sci-data.net/5/71/2013/, 2013.

Bengtsson, L., Hagemann, S., and Hodges, K.: Can climate trends be calculated from reanalysis data?, J. Geophys. Res-Atmos., 109, doi:10.1029/2004JD004536, 2004.

Benn, D. and Owen, L.: The role of the Indian summer monsoon and the mid-latitude westerlies in Himalayan glaciation: review and speculative discussion, J. Geol. Soc. London., 155, 353–363, doi:10.1144/gsjgs.155.2.0353, 1998.

Biermann, T., Babel, W., Ma, W., Thiem, E., Ma, Y., Chen, X., and Foken, T.: Turbulent flux observations and modelling over a shallow lake and a wet grassland in the Nam Co basin, Tibetan Plateau, Theor. Appl. Climatol., doi:10.1007/s00704-013-0953-6, 2013.

Biskop, S., Krause, P., Helmschrot, J., Fink, M., and Flügel, W.-A.: Assessment of data uncertainty and plausibility over the Nam Co Region, Tibet, Advances in Geosciences, 31, 57–65, doi:10.5194/adgeo-31-57-2012, 2012.

Biskop, S., Maussion, F., Kropacek, J., Fink, M., and Flügel, W.: A comprehensive data assimilation approach for reliable hydrological predictions in data-scarce endorheic basins, Tibetan Plateau, in: EGU General Assembly Conference Abstracts, vol. 15, p. 10640, URL http://meetingorganizer.copernicus.org/EGU2013/EGU2013-10640-1.pdf, 2013.

Bohner, J.: General climatic controls and topoclimatic variations in Central and High Asia, Boreas., 35, 279–295, doi:10.1080/03009480500456073, 2006.

Bolch, T., Kulkarni, A., Kaab, A., Huggel, C., Paul, F., Cogley, J. G., Frey, H., Kargel, J. S., Fujita, K., Scheel, M., Bajracharya, S., and Stoffel, M.: The State and Fate of Himalayan Glaciers, Science., 336, 310–314, doi:10.1126/science.1215828, 2012.

Bonvalot, G.: De Paris au Tonkin à travers le Tibet inconnu, Hachette, URL http://books.google.de/books?id=o8lWC6foNbQC, 1892.

Bookhagen, B. and Burbank, D. W.: Toward a complete Himalayan hydrological budget: Spatiotemporal distribution of snowmelt and rainfall and their impact on river discharge, Journal of Geophysical Research-earth Surface, 115, F03 019, doi:10.1029/2009JF001426, 2010.

Boos, W. R. and Kuang, Z.: Dominant control of the South Asian monsoon by orographic insulation versus plateau heating, Nature., 463, 218–U102, doi:10.1038/nature08707, 2010.

Boos, W. R. and Kuang, Z.: Sensitivity of the South Asian monsoon to elevated and non-elevated heating, Scientific Reports, 3, doi:10.1038/srep01192, 2013.

Bothe, O., Fraedrich, K., and Zhub, X.: Large-scale circulations and Tibetan Plateau summer drought and wetness in a high-resolution climate model, Int. J. Climatol., doi:10.1002/joc.2124, 2010.

Bothe, O., Fraedrich, K., and Zhu, X.: Tibetan Plateau summer precipitation: covariability with circulation indices, Theor. Appl. Climatol., 108, 293–300, doi:10.1007/s00704-011-0538-1, 2012.

Box, G. E. P. and Draper, N. R.: Empirical model-building and response surface, John Wiley & Sons, Inc., New York, NY, USA, 1986.

Burnett, A., Kirby, M., Mullins, H., and Patterson, W.: Increasing Great Lake-effect snowfall during the twentieth century: A regional response to global warming?, J. Climate., 16, 3535–3542, 2003.

Caidong, C. and Sorteberg, A.: Modelled mass balance of Xibu glacier, Tibetan Plateau: sensitivity to climate change, J. Glaciol., 56, 235–248, 2010.

Chen, B., Xu, X.-D., Yang, S., and Zhang, W.: On the origin and destination of atmospheric moisture and air mass over the Tibetan Plateau, Theor. Appl. Climatol., p. 54, doi:10.1007/s00704-012-0641-y, 2012.

Curio, J., Maussion, F., and Scherer, D.: On the relative importance of water vapour advection and evapotranspiration for precipitation in the Nam Co drainage basin on the Tibetan Plateau, in: EGU General Assembly Conference Abstracts, edited by EGU, vol. 15, URL http://meetingorganizer.copernicus.org/EGU2013/EGU2013-11738-1.pdf, 2013.

Daut, G., Mäusbacher, R., Baade, J., Gleixner, G., Kroemer, E., Mügler, I., Wallner, J., Wang, J., and Zhu, L.: Late Quaternary hydrological changes inferred from lake level fluctuations of Nam Co (Tibetan Plateau, China), Quaternary International, 218, 86–93, doi:10.1016/j.quaint.2010.01.001, 2010.

Dee, D. P., Uppala, S. M., Simmons, A. J., Berrisford, P., Poli, P., Kobayashi, S., Andrae, U., Balmaseda, M. A., Balsamo, G., Bauer, P., Bechtold, P., Beljaars, A. C. M., van de Berg, L., Bidlot, J., Bormann, N., Delsol, C., Dragani, R., Fuentes, M., Geer, A. J., Haimberger, L., Healy, S. B., Hersbach, H., Holm, E. V., Isaksen, L., Kallberg, P., Koehler, M., Matricardi, M., McNally, A. P., Monge-Sanz, B. M., Morcrette, J. J., Park, B. K., Peubey, C., de Rosnay, P., Tavolato, C., Thepaut, J. N., and Vitart, F.: The ERA-Interim reanalysis: configuration and performance of the data assimilation system, Q. J. Roy. Meteor. Soc., 137, 553–597, doi:10.1002/qj.828, 2011.

Dietze, E., Maussion, F., Ahlborn, M., Diekmann, B., Hartmann, K., Henkel, K., Kasper, T., Lockot, G., Opitz, S., and Haberzettl, T.: Sediment transport processes across the Tibetan Plateau inferred from robust grain-size end members in lake sediments, Clim. Past, 10, 91–106, doi:10.5194/cp-10-91-2014, 2014.

Edel, C.: Fous Du Tibet. Six Découvreurs Du Toit Du Monde 1889-1908. Récits de Gabriel Bonvalot, Henri D'orléans, Jules Dutreuil De Rhins, Fernand Grenard, Ovché Narzounof, Sven Hedin. (in French), Editions des Riaux, doi:ISBN:978284901058, 2007.

Feng, L. and Zhou, T. J.: Water vapor transport for summer precipitation over the Tibetan Plateau: Multidata set analysis, J. Geophys. Res-Atmos., 117, D20 114, doi:10.1029/2011JD017012, 2012.

Finkelnburg, R.: Climate variability of Svalbard in the first decade of the 21st century and its impact on Vestfonna ice cap, Nordaustlandet : An analysis based on field observations, remote sensing and numerical modeling, Ph.D. thesis, Technische Universität Berlin, doi:urn:nbn:de:kobv:83-opus-39807, 2013.

Flohn, H.: Large-scale aspects of the "summer monsoon" in South and East Asia, J. Meteorol. Soc. Jpn., 75, 180–186, URL http://ci.nii.ac.jp/naid/10014595971/en/, 1957.

Fowler, H. J., Blenkinsop, S., and Tebaldi, C.: Linking climate change modelling to impacts studies: recent advances in downscaling techniques for hydrological modelling, Int. J. Climatol., 27, 1547–1578, doi:10.1002/joc.1556, 2007.

Gardner, A. S., Moholdt, G., Cogley, J. G., Wouters, B., Arendt, A. A., Wahr, J., Berthier, E., Hock, R., Pfeffer, W. T., Kaser, G., Ligtenberg, S. R. M., Bolch, T., Sharp, M. J., Hagen, J. O., van den Broeke, M. R., and Paul, F.: A Reconciled Estimate of Glacier Contributions to Sea Level Rise: 2003 to 2009, Science., 340, 852–857, doi:10.1126/science.1234532, 2013.

Gerken, T., Biermann, T., Babel, W., Herzog, M., Ma, Y., Foken, T., and Graf, H.: A modelling investigation into lake-breeze development and convection triggering in the Nam Co Lake basin, Tibetan Plateau, Theor. Appl. Climatol., doi:doi:10.1007/s00704-013-0987-9, 2013.

Gula, J. and Peltier, W. R.: Dynamical Downscaling over the Great Lakes Basin of North America Using the WRF Regional Climate Model: The Impact of the Great Lakes System on Regional Greenhouse Warming, J. Climate., 25, 7723–7742, doi:10.1175/JCLI-D-11-00388.1, 2012.

Haginoya, S., Fujii, H., Kuwagata, T., Xu, J., Ishigooka, Y., Kang, S., and Zhang, Y.: Air-Lake Interaction Features Found in Heat and Water Exchanges over Nam Co on the Tibetan Plateau, SOLA, 5, 172–175, doi:10.2151/sola.2009-044, 2009.

Hahn, D. and Manabe, S.: Role of mountains in south asian monsoon circulation, J. Atmos. Sci., 32, 1515–1541, 1975.

Held, I. M., Ting, M., and Wang, H.: Northern Winter Stationary Waves: Theory and Modeling, J. Climate., 15, 2125–2144, doi:10.1175/1520-0442(2002)015⟨2125:NWSWTA⟩2.0.CO;2, 2002.

Hou, A. Y., Kakar, R. K., Neeck, S., Azarbarzin, A. A., Kummerow, C. D., Kojima, M., Oki, R., Nakamura, K., and Iguchi, T.: The Global Precipitation Measurement (GPM) Mission, B. Am. Meteorol. Soc., pp. –, doi:10.1175/BAMS-D-13-00164.1, 2013.

Huintjes, E., Neckel, N., Maussion, F., Spieß, M., Scherer, D., Hochschild, V., Sauter, T., and Schneider, C.: Evolution of Purogangri Ice Cap, central Tibetan Plateau, 2000-2012 – a comparison of two glaciological methods., in: Himalayan Karakorum Tibet Workshop & International Symposium on Tibetan Plateau, Tübingen., 2013.

Immerzeel, W., van Beek, L., and Bierkens, M.: Climate Change Will Affect the Asian Water Towers, Science., 328, 1382–1385, doi:10.1126/science.1183188, 2010.

IPCC: Working group I contribution to the IPCC fifth assessment report - climate change 2013: the physical science basis - Chapter 4: Observations: Cryosphere - Final Draft Underlying Scientific-Technical Assessment, WMO, UNEP, 2013.

Jiang, Q., Fang, H., Li, Y., and Zhang, J.: Dynamic changes of lakes and the geo-mechanism in Tibet based on RS and GIS technology, vol. 7123, pp. 71 230S–71 230S–8, doi:10.1117/12.816189, 2008.

Kaab, A., Berthier, E., Nuth, C., Gardelle, J., and Arnaud, Y.: Contrasting patterns of early twenty-first-century glacier mass change in the Himalayas, Nature., 488, 495–498, doi:10.1038/nature11324, 2012.

Kain, J.: The Kain-Fritsch convective parameterization: An update, J. Appl. Meteorol., 43, 170–181, doi:10.1175/1520-0450(2004)043⟨0170:TKCPAU⟩2.0.CO;2, 2004.

Kang, S., Xu, Y., You, Q., Fluegel, W.-A., Pepin, N., and Yao, T.: Review of climate and cryospheric change in the Tibetan Plateau, Environ. Res. Lett., 5, 015 101, doi:10.1088/1748-9326/5/1/015101, 2010.

Kaser, G., Grosshauser, M., and Marzeion, B.: Contribution potential of glaciers to water availability in different climate regimes, P. Natl. Acad. Sci. Usa., 107, 20 223–20 227, doi:10.1073/pnas.1008162107, 2010.

Klein, C.: Analysis of near-surface temperature elevational gradients on the Tibetan Plateau based on regional reanalysis data for the decade 2001-2010 (in German), Master's thesis, Technische Universität Berlin, 2013.

Kristovich, D. and Spinar, M.: Diurnal variations in lake-effect precipitation near the Western Great Lakes, J. Hydrometeorol., 6, 210–218, 2004.

Kropacek, J., Feng, C., Alle, M., Kang, S., and Hochschild, V.: Temporal and Spatial Aspects of Snow Distribution in the Nam Co Basin on the Tibetan Plateau from MODIS Data, Remote Sensing, 2, 2700–2712, doi:10.3390/rs2122700, 2010.

Kropacek, J., Maussion, F., Chen, F., Hoerz, S., and Hochschild, V.: Analysis of ice phenology of lakes on the Tibetan Plateau from MODIS data, The Cryosphere, 7, 287–301, doi:10.5194/tc-7-287-2013, 2013.

Laird, N. F., Desrochers, J., and Payer, M.: Climatology of Lake-Effect Precipitation Events over Lake Champlain, J. Appl. Meteorol. Clim., 48, 232–250, doi:10.1175/2008JAMC1923.1, 2009.

Laprise, R., de Elia, R., Caya, D., Biner, S., Lucas-Picher, P., Diaconescu, E., Leduc, M., Alexandru, A., Separovic, L., and Climate, C. N. R.: Challenging some tenets of Regional Climate Modelling, Meteorol. Atmos. Phys., 100, 3–22, doi:10.1007/s00703-008-0292-9, 2008.

Li, M., Ma, Y., Hu, Z., Ishikawa, H., and Oku, Y.: Snow distribution over the Namco lake area of the Tibetan Plateau, Hydrol. Earth. Syst. Sc., 13, 2023–2030, 2009.

Liu, J., Kang, S., Gong, T., and Lu, A.: Growth of a high-elevation large inland lake, associated with climate change and permafrost degradation in Tibet, Hydrol. Earth. Syst. Sc., 14, 481–489, 2010.

MacCallum, S. and Merchant, C.: ARC-Lake v1.1, 1995-2009 [Dataset], URL http://hdl.handle.net/10283/88, 2011.

MacCallum, S. N. and Merchant, C. J.: Surface water temperature observations of large lakes by optimal estimation, Canadian Journal of Remote Sensing, 38, 25–45, doi:10.5589/m12-010, 2012.

Mannig, B., Müller, M., Starke, E., Merkenschlager, C., Mao, W., Zhi, X., Podzun, R., Jacob, D., and Paeth, H.: Dynamical downscaling of climate change in Central Asia, Global and Planetary Change, pp. –, doi:10.1016/j.gloplacha.2013.05.008, 2013.

Maraun, D., Wetterhall, F., Ireson, A. M., Chandler, R. E., Kendon, E. J., Widmann, M., Brienen, S., Rust, H. W., Sauter, T., Themessl, M., Venema, V. K. C., Chun, K. P., Goodess, C. M., Jones, R. G., Onof, C., Vrac, M., and Thiele-Eich, I.: Precipitation downscaling under climate change: recent developments to bridge the gap between dynamical models and the end user, Reviews of Geophysicseophysics, 48, doi:10.1029/2009RG000314, 2010.

Marzeion, B., Jarosch, A. H., and Hofer, M.: Past and future sea-level change from the surface mass balance of glaciers, The Cryosphere, 6, 1295–1322, doi:10.5194/tc-6-1295-2012, 2012.

Maussion, F., Scherer, D., Finkelnburg, R., Richters, J., Yang, W., and Yao, T.: WRF simulation of a precipitation event over the Tibetan Plateau, China - an assessment using remote sensing and ground observations, Hydrol. Earth. Syst. Sc., 15, 1795–1817, doi:10.5194/hess-15-1795-2011, 2011a.

Maussion, F., Wei, Y., Huintjes, E., Pieczonka, T., Scherer, D., Yao, T., Kang, S., Bolch, T., Buchroithner, M., and Schneider, C.: Glaciological field studies at Zhadang Glacier (5500–6095 m), Tibetan Plateau, Workshop on the use of automatic measuring systems on glaciers–Extended abstracts and recommendations of the IASC Workshop, edited by: Tijm-Reijmer, CH and Oerlemans, J, pp. 23–26, 2011b.

Maussion, F., Scherer, D., Mölg, T., Collier, E., Curio, J., and Finkelnburg, R.: Precipitation seasonality and variability over the Tibetan Plateau as resolved by the High Asia Reanalysis, J. Climate., 27, 1910–1927, doi:10.1175/JCLI-D-13-00282.1, 2014.

Mitchell, T. and Jones, P.: An improved method of constructing a database of monthly climate observations and associated high-resolution grids, Int. J. Climatol., 25, 693–712, doi:10.1002/joc.1181, 2005.

Mölg, T. and Kaser, G.: A new approach to resolving climate-cryosphere relations: Downscaling climate dynamics to glacier-scale mass and energy balance without statistical scale linking, J. Geophys. Res-Atmos., 116, D16 101, doi:10.1029/2011JD015669, 2011.

Mölg, T., Cullen, N. J., Hardy, D. R., Kaser, G., and Klok, L.: Mass balance of a slope glacier on Kilimanjaro and its sensitivity to climate, Int. J. Climatol., 28, 881–892, doi:10.1002/joc.1589, 2008.

Mölg, T., Cullen, N. J., Hardy, D. R., Winkler, M., and Kaser, G.: Quantifying Climate Change in the Tropical Midtroposphere over East Africa from Glacier Shrinkage on Kilimanjaro, J. Climate., 22, 4162–4181, doi:10.1175/2009JCLI2954.1, 2009.

Mölg, T., Maussion, F., and Scherer, D.: Mid-latitude westerlies as a driver of glacier variability in monsoonal High Asia, Nature Climate Change, 4, 68–73, doi:10.1038/nclimate2055, 2014.

Molnar, P., Boos, W. R., and Battisti, D. S.: Orographic Controls on Climate and Paleoclimate of Asia: Thermal and Mechanical Roles for the Tibetan Plateau, in: Annual Review Of Earth And Planetary Sciences, Vol 38, edited by Jeanloz, R. and Freeman, K., vol. 38 of *Annual Review of Earth and Planetary Sciences*, pp. 77–102, Annual Reviews, doi:10.1146/annurev-earth-040809-152456, 2010.

NCAR: Climate Data Guide from NCAR's Climate Analysis Section, [Available online at http://climatedataguide.ucar.edu], 2013.

NCEP: NCEP FNL Operational Model Global Tropospheric Analyses, continuing from July 1999, URL http://rda.ucar.edu/datasets/ds083.2, 2000.

Neckel, N., Braun, A., Kropáček, J., and Hochschild, V.: Recent mass balance of the Purogangri Ice Cap, central Tibetan Plateau, by means of differential X-band SAR interferometry, The Cryosphere, 7, 1623–1633, doi:10.5194/tc-7-1623-2013, 2013.

Oliver, J. E.: Reanalysis projects, in: Encyclopedia of world climatology, edited by Oliver, J. E., pp. 615–617, Springer-Verlag, 2005.

Opitz, S., Wünnemann, B., Aichner, B., Dietze, E., Hartmann, K., Herzschuh, U., IJmker, J., Lehmkuhl, F., Li, S., Mischke, S., Plotzki, A., Stauch, G., and Diekmann, B.: Late Glacial and Holocene development of Lake Donggi Cona, north-eastern Tibetan Plateau, inferred from sedimentological analysis, Palaeogeography, Palaeoclimatology, Palaeoecology, 337–338, 159 – 176, doi:http://dx.doi.org/10.1016/j.palaeo.2012.04.013, 2012.

Oreskes, N., Shrader-Frechette, K., and Belitz, K.: Verification, Validation, and Confirmation of Numerical Models in the Earth Sciences, Science., 263, 641–646, doi:10.1126/science.263.5147.641, 1994.

Palazzi, E., von Hardenberg, J., and Provenzale, A.: Precipitation in the Hindu-Kush Karakoram Himalaya: Observations and future scenarios, Journal of Geophysical Research: Atmospheres, 118, 85–100, doi:10.1029/2012JD018697, 2013.

Phan, V. H., Lindenbergh, R. C., and Menenti, M.: Geometric dependency of Tibetan lakes on glacial runoff, Hydrol. Earth. Syst. Sc., 17, 4061–4077, doi:10.5194/hess-17-4061-2013, 2013.

Pohl, B., Cretat, J., and Camberlin, P.: Testing WRF capability in simulating the atmospheric water cycle over Equatorial East Africa, Clim. Dynam., 37, 1357–1379, doi:10.1007/s00382-011-1024-2, 2011.

Prasad, V. S. and Hayashi, T.: Active, weak and break spells in the Indian summer monsoon, Meteorol. Atmos. Phys., 95, 53–61, doi:10.1007/s00703-006-0197-4, 2007.

Qin, J., Yang, K., Liang, S., and Guo, X.: The altitudinal dependence of recent rapid warming over the Tibetan Plateau, Climatic. Change., 97, 321–327, doi:10.1007/s10584-009-9733-9, 2009.

Qiu, J.: China: The third pole, Nature News, 454, 393–396, 2008.

Rajagopalan, B. and Molnar, P.: Signatures of Tibetan Plateau heating on Indian summer monsoon rainfall variability, Journal of Geophysical Research: Atmospheres, 118, 1170–1178, doi:10.1002/jgrd.50124, 2013.

Rakesh, V., Singh, R., Pal, P. K., and Joshi, P. C.: Sensitivity of mesoscale model forecast during a satellite launch to different cumulus parameterization schemes in MM5, Pure. Appl. Geophys., 164, 1617–1637, doi:10.1007/s00024-007-0245-0, 2007.

Rupper, S. and Roe, G.: Glacier Changes and Regional Climate: A Mass and Energy Balance Approach, J. Climate., 21, 5384–5401, doi:10.1175/2008JCLI2219.1, 2008.

Rüthrich, F., Thies, B., Reudenbach, C., and Bendix, J.: Cloud detection and analysis on the Tibetan Plateau using Meteosat and CloudSat, Journal of Geophysical Research: Atmospheres, pp. n/a–n/a, doi:10.1002/jgrd.50790, 2013.

Samuelsson, P., Kourzeneva, E., and Mironov, D.: The impact of lakes on the European climate as simulated by a regional climate model, Boreal Environment Research, 15, 113–129, 2010.

Schiemann, R., Luethi, D., and Schaer, C.: Seasonality and Interannual Variability of the Westerly Jet in the Tibetan Plateau Region, J. Climate., 22, 2940–2957, doi:10.1175/2008JCLI2625.1, 2009.

Schneider, D. P., Deser, C., Fasullo, J., and Trenberth, K. E.: Climate Data Guide Spurs Discovery and Understanding, Eos, Transactions American Geophysical Union, 94, 121–122, doi:10.1002/2013EO130001, 2013.

Schütt, B., Berking, J., Frechen, M., and Yi, C.: Late Pleistocene Lake Level Fluctuations of the Nam Co, Tibetan Plateau, China, Zeitschrift für Geomorphologie, Supplementary Issues, 52, 57–75, doi:doi:10.1127/0372-8854/2008/0052S2-0057, 2008.

Shea, J. D., Worley, S. J., Stern, I. R., and Hoar, T. J.: An Introduction to Atmospheric and Oceanographic Data, NCAR Tech. Note NCAR/TN-404+IA, National Center for Atmospheric Research (NCAR), Climate and Global Dynamics Division, 1994.

Shi, Y. and Liu, S.: Estimation on the response of glaciers in China to the global warming in the 21st century, Chinese. Sci. Bull., 45, 668–672, 2000.

Skamarock, W. C. and Klemp, J. B.: A time-split nonhydrostatic atmospheric model for weather research and forecasting applications, J. Comput. Phys., 227, 3465–3485, doi:10.1016/j.jcp.2007.01.037, 2008.

Stauch, G., IJmker, J., Pötsch, S., Zhao, H., Hilgers, A., Diekmann, B., Dietze, E., Hartmann, K., Opitz, S., Wünnemann, B., and Lehmkuhl, F.: Aeolian sediments on the north-eastern Tibetan Plateau, Quaternary Science Reviews, 57, 71 – 84, doi:http://dx.doi.org/10.1016/j.quascirev.2012.10.001, 2012.

Takahashi, K. and Battisti, D. S.: Processes controlling the mean tropical pacific precipitation pattern. Part I: The Andes and the eastern Pacific ITCZ, J. Climate., 20, 3434–3451, doi:10.1175/JCLI4198.1, 2007.

Tao, S. and Ding, Y.: Observational evidence of the influence of the qinghai-xizang (tibet) plateau on the occurrence of heavy rain and severe convective storms in china, B. Am. Meteorol. Soc., 62, 23–30, 1981.

Tong, K., Su, F., Yang, D., Zhang, L., and Hao, Z.: Tibetan Plateau precipitation as depicted by gauge observations, reanalyses and satellite retrievals, Int. J. Climatol., pp. n/a–n/a, doi:10.1002/joc.3682, 2013.

Uppala, S., Kallberg, P., Simmons, A., Andrae, U., Bechtold, V., Fiorino, M., Gibson, J., Haseler, J., Hernandez, A., Kelly, G., Li, X., Onogi, K., Saarinen, S., Sokka, N., Allan, R., Andersson, E., Arpe, K., Balmaseda, M., Beljaars, A., Van De Berg, L., Bidlot, J., Bormann, N., Caires, S., Chevallier, F., Dethof, A., Dragosavac, M., Fisher, M., Fuentes, M., Hagemann, S., Holm, E., Hoskins, B., Isaksen, L., Janssen, P., Jenne, R., McNally, A., Mahfouf, J., Morcrette, J., Rayner, N., Saunders, R., Simon, P., Sterl, A., Trenberth, K., Untch, A., Vasiljevic, D., Viterbo, P., and Woollen, J.: The ERA-40 re-analysis, Q. J. Roy. Meteor. Soc., 131, 2961–3012, doi:10.1256/qj.04.176, 2005.

Wang, B.: The Asian Monsoon, Springer-Praxis books in environmental sciences, 2006.

Wang, Y., Leung, L., McGregor, J., Lee, D., Wang, W., Ding, Y., and Kimura, F.: Regional climate modeling: Progress, challenges, and prospects, J. Meteorol. Soc. Jpn., 82, 1599–1628, 2nd Workshop on Regional Climate Modeling for Monson Systems, Yokohama, JAPAN, MAR 04-06, 2003, 2004.

Wilby, R. and Wigley, T.: Downscaling general circulation model output: a review of methods and limitations, Prog. Phys. Geog., 21, 530–548, doi:10.1177/030913339702100403, 1997.

Wilson, J.: Effect of Lake Ontario on precipitation, Mon. Weather. Rev., 105, 207–214, 1977.

Wu, G., Liu, Y., He, B., Bao, Q., Duan, A., and Jin, F.-F.: Thermal Controls on the Asian Summer Monsoon, Scientific Reports, 2, 404, doi:10.1038/srep00404, 2012.

Yang, M. and Tung, Q.: Evaluation of rainfall forecasts over Taiwan by four cumulus parameterization schemes, J. Meteorol. Soc. Jpn., 81, 1163–1183, 2003.

Yao, T., Thompson, L., Yang, W., Yu, W., Gao, Y., Guo, X., Yang, X., Duan, K., Zhao, H., Xu, B., Pu, J., Lu, A., Xiang, Y., Kattel, D. B., and Joswiak, D.: Different glacier status with atmospheric circulations in Tibetan Plateau and surroundings, Nature Climate Change, doi: 10.1038/nclimate1580, 2012.

Yao, T., Masson-Delmotte, V., Gao, J., Yu, W., Yang, X., Risi, C., Sturm, C., Werner, M., Zhao, H., He, Y., Ren, W., Tian, L., Shi, C., and Hou, S.: A review of climatic controls on $\delta^{18}O$ in precipitation over the Tibetan Plateau: Observations and simulations, Rev. Geophys., pp. n/a–n/a, doi:10.1002/rog.20023, 2013.

Yaodong, L., Yun, W., Yang, S., Liang, H., Shouting, G., and Fu, R.: Characteristics of Summer Convective Systems Initiated over the Tibetan Plateau. Part I: Origin, Track, Development, and Precipitation, J. Appl. Meteorol. Clim., 47, 2679–2695, doi:10.1175/2008JAMC1695.1, 2008.

Yatagai, A., Kamiguchi, K., Arakawa, O., Hamada, A., Yasutomi, N., and Kitoh, A.: APHRODITE Constructing a Long-Term Daily Gridded Precipitation Dataset for Asia Based on a Dense Network of Rain Gauges, B. Am. Meteorol. Soc., 93, 1401–1415, doi: 10.1175/BAMS-D-11-00122.1, 2012.

Ye, D.: Some characteristics of the summer circulation over the qinghai-xizang (tibet) plateau and its neighborhood, B. Am. Meteorol. Soc., 62, 14–19, 1981.

You, Q., Kang, S., Pepin, N., Fluegel, W.-A., Yan, Y., Behrawan, H., and Huang, J.: Relationship between temperature trend magnitude, elevation and mean temperature in the Tibetan Plateau from homogenized surface stations and reanalysis data, Global. Planet. Change., 71, 124–133, doi:10.1016/j.gloplacha.2010.01.020, 2010.

You, Q., Fraedrich, K., Ren, G., Ye, B., Meng, X., and Kang, S.: Inconsistencies of precipitation in the eastern and central Tibetan Plateau between surface adjusted data and reanalysis, Theor. Appl. Climatol., 109, 485–496, doi:10.1007/s00704-012-0594-1, 2012.

Zhang, G., Kang, S., Fujita, K., Huintjes, E., Xu, J., Yamazaki, T., Haginoya, S., Wei, Y., Scherer, D., Schneider, C., and Yao, T.: Energy and mass balance of Zhadang glacier surface, central Tibetan Plateau, J. Glaciol., 59, 137–148, doi:doi:10.3189/2013JoG12J152, 2013a.

Zhang, G., Yao, T., Xie, H., Kang, S., and Lei, Y.: Increased mass over the Tibetan Plateau: From lakes or glaciers?, Geophys. Res. Lett., 40, 2125–2130, doi:10.1002/grl.50462, 2013b.

Zhou, T., Yu, R., Chen, H., Dai, A., and Pan, Y.: Summer precipitation frequency, intensity, and diurnal cycle over China: A comparison of satellite data with rain gauge observations, J. Climate., 21, 3997–4010, doi:10.1175/2008JCLI2028.1, 2008.

Acknowledgements

I would like to warmly thank Dieter Scherer, whom I met when I was a student heading towards a carrier as an aerospace engineer. He trusted me and offered me the possibility to do some "seeing around" (at least I was thinking so the day I started this PhD). He is a never-ending source of ideas and a great supervisor.

My passion for climate science and for glaciers did not come alone, but thanks to the many encounters which inspired me and gave me confidence to go further. Christoph meditating near Nam Co lake, or a walk back to the conference hotel under Tromsø's midnight sun with Georg certainly belong to these moments. I am also very grateful to Thomas, whom I could visit at Innsbruck for a simple WRF meeting, which turned out to be the start of a great collaboration. Special thanks go to Emily, Roman, Fredo, Marco, Juli, Dani, Britta, Vanessa, Tom, Alex, Albert, Christian, Hartmut, Ingo, Heidi, everyone at the institute for the friendship (always) and the high-level scientific discussions (sometimes). Many thanks also to my fellow Tibet explorers Eva, Tobi, Tino, Sophie, Champ', Manfred, Jan, Niklas, Frank, Nicolai, Marinka, Oli, Volker, Holm, Manfred...

During my "seven trips to Tibet" I was very lucky to meet my friend and colleague Yang Wei. Against all odds, he managed to bring everyone to the Glacier and back home (alive). I would have never get to know and appreciate China so well without the long fruitful discussions we had together.

I would also like to mention the DFG TiP and BMBF CAME programmes, especially their "early carrier" programme which was very stimulating and through which I met so many great people.

Finally, my very personal thanks go to Cornelia, to my family and to my friends, for their support through the good and the hard times.

Lake La'nga Co near Mount Kailash and Lake Mapam Yumco. Photo by F.M., August 2012.